Dissertation zur Erlangung des Doktorgrades
der Fakultät für Chemie und Pharmazie
der Ludwig-Maximilians-Universität München

Synthesis, Characterisation and DFT Analysis of $\{Ru(NO)_2\}^8$ Compounds

Anna Katharina Elisabeth Gallien, geb. Filser

aus

Mainz, Deutschland

2014

Erklärung

Diese Dissertation wurde im Sinne von § 7 der Promotionsordnung vom 28. November 2011 von Herrn Prof. Dr. Peter Klüfers betreut.

Eidesstattliche Versicherung

Diese Dissertation wurde eigenständig und ohne unerlaubte Hilfe erarbeitet.

München, 17.01.2014

Anna Gallien

Dissertation eingereicht am: 17.01.2014

1. Gutachter: Prof. Dr. Peter Klüfers

2. Gutachter: Prof. Dr. H.-C. Böttcher

Mündliche Prüfung am: 26.02.2014

Diese Arbeit wurde in der Zeit von Oktober 2009 bis Januar 2014 am Departement für Chemie und Pharmazie der Ludwig-Maximilians-Universität München am Lehrstuhl für Bioanorganische Chemie und Koordinationschemie unter Anleitung von Herrn Prof. Dr. Peter Klüfers durchgeführt.

Table of contents

List of Figures

List of tables

Abbreviations

ADP	atomic displacement parameter
Bn	benzyl
CaM	calcium/calmodulin
cGMP	cyclic guanosine monophosphate
Cy	cyclohexyl
Cyp	cyclopentyl
DCM	dichloromethane
diazald	*N*-methyl-*N*-nitroso-*p*-toluenesulfonamide
DSC	differential scanning calorimetry
EA	elemental analysis
EI	electron ionisation
eNOS	endothelial nitric oxide synthase
Et	ethyl
FAB	fast atom bombardement
GC	guanylyl cyclase
GTP	guanosine triphosphate
Hb	desoxy-hemoglobin
iNOS	inducible nitric oxide synthase
^{i}Pr	*iso*-propyl
IR	infrared spectroscopy
m	medium
Mb	desoxy-myoglobin
Me	methyl
metHb	met-hemoglobin
metMb	met-myoglobin
MS	mass spectrometry
NMR	nuclear magnetic resonance
nNOS	neuronal nitric oxide synthase
NOS	nitric oxide synthase

oxyHb	oxy-hemoglobin
Ph	phenyl
PLI	photoinduced linkage isomerism
RRS	Roussin's red salt
s	strong
sGC	soluble guanylyl cyclase
SPY-5	square pyramid
^{t}Bu	*tert*-butyl
TBPY-5	trigonal bipyramid
THF	tetrahydrofurane
TNG	trinitroglycerin
VOC-5	vacant octahedron
vs	very strong
vw	very weak
w	weak

Ligand overview

PPh_3 = triphenylphosphane

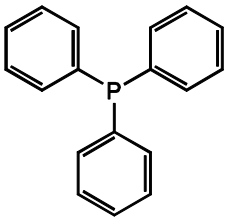

$C_{18}H_{15}P$
M_r = 262.29 g/mol

PPh_2Bn = benzyldiphenylphosphane

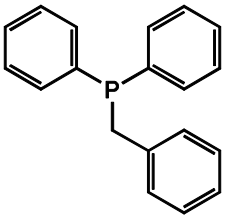

$C_{19}H_{17}P$
M_r = 276.11 g/mol

P(*p*-tolyl)$_3$ = tri(*para*-tolyl)phosphane

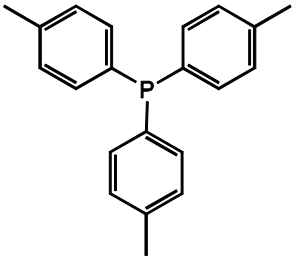

$C_{21}H_{21}P$
M_r = 304.37 g/mol

$PPh_2{}^tBu$ = *tert*-butyldiphenylphosphane

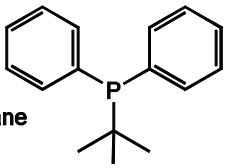

$C_{16}H_{19}P$
M_r = 242.30 g/mol

P(*p*-PhOMe)$_3$ = tri(4-methoxyphenyl)phosphane

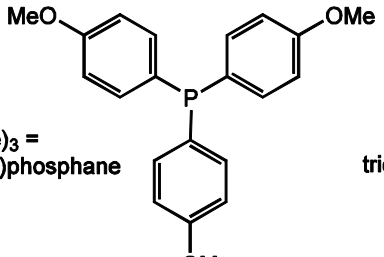

$C_{21}H_{21}O_3P$
M_r = 352.36 g/mol

PCy_3 = tricyclohexylphosphane

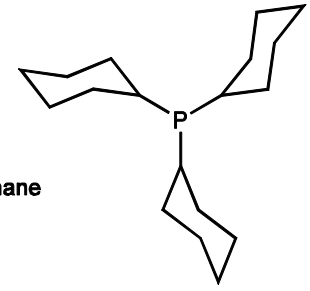

$C_{18}H_{33}P$
M_r = 280.43 g/mol

P^iPr_3 = tri-isopropylphosphane

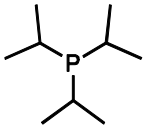

$C_9H_{21}P$
M_r = 160.24 g/mol

$PCyp_3$ = tricyclopentylphosphane

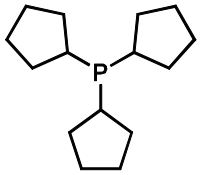

$C_{15}H_{27}P$
M_r = 238.35 g/mol

Precursor compounds and their numbering

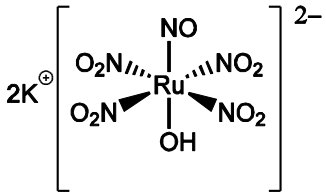

$K_2[Ru(NO_2)_4(OH)(NO)]$
$HK_2N_5O_{10}Ru$
M_r = 410.30 g mol^{-1}

2

$RuCl_3(NO) \cdot x\ H_2O$

1

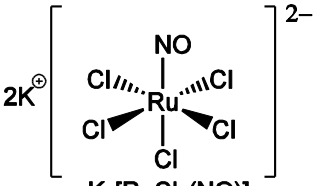

$K_2[RuCl_5(NO)]$
Cl_5K_2NORu
M_r = 386.54 g mol^{-1}

3

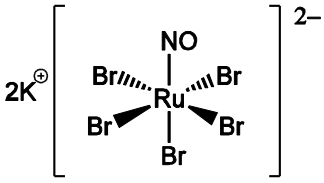

$K_2[RuBr_5(NO)]$
Br_5K_2NORu
M_r = 608.79 g mol^{-1}

4

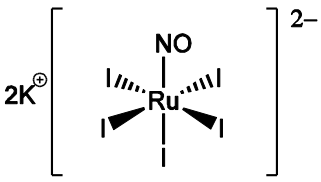

$K_2[RuI_5(NO)]$
I_5K_2NORu
M_r = 843.79 g mol^{-1}

5

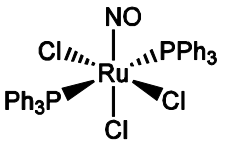

$[RuCl_3(NO)(PPh_3)_2]$
$C_{36}H_{30}Cl_3NOP_2Ru$
M_r = 762.01 g mol^{-1}

6a

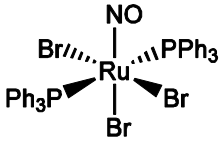

$[RuBr_3(NO)(PPh_3)_2]$
$C_{36}H_{30}Br_3NOP_2Ru$
M_r = 895.36 g mol^{-1}

7a

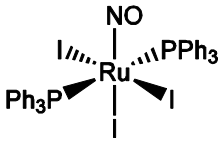

$[RuI_3(NO)(PPh_3)_2]$
$C_{36}H_{30}I_3NOP_2Ru$
M_r = 1036.36 g mol^{-1}

8a*

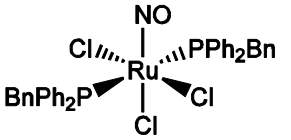

$[RuCl_3(NO)(PPh_2Bn)_2]$
$C_{38}H_{34}Cl_3NOP_2Ru$
M_r = 790.64 g mol^{-1}

9a

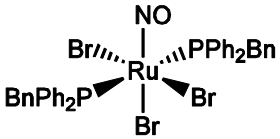

$[RuBr_3(NO)(PPh_2Bn)_2]$
$C_{38}H_{34}Br_3NOP_2Ru$
M_r = 923.41 g mol^{-1}

10a

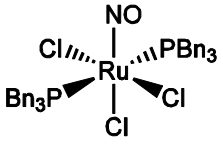

$[RuCl_3(NO)(PBn_3)_2]$
$C_{42}H_{42}Cl_3NOP_2Ru$
M_r = 846.17 g mol^{-1}

11a

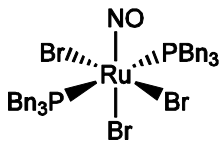

$[RuBr_3(NO)(PBn_3)_2]$
$C_{42}H_{42}Br_3NOP_2Ru$
M_r = 979.52 g mol^{-1}

12a

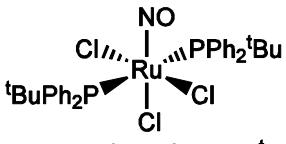

$[RuCl_3(NO)(PPh_2{}^tBu)_2]$
$C_{32}H_{38}Br_3NOP_2Ru$
M_r = 722.03 g mol^{-1}

13a

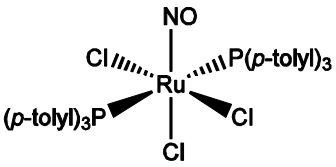

$C_{42}H_{42}Cl_3NOP_2Ru$

M_r = 846.17 g mol $^{-1}$

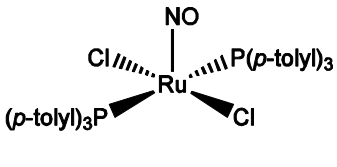

$C_{42}H_{42}Cl_2NOP_2Ru$

M_r = 810.71 g mol $^{-1}$

$C_{42}H_{42}ClNOP_2Ru$

M_r = 775.16 g mol $^{-1}$

$[RuCl_{1\text{-}3}(NO)\{P(p\text{-tolyl})_3\}_2]$

14a*

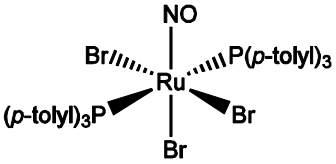

$C_{42}H_{42}Br_3NOP_2Ru$

M_r = 979.51 g mol $^{-1}$

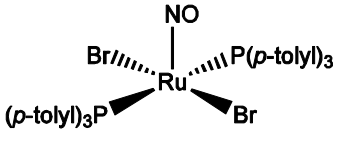

$C_{42}H_{42}Br_2NOP_2Ru$

M_r = 899.61 g mol $^{-1}$

$C_{42}H_{42}BrNOP_2Ru$

M_r = 819.71 g mol $^{-1}$

$[RuBr_{1\text{-}3}(NO)\{P(p\text{-tolyl})_3\}_2]$

15a*

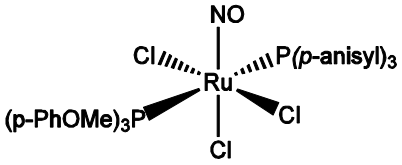

$C_{42}H_{42}Cl_3NO_7P_2Ru$

M_r = 942.61 g mol $^{-1}$

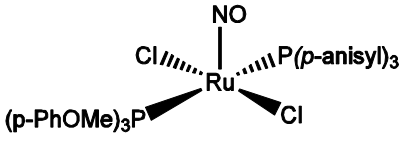

$C_{42}H_{42}Cl_2NO_7P_2Ru$

M_r = 906.70 g mol $^{-1}$

$[RuCl_{2\text{-}3}(NO)\{P(p\text{-anisyl})_3\}_2]$

16a*

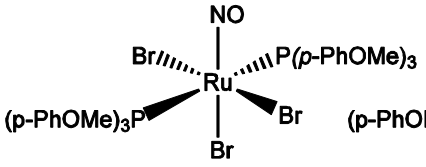

$C_{42}H_{42}Br_3NO_7P_2Ru$

M_r = 1075.51 g mol $^{-1}$

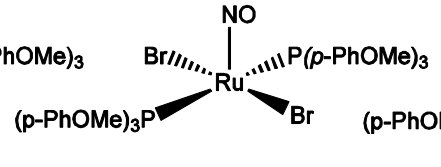

$C_{42}H_{42}Br_2NO_7P_2Ru$

M_r = 995.61 g mol $^{-1}$

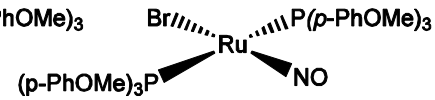

$C_{42}H_{42}BrNO_7P_2Ru$

M_r = 915.70 g mol $^{-1}$

$[RuBr_{1\text{-}3}(NO)\{P(p\text{-anisyl})_3\}_2]$

17a*

*Products were isolated as a $\{RuNO\}^n$ mixture.

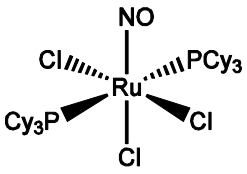

$C_{36}H_{66}Cl_3NOP_2Ru$

M_r = 798.29 g mol $^{-1}$

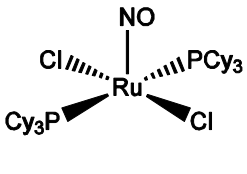

$C_{36}H_{66}Cl_2NOP_2Ru$

M_r = 762.84 g mol $^{-1}$

$C_{36}H_{66}ClNOP_2Ru$

M_r =727.39 g mol $^{-1}$

$[RuCl_{1\text{-}3}(NO)(PCy_3)_2]$

18a*

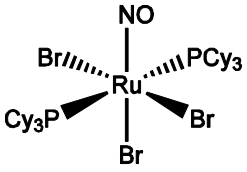

$C_{36}H_{66}Br_3NOP_2Ru$

M_r = 931.64 g mol $^{-1}$

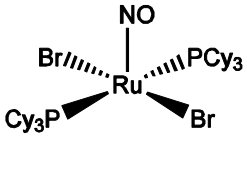

$C_{36}H_{66}Br_2NOP_2Ru$

M_r = 851.74 g mol $^{-1}$

$C_{36}H_{66}BrNOP_2Ru$

M_r = 771.84 g mol $^{-1}$

$[RuBr_{1\text{-}3}(NO)(PCy_3)_2]$

19a*

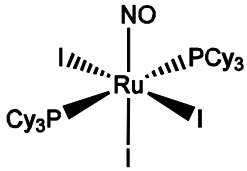

$C_{36}H_{66}I_3NOP_2Ru$

M_r = 1072.64 g mol $^{-1}$

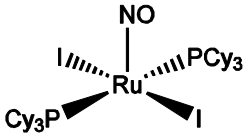

$C_{36}H_{66}I_2NOP_2Ru$

M_r = 945.74 g mol $^{-1}$

$C_{36}H_{66}INOP_2Ru$

M_r = 818.84 g mol $^{-1}$

$[RuI_{1\text{-}3}(NO)(PCy_3)_2]$

20a*

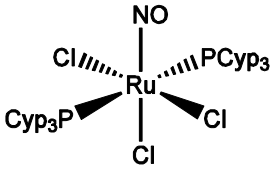

$C_{30}H_{54}Cl_3NOP_2Ru$

M_r = 714.13 g mol $^{-1}$

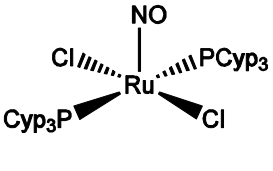

$C_{30}H_{54}Cl_2NOP_2Ru$

M_r = 678.68 g mol $^{-1}$

$C_{30}H_{54}ClNOP_2Ru$

M_r = 643.23 g mol $^{-1}$

$[RuCl_{1\text{-}3}(NO)(PCyp_3)_2]$

21a*

*Products were isolated as a $\{RuNO\}^n$ mixture.

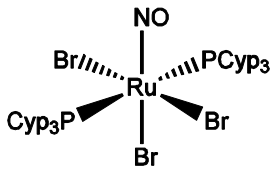

$C_{30}H_{54}Br_3NOP_2Ru$
M_r = 847.49 g mol $^{-1}$

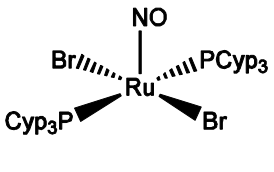

$C_{30}H_{54}Br_2NOP_2Ru$
M_r = 767.58 g mol $^{-1}$

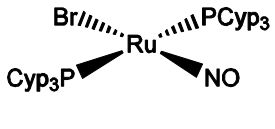

$C_{30}H_{54}BrNOP_2Ru$
M_r = 687.68 g mol $^{-1}$

$[RuBr_{1\text{-}3}(NO)(PCyp_3)_2]$

22a*

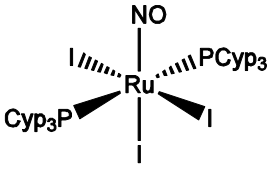

$C_{30}H_{54}I_3NOP_2Ru$
M_r = 988.49 g mol $^{-1}$

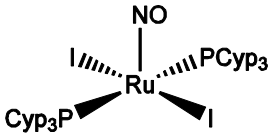

$C_{30}H_{54}I_2NOP_2Ru$
M_r = 861.58 g mol $^{-1}$

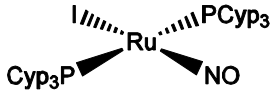

$C_{30}H_{54}INOP_2Ru$
M_r = 734.68 g mol $^{-1}$

$[RuI_{1\text{-}3}(NO)(PCyp_3)_2]$

23a*

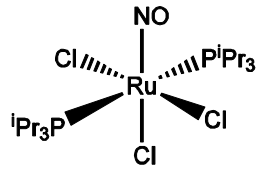

$C_{18}H_{42}Cl_3NOP_2Ru$
M_r = 557.91 g mol $^{-1}$

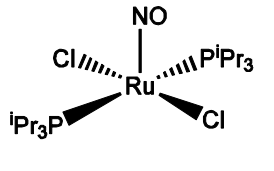

$C_{18}H_{42}Cl_2NOP_2Ru$
M_r = 522.46 g mol $^{-1}$

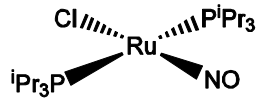

$C_{18}H_{42}ClNOP_2Ru$
M_r = 487.00 g mol $^{-1}$

$[RuCl_{1\text{-}3}(NO)(P^iPr_3)_2]$

24a*

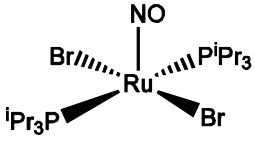

$C_{18}H_{42}Br_2NOP_2Ru$
M_r = 611.36 g mol $^{-1}$

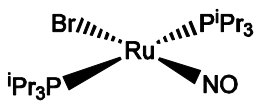

$C_{18}H_{42}BrNOP_2Ru$
M_r = 531.45 g mol $^{-1}$

$[RuBr_{1\text{-}2}(NO)(PiPr_3)_2]$

25a*

*Products were isolated as a $\{RuNO\}^n$ mixture.

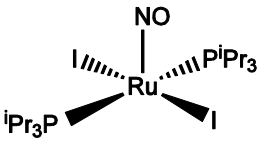

$C_{18}H_{42}I_2NOP_2Ru$

M_r = 705.36 g mol $^{-1}$

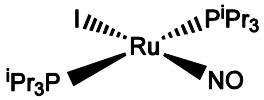

$C_{18}H_{42}INOP_2Ru$

M_r = 578.45 g mol $^{-1}$

$[RuI_{1\text{-}2}(NO)(P^iPr_3)_2]$

26a*

*Product was isolated as a $\{RuNO\}^n$ mixture.

Dinitrosyl compounds and their numbering

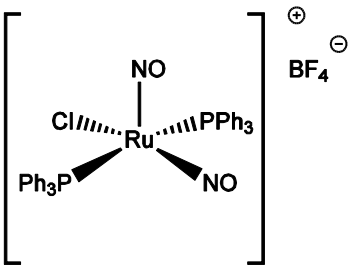

$[RuCl(NO)_2(PPh_3)_2]BF_4$

$C_{36}H_{30}BClF_4N_2O_2P_2Ru$

M_r = 807.91 g mol $^{-1}$

6b

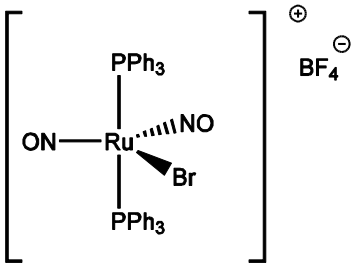

$[RuBr(NO)_2(PPh_3)_2]BF_4$

$C_{36}H_{30}BBrF_4N_2O_2P_2Ru$

M_r = 852.36 g mol $^{-1}$

7b

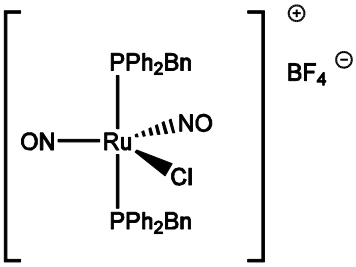

$[RuCl(NO)_2(PPh_2Bn)_2]BF_4$

$C_{38}H_{34}BClF_4N_2O_2P_2Ru$

M_r = 835.96 g mol $^{-1}$

9b

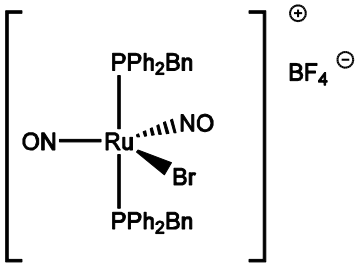

$[RuBr(NO)_2(PPh_2Bn)_2]BF_4$

$C_{38}H_{34}BBrF_4N_2O_2P_2Ru$

M_r = 880.41 g mol $^{-1}$

10b

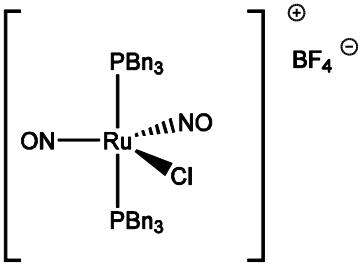

$[RuCl(NO)_2(PBn_3)_2]BF_4$

$C_{42}H_{42}BClF_4N_2O_2P_2Ru$

M_r = 892.07 g mol $^{-1}$

11b

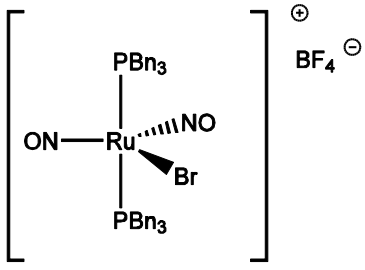

$[RuBr(NO)_2(PBn_3)_2]BF_4$

$C_{42}H_{42}BBrF_4N_2O_2P_2Ru$

M_r = 936.52 g mol $^{-1}$

12b

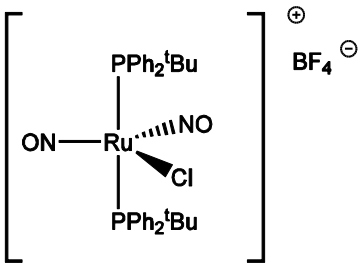

$[RuCl(NO)_2(PPh_2{}^tBu)_2]BF_4$

$C_{32}H_{38}BClF_4N_2O_2P_2Ru$

M_r = 767.93 g mol^{-1}

13b

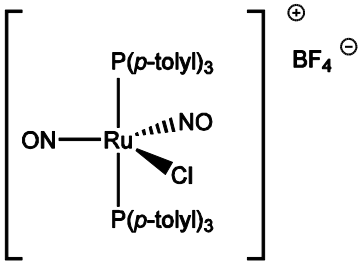

$[RuCl(NO)_2\{P(p\text{-tolyl})_3\}_2]BF_4$

$C_{42}H_{42}BClF_4N_2O_2P_2Ru$

M_r = 892.07 g mol^{-1}

14b

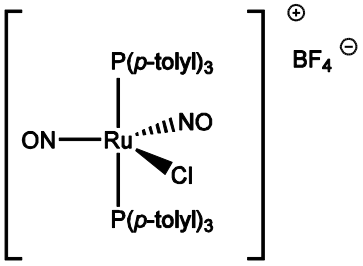

$[RuBr(NO)_2\{P(p\text{-tolyl})_3\}_2]BF_4$

$C_{42}H_{42}BBrF_4N_2O_2P_2Ru$

M_r = 936.52 g mol^{-1}

15b

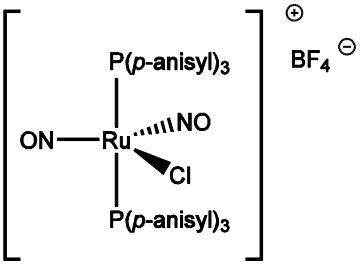

$[RuCl(NO)_2\{P(p\text{-anisyl})_3\}_2]BF_4$

$C_{42}H_{42}BClF_4N_2O_7P_2Ru$

M_r = 972.06 g mol^{-1}

16b

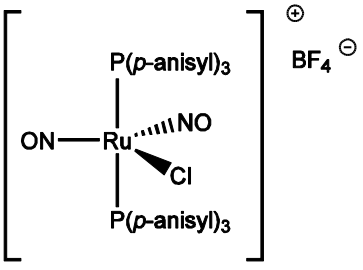

$[RuBr(NO)_2\{P(p\text{-anisyl})_3\}_2]BF_4$

$C_{42}H_{42}BBrF_4N_2O_7P_2Ru$

M_r = 1016.51 g mol^{-1}

17b

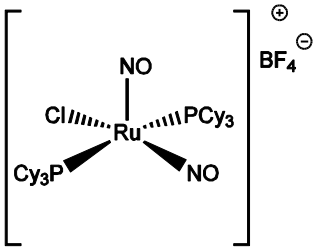

$[RuCl(NO)_2(PCy_3)_2]BF_4$

$C_{36}H_{66}BClF_4N_2O_2P_2Ru$

M_r: 844.20 g mol^{-1}

18b

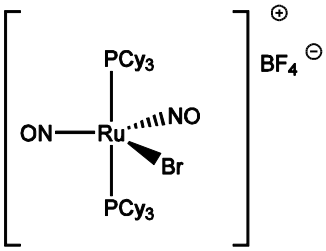

$[RuBr(NO)_2(PCy_3)_2]BF_4$

$C_{36}H_{66}BBrF_4N_2O_2P_2Ru$

Mr = 888.65 g mol^{-1}

19b

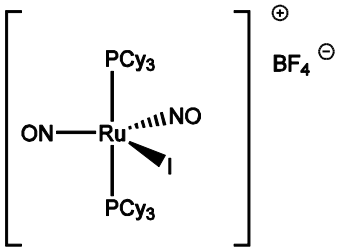

$[RuI(NO)_2(PCy_3)_2]BF_4$

$C_{36}H_{66}BIF_4N_2O_2P_2Ru$

Mr = 935.65 g mol^{-1}

20b-1
20b-2

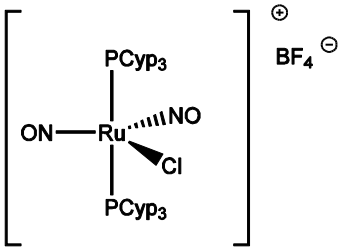

$[RuCl(NO)_2(PCyp_3)_2]BF_4$

$C_{30}H_{54}BClF_4N_2O_2P_2Ru$

M_r = 760.04 g mol^{-1}

21b-1
21b-2

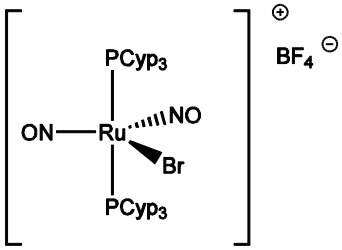

$[RuBr(NO)_2(PCyp_3)_2]BF_4$

$C_{30}H_{54}BBrF_4N_2O_2P_2Ru$

M_r = 804.49 g mol^{-1}

22b

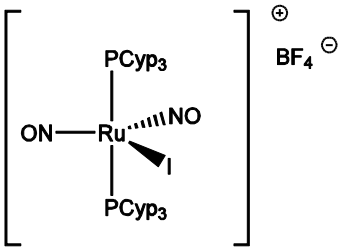

$[RuI(NO)_2(PCyp_3)_2]BF_4$

$C_{30}H_{54}BIF_4N_2O_2P_2Ru$

M_r = 851.49 g mol^{-1}

23b

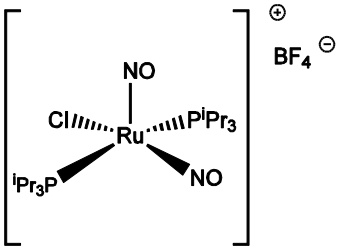

$[RuCl(NO)_2(P^iPr_3)_2]BF_4$

$C_{18}H_{42}BClF_4N_2O_2P_2Ru$

M_r = 603.81 g mol^{-1}

24b

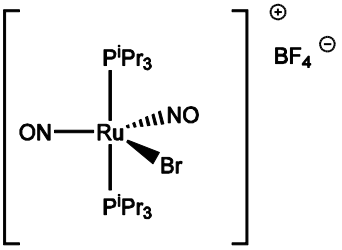

$[RuBr(NO)_2(P^iPr_3)_2]BF_4$

$C_{18}H_{42}BBrF_4N_2O_2P_2Ru$

M_r = 648.26 g mol^{-1}

25b-1
25b-2

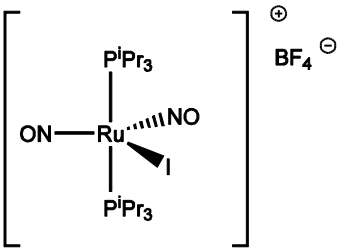

$[RuI(NO)_2(P^iPr_3)_2]BF_4$

$C_{18}H_{42}BIF_4N_2O_2P_2Ru$

M_r = 695.26 g mol^{-1}

26b-1
26b-2

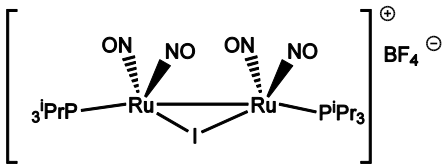

$[\{Ru(NO)_2(P^iPr_3)\}_2(\mu\text{-}I)]BF_4$

$C_{18}H_{42}BIF_4N_4O_4P_2Ru_2$

M_r = 856.35 g mol^{-1}

26c

Listing of the crystalline compounds

Index	Compound	Net formula	M_r /g mol^{-1}
	Mononitrosyls		
6c*	$[RuCl(NO)(PPh_3)_2]$	$C_{36}H_{30}ClNOP_2Ru$	691.10
7c*	$[\{RuBr_2(NO)(PPh_3)\}_2(\mu\text{-}Br)_2]$	$C_{36}H_{30}Br_6N_2O_2P_2Ru_2$	1165.07
8a*	$[RuI_3(NO)(PPh_3)_2]$	$C_{36}H_{30}I_3NOP_2Ru$	1036.36
8c*	$[\{RuI_2(NO)(PPh_3)\}_2(\mu\text{-}I)_2]$	$C_{36}H_{30}I_6N_2O_2P_2Ru_2$	1447.08
13c*	$[RuCl(NO)(PPh_2{}^tBu)_2]$	$C_{32}H_{38}ClNOP_2Ru$	651.17
	Dinitrosyls		
6b*	$[RuCl(NO)_2(PPh_3)_2]BF_4$	$C_{36}H_{30}BClF_4N_2O_2P_2Ru$	807.91
7b*	$[RuBr(NO)_2(PPh_3)_2]BF_4$	$C_{36}H_{30}BBrF_4N_2O_2P_2Ru$	852.36
9b*	$[RuCl(NO)_2(PBnPh_2)_2]BF_4$	$C_{38}H_{34}BClF_4N_2O_2P_2Ru$	835.96
10b*	$[RuBr(NO)_2(PBnPh_2)_2]BF_4$	$C_{38}H_{34}BClF_4N_2O_2P_2Ru$	880.41
14b*	$[RuCl(NO)_2\{P(p\text{-tolyl})_3\}_2]BF_4$	$C_{42}H_{42}BClF_4N_2O_2P_2Ru$	892.07
15b*	$[RuBr(NO)_2\{P(p\text{-tolyl})_3\}_2]BF_4$	$C_{42}H_{42}BBrF_4N_2O_2P_2Ru$	936.52
18b*	$[RuCl(NO)_2(PCy_3)_2]BF_4$	$C_{36}H_{66}BClF_4N_2O_2P_2Ru$	844.20
19b*	$[RuBr(NO)_2(PCy_3)_2]BF_4$	$C_{36}H_{30}BBrF_4N_2O_2P_2Ru$	888.65
20b*	$[RuI(NO)_2(PCy_3)_2]BF_4$	$C_{36}H_{30}BF_4IN_2O_2P_2Ru$	935.65
21b*	$[RuCl(NO)_2(PCyp_3)_2]BF_4$	$C_{30}H_{54}BBrF_4N_2O_2P_2Ru$	760.04
22b*	$[RuBr(NO)_2(PCyp_3)_2]BF_4$	$C_{30}H_{54}BBrF_4N_2O_2P_2Ru$	804.49
23b*	$[RuI(NO)_2(PCyp_3)_2]BF_4$	$C_{30}H_{54}BF_4IN_2O_2P_2Ru$	851.49
24b*	$[RuCl(NO)_2(P^iPr_3)_2]BF_4$	$C_{18}H_{42}BClF_4N_2O_2P_2Ru$	603.81
25b*	$[RuBr(NO)_2(PiPr_3)_2]BF_4$	$C_{18}H_{42}BBrF_4N_2O_2P_2Ru$	648.26
26b*	$[RuI(NO)_2(P^iPr_3)_2]BF_4$	$C_{18}H_{42}BF_4IN_2O_2P_2Ru$	695.26
26c*	$[\{Ru(NO)_2(P^iPr_3)\}_2(\mu\text{-}I)]BF_4$	$C_{18}H_{42}BF_4IN_4O_4P_2Ru_2$	856.35

1 Introduction

1.1 Natural and anthropogenic sources of nitrogen monoxide

Nitrogen monoxide ($NO^{\cdot}$, nitric oxide)—which was declared molecule of the year in 1992 by the journal *Science*,[1] albeit one of the most simple molecules in chemistry—plays a central role within the nitrogen cycle (Fig. 1.1). Natural sources for nitrogen monoxide are the lightning-induced reaction of atmospheric nitrogen with oxygen and the denitrification and nitrification process in bacteria.[2,3] The combustion of fossil fuels and the Ostwald process are anthropogenic sources for nitrogen monoxide.[4,5]

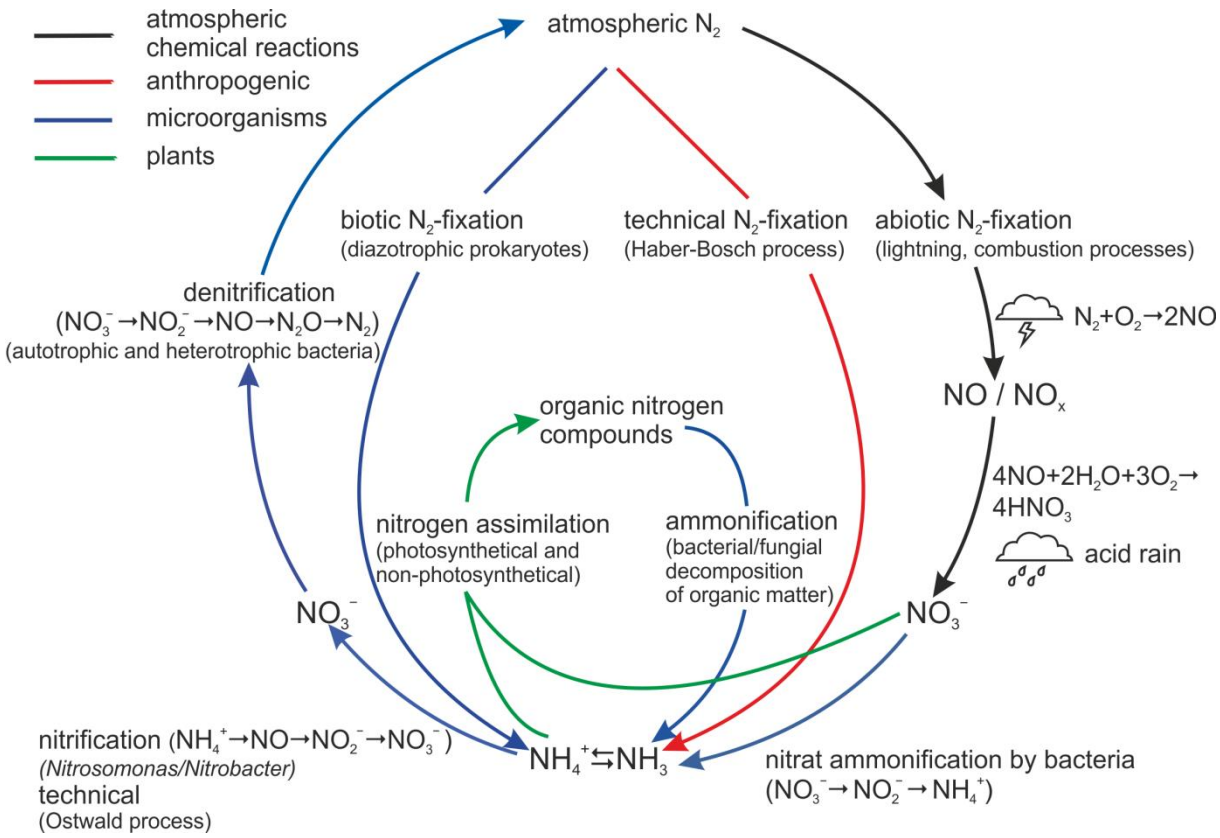

Fig. 1.1: The nitrogen cycle. Adapted from Reference [6].

Naturally or artificially generated nitrogen monoxide can react with water and oxygen in the atmosphere to give nitric acid. This acid is a component of so-called acid rain which heavily damages the lime facades of buildings and is also involved in forest deterioration.[7] Nitrogen monoxide, nitrogen dioxide and nitrate are toxic to humans, especially to infants. Methemoglobinemia and pulmonary edema followed by cyanosis can be the results of an intoxication.[8] A further negative effect is the ability of nitrogen monoxide to destroy the ozone layer in the upper troposphere.[9] For these reasons nitrogen monoxide was, for a long time, regarded only as an environmentally harmful and toxic substance. In the late 1980s this view changed radically when it became obvious that the poisonous, destructive nitrogen monoxide is an endogenous substance in all higher animals, including humans, and in some bacteria.[10]

1.2 Nitrogen monoxide – biochemical properties

1.2.1 The discovery of nitric oxide as an endogenous gasotransmitter

"Isn't it an irony of fate, that I was prescribed nitroglycerin, for oral administration. They call it trinitrin in order not to affright the public."[11] This quotation is taken from a letter by Alfred Nobel to one of his colleagues less than two months before his death in December 1896. In his late years he suffered from *angina pectoris*. Physicians then knew that nitroglycerin could provide some relief, but did not know the biochemical and physiological mechanisms by which the drug works. Ironically, Nobel earned his money—which he donated to the Nobel Prize Foundation—from the production and selling of dynamite, which contains nitroglycerin as the explosion-prone component.
Not less than a century later the pharmacologists R. Furchgott, F. Murad and L.J. Ignarro were awarded the Nobel Prize in Physiology or Medicine, appropriately for the elucidation of the biochemical and physiological effects of organic nitrates, a pharmacological class of substances to which nitroglycerin also belongs.[12]

Robert Furchgott studied the effects of various vasoactive substances and classified their receptors. He received contradictory results for *in vivo* and *in vitro* experiments with acetylcholin (ACh): in *in vivo* experiments the response of the smooth muscle cells to the vasodilator ACh was always a relaxation, whereas the *in vitro* experiments resulted in both responses—vasoconstriction and vasodilatation—depending on the tissue system used. He observed that the fine endothelial layer of the rabbit helical strip aorta used in earlier experiments was damaged during preparations for *in vitro* studies, whereas the mechanically more stable rabbit transverse ring aorta remained undamaged during preparation. From this observation he concluded—and was able to show experimentally—that the endothelium had to be intact to evoke vasodilatation of the underlying smooth muscle cells. He concluded that the endothelial cells, activated by ACh, must liberate a substance which then diffuses into the smooth muscle cells, there inducing vasodilatation. He called this unknown substance EDRF (endothelium-derived relaxing factor).[13]

Ferid Murad studied the effects of various hormones on the different isoforms of the enzyme guanylate cyclase (GC) and the concomitant decrease or increase in the cyclic guanosine monophosphate (cGMP) level which was known to be a second messenger and wondered what the biological functions resulting from an increased cGMP level might be. He began to use various nitrogen-containing substances (azide, hydroxylamine, nitrates), which were known to activate GC, and observed increasing cGMP levels. In order to study motility and cGMP accumulation, he used smooth-muscle cell preparations and observed a cGMP-dependent relaxation of precontracted muscles. Hereupon he examined other smooth-muscle relaxants (nitroglycerin, nitroprusside, hydrazine) and called these substances nitrovasodilators. He set up the working hypothesis—and also found evidence—for NO, somehow released from the nitrovasodilators, serving as the effective relaxant and activating GC.[14]

Luis Ignarro examined and developed anti-inflammatory drugs and tried to elucidate whether they worked on a cGMP-dependent process. He knew from a paper by Murad that organic nitrates and

nitric oxide activated cytosolic GC and stimulated cGMP production. He began to study extensively in which way the various nitrovasodilators liberated NO in tissue. He assumed that nitric oxide could account for the vasodilating effect and showed that nitric oxide activates GC, which enabled him to elucidate parts of the activation mechanism of GC. Ignarro also found proof that GC is a heme protein and that the function of the prosthetic heme group is to bind NO, thereby allowing an NO-dependent enzyme activation. Wondering why organisms should have a receptor for organic nitrates or nitric oxide, he started working with EDRF and in a parallel experiment, with nitric oxide. This resulted in the observation that the vasorelaxant effect of ACh and nitric oxide are pharmacologically similar.[15]

At a conference in July 1986, Furchgott and Ignarro proposed simultaneously, and independently of one another, that EDRF is nitric oxide (for the relations of the discoveries made by Furchgott, Ignarro and Murad see Fig. 1.2). This set off an avalanche of further research on nitric oxide whereby other important physiological effects of NO were discovered (see Fig. 1.3) and the endogenous source of NO was detected.

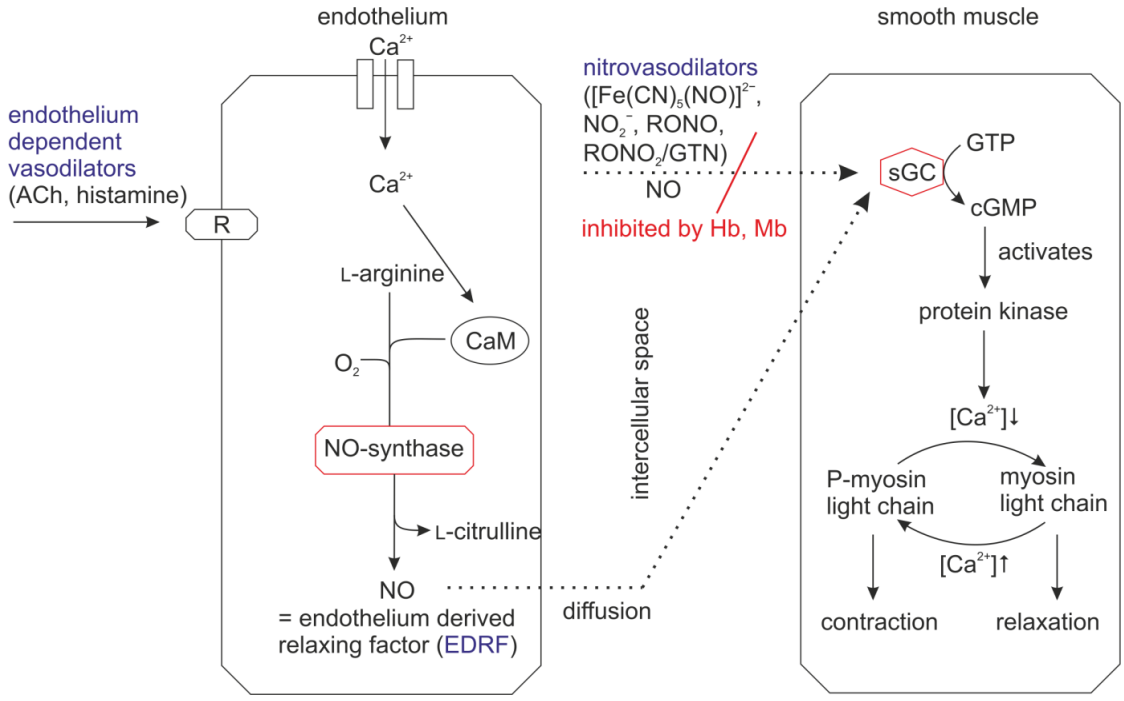

Fig. 1.2: The observations that similar physiological responses to endothelium dependent vasodilators, nitrovasodilators and NO occur, led to the finding that EDRF is nitric oxide. R = receptor, CaM = calmodulin, sGC = soluble guanylate cyclase, GTN = nitroglycerin. Adopted and modified from References [13, 14, 15].
On the binding of endothelium-dependent vasodilators to receptor proteins, calcium ion channels on the membrane of the endothelial cell will open. The inward-directed calcium flux leads to the formation of the Ca^{2+}/calmodulin complex which in turn, leads to the formation of the active form of nitric oxide synthase (NOS). Thus, NOS can produce NO and L-citrulline form L-arginine and activated heme-bound O_2. NO diffuses into the adjacent muscle cells. Alternative sources of NO are nitrovasodilators, which liberate NO in solution or require chemical interaction with thiols in order to decompose with the liberation of NO. NO then activates sGC, which causes the cyclisation of GTP to cGMP. cGMP serves as a second messenger and activates protein kinases whereupon the intracellular Ca^{2+} level decreases and the myosin light chain within the muscle filament is dephosphorylated. Hereby, the cross-bridge cycle is interrupted and relaxation of the muscle is caused. In blood vessels this leads to a decrease in blood pressure and a better oxygen supply.[16]

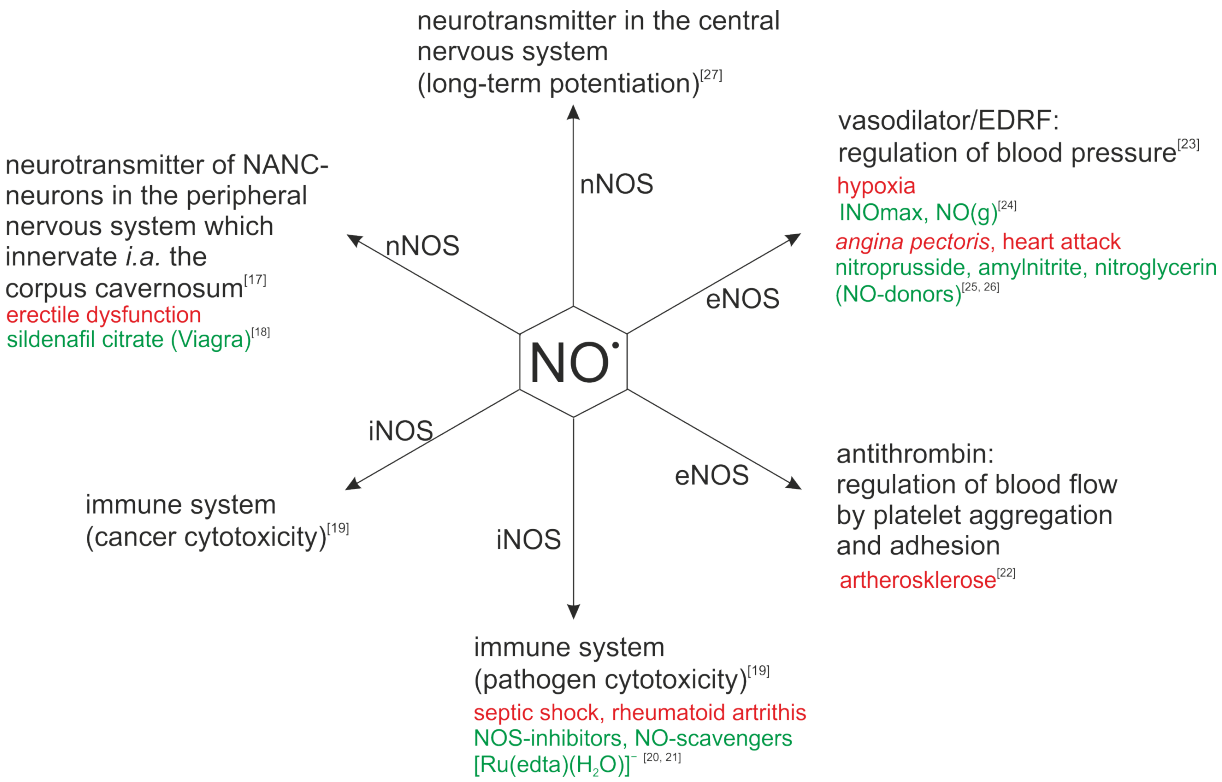

Fig. 1.3: The various physiological processes, regulated by the signalling molecule NO, as well as related diseases (red) and their medication (green). eNOS = endothelial nitric oxide synthase, nNOS = neuronal nitric oxide synthase, iNOS = inducible nitric oxide synthase.

1.2.2 Endogenous sources and cellular targets of nitric oxide

Two years after nitrogen monoxide was recognised as Furchgott's EDRF, Moncada and Palmer identified the enzyme responsible for the endogenous synthesis of NO.[28] Thus, they were able to provide a final proof that endothelial cells indeed produce nitric oxide.

The source of nitrogen monoxide within an organism is the enzymatic reaction of L-arginine with oxygen, which is catalyzed by the so-called nitric oxide synthases (NOSs). In humans, three isoforms can be differentiated: the endothelial NOS (eNOS or Type-I NOS)[28], the neuronal NOS (nNOS or Type-II NOS)[29] and the inducible NOS (iNOS or Type-III NOS)[30]. iNOS and nNOS are found predominantly in the cytosol, while eNOS is membrane-associated.[31]

eNOS and nNOS are expressed constitutively in order to ensure a constant generation of NO due to its short half life in physiological media of 2 ms–2 s and are subjected to Ca^{2+}-dependent regulation.[32,33] iNOS is induced by cytokines on a transcriptional level as a response of the immune system.

In the catalytically active state, all NOSs are homodimeric proteins, with each subunit constituted of a C-terminal reductase domain and an N-terminal oxygenase domain (see Fig. 1.4 and Fig. 1.5). The reductase domain possesses a high sequence homology to cytochrome P450 reductase.

NOSs are the only eukaryotic cytochrome-P450 enzymes which have a reductase domain as an integral part of the enzyme. The prosthetic heme group is bound to the apoprotein by a thiol function.[31]

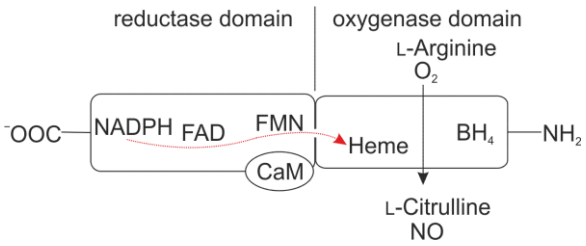

Fig. 1.4: Domains and cofactors of NO-synthase. Reprinted from Reference [31]. The red arrow shows the electron flow, triggered by the binding of Calmodulin (CaM), from the cofactor NADPH *via* FAD and FMN to heme. BH_4: Tetrahydrobiopterin.

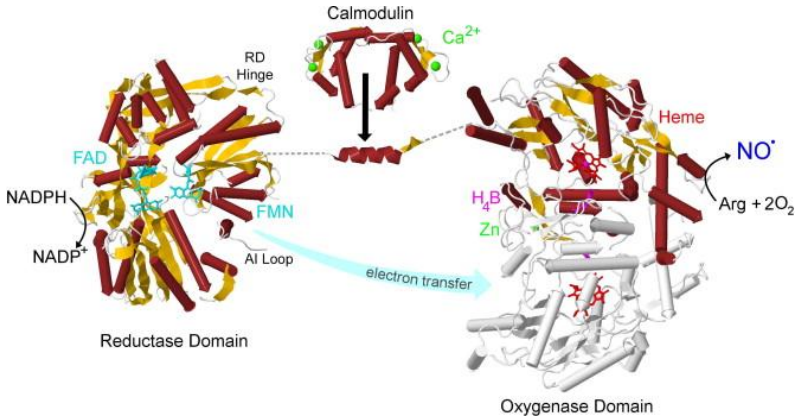

Fig. 1.5: Structures of the various fragments of NO synthase aligned in order of amino-acid sequence. The dimeric oxygenase domain of nNOS, CaM-binding linker of eNOS with bound CaM and the reductase domain of nNOS. Reprinted from Reference [34].

The NOS-catalyzed reaction is a five-electron oxidation of the guanidine nitrogen atom of L-arginine, which takes place in two steps with NOHLA (N^{ω}-hydroxy-L-arginine) as the intermediate (see Fig. 1.6).[31] In this context the enzyme catalyzes two consecutive monooxygenation reactions. The mechanism is similar to that of cytochrome P450, an enzyme which is responsible for the metabolism of xenobiotics and also functions as a monooxygenase. Since L-citrulline is formed as the by-product, the reaction can be regarded as a short circuit of the ornithine cycle.[10] In the case of eNOS, the enzymatic reduction of oxygen can be decoupled from the catalytic reaction with L-arginine, thereby giving rise to the formation of superoxide which can form peroxynitrite from a subsequent, almost diffusion-limited, reaction with nearby nitric oxide.[35] Hence the reaction is three times faster than the disproportionation reaction with CuZnSOD (copper-zinc superoxide dismutase).[36] Peroxynitrite is a strong oxidizing agent ($E^{\circ\prime}$ = 1.6 V at pH 7) and reacts with virtually all biomolecules *in vitro*.[37] This reaction is known to be used by the horseshoe crab, a living fossil, for protection against bacteria.[38]

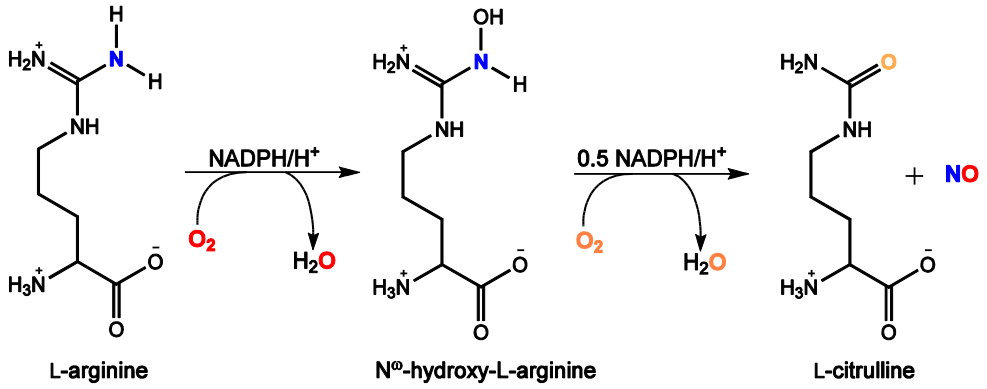

Fig. 1.6: The nitric oxide synthetic pathway.[34] A detailed mechanism of the synthesis of NO by NOS is provided in the supplementary information in the appendix.[34]

After synthesis nitric oxide can diffuse to its cellular target site. Most NO regulated physiological processes are initiated by the activation of guanylate cyclase, a heme protein. The switching stimulus is assumed to be triggered by interaction with NO at the distal site and concomitant bond cleavage between the proximal histidine and the low-spin Fe^{II}-heme centre (see Fig. 1.7).[31]

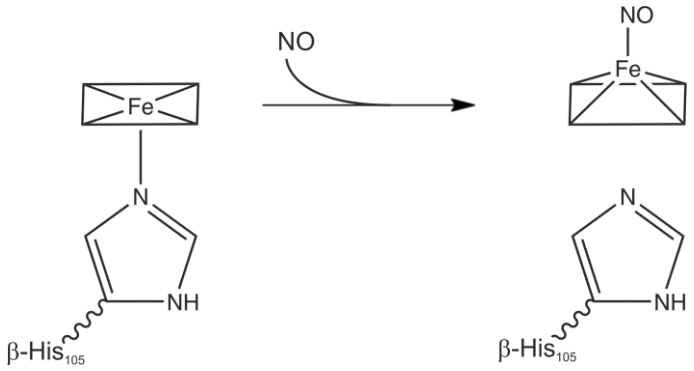

Fig. 1.7: Schematic mechanism of the NO-dependent activation of sGC. The bond breakage of the axial ligand to the iron centre allows better accessibility of the substrate MgGTP to the active site of the enzyme. The activated enzyme thus shows up to a 400-fold increase in V_{max} and a threefold decrease in K_m for MgGTP.[15,31]

Blood-sucking insects of the genus *Cimex* or *Rhodnius* take advantage of this effect by injecting nitric oxide-loaded nitrophorines (NO-binding Fe^{III}-heme-enzymes)—another cellular target of NO—into the bloodstream of their victims, where the NO is then liberated. The bloodsuckers thereby increase the availability of blood.[39] Furthermore, NO is produced by another class of insects, fireflies, for bioluminescence.[40]

Besides these target locations nitric oxide can also react with metHb, metMb, Hb, Mb, oxyMb and oxyHb.[31, 41, 42] Thus, the reaction of NO with sGC—as shown in Fig. 1.2—can be inhibited by oxyHb and oxyMb. The reaction of oxyHb with nitric oxide may initially have served as a detoxification mechanism for NO or O_2 and the oxygen transport is a characteristic that evolved later. This hypothesis is supported by the fact that hemoglobin existed long before the atmosphere was rich in oxygen when NO and then O_2 were still cell poisons. A study by Stamler *et al.* with the hemoglobin of *ascaris lumbricoides* could be evidence for the hypothesis. The parasitic worm lives facultatively anaerobic in the gut of its host and can thus be regarded as a relic of the time when aerobic and anaerobic life forms separated. The author refers to the ascaris hemoglobin as a "nitric-oxide-activated deoxygenase" thereby protecting the worm from toxic oxygen and perhaps also from toxic nitric oxide, which is produced by the immune system of the host organism.[43] The reaction can be formulated according to Fig. 1.8.

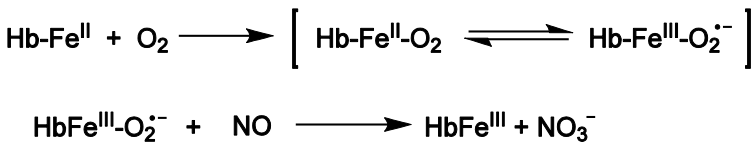

Fig. 1.8: The reaction of NO with oxyHb serving as a detoxification mechanism for NO and/or O_2 and a possible degradative reaction in the case of NO overproduction.

The progression of the evolution of nitric oxide in biological systems thus consisted in the following steps:[38]

- Poison (bacteria, Hb for detoxification of NO)
- Protective reaction (Ascaris, Hb for the detoxification of O_2)
- Functional use / signal (heme systems for transport of NO, O_2) → generating system (NOS)

The interaction of the named enzymes, which react as NO-generating systems (NOS), NO donors (nitrophorines), NO acceptors (GC) or NO scavengers (oxyHb), are all based on the bonding of the NO group to heme-iron centres. As the NO ligand can react with the metal centre in a complicated and manifold way, the electronic description of the resulting metal nitrosyl is ambiguous. Following the Enemark–Feltham formalism, which will be explained later on (see DISCUSSION, chapter 3.2), the resulting iron nitrosyls can be described as $\{FeNO\}^7$ and $\{FeNO\}^6$ compounds.[44]

For the targeted development of appropriate drugs, which inhibit unwanted physiological reactions and give rise to or enhance the desired ones (see Fig. 1.3), and for understanding the negative as well as the positive effects of nitrogen monoxide for environmental and human health, it is essential to

get acquainted with some general chemical and physical aspects of NO and the more special and versatile properties of NO as a ligand.

1.3 General chemical and physical properties of NO

Nitrogen monoxide (NO) is the product of a strongly endothermic reaction of nitrogen with oxygen (ΔG = +90.31 kJ mol^{-1}).[45] Below 450 °C, nitrogen monoxide is a metastable compound with regard to the decomposition into the elements. It is a diatomic molecule with a molecular weight of 30.01 g mol^{-1} and a relatively low dipole moment of 0.15 Debye.[46] With a boiling-point temperature of −151.77 °C and a freezing-point temperature of −163.65 °C, it is, at room temperature, in a gaseous state. In the liquid and solid state NO is, to a large extent, dimerised *via* the nitrogen atom to a mixture of *cis*- and *trans*-N_2O_2.[45] Being a weak dipole, nitrogen monoxide is poorly soluble in water (1.94 ± 0.03 mmol L^{-1}).[47] Due to its odd electron number of fifteen, the compound is a paramagnetic, free radical. The description of the bonding situation by means of the Lewis formalism as well as the molecular orbital theory leads to the same bond order of 2.5 (for the MO diagram see Fig. 1.10; for Lewis formulae see Fig. 1.11).

According to its radical character (one of the π*-orbitals is only half occupied), NO can easily either donate an electron and is then oxidised to the nitrosonium cation (NO^+, nitrosyl cation) or it can accept an electron and is then reduced to the nitroxyl anion (NO^-, nitrosyl anion), which possesses a triplet ground state (for some properties of $NO^{\cdot}$, NO^+ and $^3NO^-$ see Fig. 1.9).

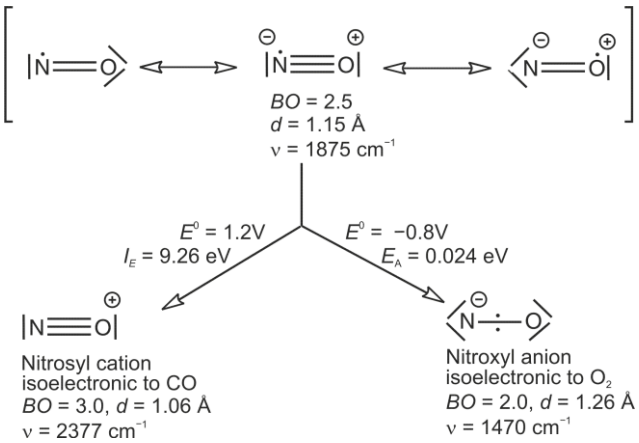

Fig. 1.9: Some physical and chemical properties of NO, NO^+ and NO^-.E^0 are the reduction potentials *vs.* NHE. For the excited $^1NO^-$ E^0 would be −1.7 V, making it physiologically inaccessible. Data taken from References [45, 48].

The colourless radical nitrogen monoxide reacts with the biradical oxygen to form the brown gas NO_2. In contrast to nitrogen dioxide, NO does not react with oxygen-free water.

Reaction with transition metal salts and transition metal complexes results in the formation of complexes called metal nitrosyls, which exhibit a variety of stabilities.

1.4 NO as a ligand

1.4.1 The metal-nitrosyl bond

The term nitrosyl refers to the atom group NO as a ligand.
Under normal conditions, the N atom of NO serves as the donor atom for the formation of the metal-nitrosyl bond, hence the bonding mode is denoted as κ*N*. As can be derived from the molecular orbital diagram (see Fig. 1.10), this bonding situation leads to a more stable complex compared to a possible κ*O*-bonding mode. The shape of the HOMO and HOMO−1 orbitals clearly shows an asymmetry in favour of the nitrogen atom. A metal approaching from the left can thus interact constructively with the protruding HOMO and HOMO−1 orbital lopes on the nitrogen atom. For symmetry reasons the 2σ-state can interact with the metal e orbitals to form a σ-type bond, whereas the energetically higher, degenerated π* orbitals can form two π-type bonds with the metal t_2 orbitals (see Fig. 1.14).
By donating the two electrons located in the 2σ orbital in order to form the M–NO bond, NO acts as a σ base. As the two π* orbitals are occupied with only one electron, both can accept electrons from filled metal t_{2g} orbitals, thus the NO ligand is additionally a π acid (for orbital schemes depicting the σ bonding and the π backdonation see Fig. 1.14).

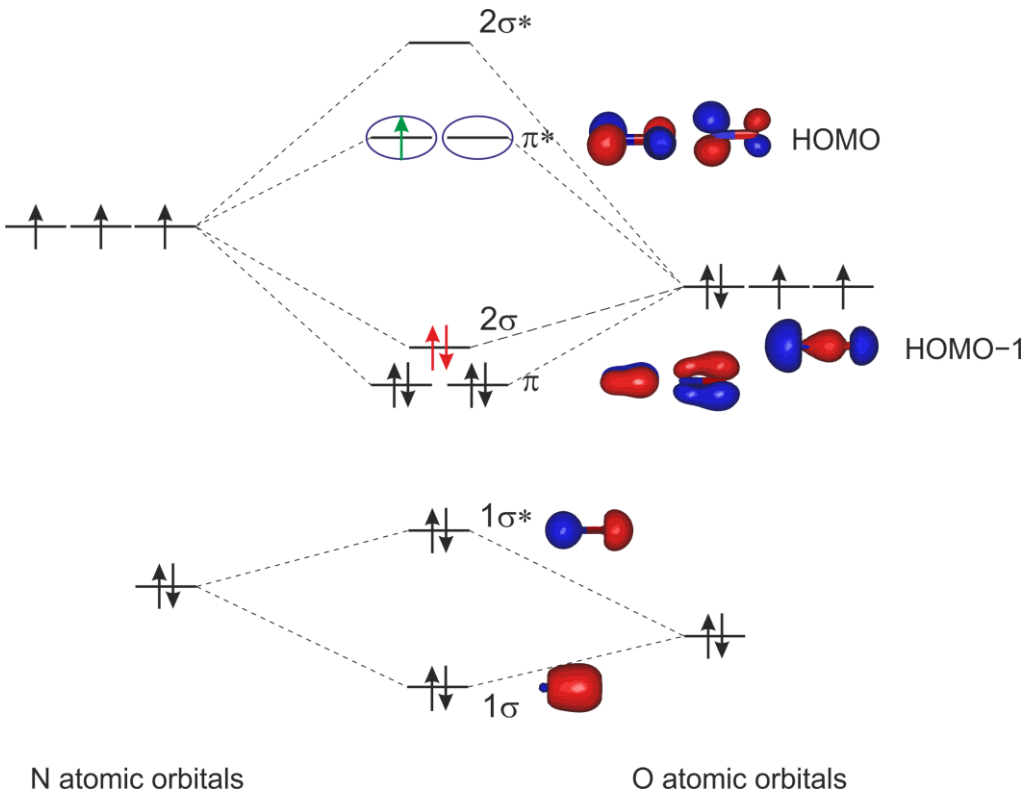

Fig. 1.10: Qualitative molecular orbital diagram of the neutral NO radical. Blue: π-accepting orbitals; green: electron in single occupied orbital, responsible for the redox activity; red: electron pair responsible for σ-basicity. Adapted from Reference [48]. Orbitals were calculated on the theoretical level mp2/6-311G, isovalue 0.14.

1.4.2 NO as a redoxactive ligand

The less the π*-orbitals are occupied with electrons, the better they can act as π-acceptors. Therefore NO^+ is a stronger ligand than neutral NO, followed by NO^-, which is the poorest π-acid. NO^+ and NO^- can form upon reaction of NO with metal complexes or metal salts. The metal centre can thus be reduced (reductive nitrosylation) or oxidised (oxidative nitrosylation) by the NO ligand, depending on the metal oxidation state (see Fig. 1.11). In this case, NO is referred to as a non-innocent ligand, a property which enables the formation of four different coordination modes (depicted in Fig. 1.11): linear as NO^+, weakly bent (ca. 140°) as neutral NO in low-spin complexes, strongly bent (ca. 120°) as $^1NO^-$ in low-spin complexes and as $^3NO^-$ in high-spin complexes. The similarity of NO^- and O_2 (both existing in a triplet ground state), makes NO an interesting ligand for studying biological oxygen activators.[48]

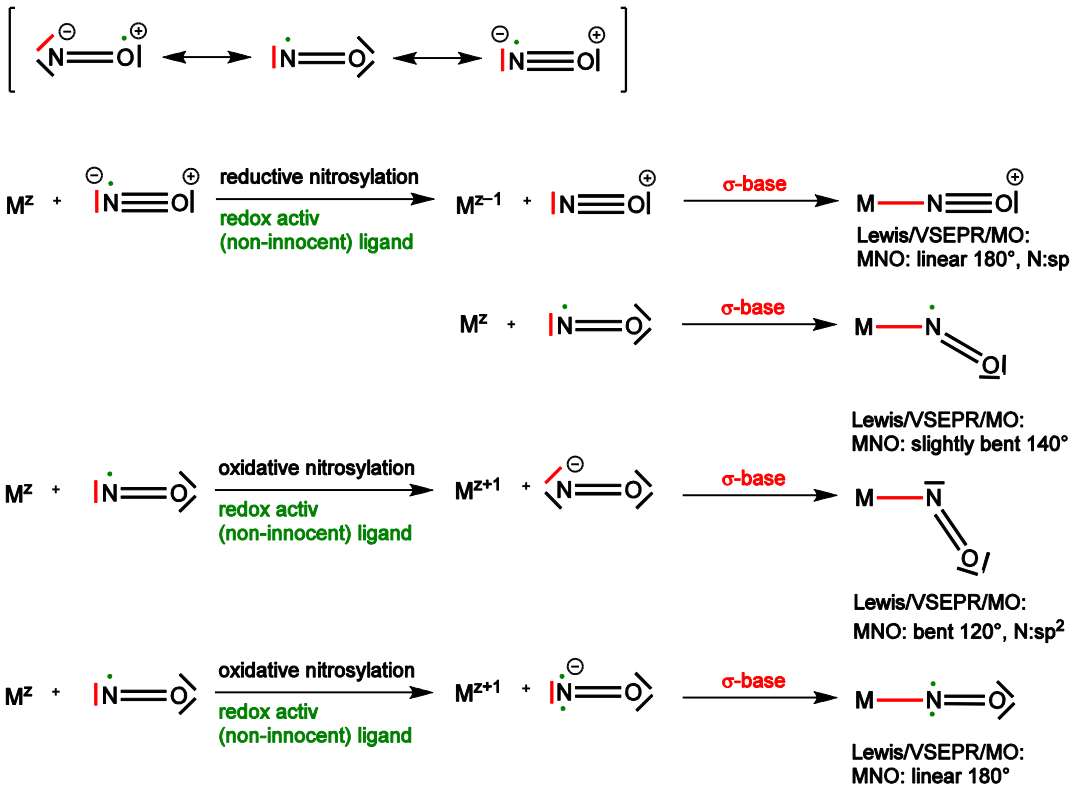

Fig. 1.11: Resonance structures of nitric oxide and the formation of the various bonding modes resulting from the property of the ligand as non-innocent. The reaction of NO with third-row transition-metal complexes can result in $^3NO^-$ complexes with high or intermediate spin systems, the latter due to antiferromagnetic coupling with the $^3NO^-$ ligand. The bond angle in these complexes can vary between 160-180°.

Due to the possible redox chemistry taking place when metal nitrosyls form, there are several ways to distribute charges and ascertain oxidation states. To account for this confusing abundance of possible descriptions of the electronic state of metal nitrosyl compounds (see DISCUSSION, chapter 3.2) the Enemark–Feltham notation was introduced. Herein the metal nitrosyl fragment is regarded as a covalent $\{M(NO)_x\}^n$-unity, wherein *x* is the number of NO ligands attached to the metal and the superscript *n* is the sum of electrons in metal d– and π*(NO)-orbitals.[44]

To elucidate which bonding situation is adopted, various spectroscopic parameters can be useful. As already shown in Fig. 1.9 the bond order is reflected in IR-stretching frequencies, with higher frequencies indicating a stronger N–O bond (*ν*(NO)-range for a linear MNO arrangement: 1450–1950 cm^{-1}, *ν*(NO)-range for a bent MNO arrangement: 1400–1720 cm^{-1} [48]). But, other than in carbonyl complexes, there is no unambiguous correlation between the *ν*(NO)-stretching frequency and the M–N–O bond angle, since the ranges overlap significantly.[48] X-ray studies can allow a statement on the M–N–O bond angle and distance, with short bond distances indicating a higher bond order. In this context it has to be mentioned that caution is required when determining and discussing the M–N–O bond angle in X-ray structures with a bent M−N−O moiety due to a relatively high degree of thermal motion and possible disorder of the oxygen atom. ^{15}N-NMR studies can be used as a second tool to reveal whether the NO ligand is coordinated in a linear or bent fashion. The ^{15}N-shifting-range lies between −110–200 ppm for linear coordination and between 350–950 ppm for bent coordination, relative to liquid nitromethane.[49,50] Hence the spectroscopic parameters can give hints concerning the coordination geometry. Another hint can be the chemical reactivity of the bound nitrosyl, since a nitrosonium N-atom can be attacked nucleophilicly, for example by bases, whereas the nitrogen atom of a nitroxyl ligand is easily attacked by electrophiles.

1.4.3 NO as an ambident ligand

As mentioned above, under normal conditions the nitrosyl ligand is attached to the metal centre *via* the nitrogen atom. As with the nitrogen atom, the oxygen atom owns lone electron pairs making NO a potential ambident ligand. By irradiation with light of an appropriate wave length (350–580 nm, equivalent to the blue to green range), two different excited states can be achieved for the ambident NO ligand, a phenomenon which is called photoinduced linkage isomerism, abbreviated as PLI: η^1-κ*O*-bound (isonitrosyl) or η^2-κ^2*N*,*O*-bound (side-on). If these are sufficiently stable below a discrete temperature of decay, they can be detected and analysed *via* low-temperature IR spectroscopy, differential scanning calorimetry (DSC) measurements and photocrystallography.[51, 52] After irradiation with light in the red spectral range or upon heating, the metastable states can be transferred back into the ground state. Usually the metastable states lie above the ground state by 1 eV.[53] The phenomenon of PLI was first observed coincidentally in crystals of sodium nitroprusside (SNP) by Hauser *et al. via* Mößbauer spectroscopy in 1977.[54] In 1997, Carducci *et al.* were able to provide an X-ray crystallographic evidence (see Fig. 1.12).[55]

Later on, the effect of NO-based PLI was found to be a quite widespread phenomenon and not limited to $\{FeNO\}^6$ compounds, but also found in $\{RuNO\}^6$ [51, 56, 57, 58], $\{OsNO\}^6$ [59], $\{NiNO\}^{10}$ [60, 61], $\{MnNO\}^{10}$ [62], $\{MnNO\}^8$ [63] and $\{PtNO\}^8$ [64] compounds. Substances showing PLI are interesting with respect to potential physical applications. The ground state and the metastable states show different refractive indices *n* ($\Delta n \approx 10^{-2}$), enabling their use as holographic data storage devices.[65, 66] For this purpose the maximum population and lifetime of the metastable states are of utmost interest. Through variation of the ligand sphere of ruthenium nitrosyls which are thermally more stable than comparable iron nitrosyls, the best results regarding the lifetime and the degree of population were

found for the substances *trans*-$[Ru(NO)(NH_3)_4(H_2O)]Cl_3 \cdot H_2O$ [67] (τ_{MS1} = 46 s at 300 K) and $[Ru(NO)(py)_4Cl](PF_6)_2 \cdot 0.5\ H_2O$ [68] (P_{MS1} = 76%, P_{MS2} = 56%).

Besides a terminal bonding *via* the N or O atom or a side-on bonding pattern, the NO can also function as a bridging ligand between multiple metal centres.

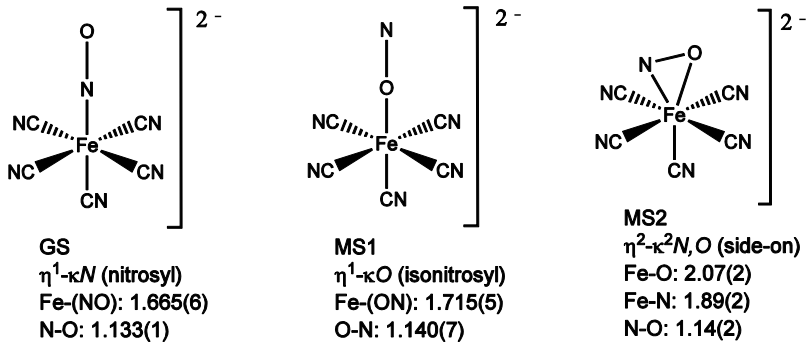

Fig. 1.12: Schematic representation of the bonding situation in the ground state and the metastable states of sodium nitroprusside (SNP) as an example for the PLI-effect. Data taken from Reference [55]. Distances are given in Å.

1.5 Nitrosyl complexes

So far only three homoleptic nitrosyl compounds are known—$Cr(NO)_4$[69], $Fe(NO)_4$[70] and $Co(NO)_3$[71]—but an unequivocal confirmation of the existence of the last two is still missing. In contrast to this, numerous heteroleptic complexes $[L_pM(NO)_x]$ or $[L_pM_m(NO)_x]$ were shown to be synthesizable.

The first nitrosyl complexes to be synthesised were $[Fe(H_2O)_5(NO)]^{2+}$ in 1790 by J. Priestley[45] and the medically relevant nitroprusside ion $[Fe(CN)_5(NO)]^{2-}$ in 1849 by K.L. Playfair.[72] The first structural characterisations were made on $[Co(NO)(S_2CNMe_2)_2]$ by Alderman *et al.*[73] in 1962 and on $[IrCl(CO)(NO)(PPh_3)_2]^+$ by Hodgson and Ibers[74] in 1968 (see Fig. 1.13).

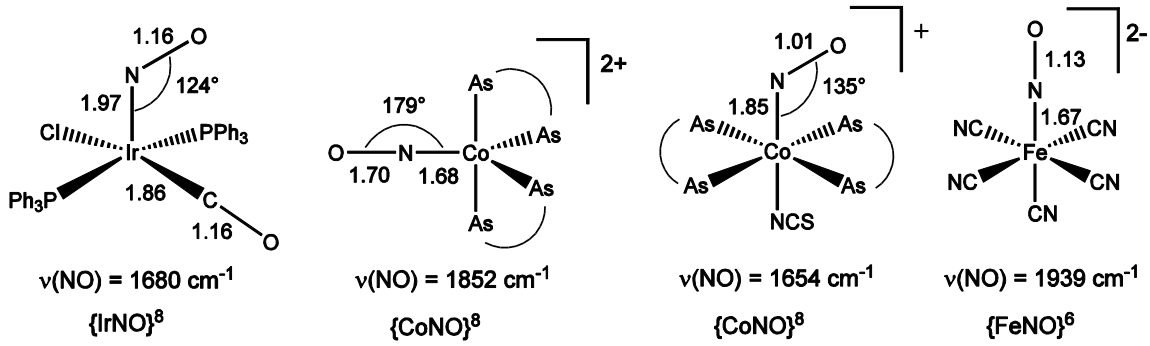

Fig. 1.13: Some examples for mononitrosyl complexes. Distances in Å. As∩As = *o*-phenylenebis(dimethyl-arsane). Data taken from References [48, 55, 74, 75].

Due to the chemical and physical similarity of some nitrosyl complexes to carbonyl complexes, F. Seel established the *nitrosyl shift rule* in 1942[76] and Sidgwick *et al*., in 1934, proposed to regard metal nitrosyls as derivatives of either NO^+ or NO^-.[77] Since attempts to correlate their structures, physical properties and reactivity with the formal oxidation state of the metal and NO arising from this approach failed, Enemark and Feltham introduced an alternative description. Based on the

assumption that the π*(NO) orbitals and the metal d orbitals are of similar energy, they regard the metal nitrosyl group as a highly covalent {M(NO)$_x$} entity which allows them to extend the molecular orbital correlation method, set up by Walsh for triatomic species of the non-transition elements,[78] to metal nitrosyls. In order to correctly apply the correlation method which allows to derive the geometry of the MNO moiety, the distribution of the electrons of the metal and of the nitrosyl ligands have to be regarded, *i.e.* the Enemark–Feltham notation has to be applied.

1.5.1 Mononitrosyl complexes

Due to the fact that NO has one electron more than CO, the introduction of NO into a transition metal complex leads to some valence-chemical peculiarities which will now be described using both the molecular-orbital and the valence-bond theoretical approach.

Fig. 1.14 shows the molecular orbital diagram of a [ML$_5$(NO)] complex, assuming octahedral geometry.

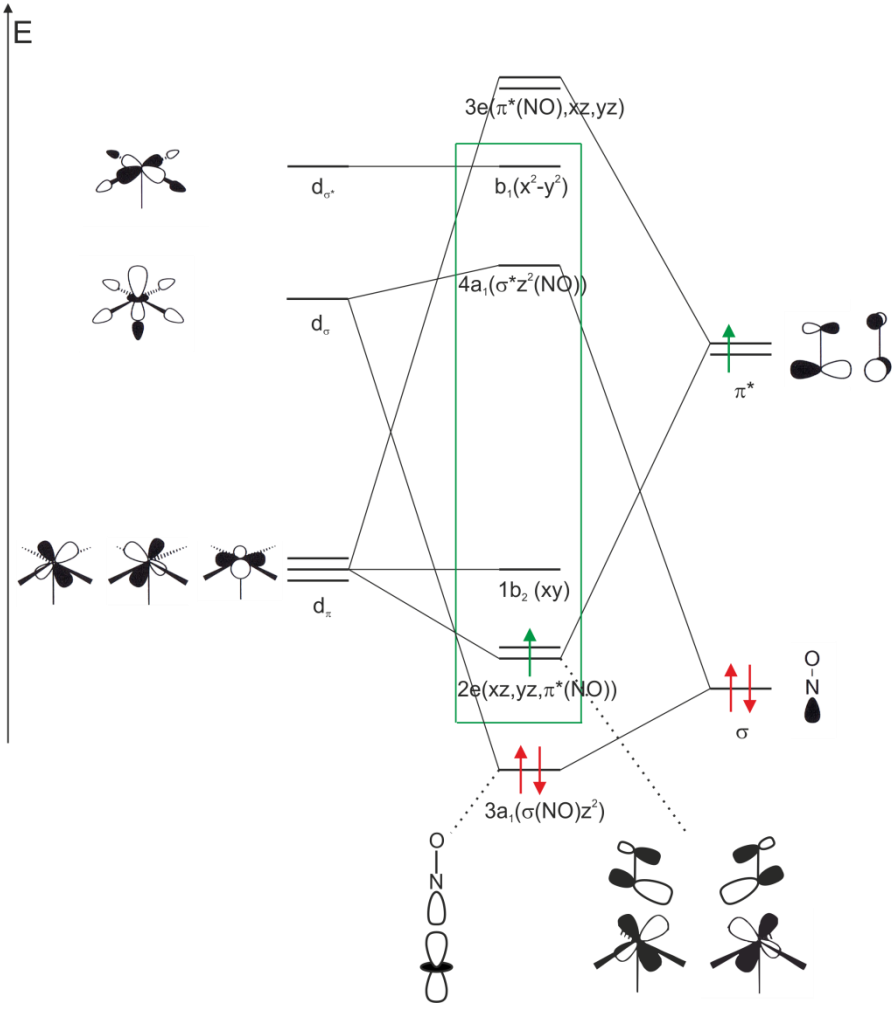

Fig. 1.14: Orbital diagram for the interaction of a linearly coordinated NO with an octahedral ML$_5$ complex. Green box: metal d-block (the number of electrons within this box corresponds to the superscript of the Enemark–Feltham-notation); green electron: is formally accounted to the metal (non-innocent ligand); red electrons: forming the σ-bond (σ-basicity). Adapted from References [44] and [50]. The energetic order of the 4a$_1$ and the 3e level can also be inverted.

As seen from the figure, there are three bonding interactions between the metal atom and the NO ligand, one of which is of the σ-type ($3a_1$ orbital, primarily localised on the N atom) and two of which are of the π type (degenerate 2e orbitals, consisting primarily of the metal d_{xz}, d_{yz} and π* orbitals of NO), corresponding to the π backdonation. If only these orbitals are occupied, as is the case in a $\{RuNO\}^4$ system, the M–N–O bond angle will be linear. For a $\{RuNO\}^6$ species the electronic configuration is $(3a_1)^2(2e)^4(1b_2)^2$. Since the $1b_2$ orbital is non-bonding and localised on the metal (d_{xy}), the MNO angle will still be linear (170–180°)[44].

The two additional electrons for a $\{RuNO\}^8$ system will occupy either the degenerate 3e level or the $4a_1$ level, depending on which is lower in energy. The 3e orbitals are anti-bonding with respect to M, N and O and have a large contribution from the N atom. When compared to Walsh's rule for the triatomic species NO_2^+, it is obvious that, when the 3e orbital is filled, a decrease in the MNO angle will lead to a decrease in the total energy of the system, since an additional interaction is formed between the terminal atoms (see Fig. 1.15). Due to the fact that the 3e orbital is energetically similar to the nitrogen atom, the electrons will reside on the N atom as a lone pair, which results in a bent NO ligand found in several $\{CoNO\}^8$ species, for instance (CoNO angle 119–134°)[44]. The filling of the $4a_1$ level, on the other hand, will destabilise the σ-bond, which will result in ligand labilisation or ligand loss and the concomitant generation of a pentacoordinated $[ML_4(NO)]$ complex.

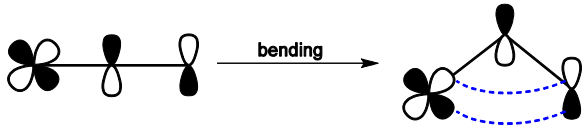

Fig. 1.15: Upon bending of the MNO moiety the energy of the anti-bonding 3e orbital will be lowered as a new interaction between the terminal atoms is formed.

In conclusion it must be mentioned, that the ultimate geometry of the MNO group depends not only on the superscript *n* of the Enemark–Feltham notation but also on the nature of the HOMO.

A valence-bond theoretical examination leads to the same results, as is shown in Fig. 1.16.

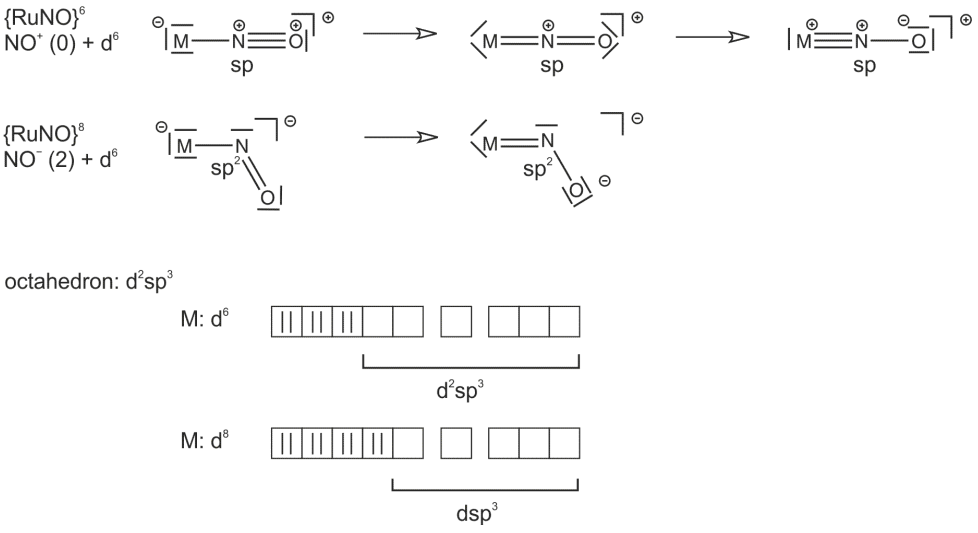

Fig. 1.16: Possible resonance structures and hybridisations for a six-coordinate $\{MNO\}^6$ complex and $\{MNO\}^8$ complex. If the two additional electrons are localised at the metal, a six-coordination is no longer possible and the coordination number is lowered by one.

If the two additional electrons, when going from a $\{RuNO\}^6$ to a $\{RuNO\}^8$ compound, are localised on the metal atom, hexa-coordination is no longer possible since a d^2sp^3 hybridisation, needed for this coordination geometry, is impossible. If the additional electrons are localised on the N atom, which is shown in the resonance structures for the $\{RuNO\}^8$ compound, the NO group can be regarded as an NO^- ligand and the metal is d^6 configured. The resonance structures clearly demonstrate that it is tenuous to infer the MNO bond angle from *v*(NO) frequencies, since both geometries give rise to formal bond orders of one and two. The *v*(NO) frequency is thus dependent on the effective charge on the NO group and not necessarily on its geometry.

As is clear from these considerations, a metal complex in a high oxidation state will stabilise a linear NO group, since the additional electrons can be localised on the metal atom, whereas a metal complex in a low oxidation state will either stabilise a low coordination sphere with a linearly attached NO ligand or a higher coordinated species with a bent NO moiety, in which the additional electrons are localised on the nitrogen atom. This aspect is crucial with regard to a targeted synthesis of one or the other MNO geometry. In fact, it is possible to determine the MNO angle *via* valence-chemical alterations (for an example see the cobalt structures in Fig. 1.13).

1.5.2 Dinitrosyl complexes

While nearly all transition metals are able to form mononitrosyl complexes, X-ray crystallographic evidence for the formation of dinitrosyls is available only for one third of the transition metals. Among those are V, Nb, Cr, Mo, W, Mn, Re, Fe, Ru, Os, Co, Rh and Ir. A view into the *Cambridge Structural Database* (CSD, version 5.34, november 2012) shows that there is only one dinitrosyl structure for Rh, Ir, V and Nb, each. Dinitrosyls of Cr, Mo and W often possess an additional Cp or Cp* ligand. Re, Co and Mn dinitrosyls often have additional phosphorus or carbonyl ligands. With ca. 145 dinitrosyl structures, iron is above competition. The so-called DNICs (dinitrosyl iron compounds) are usually accompanied by S/N/P donor atoms. In contrast, there are only six structurally known ruthenium dinitrosyl complexes (shown in Fig. 1.21). The majority of metal dinitrosyls possess two nearly equally coordinated NO ligands with MNO angles between 160°–180°. Thus it can be assumed that in most dinitrosyls the NO ligands are coordinated as formal NO^+ or $NO^{\cdot}$. Some examples of metal dinitrosyls are shown in Fig. 1.17.

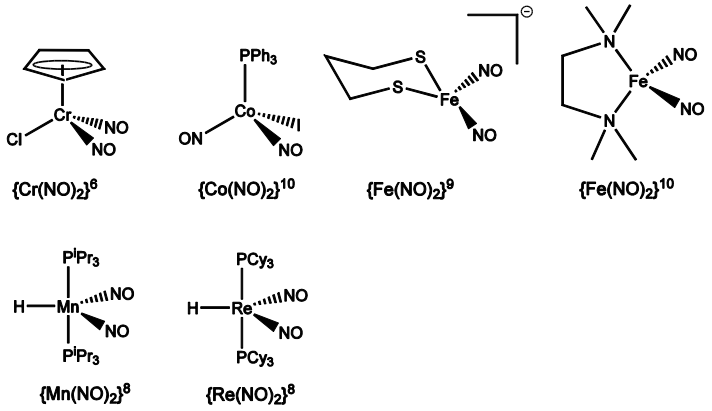

Fig. 1.17: Some examples of dinitrosyl structures, deposited in the CSD.

The Mn and the Re dinitrosyls were selected since they are pentacoordinated as are the ruthenium dinitrosyls of this work. The iron compounds are representatives of DNICs. The selection was extended by one Cr and one Co example. All six dinitrosyls have two nearly equal NO ligands. Table 1.1 enlists structural and spectroscopic data for the compounds shown in Fig. 1.17. For molecular orbital theoretical considerations on metal dinitrosyls see DISCUSSION, chapter 3.4.2.

Table 1.1: Some structural and spectroscopic parameters for the dinitrosyl examples given in Fig. 18.

Compound	Ref.	ν(NO)/cm^{-1}	M–N(O)/Å	N–O/Å	M–N–O/°	N–M–N/°
$[CrClCp(NO)_2]$	[79]	1816, 1711	1.72, 1.72	1.16, 1.16	170.0, 168.8	93.9
$[CoI(NO)_2(PPh_3)]$	[80]	1830, 1771	1.66, 1.67	1.15, 1.15	165.2, 163.3	121.7
$[MnH(NO)_2(PMe_3)_2]$	[81]	1683, 1637	1.66	1.20	173.0	121.7
$[ReH(NO)_2(PCy_3)_2]^a$	[82]	1604, 1554	1.78, 1.78	1.24, 1.21	175.8, 174.0	126.6
$[Fe(NO)_2\{S(CH_2)_3S\}]$	[83]	1712, 1671	1.67, 1.68	1.18, 1.17	172.8, 167.4	118.6
$[Fe(NO)_2(tmeda)]$	[83]	1698, 1644	1.64, 1.64	1.19, 1.20	169.9. 166.9	112.1

Tmeda = tetramethylethylendiamin. [a]For symmetry reasons only one value for the nitrosyl ligands.

Dinitrosyl complexes (as well as mononitrosyl complexes) are catalytically interesting, since it is known that they are able to activate metal-ligand bonds. Being isoelectronic to Vaskas compound and possessing a nitrosyl ligand as well as the fine-tunable phosphane ligands, the intermediate products of the dinitrosyls of this work might have some relevance for catalytic applications.

$\{Ru(NO)_2\}^8$ compounds are, to some degree, related to the biochemically interesting DNICs (dinitrosyl iron compounds, $\{Fe(NO)_2\}^9$ and $\{Fe(NO)_2\}^{10}$), but possess one or two electrons less than DNICs (two DNIC-analogous compounds are depicted in Fig. 1.17). The known stable DNICs can be classified into four groups: the paramagnetic, EPR-active (g_{av} = 2.03)[84] mononuclear anionic/neutral/cationic $\{Fe(NO)_2\}^9$ of the general formula $[FeL_2(NO)_2]^{1-/0/1+}$ (L = S/O/N/P-containing ligands), the dimerized forms of $\{Fe(NO)_2\}^9$, which are diamagnetic and EPR-silent due to electron pairing (diamagnetically coupled if the iron-iron distance is not too long), the diamagnetic, EPR-silent $\{Fe(NO)_2\}^{10}$ DNICs coordinated by CO, PPh_3 and N-containing ligands and the EPR-active, dinuclear DNICs with two $\{Fe(NO)_2\}$ motives stabilised by the delocalised mixed-valence $\{Fe(NO)_2\}^{10}$–$\{Fe(NO)_2\}^9$ core.[84, 86]

The ligands of cellular DNICs are coordinated through either a thiol, amino, imino or carboxyl group. Among the sources of ligands are low-molecular components of the cellular milieu, such as glutathione, cysteine and homocysteine, as well as proteins. Among the main protein targets of NO are iron-sulfur centre proteins, which are the first to be nitrosylated during excess NO production, a process leading to the formation of DNICs.[85] Thus, like NO, DNICs have some relevance in NO mediated physiological processes. DNICs are assumed to play a role in transport and storage of nitric oxide and in the nitrosative pathway, leading to the physiologically and pathophysiologically active nitrosothiols. The biologically occurring DNICs are either built from the reaction of Fe_xS_x-clusters with NO or from reaction of NO with iron derived from the chelatable iron pool (CIP). The desired cytotoxicity of nitric oxide, for example when activated macrophages build large amounts of NO during the immune response to pathogens or tumour cells, is based on the high affinity of NO for Fe^{II}, leading to the degradation of iron sulfur clusters within proteins and the concomitant formation of monomeric DNICs with the formula $[Fe(RS)_2(NO)_2]$ or of Roussin's red esters (RRE), which are dimeric DNICs with the formula $[\{Fe(NO)_2\}_2(\mu\text{-}SR)_2]$.[84, 86, 87, 88] RREs can be obtained by alkylation of Roussin's red salt $K_2[\{Fe(NO)_2\}_2(\mu\text{-}S)_2]$ (depicted in RESULTS, Fig. 2.39).[89]

Another toxic effect is the mobilisation of iron which is important for tumour cell proliferation. The NO-mediated iron efflux from tumour cells most probably takes place *via* the formation of a dinitrosyl-diglutathionyl-Fe complex.[87, 88] The chemically quite similar $\{Ru(NO)_2\}^8$ compounds could also help to elucidate the kind of metal nitrosyl interaction in DNICs.

1.6 Metal nitrosylation

There are multiple possibilities for the generation of metal nitrosyl compounds. A simple approach is the addition of NO, NO^+ or NO^- to a metal complex (Fig. 1.18, 1a–c). Another possibility is the substitution of one two-electron donor and one one-electron donor by NO (Fig. 1.18, 2a), or the substitution reaction of carbonyl ligands by NO in accordance to the nitrosyl shift rule (Fig. 1.18, 2b), or the substitution of a two electron ligand by NO^+ (Fig. 1.18, 2c). A further possible reaction is the derivatisation of a nitrogen containing ligand (Fig. 1.18, 3a–c) *via* acid-base or redox reaction.

[M]	+	NO	→	[M–NO]	(1a)
[M]	+	NO^+	→	$[M–NO]^+$	(1b)
[M]	+	NO^-	→	$[M–NO]^-$	(1c)
[M(L)(X)]	+	NO	→	[M–NO] + :L + ·X	(2a)
$[M(L)_3]$	+	2 NO	→	$[M–(NO)_2]$ + 3 :L	(2b)
[M(L)]	+	NO^+	→	$[M–NO]^+$ + :L	(2c)
$[M(NO_3)]$	+	2 CO	→	[M–NO] + 2 CO_2	(3a)
$[M(NO_2)]$	+	2 H^+	→	[M–NO] + H_2O	(3b)
2 $[M(NH_3)]$	+ 10 OH^- +	5 Cl_2	→	2 [M–NO] + 10Cl^- + 8 H_2O	(3c)

Fig. 1.18: The various possibilities for introducing NO or generating a nitrosyl ligand in a metal complex. Equation 1a: Direct reaction with gaseous NO or NO-liberating substances (diazald, tritylthionitrit). Equation 1b: Reaction with an NO^+ containing substance. Equation 1c: Reaction with an NO^- generating substance (oxidation of NH_2OH; Angeli's salt, $Na_2N_2O_3$). Equation 2a: Substitution of a three-electron donor equivalent with the 3-electron donor NO. Equation 2b: Substitution of 3 equivalents of a two-electron donor with two equivalents of the three-electron donor NO. Equation 2c: Substitution of a two-electron donor equivalent with the 2-electron donor NO^+. Equations 3a–b: Derivatisation of a nitrogen containing ligand.

1.7 Properties of ruthenium and its compounds

Naturally occurring ruthenium is composed of seven stable isotopes (for the specific isotope pattern see RESULTS, Fig. 2.7). It is a silvery-white, noble metal and belongs to the platinum group. This very rare metal has a mass percentage of the earth's geosphere of 0.02 ppm, making it the 74th most abundant metal on earth.[90] Commonly, ruthenium is found in association with the other platinum metals. There are several ruthenium minerals, such as laurite (RuS_2) or ruthenarsenite ((Ru,Ni)As) in addition to elemental ruthenium.[45, 91] The most important applications of this metal are found in the electronics industry for perpendicular recording, a data storage procedure for hard disks, in

hardening of platinum and palladium alloys, and in catalytic processes, such as olefin metatheses, methanation, hydrogenation and ammonia synthesis.[45, 92, 93] Further, but less important applications are the use of ruthenium complexes as dyes in the Grätzel cells, as optode sensors for oxygen and as stains for polyanionic biomolecules for histochemical studies.[94–96] Currently, some ruthenium compounds are studied as an alternative for Cisplatin or Carboplatin, since the ruthenium complexes are inert against ligand substitution, are able to adopt different oxidation states under physiological conditions and have some features in common with iron, enabling them to substitute for iron within proteins such as transferrin or siderophores.[97] Harmful cells such as cancer cells or microorganisms both of which have a high iron demand during growth phases are thereby hindered in reproduction by incorporating ruthenium instead of iron. At the same time the healthy cells or host cells can lower their potentially toxic amount of ruthenium, making the ruthenium-based drugs less toxic than the platinum-based ones. Another advantage of ruthenium-based chemotherapeutic agents is their more selective action. Ruthenium in the oxidation state +III is biologically relatively inactive, whereas ruthenium(II) shows a high anti-tumour activity. Thus, it should be possible to introduce ruthenium(III) into the cancer cell, where it could be activated by reduction. Ruthenium-based drugs are studied as immunosupressants, antimicrobials, antibiotics, NO-scavengers and anti-tumour agents. So far however, there are no approved ruthenium-based drugs on the pharmaceutical market.[97, 98]

1.8 Phosphanes as ligands

Phosphanes (PR_3) play an outstanding role as ligands in homogenic catalysis, since they are able to stabilise low-coordinated catalyst species, have the property to be spectator rather than actor ligands and allow a systematic and predictable fine tuning of the catalyst's properties by varying the substituent R.

The tool for this task is the Tolman plot[99], from which it is possible to choose a phosphane ligand which promotes the desired properties of the (catalyst) complex.

The Tolman plot depicts electronic effects (reflected by the *v*(CO) valence vibration) on the y-axis *versus* steric effects (reflected by the Tolman's cone angle) on the x-axis (see Fig. 1.19).

The magnitude of the Tolman electronic parameter corresponds to the value of the *v*(CO) stretching vibration of $[Ni(CO)_3(PR_3)]$ complexes and describes the ability with which the phosphane ligand donates electron density to the Ni centre, thus weakening the C–O bond by populating the π*(C–O) orbitals. This means, the higher the electron donating ability of the phosphane is, the lower the value of *v*(CO) turns out (for an illustration see Fig. 1.20).

In contrast to their lighter homologues, the amines, phosphanes are both σ-donor and π-acceptor ligands (actually they are σ* acceptors), for example PF_3 is as strong a π acid as CO. While the π acidity of carbonyl and nitrosyl ligands is due to empty π* orbitals, the π acidity of phosphanes is the result of unoccupied σ* orbitals. Thus, the electronic parameter of a phosphane is not only reflected in σ-donation, but also in σ* backdonation. These two have opposing effects, since σ-donation lowers the value of *v*(CO) as explained above, whereas σ* backdonation withdraws electron density from the metal, thereby strengthening the C-O bond and increasing the *v*(CO) value (see Fig. 1.20).

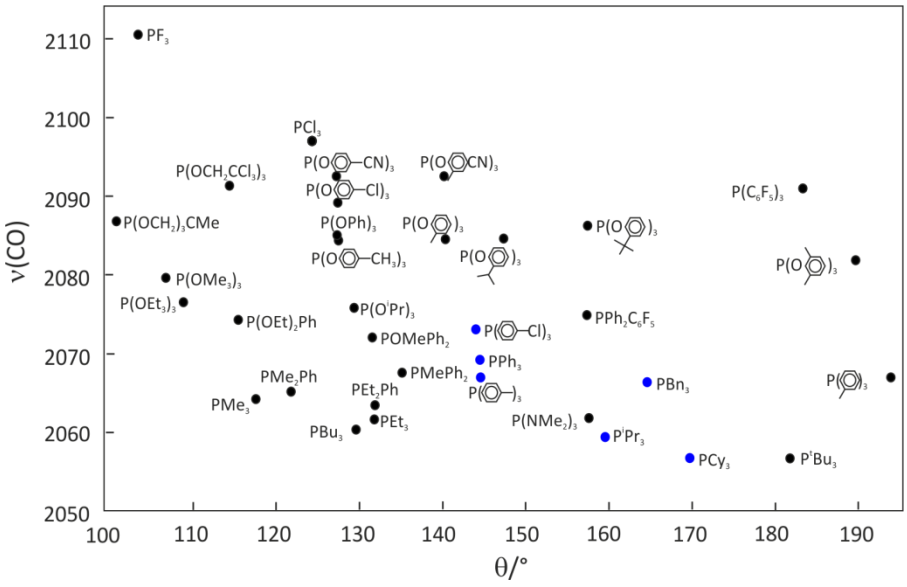

Fig. 1.19: Electronic and steric effects of common P donor ligands plotted on a map according to Tolman (ν in cm^{-1}).[99] Blue: phosphanes used in this work. The Tolman plot allows one to predict easily how to change steric effects without changing electronic effects (by moving parallel to the x-axis) or to change electronic effects without changing steric effects (by moving parallel to the y-axis).

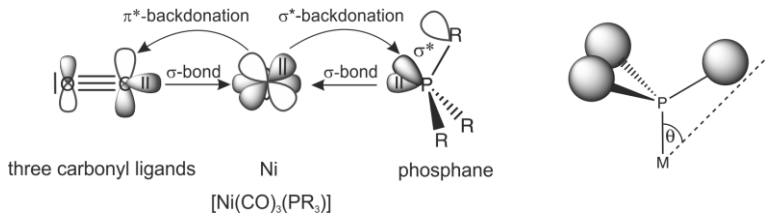

Fig. 1.20: Visualisation of Tolman's electronic and steric parameter.

Since the contributions to the electronic parameter of the individual substituents on the phosphorus atom are additive, Tolman's electronic parameter can be calculated for asymmetrically substituted phosphanes with the empirical formula, where χ_i is the contribution of the individual substituent:

$$\upsilon = 2056.1 + \sum_{i=1}^{3} \chi_i \tag{1.1}$$

Tolman's steric parameter is expressed in the cone angle θ, which is obtained by taking a space-filling model of the $M(PR_3)$ group (see Fig. 1.20). For symmetrically substituted phosphanes θ is the apex angle of a cylindric cone, whose end is situated 2.28 Å away from the centre of the phosphorus atom. If internal degrees of freedom exist, the substituents are folded back in such a way as to give a minimum cone. Since the contributions of the individual substituents (χ_i) are additive, there is an easy formula to calculate the cone angle for asymmetrically substituted phosphanes:

$$\theta = {}^{2}/_{3} \sum_{i=1}^{3} \chi_i \tag{1.2}$$

It should be mentioned, that steric and electron effects can influence each other, thus it is not possible to separate the two effects from each other precisely.

Tolman's steric and electronic factors as well as some pK_a values of the phosphane ligands used in this work are listed in Table 1.2.

Table 1.2: Tolman's steric and electronic factors as well as some pK_a vlues of the phosphane ligands used in this work.

phosphane	***ν*(CO)/cm^{-1}**	**θ/°**	**p$K_{a\ (in\ water)}$** [100]
PPh_3	2068.9	145	2.73
PPh_2Bn	2068.1	152	—[b]
P(*p*-tolyl)$_3$	2066.7	145	—[b]
PBn_3	2066.4	165	—[b]
P(*p*-anisyl)	2066.1	—[b]	4.46
P^{t}BuPh$_2$	2064.7[a]	175	—[b]
P^{i}Pr$_3$	2059.2	160	—[b]
PCy_3	2056.4	170	9.7

Data of the Tolman's factors were taken from ref [99]. [a] Value was calculated from equation 1.1. [b] No value could be found in the literature.

PCy_3 and PPh_3 are both common ligands in coordination chemistry and frequently used agents in organic synthesis. Tricyclohexylphosphane, a symmetrically substituted organophosphorus compound, is a relatively strong base, the pK_a value being 9.7[100] and a strong nucleophile and has reducing character. Triphenylphosphane is a weak base (pK_a 2.73)[100] but a strong nucleophile and has reducing character. It can be obtained by the reaction of phosphorus trichloride with the Grignard compound phenylmagnesium bromide. In air, both phosphanes are oxidised to the respective phosphane oxides, but PCy_3 more swiftly. Their strong coordination to transition metals of the group 7–10 (ν(CO) = 2068.9 cm^{-1} and 2056.4 cm^{-1}) and their steric demand (Tolman cone angle of 145° and 170°), disabling other ligands from coordinating and thus stabilizing low coordinated species, makes them powerful ligands in catalytic processes. Triphenylphosphane for example, is found in the Wilkinson catalyst ([$RhH(PPh_3)_2(CO)_2$]) for hydroformylation reactions or the well known Vaska's compound *trans*-[$IrCl(CO)(PPh_3)_2$] which, due to its property of undergoing oxidative addition reactions, fundamentally contributed to the research on homogenous catalysis.[101, 102] Tricyclopentylphosphane can be found in the Grubbs' catalysts of the first and second generation.[102]

1.9 Aims of this work

As explained in the introduction, two major goals in the applied research on metal nitrosyls are their use in medicine as NO-donors (NO release) or NO-scavengers wherever nitric oxide plays a role in physiological processes and their use in engineering as holographic storage devices (PLI).

The introduction of NO in metal complexes, release of NO from metal complexes and the generation of linkage isomers in nitrosyl complexes are highly correlated to the strength of the metal nitrosyl bond. Especially for PLI, where the NO should neither photo-dissociate nor be non-affected by photo-irradiation, it is necessary to reach a certain range of stability of the metal-nitrogen bond. But also for potential medicinal applications, for example in PDT (photodynamic therapy), the M–NO bond must have a certain inertness in order to reach the target organ without decomposition but has to be labile enough to release NO when and where it is wished. Thus, it is inevitable to get insight into the nature of the metal nitrosyl bond when regarding a targeted synthesis of compounds, applicable in the mentioned fields.

Hence, the aim of this work is to contribute to a better understanding of the metal nitrosyl bond, with its special peculiarities due to the fact that NO is a non-innocent ligand. Special attention will therefore be focused on the ability of NO to be an NO^+, $NO^{\cdot}$ and NO^- ligand.

An adequate system for studying the mentioned properties are the $\{Ru(NO)_2\}^8$ compounds. On the one hand, with only four representatives (depicted in Fig. 1.21), they are structurally less known. On the other hand, they are derivates of an NO^+ and an NO^- ligand. Three of the $\{Ru^{II}(NO^+/NO^-)\}^8$ compounds of Fig. 1.21 are pentacoordinated and adopt a square-pyramidal structure (*SPY*-5, for some structural and spectroscopic data see Table 1.3). When compared to the other structurally known $\{M(NO)_2\}^8$ dinitrosyls, for example $[MnH(NO)_2(P^iPr_3)_2]$ or $[ReH(NO)_2(PCy_3)_2]$ (both shaped in a trigonal bipyramid (*TBPY*-5), see Fig. 1.17), the questions are posed, under which conditions will $\{M(NO)_2\}^8$ compounds adopt a *TBPY*-5 or *SPY*-5 structure, whether a *TBPY*-5 structure is also possible for $\{Ru(NO)_2\}^8$ compounds and whether this structure is always accompanied by two nearly equal nitrosyl ligands. The analytical focus for answering these questions will be concentrated on single-crystal X-ray diffraction and IR spectroscopy.

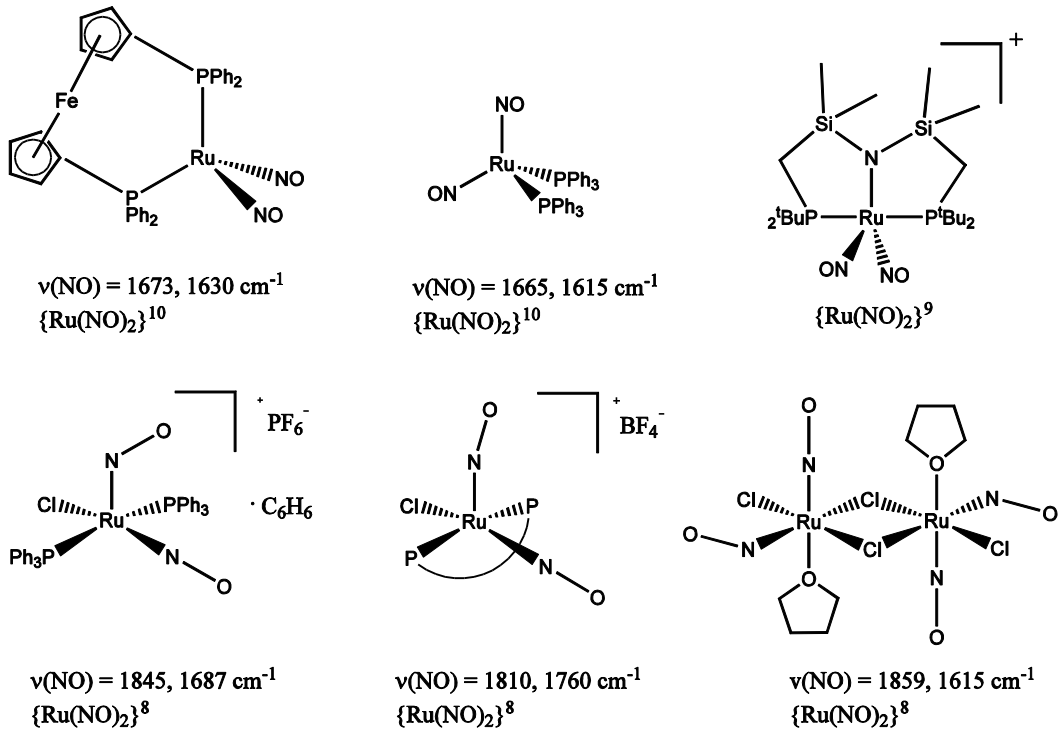

Fig. 1.21: The ruthenium dinitrosyls known in literature. P∩P = 1,10-bis(diphenylphosphinomethyl)benzophenanthrene (dppbp), OR = tetrahydrofurane (THF). Data taken from Refs. [103–108].

Dinitrosyl	Ref.	M–N(O)/Å	N–O/Å	M–N–O/°	N–M–N/°
$[Ru(NO)_2(PPh_3)_2]$	[103]	1.762, 1.776	1.190, 1.194	177.7, 170.6	139.2
$[Ru(NO)_2\{Fe(C_5H_4PPh_2)_2\}]$	[104]	1.762, 1.781	1.282, 1.166	161.5, 179.5	132.1
$[Ru(NO)_2\{^tBu_2PCH_2Si(CH_3)_2N\}_2]^+$	[105]	1.910, 1.760	1.174, 1.156	128.99, 176.02	97.58
$[RuCl(NO)_2\{(Ph_2PCH_2)_2\text{-}C_{18}H_{10}\}]BF_4$	[106]	1.810, 1.760	1.130, 1.148	156.2, 172.5	115.4
$[RuCl(NO)_2(PPh_3)_2]PF_6{\cdot}C_6H_6$	[107]	1.853, 1.743	1.166, 1.158	138, 178	102
$[\{RuCl_2(NO)_2(THF)\}_2]$	[108]	1.727, 1.915	1.147, 1.181	178.5. 124.0	97.6

Table 1.3: Some structural parameters of the ruthenium dinitrosyls known in literature.

2 Results

The RESULTS part will at first deal with the synthesis of the precursor compounds, followed by the side as well as intermediate products and the target compounds (the synthetic route is shown in Fig. 2.1). Next, the characterisation of the precursor compounds and some side and intermediate products will be dealt with, followed by the characterisation of the target compounds—the $\{Ru(NO)_2\}^8$ dinitrosyls—by various spectroscopic methods and single crystal X-ray diffraction. The crystallographically determined nitrosyl bonding mode, which is afflicted with some uncertainty but to which special attention is paid in this work, will be verified by various techniques, such as temperature dependence of atomic displacement parameters (ADPs), IR measurements of the dissolved state and comparative quantum chemical calculations, based on DFT. A following part is dedicated to the analysis of a DNIC analogous ruthenium dinitrosyl. The chapter will close with the PLI behaviour of the $\{Ru(NO)_2\}^8$ compounds.

2.1 Synthesis of the $\{RuNO\}^n$ precursor compounds

The synthesis of $K_2[RuCl_5(NO)]$ (**2**) followed a procedure known from literature and started directly from the commercially available $RuCl_3 \cdot x\ H_2O$ by reaction with 3 equivalents nitrite (equation 2.1).[109] $K_2[RuBr_5(NO)]$ (**4**) and $K_2[RuI_5(NO)]$ (**5**) had to be synthesised by procedures known from literature,[110] *via* the complex $K_2[Ru(OH)(NO_2)_4(NO)]$ (**3**) (equation 2.3), which in turn was gained by the reaction of $RuCl_3 \cdot x\ H_2O$ with 8 equivalents nitrite (equation 2.2a and 2.2b), known from literature.[111] $RuCl_3(NO) \cdot x\ H_2O$ (**1**) could be obtained by a procedure known from literature, *via* the chemical equation 2.2a and subsequent dissolving in ethanol.[111]

$$2\ RuCl_3 \cdot x\ H_2O + 6\ KNO_2 + 6\ HCl \longrightarrow 2\ K_2[RuCl_5(NO)] + 3\ KNO_2 + NO + 2\ KCl + (x + 3\ H_2O) \qquad (2.1)$$

$$2\ RuCl_3 \cdot x\ H_2O + 6\ KNO_2 \longrightarrow 2\ [RuCl_3(NO)] + 3\ NO_2 + NO + 6\ KCl + (x + 3\ H_2O) \qquad (2.2a)$$

$$2\ [RuCl_3(NO)] + 10\ KNO_2 + 2\ H_2O \longrightarrow 2\ K_2[Ru(OH)(NO_2)_4(NO)] + HNO_2 + 6\ KCl \qquad (2.2b)$$

$$K_2[Ru(OH)(NO_2)_4(NO)] + HX \longrightarrow K_2[RuX_5(NO)] + 2\ NO_2 + 2\ NO + 3\ H_2O \qquad (2.3)$$

Reaction conditions: 2.1) Solvent: water, 6 M HCl, temperature: 80 °C, time: 75 min. 2.2a) Solvent: 1 M HCl, temperature: reflux, time: 1 h. 2.2b) Solvent: 1 M HCl, temperature: 80 °C, time: 4 h. 2.3) X = Br, I, Solvent: H_2O, temperature: 80 °C (X = Br), 50, 80 °C (X = I), time: 2 h (X = Br), 1.5 h (X = I).

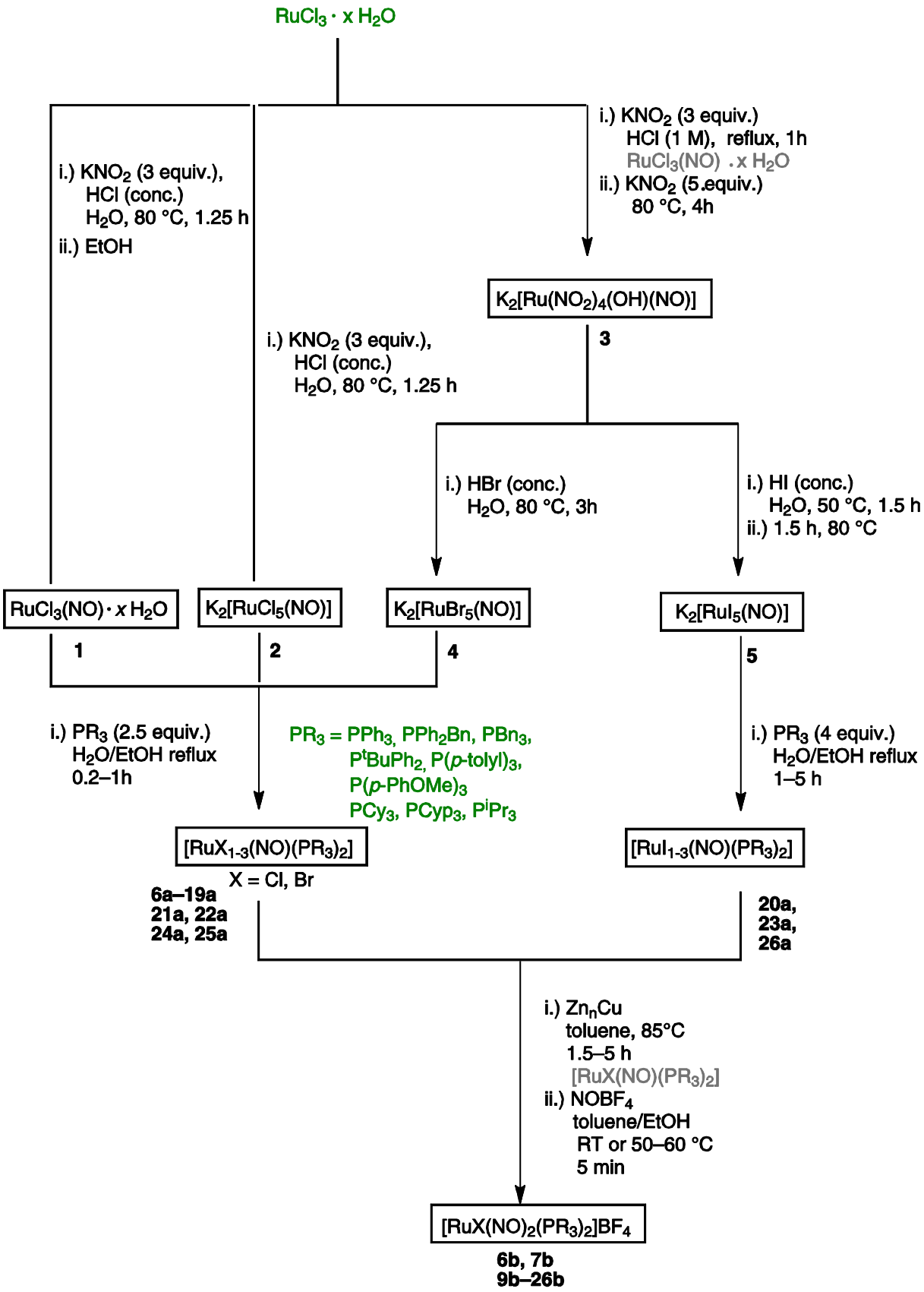

Fig. 2.1: Synthetic route for the dinitrosyls prepared in this work. Green: Commercially available phosphane ligands and precursor compounds. Grey: Intermediate products, which were not isolated (except for $PR_3 = PPh_3$, P^tBuPh_2).

The phosphane-containing mononitrosyls with chlorido or bromido ligands were synthesised by reaction of **2** or **4** with 2.5 equivalents, whereas **5** had to be treated with 4–5 equivalents. The reaction either took place as a simple ligand substitution (equation 2.4) or a redox reaction with a simultaneous addition of two equivalents of the respective phosphane (equation 2.5). When simple ligand substitution occured, the colour of the phosphane-containing products of the $\{RuNO\}^6$ type varied from light yellow to deep orange (general formula $[RuX_3(NO)(PR_3)_2]$). If the reaction took place as a redox reaction with the addition of two phosphanes, the products were greenish in colour and the isolated solid was a $\{RuNO\}^n$ mixture (n = 6, 7, 8; general formula $[RuX_{1-3}(NO)(PR_3)_2]$).

$$K_2[RuX_5(NO)] + 2\ PR_3 \longrightarrow [RuX_3(NO)(PR_3)_2] + 2\ KX \qquad (2.4)$$

$$[RuX_5(NO)]^{2-} + 2\ PR_3 \longrightarrow [RuX_{1-3}(NO)(PR_3)_2] + 2\text{–}4\ X^- \qquad (2.5)$$

Reaction conditions: 2.4) inert gas atmosphere; X = Cl, Br, I; 2.5 equiv. PR_3 = PPh_3, PPh_2Bn, PBn_3, P^tBuPh_2; solvent: ethanol/water, temperature: 85 °C, time: 10 min–45min. 2.5) inert gas atmosphere ; X = Cl, Br, I; 2.5–5 equiv. PR_3 = PCy_3, $PCyp_3$, P^iPr_3, P(*p*-tolyl)$_3$, P(*p*-anisyl)$_3$; solvent: ethanol/water, temperature: 85 °C, time: 30 min–5 h.

2.2 Synthesis of the $\{RuNO\}^8$ intermediate products

As mentioned above, in some cases the reaction of the pentahalogenido compound with the phosphane resulted in a partially reduced product. For reasons of yield, these mononitrosyl complexes were further reduced with Zn_nCu (Na was also possible, but led to smaller yields due to increased decomposition) to ensure that the $\{RuNO\}^n$ mixture ($[RuX_{1-3}(NO)(PR_3)_2]$) was reduced to the corresponding $\{RuNO\}^8$ fragment ($[RuX(NO)(PR_3)_2]$) as completely as possible (equation 2.6a). The alloy-supported reduction to $[RuX(NO)(PR_3)_2]$ was not possible, when the phosphane containing mononitrosyl complex ($[RuX_{1-3}(NO)(PR_3)_2]$, R = P(*p*-anisyl)$_3$, P(*p*-tolyl)$_3$, Cy, Cyp, ^{i}Pr) was not already partially reduced, except for PR_3 = PPh_3, PPh_2Bn, PBn_3, P^tBuPh_2 where reduction was also possible for pure $\{RuNO\}^6$ compounds when X = Cl, Br.

Experiments were also performed for S- and N-donor ligands such as bipyridine, phenanthroline and tetrahydrothiophene. The $\{RuNO\}^6$ compounds were obtained easily, but reduction to the corresponding $\{RuNO\}^8$ compounds failed with both Zn_nCu and Na as reduction agents.

Experiments with compounds of the sterically small triethylphosphane and trimethylphosphane ligands indicated that the reducibility is no longer given when Tolman's θ value (see INTRODUCTION, chapter 1.8) becomes too low. This is most probably due to the instability of the reduced form since the bulkiness of the phosphanes is not as great as to prevent other ligands (X, PR_3) from coordinating. Tolman's electronic parameter can't count for this observation since the ν(CO) value is between the ν(CO) value of the aromatic and the other aliphatic phosphanes (PCy_3, $PCyp_3$, P^iPr_3, P^tBu_3) which were reducible under the given conditions. On the other hand, the electronically also well suitable tri-butylphosphane ligand—whose mononitrosyl complex is reducible—seems to be too sterically demanding for the consecutive addition reaction of the nitrosonium cation. Thus, the chosen synthetic pathway is clearly not only limited to phosphanes but also to the kind of phosphane used.

The change in colour, connected to the reduction from a $\{RuNO\}^6$ (yellow, orange) to a $\{RuNO\}^8$ (green) species, is a simple indicator for the success of the reduction process.

$$\underset{\text{(orange, brown, light green)}}{[RuX_{1-3}(NO)(PR_3)_2]} \xrightarrow{Zn_nCu} \underset{\text{(emerald green)}}{[RuX(NO)(PR_3)_2]} + 2\,X^- \qquad (2.6a)$$

Reaction conditions: 2.6a) inert gas atmosphere ; X = Cl, Br, I; PR_3 = PPh_3, PPh_2Bn, PBn_3, P(*p*-tolyl)$_3$, P(*p*-anisyl)$_3$, P^tBuPh_2, PCy_3, $PCyp_3$, P^iPr_3; solvent: toluene, temperature: 85 °C, time: 1.5–5 h.

2.3 Synthesis of the $\{Ru(NO)_2\}^8$ products

The second NO group was introduced to the *in situ* generated $[RuX(NO)(PR_3)_2]$ compound by an oxidative addition reaction with the nitrosonium cation of $NOBF_4$ to form a pentacoordinated dinitrosyl of the general formula $[RuX(NO)_2(PR_3)_2]BF_4$ (equation 2.6b). The nitrosonium tetrafluoroborate was added either in solution—dissolved in ethanol/toluene—or as a solid, depending on the reactivity and the batch used. If it was added as solid, ethanol had to be added to the $\{RuNO\}^8$ solution first since, otherwise, the $NOBF_4$ would not react but would remain undissolved in the reaction mixture. The change in colour, connected to the oxidation from a $\{RuNO\}^8$ (green) to a $\{Ru(NO)_2\}^8$ (red-orange) species, is a simple indicator for the success of the nitrosylation reaction.

$$\underset{\text{(green)}}{[RuX(NO)(PR_3)_2] + NOBF_4} \longrightarrow \underset{\text{(red-orange)}}{[RuX(NO)_2(PR_3)_2]BF_4} \qquad (2.6b)$$

Reaction conditions: 2.6b) inert gas atmosphere; X = Cl, Br, I; PR_3 = PPh_3, PPh_2Bn, PBn_3, P(*p*-tolyl)$_3$, P(*p*-anisyl)$_3$, P^tBuPh_2, PCy_3, $PCyp_3$, P^iPr_3; solvent: toluene/ethanol, temperature: room temperature or 40–60 °C, time: 5–10 min.

Crystals of the air-stable salts were obtained directly from the reaction solutions upon cooling or by dissolving the compounds in dichloromethane and covering the solution with a layer of diethyl ether or *n*-pentane. The compounds are easily soluble in dichloromethane, soluble in aceton and ethanol, poorly soluble in toluene and insoluble in diethyl ether and hydrocarbons such as n-pentane or n-hexane. In dichloromethane, slow decomposition was observed in solution (the solid is stable against decomposition).

In the case of X = I and PR_3 = P^iPr_3, a dinuclear $\{Ru(NO)_2\}^9$–$(Ru(NO)_2\}^9$ complex formed. The compound might be the secondary product of the reduction of the mononuclear $\{Ru(NO)_2\}^8$ species. This reaction might only take place in the case of an iodido and tri-isopropylphosphane ligand due to their high steric demand (stabilisation of the low-coordinated dinuclear species) and the relatively easy oxidation of the phosphane ligand to diiodphosphorane and phosphane oxide.

As mentioned in chapter 2.2, the synthesis described above is limited to special phosphane ligands. An alternative synthetic route to $\{Ru(NO)_2\}^8$ compounds was described by Bergman *et al.*[108] Herein $[\{RuCl_2(cymene)\}_2]$, which can be synthesised by the reduction of $RuCl_3 \cdot x\,H_2O$ with α-phellandrene, is nitrosylated with gaseous nitric oxide in THF to the compound $[\{RuCl_2(NO)_2(THF)\}_2]$ (**27**), in which the ruthenium atom is hexacoordinated. By the alteration of the solvent (which has to be

coordinating) or the addition of ligands, before or after nitrosylation, new dinitrosyls could be gained, avoiding the limiting reduction route. A disadvantage could be the low selectivity of this synthetic route leading to product mixtures difficult to describe analytically due to a non-quantitative ligand substitution. If the substitution of two ligands in **27** is desired, for example to synthesise compounds of the general formula $[RuX(NO)_2(PR_3)_2]BF_4$ with phosphane ligands for which the reductive route is excluded, the THF and one of the chlorido ligands have to be the most labile ligands. Surely, THF is the most labile ligand in **27**, but it is imaginable that the nitroxyl ligand is more labile than a chlorido ligand, which would lead to a mononitrosyl complex, making this route inapplicable.

2.4 Characterisation of the $\{RuNO\}^n$ precursor compounds

1–**5** could be characterised by IR spectroscopy, mass spectrometry and elemental analysis. The elemental analysis of the mononitrosyls corresponded to a formulation of the isolated products as pure $\{RuNO\}^6$ compounds. The mass spectra of the dipotassium salts were recorded in a glycerine/water matrix in the ESI^+ and ESI^- mode. The *ν*(NO) frequencies of **2**, **4** and **5** decrease in the order Cl > Br > I, whereas the π basicity of the halogenido ligand X increases in the same order. The higher the π basicity of X, *i.e.* the better the donation of electron from X to the ruthenium centre, the stronger the π backdonation. Strengthening of the backdonation will lead to a higher degree of occupation of the π* orbitals of the nitrosyl ligand, which in turn will weaken the N–O bond, leading to smaller *ν*(NO) stretching frequencies.

The products of the type $[RuX_{1-3}(NO)(PR_3)_2]$ (**6a**–**26a**) were characterised by IR spectroscopy, $^{31}P\{^1H\}$-NMR spectroscopy, elemental analysis. Except of the insoluble nitrosyls **6a**–**8a**, for which $PR_3 = PPh_3$, the compounds could further be analyzed by mass spectrometry in the FAB^+/FAB^- mode with nitrobenzyl alcohol as matrix. Compound **8a** was also characterised by single-crystal X-ray diffraction, the results of which will be presented below.

Pure $\{RuNO\}^6$ compounds as products of recation 2.4 were found for **6a**–**13a**. These compounds showed only one band in the *ν*(NO) range and only one signal in the ^{31}P-NMR spectra. Elemental analysis were consitent with the empirical formulae $[RuX_3(NO)(PR_3)_2]$. $\{RuNO\}^n$ mixtures were found as products of reaction 2.5 for **14a**–**26a**. These compounds showed several bands in the *ν*(NO) range and multiple signals in the ^{31}P-NMR spectra, which were assigned to the mononitrosyl species of the $\{RuNO\}^6$, $\{RuNO\}^7$ and $\{RuNO\}^8$ type, as well as the phosphane ligand in the free and oxidised form. Hence, the number of observable NMR signals in the spectrum could be up to five. Elemental analysis were inconsitent with the empirical formulae $[RuX_3(NO)(PR_3)_2]$, since they showed a significantly too high carbon, nitrogen and hydrogen content when taking into account a pure $\{RuNO\}^6$ compound. Based on elemental analysis and IR data, **14a-19a** and **21a-24a** can thus be formulated as $\{RuNO\}^n$ mixtures with n = 6, 7, 8. Compounds **20a**, **25a** and **26a** can be formulated as $\{RuNO\}^n$ mixtures with n = 7, 8.

The trend found for **2**, **4** and **5**, decreasing *ν*(NO) values in the order Cl > Br >I, is also valid for compounds of the $[RuX_{1-3}(NO)(PR_3)_2]$ type, when regarding groups of the same phosphane ligand.

Structure solution for **8a** · C_7H_8 succeeded in the monoclinic space group *C*2/*c*. The unit cell contains four formula units, the asymmetric unit contains half a complex molecule and half a co-crystallised solvent molecule (both shown in Fig. 2.2). The complex molecule is supplemented *via* a C_2 axis, the toluene molecule *via* an inversion centre. Accordingly, the toluene molecule lies on a special site with site symmetry $\bar{1}$, the complex molecule on a special site with the site symmetry 2. The central atom is coordinated in a distorted octahedral fashion ($CShM_{OC}$-value of 1.756), where the axial positions are occupied by the nitrosyl ligand and the *trans*-NO iodido ligand. The equatorial positions are occupied by two phosphorus atoms and two iodine atoms. The N–Ru–$I2_{ax}$ angle of the axis of the octahedron is exactly linear (180.00°). All equatorial positioned atoms take up L_{eq}–Ru–NO angles < 90° (88.85° and 89.09°) and L_{eq}–Ru–L_{eq} angles > 90° (91.27°, 91.14° and 91.15°) except for I1–Ru–P (88.69°), giving rise to a distorted octahedron. The Ru–NO (1.73 Å) and N–O (1.15 Å) bond lengths are within the common range for $\{RuNO\}^6$ complexes.[112]

Possessing a C_2 axis, the complex exhibits C_2 symmetry. The molecules are stacked along the crystallographic *a* axis.

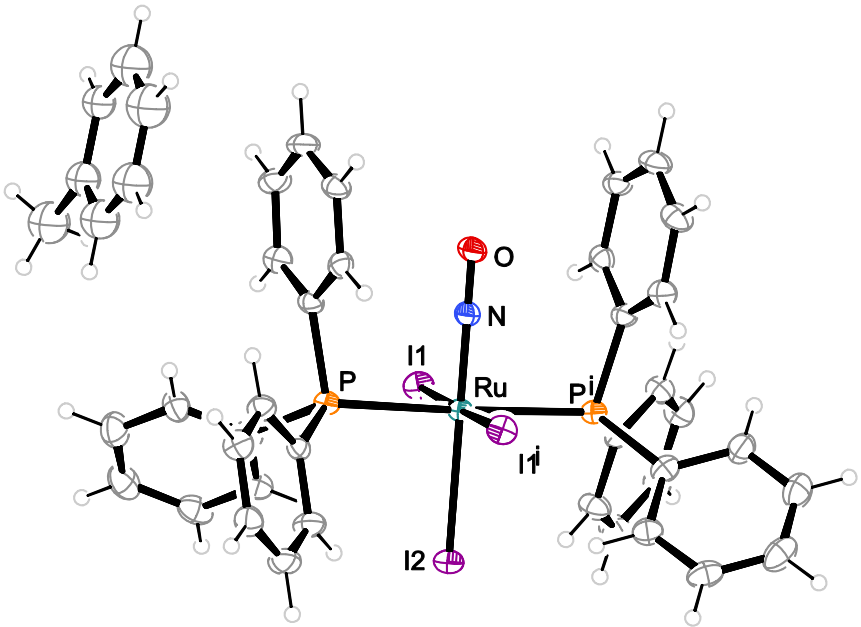

Fig. 2.2: ORTEP plot of the complex and the solvent molecule in crystals of **8a** · 4 C_7H_8. The thermal ellipsoids are drawn at 50% probability level at 173 K. Interatomic distances (Å) and angles (°), the standard deviation of the last decimal place is given in parentheses: Ru–N 1.7298(56), Ru–I 2.7238(3), Ru–I2 2.7142(6), Ru–P1 2.4796(11), O–N 1.1490(65); O–N–Ru 180.00, N–Ru–P 88.85(3), N–Ru–I1 89.09(1), N–Ru–I2 180.00, I1–Ru–P 88.69(3), I1–Ru–P^i 91.27(3), I2–Ru–P 91.14(3), I2–Ru–P^i 91.15(3), I1–Ru–I2 90.91(1), I1–Ru–$I1^i$ 178.18(2), P–Ru–P^i 177.71(6). Selected torsion angles: I2–Ru–N–O 0.00. Symmetry code: ^{i} −x, y, −z+½.

2.5 Characterisation of {RuNO}^{6} side and {RuNO}^{8} intermediate products

It proved possible to crystallise the {RuNO}^{8} intermediates **6c** and **13c** which allowed to compare alterations of the RuNO moiety in dependence of the oxidation state and coordination number of the ruthenium atom. **8c** and **7c** formed as side products of the reduction of the respective precursor compounds **8a** and **7a**.

2.5.1 {RuNO}^{8} compound with triphenylphosphane

The synthesis of compound **6c** followed a procedure, known from literature.[113] The compound was isolated in the form of green crystals. A yield was not specified.

IR spectroscopy showed the product to be of the {RuNO}^{8} type: the infrared spectrum revealed two bands in the *v*(NO) range at 1767 and 1729 cm^{-1}. The frequency at 1767 cm^{-1} is less intensive and is most probably the result of a partial oxidation of the {RuNO}^{8} compound to the respective {RuNO}^{7} compound, since the analogous {RuNO}^{6} compound would have a *v*(NO) frequency of 1858 cm^{-1}. The far more intensive and lower energetic band at 1729 cm^{-1} can be assigned to the {RuNO}^{8} species, which is confirmed by X-ray crystallography. The elemental analysis confirmed the empirical formula $C_{36}H_{30}ClNOP_2Ru$, denoted as [RuCl(NO)(PPh_3)$_2$], to be an {RuNO}^{8} species. Due to the chemical equivalence of the phosphane ligands the $^{31}P\{^1H\}$ NMR spectrum showed only one signal at 33.6 ppm. The mass spectrum showed one peak at 691.5 *m/z*.

Structure solution succeeded in the monoclinic space group $P2_1/n$. The unit cell contains four formula units. The structure of compound **6c** within crystals of **6c** · 0.5 C_7H_8 is shown in Fig. 2.3.

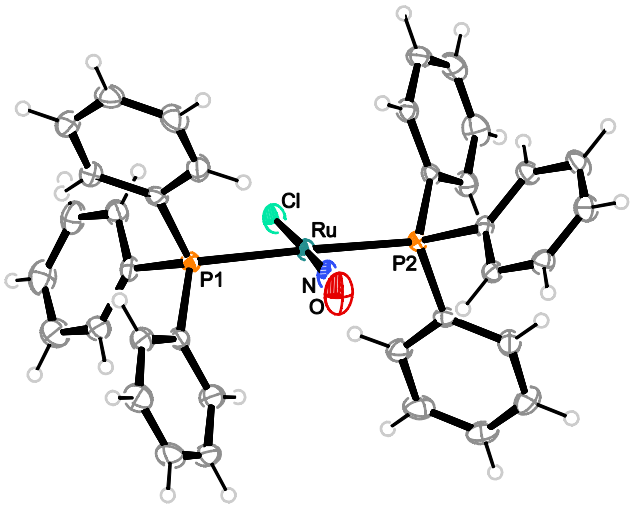

Fig. 2.3: ORTEP plot of the complex [RuCl(NO)(PPh_3)$_2$] in crystals of **6c**. The thermal ellipsoids are drawn at 50% probability level at 273 K. Interatomic distances (Å) and angles (°), the standard deviation of the last decimal place is given in parentheses: Ru–N1 1.7216(19), Ru–Cl 2.3149(5), Ru–P1 2.3865(6), Ru–P2 2.3828(5), O1–N1 1.1574(23); O1–N1–Ru 176.64(18), N1–Ru–Cl 178.08(6), N1–Ru–P1 88.91(6), N1–Ru–P2 95.96(6), Cl–Ru–P1 89.83(2), Cl–Ru–P2 85.22(2), P1–Ru–P2 174.10(2). Selected torsion angle: P1–Ru1–N1–O1 14.33(3.57).

The coordination polyhedron of the cation is best described as a square ($CShM_{SP}$-value of 1.111). The *trans*-arranged phosphane ligands and the *trans*-arranged chlorine and nitrogen atom of the NO group form the tetragonal base. The ruthenium atom lies above the basal plane by 0.047 Å.

The P–Ru–P angle deviates from the ideal value of 180° by 5.9°, the Cl–Ru–N angle by 1.9°. In both cases the *trans*-arranged atoms are bent in a *cisoid* fashion. Thus, the torsion angle of the atom group P1–Ru1–N1–O1 is neither 0° nor 180°. The nitrosyl ligand is coordinated in a linear mode (RuNO 176.58°). The relatively short Ru–N distance of 1.7216 Å indicates a high degree of π backdonation of the formal ruthenium(I) atom to the π-acidic nitrosyl ligand. Considering the spectroscopic data, the oxidation state of the ruthenium atom has to be ±0, the nitrosyl ligand can be regarded as an NO^+ ligand. The compound is isoster to Vaska's complex $[IrCl(CO)(PPh_3)_2]$. The substituents of the phosphorus atoms arrange in a staggered conformation, thus the structure has no symmetry element and is therefore C_1-symmetrical. The co-crystallised solvent molecules (toluene) are disordered *via* an inversion centre and lie on a special site with the site symmetry $\bar{1}$. The toluene molecules are stacked along all three crystallographic axes.

[{RuBr$_2$(NO)(PPh$_3$)}$_2$(μ-Br)$_2$] **(7c)**

The reduction of compound **7a** with zinc-copper couple to $[RuBr(NO)(PPh_3)_2]$ and the consecutive addition of $NOBF_4$ leads, in some cases, not only to the desired dinitrosyl but also to a dimeric mononitrosyl complex, whose structure is shown in Fig. 2.4. Crystals formed upon storage at 4 °C. Structure solution for **7c** succeeded in the monoclinic space group $P2_1/c$. The unit cell contains two formula units, the asymmetric unit contains half a complex molecule, which is supplemented to a complete molecule *via* an inversion centre.

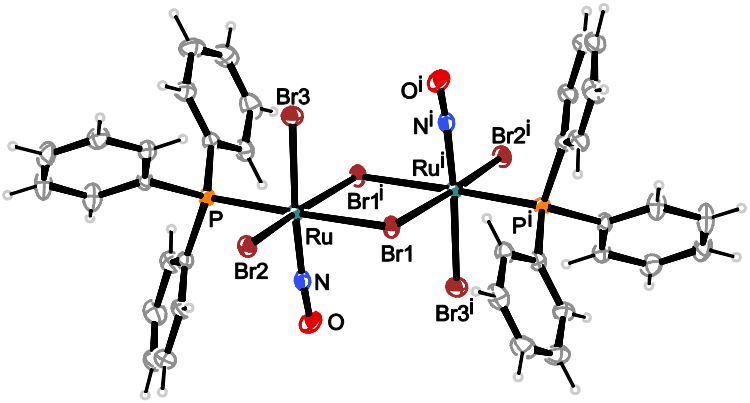

Fig. 2.4: ORTEP plot of the complex $[\{RuBr_2(NO)(PPh_3)\}_2(\mu\text{-}Br)_2]$ in crystals of **8c**. The thermal ellipsoids are drawn at 50% probability level at 173 K. Interatomic distances (Å) and angles (°), the standard deviation of the last decimal place is given in parentheses: Ru–N 1.7610(34), Ru–P1 2.3787(9), Ru–Br1 2.6168(4), Ru–Br1^i 2.5445(4), Ru–Br2 2.4954(4), Ru–Br3 2.4614(5), O–N 1.1021(43); O–N–Ru 175.68(30), N–Ru–P 93.78(10), N–Ru–Br1 88.48(10), N–Ru–Br1^i 89.34(10), N–Ru–Br2 93.44(10), N–Ru–Br3 174.92(10), Br1–Ru–P 177.59(3), Br1–Ru–Br1^i 83.78(1), Br1–Ru–Br2 87.49(1), Br1–Ru–Br3 89.44(2), Br1^i–Ru–P 97.08(2), Br1^i–Ru–Br2 170.77(2), Br1^i-Ru-Br3 85.83(2), Br2-Ru-P 91.52(2), Br2-Ru-Br3 91.09(2) Br3–Ru–P 88.38(3). Selected torsion angles: Br1^i–Ru–Br1–Ru^i 0.00, Ru^i–Br1–Ru–Br2 −176.98 (2). Symmetry code: ^{i}–x, –y + 1, –z.

The neutral complex consists of two {RuNO}^{6} centres, connected *via* two bromido bridging-ligands. Both central atoms are coordinated in a distorted octahedral fashion ($CShM_{OC}$-value of 1.190), where the axial positions are occupied by the nitrosyl ligands and the *trans*-NO bromido ligands. The equatorial positions are occupied by one phosphorus atom and three bromine atoms. The N1–Ru–$Br3_{ax}$ angle of the axes of the octahedron is approximately linear (174.92°). The equatorial positioned phosphorus atom and the symmetry generated, bridging Br2 atom take up L_{eq}–Ru–NO angles > 90° (93.78° and 93.44°), whereas the also equatorially positioned Br1 atom and the bridging $Br1^i$ atom atom take up L_{eq}–Ru–NO angles < 90° (88.48° and 89.34°), giving rise to a distorted octahedron. The torsion angle of the four-membered $Br1^i$–Ru–Br1–Ru^i ring is 0.00°, giving rise to a planar ring system. The symmetry elements of the dimeric complex are an inversion centre, a twofold rotation axis and a twofold rotoreflection axis, the molecule is hence C_{2i} symmetrical. The molecule, through which a C_2 axis runs, lies on a special site with site symmetry $\bar{1}$. The molecules are stacked along all three crystallographic axes.

[{RuI$_2$(NO)(PPh$_3$)}$_2$(μ-I)$_2$] **(8c)**

Attempts to reduce compound **8a** with zinc-copper couple to [RuI(NO)(PPh$_3$)$_2$] were not successful. A change in colour could not be dtected and a reaction with $NOBF_4$ failed to appear. Crystals from the reaction solution were identified as the mononuclear species **8a** · C_7H_8 and the dinuclear species **8c** · C_7H_8 [{RuI$_2$(NO)(PPh$_3$)}$_2$(μ-I)$_2$] · C_7H_8, both are shown in Fig. 2.2 and Fig. 2.5.

Structure solution for **8c** · C_7H_8 succeeded in the monoclinic space group $P2_1/n$. The unit cell contains two complex molecules and four solvent molecules. The asymmetric unit contains half a complex molecule [{Ru(NO)(PPh$_3$)}$_2$(μ-I)$_2$] and one solvent molecule of toluene, the second half is symmetry generated by the inversion centre of the unit cell. The neutral complex consists of two {RuNO}^{6} centres, connected *via* two iodido bridging-ligands. Both central atoms are coordinated in a distorted octahedral fashion ($CShM_{OC}$-value of 1.724), where the axial positions are occupied by the nitrosyl ligands and the *trans*-NO iodido ligands. The equatorial positions are occupied by one phosphorus atom and three iodine atoms. The N1–Ru–$I2_{ax}$ angle of the axis of the octahedron is approximately linear (174.94°). The equatorial positioned phosphorus atom and the symmetry generated, bridging $I1^i$ atom take up L_{eq}–Ru–NO angles > 90° (96.09° and 91.41°), whereas the also equatorial positioned I3 atom and the bridging I1 atom atom take up L_{eq}–Ru–NO angles < 90° (85.27° and 87.49°), giving rise to a distorted octahedron. The torsion angle of the four-membered Ru^i–I1–Ru–$I1^i$ ring is 0.00°, giving rise to a planar ring system. The Ru–NO (1.75 Å) and N–O (1.13 Å) bond lengths are within the common range for {RuNO}^{6} complexes.[112]

The molecule, through which a C_2 axis runs, lies on a special site with site symmetry $\bar{1}$. Accordingly, the symmetry elements of the dimeric complex are an inversion centre, a twofold rotation axis and a twofold rotoreflection axis, the molecule is hence C_{2i} symmetrical. The molecules are stacked along all three crystallographic axes.

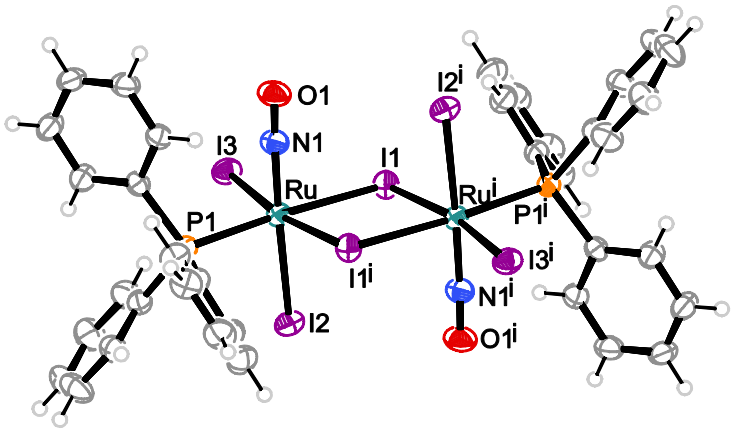

Fig. 2.5: ORTEP plot of the complex [{$RuI_2(NO)(PPh_3)$}$_2$(μ-I)$_2$] in crystals of **8c** · C_7H_8. The thermal ellipsoids are drawn at 50% probability level at 173 K. Interatomic distances (Å) and angles (°), the standard deviation of the last decimal place is given in parentheses: Ru–N1 1.7499(50), Ru–P1 2.4203(15), Ru–I1 2.7604(6), Ru–I1^i 2.7342(6), Ru–I2 2.7002(6), Ru–I3 2.7157(6), O1–N1 1.1272(61); O1–N1–Ru 173.81(48), N1–Ru–P 96.09(16), N1–Ru–I1 87.49(16), N1–Ru–I1^i 91.41(17), N1–Ru–I2 174.94(16), N1–Ru–I3 85.27(17), I1–Ru–P 176.38(4), I1–Ru–I1^i 84.43(2), I1–Ru–I2 88.27(2), I1–Ru–I3 85.56(2), I1^i–Ru–P 94.90(4), I1^i–Ru–I2 90.92(2), I1^i-Ru-I3 169.58(2), I2-Ru-P 88.18(4), I2-Ru-I3 91.65(2) I3–Ru–P 95.28(4). Selected torsion angles: Ru^i–I1–Ru–I1^i 0.00, Ru^i–I1–Ru–I3 177.11(2). Symmetry code: ^{i} –x+1, –y, –z.

2.5.2 {RuNO}^{8} compound with *tert*-butyldiphenylphosphane

[RuCl(NO)(P^tBuPh_2)$_2$] **(13c)**

Compound **13c** was synthesised by the reduction of **13a** with Zn_nCu in toluene. The compound was isolated in the form of green crystals. A yield was not specified.

IR spectroscopic measurements showed the product to be of the {RuNO}^{8} type: The infrared spectrum revealed two bands in the *v*(NO) range at 1770 and 1713 cm^{-1}. The band at 1770 is very weak in its intensity and is the oxidised form of **13c**, which has the very intensive *v* (NO) band at 1713 cm^{-1}.

Structure solution succeeded in the monoclinic space group $P2_1/c$. The unit cell contains four formula units. The structure of compound **13c** is shown in Fig. 2.6.

The coordination polyhedron of the cation is best described as a square ($CShM_{SP}$-value of 1.072). The *trans*-arranged phosphane ligands and the *trans*-arranged chlorine and nitrogen atom of the NO group form the tetragonal base. The ruthenium atom lies above the basal plane by 0.037 Å.

The P–Ru–P angle deviates from the ideal value of 180° by 8.7°, the Cl–Ru–N angle by 3.9°. In both cases the *trans*-arranged atoms are bent in a *cisoid* fashion. Thus, the torsion angle of the atom group P1–Ru1–N1–O1 is not 0° or 180°. The nitrosyl ligand is coordinated in a linear mode (RuNO 177.32°). The relatively short Ru–N distance of 1.7139 Å indicates a high degree of π backdonation of the formal ruthenium(I) atom to the π-acidic nitrosyl ligand. Considering the spectroscopic data, the oxidation state of the ruthenium atom has to be +II, the nitrosyl ligand can be regarded as an NO^+ ligand. The substituents of the phosphorus atoms arrange in a nearly staggered conformation, thus the structure has no symmetry element and is, therefore, C_1 symmetrical. The molecules are arranged in chains along the crystallographic *a* axis.

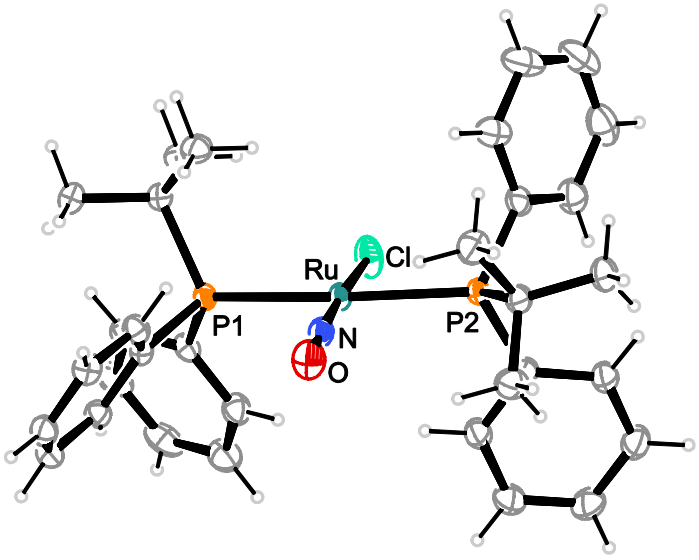

Fig. 2.6: ORTEP plot of the complex $[RuCl(NO)(P^tBuPh_2)_2]$ in crystals of **13c**. The thermal ellipsoids are drawn at 50% probability level at 173 K. Interatomic distances (Å) and angles (°), the standard deviation of the last decimal place is given in parentheses: Ru–N 1.7139(16), Ru–Cl 2.3400(5), Ru–P1 2.4061(4), Ru–P2 2.3958(5), O–N 1.1834(20); O–N–Ru 177.32(16), N–Ru–Cl 176.13(5), N–Ru–P1 93.16(5), N–Ru–P2 95.55(5), Cl–Ru–P1 87.88(2), Cl–Ru–P2 83.38(2), P1–Ru–P2 171.26(2). Selected torsion angle: Cl–Ru–N–O −5.23(3.95).

2.6 Characterisation of the $\{Ru(NO)_2\}^8$ products

Among the analytical methods suitable for the detection or characterisation of the dinitrosyls synthesised in the present work, are ^{31}P NMR spectroscopy (phosphane ligands), elemental analysis (C, H, N and X containing ligands), mass spectrometry in the FAB mode (ionic compounds), IR spectroscopy (alteration of the dipole moment during the symmetric and asymmetric stretching vibration of the NO ligands) and single-crystal X-ray diffraction (good crystallisation behaviour). The structures from X-ray diffractional experiments were characterised by means of *continuous shape measurement* and τ_5-value analysis and were additionally compared to predictions derived from calculations based on density functional theory.

2.6.1 Spectroscopic methods

The cationic dinitrosyls were analyzed with mass spectroscopy in the FAB^+ mode and were therefore dissolved in nitrobenzyl alcohol. All mass spectra showed peaks for the complex cation $[RuX(NO)_2(PR_3)_2]^+$, denoted as $[M]^+$, and the fragment cation $[RuX(NO)(PR_3)_2]^+$, denoted as $[M - NO]^+$, with the typical ruthenium isotope pattern, consisting of the seven naturally occurring isotopes (see Fig. 2.7). Infrared spectra of the complexes showed two bands in the region assignable to coordinated nitrogen monoxide. As the two oscillating N–O bonds share the ruthenium atom as common atom, the ν(NO) vibrations are coupled in a symmetrical and an asymmetrical mode, giving rise to two bands, denoted as $\nu(NO)_{sym}$ and $\nu(NO)_{asym}$ (see Fig. 2.8).

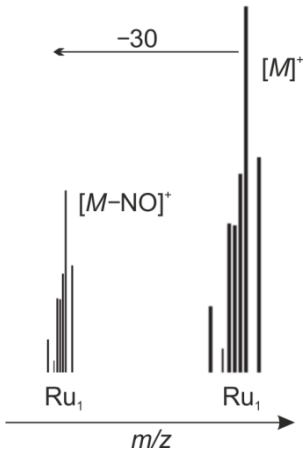

Fig. 2.7: Exemplary mass spectrum of $\{Ru(NO)_2\}^8$ compounds of the formula $[RuX(NO)_2(PR_3)_2]BF_4$.

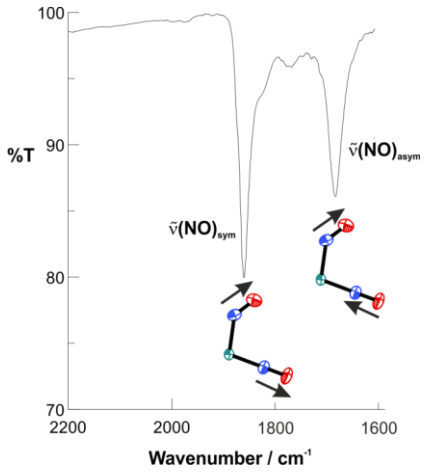

Fig. 2.8: Exemplary infrared spectrum of $\{Ru(NO)_2\}^8$ compounds of the formula $[RuX(NO)_2(PR_3)_2]BF_4$.

Since all the dinitrosyl compounds of this work are diamagnetic low-spin complexes (see INTRODUCTION, chapter 1.4.2) it is possible to characterise them by NMR spectroscopy. As there are no multiple bonding positions of the phosphane ligands, the recording of ^{13}C and ^{1}H spectra was left out. To check the purity of the compounds, $^{31}P\{^{1}H\}$ NMR spectra were recorded at 109 MHz, which bears the advantage of high NMR sensitivity and short pulse times due to the high natural abundance of the ^{31}P isotope. $^{31}P\{^{1}H\}$ NMR spectra, recorded from solutions of the respective

compounds in dichloromethane, always showed only one signal for the complex as the phosphorus atoms are chemically equivalent.

Although an adequate method for estimating the MNO angle (INTRODUCTION, chapter 1.4.2), recording of ^{14}N or ^{15}N NMR spectra of the dinitrosyls was not performed, since the purchase of ^{15}N-enriched educts is very costly (Sigma–Aldrich, 5 g $Na^{14}NO_2$ for 0.24 €, 5 g $Na^{15}NO_2$ for 755 €). A further disadvantage is the high substance consumption due to the relatively low sensitivity.

The compounds are highly soluble in dichloromethane, soluble in acetonitrile, chloroform, acetone and dimethylformamide, poorly soluble in ethanol, insoluble in diethyl ether and hydrocarbons. The colour changes from yellow to orange and reddish brown, depending on the halide. The compounds are thermally and air-stable and undergo slow decomposition in dichloromethane, thereby giving rise to an oxidised mononitrosyl compound.

2.6.2 Single-crystal X-ray crystallography and description of the structure by CShM and τ_5 values

Single-crystal X-Ray diffraction could successfully be performed for 15 of the 21 dinitrosyls, synthesised in this work. 14 of these are dinitrosyls of the $\{Ru(NO)_2\}^8$ type, namely **6b**, **7b**, **9b**, **10b**, **14b**, **15b** and **18b-25b**. Only these compounds will be analyzed in the following chapters. An own chapter is dedicated to **26c**.

In compounds of the type $[RuX(NO)_2(PR_3)_2]BF_4$, the ruthenium centre is obviously pentacoordinated. The most representative geometries for pentacoordination are the trigonal bipyramid (tbp, D_{3h}) and the square pyramid (sqp, C_{4v}). Both are resonance structures of nearly the same energy—the trigonal bipyramid being slightly more stable—and are transformed into each other in solution by the Berry mechanism (see Fig. 2.9).

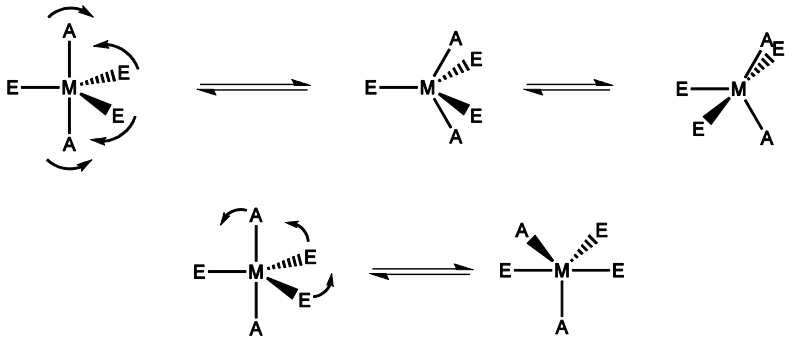

Fig. 2.9: First row: The transformation, leading from a trigonal bipyramid to a square pyramid and again to a trigonal bipyramid with exchanged equatorial (E) –axial (A) positions. Second row: The turnstile process, a mechanistic alternative without the square pyramid as intermediate structure.

Pentacoordinated, homoleptic complexes show a rapid intramolecular fluctuation in solution, resulting in an equivalence of the chemical shift of the five ligands on the NMR time scale: $[Fe(CO)_5]$ shows one ^{13}C signal down to −170 °C; $[M(PF_3)_5]$ complexes with M = Fe, Ru, Os show

one ^{31}P-NMR signal down to −160 °C.[114]

For heteroleptic coordination compounds, one conformation can be favoured in the solid state. Addisons τ_5 parameter,[115] as well as Alvarez' *continous shape measurement* (CShM) values,[116] describe the magnitude with which the one or the other structure is favoured (see EXPERIMENTAL PART, chapter 5.7). Thus, the structure of the compounds will be described by the CShM values for the trigonal bipyramid (*TBPY*-5) and the vacant octahedron (*VOC*-5) and Addison's τ_5 value[115] (tbp and sqp). The values will be enlisted togehter with distances and angles beneath the ORTEP plot of the respective structure. In some cases, especially in the shape maps, the CShM value for the square pyramid (*SPY*-5) is given. This does not correspond to Addison's τ_5 value, which does not allow to distinguish whether the central atom is part of the square base or is situated above it. For the algorithms see EXPERIMENTAL PART, chapter 5.7.

The τ_5 value as well as the CShM values do not provide any explanation why one conformation is favoured over the other. There are some rules and more or less intuitive predictions in order to estimate which sites in a tbp or sqp complex will be favoured by which ligands. The higher negatively charged ligands often have the higher spatial demand: for complexes of the type $[MX_n(PR_3)_m]$ with $n + m = 5$ the halogenido ligand is situated equatorially in a trigonal bipyramid. Thus, the arrangement of the ligands is dictated by electronic and steric effects.

In both possible geometries for the $\{Ru(NO)_2\}^8$ compounds, being part of this work, the bulky phosphane ligands will occupy *trans*-positions. Furthermore, it is expected that the NO^+ ligand will be situated approximately *trans* to the halogenido ligand. Being both a σ- and π-donor ligand, the halide will stabilise the ruthenium backdonation to the π-acidic NO^+ ligand in a better way than the NO^- ligand would do, which is a poor σ and π base. Thus, there is only one possible arrangement of the five ligands in both the tbp and the sqp structure, shown in Fig. 2.10. Which structure is adopted and favoured will be discussed in the following. A detailed, qualitative MO and crystal field theoretic approach for conformation and site preferences can be found in DISCUSSION, chapter 3.4.

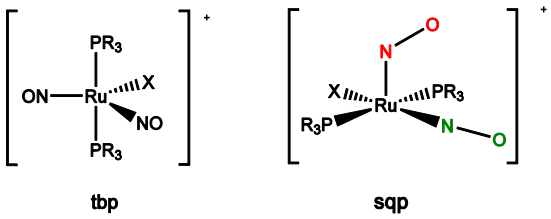

Fig. 2.10: The possible structures for the coordination cation $[RuX(NO)_2(PR_3)_2]^+$. In the sqp structure the nitrosyl ligands can occupy distinguishable positions, the nitroxyl (NO^-) ligand is printed in red, the nitrosonium (NO^+) ligand is printed in green. In the tbp structure the possible NO positions are indistinguishable from each other.

All the pentacoordinated $\{Ru(NO)_2\}^8$ compounds, of which only four are known to literature, adopt sqp structure with the bent NO ligand positioned apical and the linear NO ligand positioned basal (see AIMS, chapter 1.9). Among these, complex $[RuCl(NO)_2(PPh_3)_2]PF_6$ is the most related to the dinitrosyls of this work (the only difference to compound **6b** being the counterion) and was characterised by Pierpont and Eisenberg in 1970.[117] Electronically, the compound can be

described as a d^6 metal centre coordinated to an NO^+ and an $^1NO^-$ ligand, since there is a noticeable difference between the structural and spectroscopic parameters of the two nitrosyl ligands. This description can also be applied to the compounds **6b**, **18b**, **19b**, **21b-1** and **25b-2**. The structure of the compounds **6b**, **18b**, **19b**, **21b-1** and **25b-2** can best be described as a vacant octahedron (*VOC*-5) (CShM$_{VOC}$-values 1.56–2.59) or a square pyramid (sqp) (τ_5-values 0.09–0.36), with the bent NO group (Ru–N–O 135°–151°) forming the apex of the vacant octahedron and the *trans*-configurated phosphanes together with the halide ligand and the linear NO group comprising the square planar plane. The P–Ru–P angle deviates from the ideal value of 180° by 14.5° on average so that the phosphorus atoms are bent away from the bent NO group and are inclined to each other enabling van der Waals interactions. The two NO ligands in these compounds differ markedly from each other: the differences in the Ru–N–O angles range from 26.3°–44.1° (36.88° on average), the Ru–N bond lengths differ by 0.092 Å–0.144 Å (0.113 Å on average). The bent NO group points toward the linear NO group (*cisoid* bent of 20.26° on average), perhaps giving rise to a nucleophile-electrophile interaction. The maximum symmetry reachable in these compounds is the point group C_S. The structure of the compounds **9b**, **10b**, **20b**, **21b-2**, **22b**, **23b** and **25b-2** can best be described as a trigonal bipyramid (tbp for τ_5 value or *TBPY*-5 for CShM value) (CShM$_{TBPY}$-values 2.02–2.46, τ_5-values 0.64–0.79). The *trans*-arranged phosphane ligands build the apexes of the bipyramid, the halide together with the two NO groups form the trigonal base. Again, the P–Ru–P angle deviates from linearity by 13.3° on average and the subsituents R of the phosphanes are inclined to each other enabling van der Waals interactions. The phosphorus atoms are bent away from the NO groups, the nitrosyl ligands themselves are slightly bent (13.5° on average) in a *cisoid* fashion. In these compounds the binding situation of the two NO ligands becomes more and more equal: the differences in the Ru–N–O angles range from 0.0°–6.6° (3.65° on average), the Ru–N bond length differ by 0.000 Å–0.021 Å (0.008 Å on average). This coordination geometry has, so far, been unknown for penta-coordinated $\{Ru(NO)_2\}^8$ compounds. The maximum symmetry reachable in these structures is the point group C_{2v}, which is adopted by compound **14b**, in which the two NO ligands are indistinguishable from each other (see Table 2.4). The structure of the compounds **7b**, **14b** and **15b** is situated between trigonal biyramidal and square pyramidal (CShM$_{TBPY\text{-}5}$-values 2.44–3.10, τ_5-values 0.51–0.60). The CShM values are smaller for *TBPY*-5 than for *VOC*-5 geometry, but, in contrast to the structures of **9b**, **10b**, **20b**, **21b-2**, **22b**, **23b** and **25b-2**, the CShM$_{VOC\text{-}5}$ value is clearly smaller. The difference in the Ru–N–O angles and Ru–N bond lengths are relatively high—as is the case in the sqp structures—but smaller on average, ranging from 21.1°–32.2° (Ru–N–O) and 0.029 Å–0.101 Å (Ru–N).

Fig. 2.11 gives an overview of the adopted structures within a shape map. **21b** and **25b** are able to crystallise in both structures, sqp and tbp (the suffix b-1 refers to the sqp structure, the suffix b-2 to the tbp structure). Figures 12–28 show the crystal sructures of **6b**, **7b**, **9b**, **10b**, **14b**, **15b** and **18b**–**25b**. They are ordered with repect to the phosphane ligands. The two different conformational polymorphs of compound **21b** are shown in Fig. 2.22 and Fig. 2.23. The two co-crystallised conformers of **25b** are shown in Fig. 2.27 and Fig. 2.28. Beneath the ORTEP-plots, derived from the structure solution of single-crystal X-ray diffraction analysis, angles, distances,

the CShM and the τ_5 value are listed as well as the distance of the ruthenium central atom from the square base in the case of the sqp structures. For reasons of better comparison, the atoms of the NO group possessing the more obtuse Ru–N–O angle are always referred to as N1 and O1. Those of the NO group possessing the more acute Ru–N–O angle, are referred to as N2 and O2, respectively.

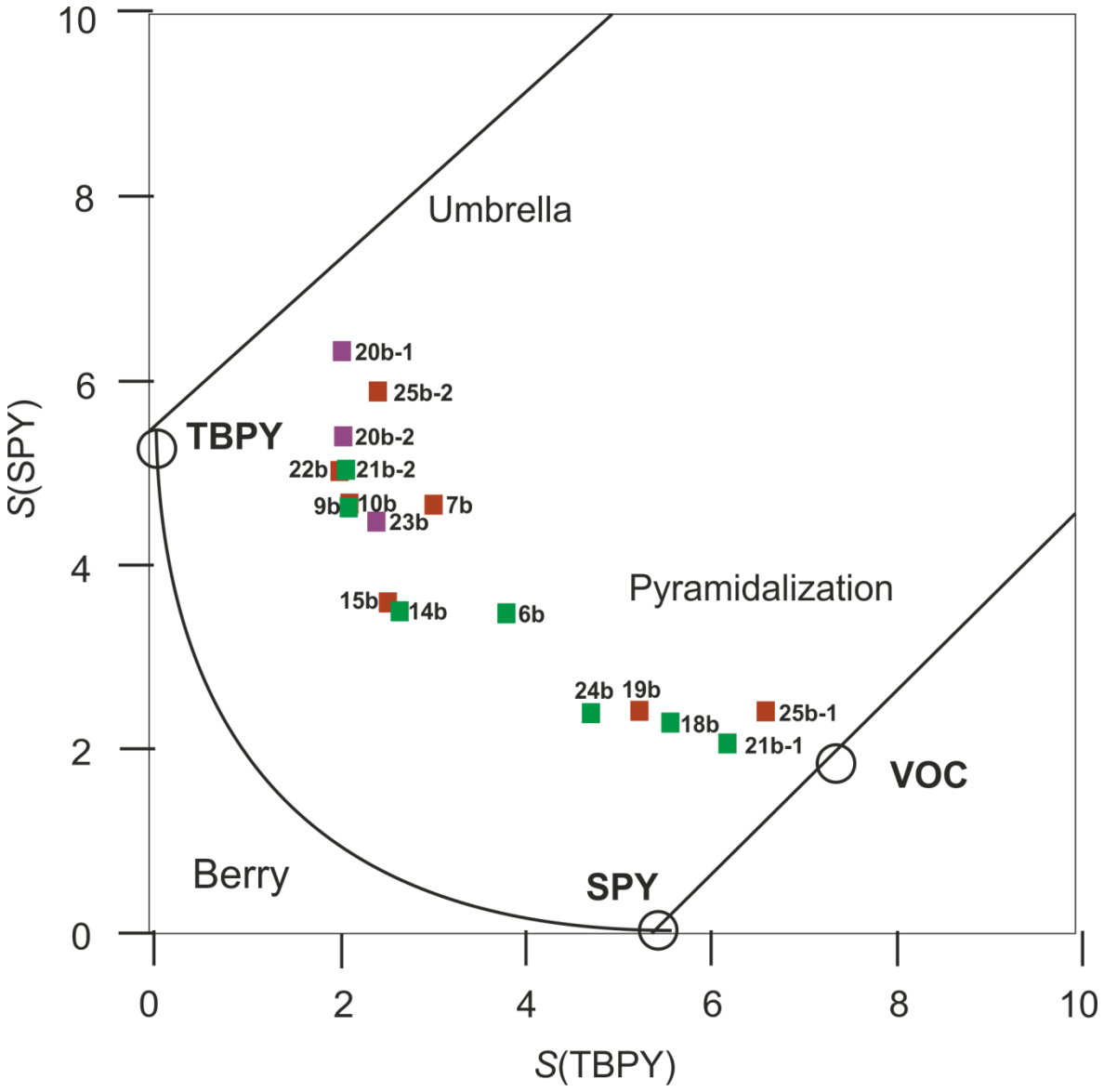

Fig. 2.11: Shape map for pentacoordinated complexes $[RuX(NO)_2(PR_3)_2]BF_4$ according to Ref. [116]. Lilac (X = I), reddish brown (X = Br), green (X = Cl). Phosphane ligands PR_3 = PPh_3 (**6b**, **7b**), PPh_2Bn (**9b**, **10b**), P(*p*-tolyl)$_3$ (**14b**, **15b**), PCy_3 (**18b**, **19b**, **20b**), $PCyp_3$ (**21b-1**, **21b-2**, **22b**, **23b**), P^iPr_3 (**24b**, **25b**).

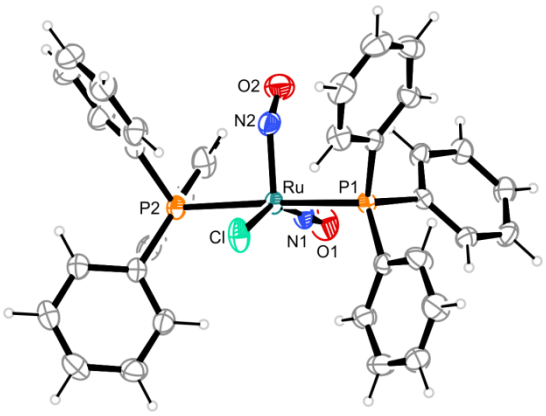

Fig. 2.12: ORTEP plot of the coordination cation in crystals of **6b**. SpGr: $P2_1/c$. The thermal ellipsoids are drawn at 50% probability level. Interatomic distances (Å) and angles (°), the standard deviation of the last decimal place is given in parentheses: Ru–N1 1.746(2), Ru–N2 1.872(2), Ru–P1 2.4470(6), Ru–P2 2.4534(6), Ru–Cl 2.3523(6), O1–N1 1.155(3), O2–N2 1.162(3); O1–N1–Ru 178.9(2), O2–N2–Ru 134.78(19), N1–Ru–Cl 151.17(7), N1–Ru–P1 92.87(7), N1–Ru–P2 92.99(7), N1–Ru–N2 102.67(10), N2–Ru–Cl 106.14(7), N2–Ru–P1 92.21(6), N2–Ru–P2 90.15(6), Cl–Ru–P1 85.13(2), Cl–Ru–P2 87.93(2), P1–Ru–P2 173.05(2). Selected torsion angles: N1–Ru–N2–O2 3.2(3), Cl–Ru–N2–O2 −177.79(24). $CShM_{VOC\text{-}5}$: 2.588, τ_5: 0.37, $d_{Ru\text{-}SP}$: 0.346.

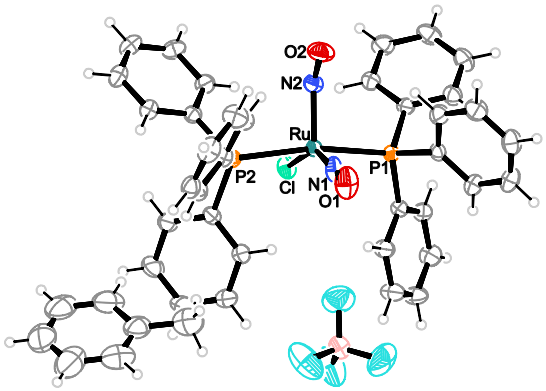

Fig. 2.13: ORTEP plot of the asymmetric unit in crystals of **6b** · C_7H_8. SpGr: *Pbca*.The thermal ellipsoids are drawn at 50% probability level. Interatomic distances (Å) and angles (°), the standard deviation of the last decimal place is given in parentheses: Ru–N1 1.752(3), Ru–N2 1.847(3), Ru–P1 2.4232(8), Ru–P2 2.4193(8), Ru–Cl 2.3796(8), O1–N1 1.141(4), O2–N2 1.150(3); O1–N1–Ru 179.3(3), O2–N2–Ru 143.6(3), N1–Ru–Cl 146.37(10), N1–Ru–P1 92.46(9), N1–Ru–P2 92.40(9), N1–Ru–N2 108.11(13), N2–Ru–Cl 105.51(9), N2–Ru–P1 95.01(8), N2–Ru–P2 95.89(8), Cl–Ru–P1 84.94(3), Cl–Ru–P2 83.78(3), P1–Ru–P2 166.06(3). Selected torsion angles: N1–Ru–N2–O2 −0.3(5), Cl–Ru–N2–O2 −179.3(4). $CShM_{VOC\text{-}5}$: 2.308, τ_5: 0.33, $d_{Ru\text{-}SP}$: 0.403.

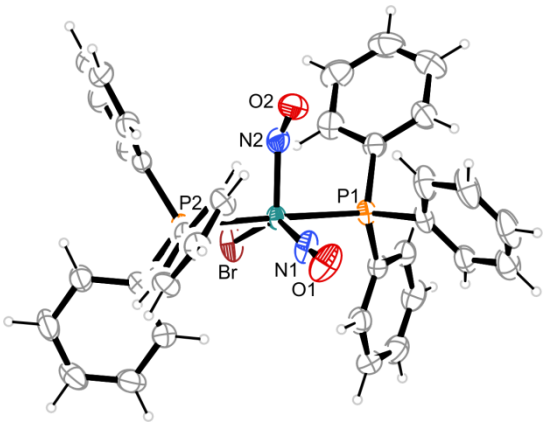

Fig. 2.14: ORTEP plot of the coordination cation in crystals of **7b**. SpGr: P21/c. The thermal ellipsoids are drawn at 50% probability level. Interatomic distances (Å) and angles (°), the standard deviation of the last decimal place is given in parentheses: Ru–N1 1.753(2), Ru–N2 1.854(2), Ru–P1 2.4537(6), Ru–P2 2.4470(6), Ru–Br 2.5062(3), O1–N1 1.135(3), O2–N2 1.148(3); O1–N1–Ru 175.3(3), O2–N2–Ru 143.1(2), N1–Ru–Br 142.03(9), N1–Ru–P1 93.50(7), N1–Ru–P2 92.21(7), N1–Ru–N2 105.75(11), N2–Ru–Br 112.20(7), N2–Ru–P1 90.11(6), N2–Ru–P2 92.59(7), Br–Ru–P1 87.71(2), Br–Ru–P2 85.06(2), P1–Ru–P2 172.78(2). Selected torsion angles: N1–Ru–N2–O2 4.4(3), Br–Ru–N2–O2 −176.8(3). $CShM_{VOC\text{-}5}$: 3.096, τ_5: 0.51, $d_{Ru\text{-}SP}$: 0.441.

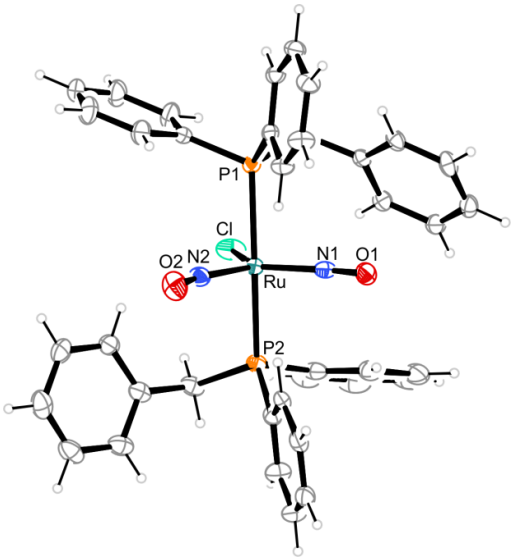

Fig. 2.15: ORTEP plot of the coordination cation $[RuCl(NO)_2(PPh_2Bn)_2]^+$ in crystals of **9b**. SPGr: $P2_1/n$. The thermal ellipsoids are drawn at 50% probability level. Interatomic distances (Å) and angles (°), the standard deviation of the last decimal place is given in parentheses: Ru–N1 1.781(2), Ru–N2 1.785(2), Ru–Cl 2.4122(7), Ru–P1 2.4110(7), Ru–P2 2.4168(7), O1–N1 1.156(3), O2–N2 1.145(3); O1–N1–Ru 167.2(2), O2–N2–Ru 164.0(2), N1–Ru–Cl 124.14(8), N1–Ru–P1 93.41(7), N1–Ru–P2 92.88(7), N1–Ru–N2 115.52(11), N2–Ru–Cl 120.34(8), N2–Ru–P1 95.58(7), N2–Ru–P2 95.83(7), Cl–Ru–P1 81.63(2), Cl–Ru–P2 81.85(2), P1–Ru–P2 163.10(2). Selected torsion angles: N2–Ru–N1–O1 0.4(9), Cl–Ru–N2–O2 −173.6(7). $CShM_{TBPY\text{-}5}$: 2.124, τ_5: 0.64.

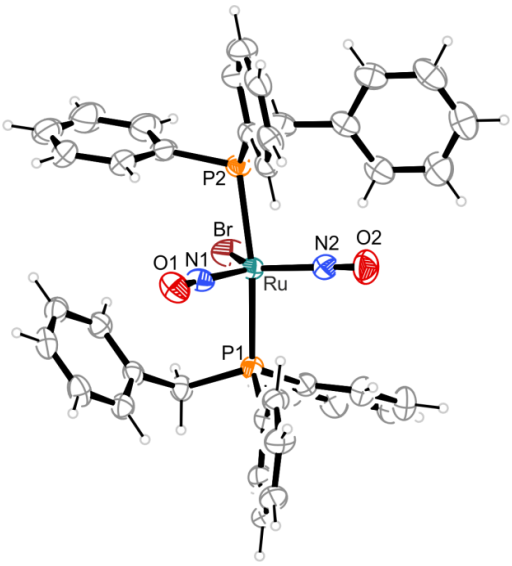

Fig. 2.16: ORTEP plot of the coordination cation $[RuBr(NO)_2(PPh_2Bn)_2]^+$ in crystals of **10b**. SpGr: $P2_1/n$. The thermal ellipsoids are drawn at 50% probability level. Interatomic distances (Å) and angles (°), the standard deviation of the last decimal place is given in parentheses: Ru–N1 1.777(2), Ru–N2 1.781(2), Ru–Br 2.5447(3), Ru–P1 2.4220(7), Ru–P2 2.4227(7), O1–N1 1.154(3), O2–N2 1.153(3); O1–N1–Ru 168.2(2), O2–N2–Ru 162.8(2), N1–Ru–Br 125.51(7), N1–Ru–P1 93.46(7), N1–Ru–P2 92.06(7), N1–Ru–N2 115.42(11), N2–Ru–Br 119.07(8), N2–Ru–P1 95.97(8), N2–Ru–P2 95.47(7), Br–Ru–P1 81.83(2), Br–Ru–P2 82.49(2), P1–Ru–P2 163.71(2). Selected torsion angles: N2–Ru–N1–O1 1.8(1.1), Br–Ru–N2–O2 −177.5(1.0). $CShM_{TBPY\text{-}5}$: 2.153, τ_5: 0.64.

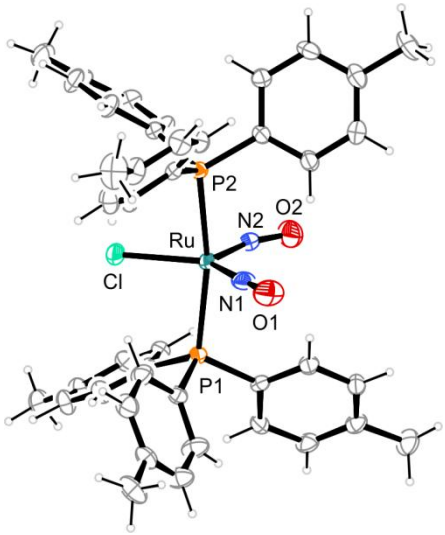

Fig. 2.17: ORTEP plot of the coordination cation $[RuCl(NO)_2\{P(p\text{-tolyl})_3\}_2]^+$ in crystals of **14b**. The thermal ellipsoids are drawn at 50% probability level. SPGr: $P2_12_12_1$. Interatomic distances (Å) and angles (°), the standard deviation of the last decimal place is given in parentheses: Ru–N1 1.753(4), Ru–N2 1.829(3), Ru–P1 2.4436(9), Ru–P2 2.4362(9), Ru–Cl 2.3803(10), O1–N1 1.151(4), O2–N2 1.139(4); O1–N1–Ru 178.0(4), O2–N2–Ru 151.2(3), N1–Ru–Cl 135.27(12), N1–Ru–P1 91.00(10), N1–Ru–P2 90.50(11), N1–Ru–N2 114.14(15), N2–Ru–Cl 110.59(10), N2–Ru–P1 95.44(10), N2–Ru–P2 94.38(10), Cl–Ru–P1 84.94(3), Cl–Ru–P2 85.95(3), P1–Ru–P2 168.46(3). Selected torsion angles: N1–Ru–N2–O2 −2.5(7), Cl–Ru–N2–O2 177.3(6). $CShM_{TBPY\text{-}5}$: 2.581, τ_5: 0.55, $d_{Ru\text{-}SP}$: 0.703.

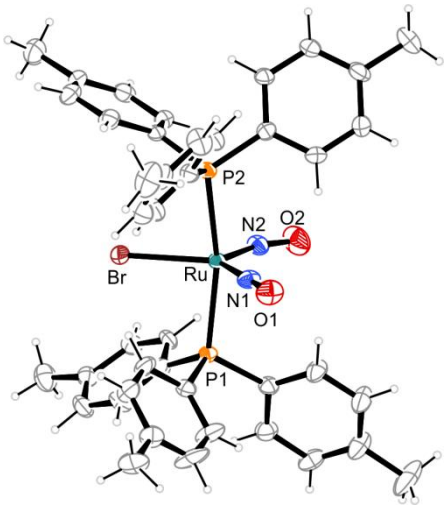

Fig. 2.18: ORTEP plot of the coordination cation $[RuBr(NO)_2\{P(p\text{-tolyl})_3\}_2]^+$ in crystals of **15b**. SpGr: $Pna2_1$. The thermal ellipsoids are drawn at 50% probability level. Interatomic distances (Å) and angles (°), the standard deviation of the last decimal place is given in parentheses: Ru–N1 1.771 (5), Ru–N2 1.800 (4), Ru–P1 2.4378 (17), Ru–P2 2.4542 (18), Ru–Br 2.530 (5), O1–N1 1.132 (6), O2–N2 1.151 (5); O1–N1–Ru 177.8 (5), O2–N2–Ru 156.7 (4), N1–Ru–Br 130.07 (14), N1–Ru–P1 88.72 (16), N1–Ru–P2 90.10 (16), N1–Ru–N2 118.0(2), N2–Ru–Br 112.0 (2), N2–Ru–P1 95.43 (16), N2–Ru–P2 97.12 (16), Br–Ru–P1 85.14 (4), Br–Ru–P2 85.23 (4), P1–Ru–P2 166.36 (4). Selected torsion angles: N1–Ru–N2–O2 5.0(1.3), Br–Ru–N2–O2 −173.4(1.2). $CShM_{TBPY\text{-}5}$: 2.435, τ_5: 0.60, $d_{Ru\text{-}SP}$: 0.563.

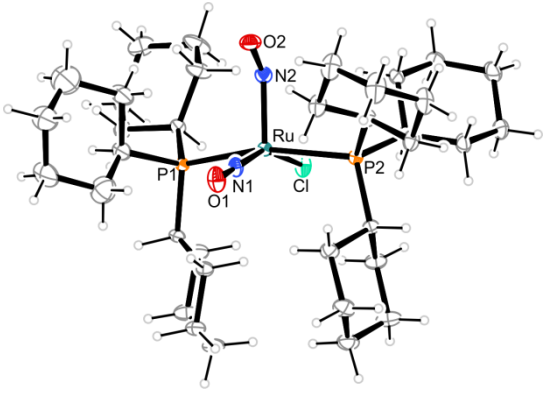

Fig. 2.19: ORTEP plot of the coordination cation $[RuCl(NO)_2(PCy_3)_2]^+$ in crystals of **18b**. SpGr: $P\bar{1}$. The thermal ellipsoids are drawn at 50% probability level. Interatomic distances (Å) and angles (°), the standard deviation of the last decimal place is given in parentheses: Ru–N1 1.739(3), Ru–N2 1.870(3), Ru–Cl 2.3738(7), Ru–P1 2.4558(8), Ru–P2 2.4792(8), O1–N1 1.162 (3), O2–N2 1.159(3); O1–N1–Ru 179.9(3), O2–N2–Ru 136.5(2), N1–Ru–Cl 154.52(9), N1–Ru–P1 92.69(8), N1–Ru–P2 92.11(8), N1–Ru–N2 103.64(12), N2–Ru–Cl 101.80(8), N2–Ru–P1 99.06(8), N2–Ru–P2 95.06(8), Cl–Ru–P1 81.97(3), Cl–Ru–P2 86.98(3), P1–Ru–P2 163.58(3). Selected torsion angles: N1–Ru–N2–O2 2.3(4), Cl–Ru–N2–O2 −179.1(3). $CShM_{VOC\text{-}5}$: 1.804, τ_5: 0.15, $d_{Ru\text{-}SP}$: 0.370.

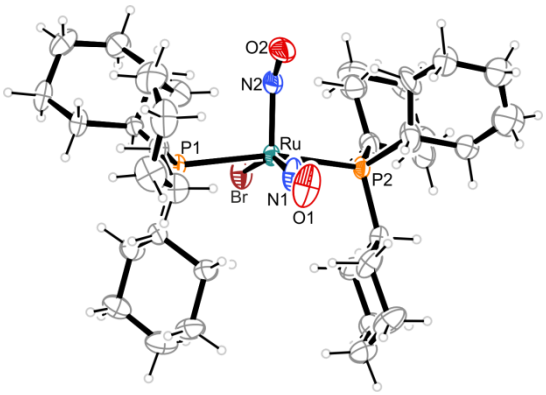

Fig. 2.20: ORTEP plot of the coordination cation $[RuBr(NO)_2(PCy_3)_2]^+$ in crystals of **19b**. SpGr: $P\bar{1}$. The thermal ellipsoids are drawn at 50% probability level. One cyclopentyl ring on P2 is disordered, atoms of the minor disordered part (occupancy ca. 46%) are not shown. Interatomic distances (Å) and angles (°), the standard deviation of the last decimal place is given in parentheses: Ru–N1 1.763(8), Ru–N2 1.856(7), Ru–Br 2.5087(14), Ru–P1 2.459(2), Ru–P2 2.477(2), O1–N1 1.102(9), O2–N2 1.135(9); O1–N1–Ru 178.0(8), O2–N2–Ru 139.5(7), N1–Ru–Br 153.1(3), N1–Ru–P1 95.0(2), N1–Ru–P2 89.4(2), N1–Ru–N2 103.9(4), N2–Ru–Br 103.1(2), N2–Ru–P1 96.8(2), N2–Ru–P2 97.1(2), Br–Ru–P1 82.25(6), Br–Ru–P2 86.84(6), P1–Ru–P2 164.00(7). Selected torsion angles: N1–Ru–N2–O2 −1(1), Br–Ru–N2–O2 179.5(9). $CShM_{VOC\text{-}5}$: 1.851, τ_5: 0.19, $d_{Ru\text{-}SP}$: 0.385.

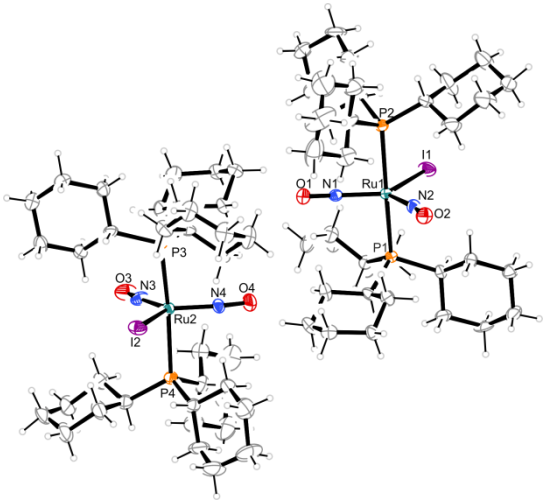

Fig. 2.21: ORTEP plot of the two crystallographic independent coordination cations $[RuI(NO)_2(PCy_3)_2]^+$ in the asymmetric unit in crystals of **20b**. The thermal ellipsoids are drawn at 50% probability level at 173 K. Interatomic distances (Å) and angles (°), the standard deviation of the last decimal place is given in parentheses: Ru1–N1 1.775(8), Ru1–N2 1.796(9), Ru1–I1 2.7227(10), Ru1–P1 2.475(2), Ru1–P2 2.480(4), O1–N1 1.15(1), O2–N2 1.16(1); O1–N1–Ru1 170.7 (8), O2–N2–Ru1 165.9(8), N1–Ru1–I1 121.9(3), N1–Ru1–P1 92.0(2), N1–Ru1–P2 88.3(2), N1–Ru1–N2 122.3(4), N2–Ru1–I1 115.8(3), N2–Ru1–P1 94.0(3), N2–Ru1–P2 94.0(3), I1–Ru1–P1 83.94(6), I1–Ru1–P2 86.69(6), P1–Ru1–P2 169.14(9); Ru2–N3 1.775(8), Ru2–N4 1.796(9), Ru2–I2 2.7301(10), Ru2–P3 2.467(3), Ru2–P4 2.485(3), O3–N3 1.15(1.0), O4–N4 1.17 (1.0); O3–N3–Ru2 169.9(8), O4–N4–Ru2 163.3(8), N3–Ru2–I2 122.8(3), N3–Ru2–P3 92.8(3), N3–Ru2–P4 92.7(3), N3–Ru2–N4 118.9(4), N4–Ru2–I2 118.4(3), N4–Ru2–P3 94.8(3), N4–Ru2–P4 89.7(3), I2–Ru2–P3 82.56(6), I2–Ru2–P4 87.57(7), P3–Ru2–P4 170.13(9). Selected torsion angles: O2–N2–Ru1–N1 −6.8(5), O2–N2–Ru1–I1 171.9(3.2), O4–N4–Ru2–N3 −3.3(2.6), O4–N4–Ru2–I2 176.7(2.4). $CShM_{TBPY\text{-}5}$: 2.110, 2.193; τ_5: 0.79, 0.78.

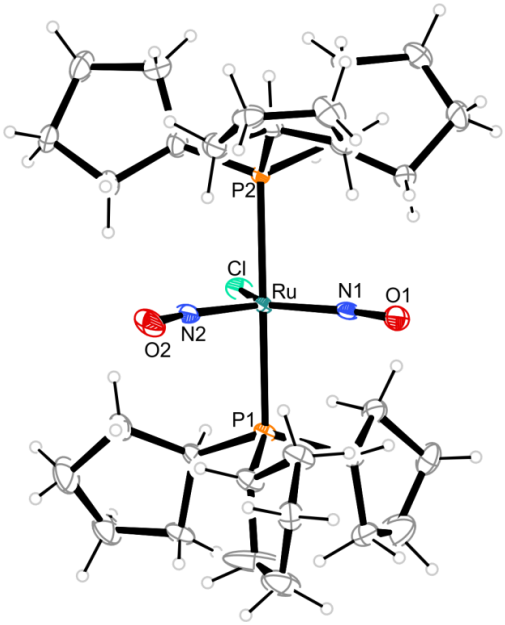

Fig. 2.22: ORTEP plot of the coordination cation $[RuCl(NO)_2(PCyp_3)_2]^+$ in rod-shaped crystals of **21b-2** (minor product). SpGr: $P2_1/c$. The thermal ellipsoids are drawn at 50% probability level. Interatomic distances (Å) and angles (°), the standard deviation of the last decimal place is given in parentheses: Ru–N1 1.775(2), Ru–N2 1.783(2), Ru–Cl 2.4185(7), Ru–P1 2.4470(7), Ru–P2 2.4480(7), O1–N1 1.154(3), O2–N2 1.153(3); O1–N1–Ru 168.1(2), O2–N2–Ru 164.4(2), N1–Ru–Cl 126.4(8), N1–Ru–P1 89.93(7), N1–Ru–P2 95.83(7), N1–Ru–N2 117.02(11), N2–Ru–Cl 116.60(8), N2–Ru–P1 91.74(7), N2–Ru–P2 96.04(7), Cl–Ru–P1 86.72(2), Cl–Ru–P2 80.42(2), P1–Ru–P2 166.94(2). Selected torsion angles: N1–Ru–N2–O2 −5.8(8), O2–N2–Ru–Cl 172.2(8). $CShM_{TBPY\text{-}5}$: 2.075, τ_5: 0.68.

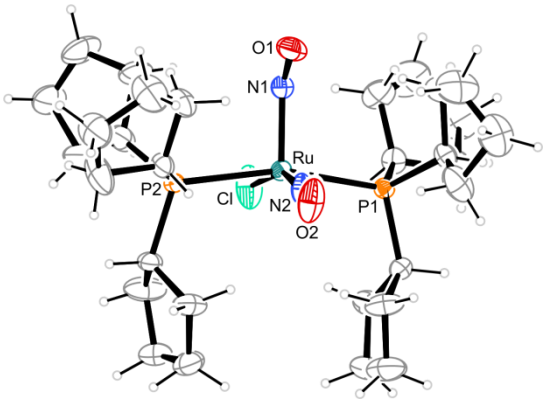

Fig. 2.23: ORTEP plot of the coordination cation $[RuCl(NO)_2(PCyp_3)_2]^+$ in block-shaped crystals of **21b-1** (main product). SpGr: $P2_1/n$. The thermal ellipsoids are drawn at 35% probability level. One cyclopentyl ring on each phosphorus atom is disordered, atoms of the minor disordered part (occupancy ca. 40%) are not shown. Interatomic distances (Å) and angles (°), the standard deviation of the last decimal place is given in parentheses: Ru–N1 1.850(4), Ru–N2 1.758(3), Ru–Cl 2.352(2), Ru–P1 2.4727(14), Ru–P2 2.4574(14), O1–N1 1.122(4), O2–N2 1.155(4); O1–N1–Ru 176.9(3), O2–N2–Ru 137.1(3), N1–Ru–N2 103.47(16), N1–Ru–Cl 157.47(13), N1–Ru–P1 92.57(11), N1–Ru–P2 90.02(11), N2–Ru–Cl 98.94(12), N2–Ru–P1 98.33(11), N2–Ru–P2 97.43(11), Cl–Ru–P1 86.21(5), Cl–Ru–P2 84.80(5), P1–Ru–P2 162.89(3). Selected torsion angles: N2–Ru–N1–O1 −0.8(5), O1–N1–Ru–Cl 176.9(5). $CShM_{VOC-5}$: 1.555, τ_5: 0.09, d_{Ru-SP}: 0.365.

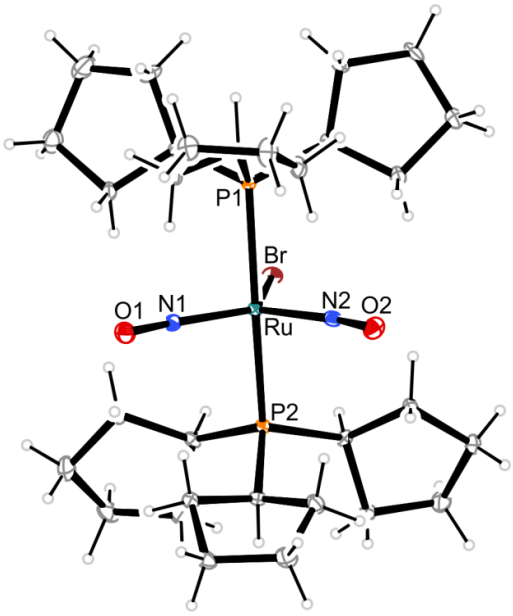

Fig. 2.24: ORTEP plot of the coordintaion cation $[RuBr(NO)_2(PCyp_3)_2]^+$ in crystals of **22b**. SpGr: $P\bar{1}$. The thermal ellipsoids are drawn at 50% probability level. Interatomic distances (Å) and angles (°), the standard deviation of the last decimal place is given in parentheses: Ru–N1 1.779(3), Ru–N2 1.780 (3), Ru–Br 2.5734(5), Ru–P1 2.4438(10), Ru–P2 2.4479(10), O1–N1 1.164(4), O2–N2 1.162(4); O1–N1–Ru 168.7(3), O2–N2–Ru 166.6(3), N1–Ru–Br 124.57(11), N1–Ru–P1 93.11(10), N1–Ru–P2 95.01(10), N1–Ru–N2 118.83(15), N2–Ru–Br 116.60(10), N2–Ru–P1 95.05(10), N2–Ru–P2 93.95(10), Br–Ru–P1 81.95(3), Br–Ru–P2 81.26(3), P1–Ru–P2 163.12(4). Selected torsion angles: N1–Ru–N2–O2 0.8(1.3), Br–Ru–N1–O1 −174.8(1.4). $CShM_{TBPY-5}$: , 2.032, τ_5: 0.66.

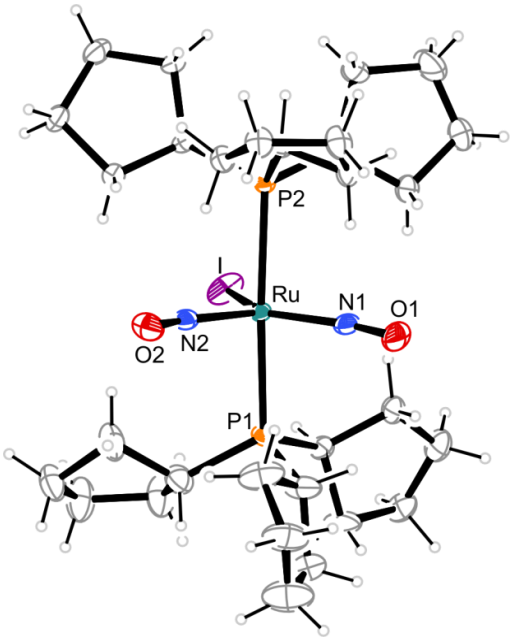

Fig. 2.25: ORTEP plot of the coordination cation $[RuI(NO)_2(PCyp_3)_2]^+$ in crystals of **23b**. SpGr: $P\bar{1}$. The thermal ellipsoids are drawn at 50% probability level. One cyclopentyl ring on P1 is disordered, atoms of the minor disordered part (occupancy ca. 44%) are not shown. Interatomic distances (Å) and angles (°), the standard deviation of the last decimal place is given in parentheses: Ru–N1 1.779(4), Ru–N2 1.787(4), Ru–I 2.7301(5), Ru–P1 2.4584(12), Ru–P2 2.4582(11), O1–N1 1.148(5), O2–N2 1.152(5); O1–N1–Ru 168.9(4), O2–N2–Ru 165.5(4), N1–Ru–I 128.30(14), N1–Ru–P1 88.00(12), N1–Ru–P2 94.50(12), N1–Ru–N2 118.45(19), N2–Ru–I 113.18(13), N2–Ru–P1 95.78(12), N2–Ru–P2 94.14(12), I–Ru–P1 84.35(3), I–Ru–P2 84.18(3), P1–Ru–P2 167.10(4). Selected torsion angles: N1–Ru–N2–O2 1.9(1.5), I–Ru–N2–O2 179.0(1.4). $CShM_{TBPY-5}$: 2.464, τ_5: 0.65.

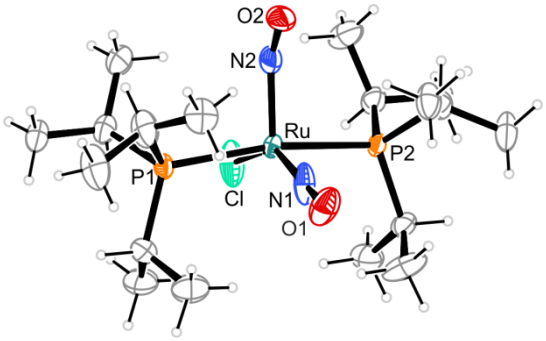

Fig. 2.26: Structure of the coordintaion cation $[RuCl(NO)2(P^iPr_3)_2]^+$ in crystals of **24b**. SpGr: $P2_1/c$. The thermal ellipsoids are drawn at 50% probability level. Interatomic distances (Å) and angles (°), the standard deviation of the last decimal place is given in parentheses: Ru–N1 1.743(7), Ru–N2 1.835 (7), Ru–Cl 2.380(2), Ru–P1 2.4572(18), Ru–P2 2.4585(18), O1–N1 1.115(8), O2–N2 1.125(8); O1–N1–Ru 178.2(8), O2–N2–Ru 149.0(7), N1–Ru–Cl 143.88(8), N1–Ru–P1 91.4(2), N1–Ru–P2 91.7(2), N1–Ru–N2 108.9(3), N2–Ru–Cl 107.2(2), N2–Ru–P1 95.6(2), N2–Ru–P2 94.9(2), Cl–Ru–P1 85.86(7), Cl–Ru–P2 84.57(7), P1–Ru–P2 167.53(6). Selected torsion angles: N1–Ru–N2–O2 1.0(1.2), Cl–Ru–N2–O2 −178.2(1.0). $CShM_{VOC\text{-}5}$: 2.170, τ_5: 0.26, $d_{Ru\text{-}SP}$: 0.418.

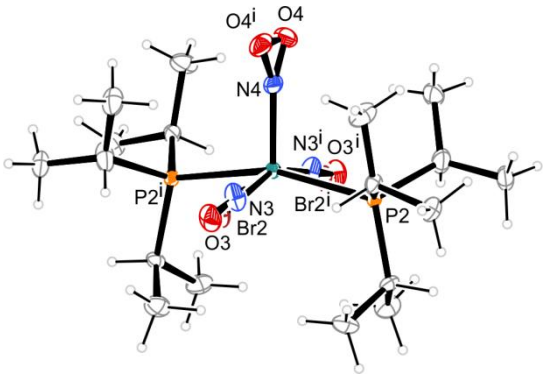

Fig. 2.27: ORTEP plot of the disordered square pyramidal conformer of the coordination cation in crystals of **25b**. SPGr: $P2_1/c$. The thermal ellipsoids are drawn at 50% probability level. Interatomic distances (Å) and angles (°), the standard deviation of the last decimal place is given in parentheses: Ru2–N3 1.717(8), Ru2–N4 1.861(4), Ru2–Br 2.4605(14), Ru2–P2 2.4703(7), O3–N3 1.217(8), O4–N4 1.060(5); O3–N3–Ru2 177.2(9), O4–N4–Ru2 150.9(3), N4–Ru2–Br 103.34(4), N4–Ru2–P2 99.13(2), N4–Ru2–N3 100.1(2), N3–Ru2–Br^i 156.50, N3–Ru2–P2 88.5(2), $Br2^i$–Ru–P2 89.17(3), P1–Ru–P2 161.75(4). Selected torsion angles: $N3^i$–Ru2–N4–O4 −2.0(6), Br2–Ru2–N4–O4 176.6(6), Symmetry code: ^{i} −x, y, −z + ½. $CShM_{TBPY\text{-}5}$: 1.999, τ_5: 0.09, d_{Ru-SP}: 0.401.

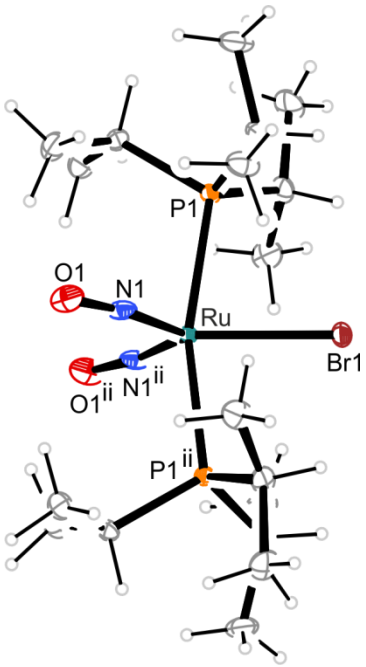

Fig. 2.28: ORTEP plot of the trigonal bipyramidal conformer of the coordination cation $[RuBr(NO)_2(P^iPr_3)_2]^+$ in crystals of **25b**.·SpGr: P21/C. The thermal ellipsoids are drawn at 50% probability level. Interatomic distances (Å) and angles (°), the standard deviation of the last decimal place is given in parentheses: Ru–N1 1.786(3), Ru–Br 2.5503(5), Ru–P1 2.4593(7), O1–N1 1.137(3), O1–N1–Ru 165.22(3), N1–Ru–Br 123.48(8), N1–Ru–P1 93.14(8), N1–Ru–$P1^{ii}$ 95.22(8), N1–Ru–$N1^{ii}$ 113.04(17), Br–Ru–P1 82.41(2), P1–Ru–$P1^{ii}$ 164.82(3). Selected torsion angles: $N2^{ii}$–Ru1–N1–O1 3.9(8), Br1–Ru1–N1–O1 176.1(8). Symmetry code: ^{ii} −x + 1, y, −z + ½. $CShM_{TBPY\text{-}5}$: 2.303, τ_5: 0.69.

All structures show a coplanarity of the Ru-NO-X moiety which enables the formation of a delocalised conjugated π system (see Fig. 2.29 for a schematic represenation of this interaction).

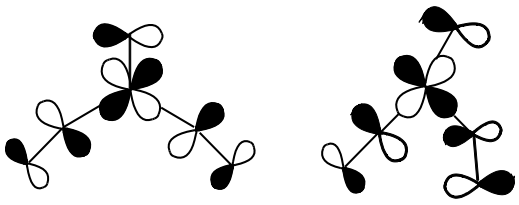

Fig. 2.29: Schematic representation of the delocalised π system in tbp (right) and sqp (left) structures.

All compounds, except of compound **20b** and **25b**, contain one molecule within the asymmetric unit. The crystallographically independent cations of **20b** shown in Fig. 2.21 seem—on the first view—to be connected through an inversion centre. On taking a closer look, it can be seen that the inversion of, for example, the slightly less bent N1O1 group would transform into the slightly more bent N4O4 group in such a way as that the potential inversion symmetry is lifted. The cations are stacked inversely arranged along the crystallographic *a* axis. The structure solution of compound **25b** suceeded in the monoclinic space group *C*2/*c*. The unit cell contains eight formula units, the asymmetric unit contains two symmetry independent coordination cations, which represent two different conformers, one of which adopts a C_{2v}-symmetrical tbp structure (**25b-2**, depicted in Fig. 2.28), the other an sqp structure (**25b-1**, depicted in Fig. 2.27). The maximum symmetry reachable for the latter structure would be C_s, due to disorder (the halide atom lies in a disordered fashion on the linear NO group and *vice versa*, the oxygen atom of the bent NO group is inclined in two directions with regard to the Ru–N axis) the higher symmetric point group C_{2v} is reached. The cations are stacked along the crystallographic *a* axis, on which the two different conformers alternate. Layers of anions alternate with layers of cations parallel to the crystallographic *b* axis. Both kinds of cations lie on special sites with the site symmetry 2.

25b is not the only compound for which two different conformers were found. **21b** was isolated in two different conformational polymorphs. The tbp conformer (**21b-2**) crystallised in the shape of rods, and takes only little part of the total amount of product (see Fig. 2.22). Structure solution succeeded in the monoclinic space group $P2_1/c$. The sqp conformer (**21b-1**) crystallised as the main product in the form of blocks or platelets, the structure solution of which succeeded in the monoclinic space group $P2_1/n$ (see Fig. 2.23). The unit cells contain four formula units, respectively. The cations of **21b-1** are stacked inversely arranged along the crystallographic *b* axis.

A mercury plot of **21b-2** revealed that the more linearly bound NO ligands of two different complex cations are in close contact to one another, O···O separated by only 2.973 Å (see Fig. 2.30). This interaction is not present in the main product **21b-1**.

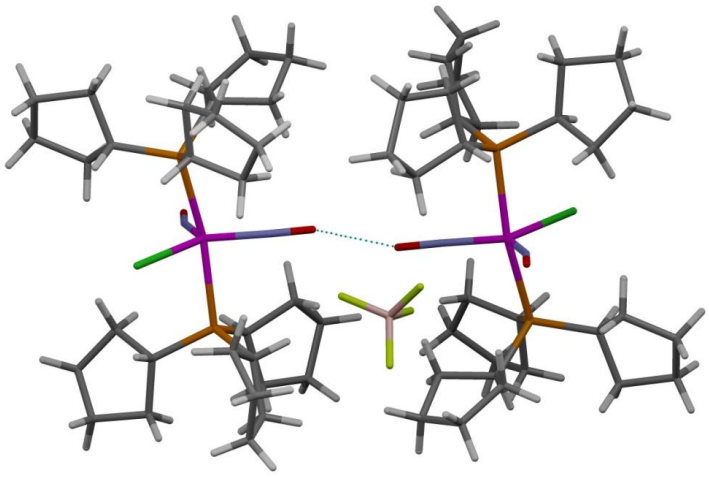

Fig. 2.30: MERCURY plot of the side product of **21b-1**. The dashed line depicts the short contact between two nitrosyl groups of adjacent complex cations.

Structure solution of **26b** succeeded in the monoclinic space group *C*2/*c*. The compound crystallised isostructural to **25b**. The refinement revealed that not only iodine is coordinated *trans* to the linear nitrosyl ligand but also nitrite or chloride. Thus, the applied $K_2[RuI_5(NO)]$ precursor had to be contaminated. Since the influence of the halide on structural and spectroscopic parameters can therefore not be determined the structure of compound **26b** will not be discussed further.

2.6.3 Comparative calculations, based on DFT

Comparative calculations were, first and foremost, done for the assignment of ν(NO) stretching frequencies to various conformers and isomers. A secondary aim was to determine whether the equal bonding situation of the nitrosyl ligands in the tbp conformers is the result of disorder phenomena. Therefore, calculations were expected to reproduce τ_5 values and frequencies as accurately as possible. Table 2.1 and Table 2.2 enlist structural parameters for compound **6b** derived from X-ray crystallographic experiments and DFT-calculations, based on various theoretical levels. The results show in general a low dependence of the agreement experiment-calculation on the basis set, but a high dependence on the functional. Hybrid methods, such as B3LYP and TPSSh, are weak in reproducing the frequencies, the $\Delta\nu(NO)_{sym\text{-}asym}$ value and the angle of the linear RuNO moiety. B3LYP gives good values for the Ru–N and N–O distances. The density functional bp gives reasonable values for the frequencies, the $\Delta\nu(NO)_{sym\text{-}asym}$ and the angle of the linear RuNO moiety. The N–O distance of the linear nitrosyl is predicted too high. In general, van der Waals corrections are good for the frequencies as well as for the $\Delta\nu(NO)_{sym\text{-}asym}$ value. The van der Waals corrections have a negative impact on the value of the P–Ru–P angle which is predicted much too low. This leads to an approximation of value of the P–Ru–P angle to the value of the Cl–Ru–N1 angle, leading to τ_5 values which are much too low. Especially when considering the prediction of the frequencies, the theoretical BP/tzvp level leads, on average, to the best results and is acceptable with regard to the cost-benefit ratio of these calculations. The BP/tzvp calculations were also done with pseudopotentials for ruthenium and iodine and lead to slightly better results regarding the frequencies but the τ_5 value, and therefore the predicted geometry, deviates more strongly. Thus, the application of pseudopotentials was left out. Calculations for **6b** with inclusion of the counterion (BF_4^-) lead to a tbp structure (τ_5 = 0.64) with a distance between cation and anion which is too short compared to the X-ray crystallographic results. If an additionally COSMO model was implied, the structure is sqp (τ_5 = 0.26) and the distance between anion and cation increases. This more isotropic surrounding fits better to the surrounding in the crystal, since one cation is surrounded by more than one anion. The counterion BF_4^- was, thus, excluded from the calculations.

Table 2.1: Results of quantum-chemical calculations with ORCA 3.0[118] for compound **6b**, using various theoretical levels.

$[RuCl(NO)_2(PPh_3)_2]^+$	**6b**	BP[119, 120]/tzvp[121]		BP/def2-tzvp[122]		B3LYP[123–127]/def2-tzvp		TPSSh[128]/def2tzvp		TPSSh/tzvp	
		vdw	without vdw	vdw	without vdw	vdw	without vdw	vdw	without vdw	vdw	without vdw
Ru-N1-O1 / °	178.9	176.2	176.9	176.9	177.4	175.6	175.8	175.3	175.2	175.3	175.2
Ru-N1 / Å	1.746	1.802	1.803	1.786	1.788	1.776	1.777	1.792	1.795	1.792	1.795
libration corrected [a]	1.752										
N1-O1 / Å	1.155	1.161	1.162	1.160	1.162	1.144	1.145	1.149	1.151	1.149	1.151
Ru-N2-O2 / °	134.8	135.3	137.7	136.8	138.9	136.1	136.5	138.0	137.8	137.9	137.8
Ru-N2 / Å	1.872	1.891	1.889	1.871	1.868	1.872	1.878	1.878	1.887	1.879	1.887
libration corrected [a]	1.875										
N2-O2 / Å	1.162	1.173	1.171	1.172	1.170	1.154	1.153	1.159	1.159	1.159	1.160
P1-Ru-P2 / °	173.0	154.1	164.8	153.9	164.6	161.7	168.9	166.6	168.3	166.0	168.4
Ru-P / Å	2.450	2.,440	2.518	2.430	2.510	2.462	2.541	2.415	2.510	2.414	2.506
Ru-Cl / Å	2.352			2.390	2.390	2.403	2.401	2.373	2.394	2.373	2.502
N1-Ru-Cl / °	151.2	154.6	149.4	153.2	148.4	151.8	150.3	147.2	147.2	147.2	147.1
τ_5	0.36	−0.01	0.26	0.01	0.27	0.17	0.31	0.32	0.35	0.31	0.36
$\nu(NO)_{asym}$ / cm^{-1}	1685	1713	1724	1714	1724	1795	1798	1789	1785	1788	1784
$\nu(NO)_{sym}$ / cm^{-1}	1842	1841	1830	1836	1826	1903	1900	1901	1890	1901	1890

[a] Libration corrected values, Reference [129].

Table 2.2 shows the results of such calculations, applying the ecp (electron-core potential) algorithm solely for the geometry optimisation or for both, geometry optimisation and frequency analysis (the latter is only possible with the ORCA 3.0 version).

Table 2.2: Results of quantum-chemical calculations, based on the BP/tzvp level.

$[RuCl(NO)_2(PPh_3)_2]^+$					
	6b	BP/tzvp (SDD)[130, 131]a		BP/tzvp (SDD)b	
		vdw	without vdw	vdw	without vdw
Ru-N1-O1 / °	178.9	176.9	177.4	176.9	177.4
Ru-N1 / Å	1.746	1.780	1.781	1.780	1.781
libration corrected [a]	1.752				
N1-O1 / Å	1.155	1.162	1.163	1.162	1.163
Ru-N2-O2 / °	134.8	135.2	137.5	135.2	137.5
Ru-N2 / Å	1.872	1.873	1.871	1.873	1.871
libration corrected [a]	1.875				
N2-O2 / Å	1.162	1.174	1.173	1.174	1.173
P1-Ru-P2 / °	173.0	154.9	163.9	154.9	163.9
Ru-P / Å	2.450	2.435	2.501	2.435	
Ru-Cl / Å	2.352	2.398	2.404	2.398	
N1-Ru-Cl / °	151.2	155.6	151.0	155.6	151.0
τ_5 [b]	0.36	−0.01	0.22	−0.01	0.22
$\nu(NO)_{asym}$ / cm^{-1}	1685	1708	1718	1707	1716
$\nu(NO)_{sym}$ / cm^{-1}	1842	1846	1837	1845	1834

[a] SDD pseudo potential was used for the geometry optimization only. [b] SDD pseudo potential was used for the geometry optimisation and the frequency analysis.

2.7 Verification of the crystallographically determined nitrosyl bonding modes

As already mentioned in the INTRODUCTION, chapter 1.4.2 one has to keep in mind that caution is required when determining and discussing the M–N–O bond angle in X-ray structures with a bent M−NO moiety due to a relatively high degree of thermal motion and possible disorder of the oxygen atom. Thus, several factors should apply if the, so far unknwon, tbp coordination geometry for the compounds **9b**, **10b**, **20b**, **21b-2**, **22b**, **23b** and **25b-2** and the concomitant approximation of the bonding situation of the NO groups is derived neither from static disorder or dynamic processes for the oxygen atom of the NO group nor from intermolecular interactions or crystal-packing effects**:**

(I) It should be expected that in the compounds possessing a sqp or a *VOC*-5 structure and two very distinct nitrosyl ligands, the *ν*(NO)-stretching frequencies should be very different for the symmetric and the asymmetric coupled vibration. Accordingly, the *ν*(NO)-stretching frequencies for the NO ligands in the more symmetrical *TBPY*-5 complexes should lie closer together in respect to their wave numbers.

(II) IR spectroscopical data obtained from the solid and dissolved state should differ markedly if static disorder for the NO moieties is existent in the crystal.

(III) Quantum-chemical calculations based on DFT should reflect the right structural and

spectroscopical parameters, *i.e.* the right geometry for the coordination polyhedron, the right RuNO bond lengths (± 0.03 Å) and angles (± 3°) and the right wavenumbers (± 40 cm^{-1}) for the symmetrical and asymmetrical vibration.

(IV) In the case of a dynamic process, the anisotropic displacement parameters should have a value of 0 $Å^2$ when extrapolated against zero Kelvin. If the value is significantly higher, static disorder is assumed.

The compliance of these factors will be investigated in the following. The search of an appropriate level of theory for comparative quantum chemical calculation was already presented in chapter 2.6.3. Thus, the next chapter will deal with the points I-III. Chapter 2.7.2 refers to point IV.

2.7.1 By comparative quantum-chemical calculations and IR measurements in solution

Table 2.3 and Table 2.4 refer to point (I–III) concerning the spectroscopical data for the NO ligands. Stretching frequencies from measurement in the solid state and in solution, as well as the ones derived from calculations are compared. The last column contains the difference in wavenumbers of the symmetrical and the asymmetrical vibration derived from measurements and calculation. Some structures were calculated with geometrical constraints as, in some cases, the crystal structure and the calculated minimum structure are not equal.

I) As was expected, the Δν(NO) values show that in the case of a sqp structure with two clearly distinct NO ligands, the difference is ≥ 71 cm^{-1} (71–157 cm^{-1}, solid state), whereas in the case of a tbp structure with nearly equal NO ligands, the difference is ≤ 41 cm^{-1} (28–41 cm^{-1}, solid state).

Table 2.3 Spectroscopical data. The symmetrical and the asymmetrical vibrations were measured in the solid and liquid state and compared to those derived from calculations based on DFT.

Number	**Compound** (PR_3/X)	**$\nu(NO)_{sym,asym}$ / cm^{-1}** in the solid	**$\nu(NO)_{sym,asym}$ / cm^{-1}** DFT	**$\nu(NO)_{sym,asym}$ / cm^{-1}** in DCM	**Δν(NO) / cm^{-1}** exp / calcd.
6b	PPh_3/Cl	1842 / 1685	1830 / 1724	1823 / 1776 / 1720	157 / 106
9b	PPh_2Bn/Cl	1799 / 1771	1811 / 1788	1818 / 1776	28 / 23
10b	PPh_2Bn/Br	1817 / 1776	1809 / 1787	1815 / 1778	41 / 22
18b	PCy_3/Cl	1789 / 1704	1806 / 1709	1812 / 1706	85 / 97
19b	PCy_3/Br	1785 / 1714	1799 / 1709	1800 / 1760 / 1716	71 / 90
20b-1	PCy_3/I	1788 / 1751	1791 / 1768	1797 / 1765	37 / 23
20b-2	PCy_3/I	1788 / 1751	1791 / 1768	1797 / 1765	37 / 23
21b-1	$PCyp_3$/Cl	1805 / 1681	1809 / 1710	1834 / 1797 / 1756 / 1710	124 / 99
21b-2	$PCyp_3$/Cl[a]	—	1788 / 1763[b]	—	—/ 25
22b	$PCyp_3$/Br	1810 / 1770	1809 / 1783	1795 / 1759	40 / 26
23b	$PCyp_3$/I	1809 / 1772	1793 / 1769	1794 / 1759	37 / 24
24b	$PiPr_3$/Cl	1808 / 1682	1815 / 1717	1809 / 1759 / 1714	126 / 98
25b-1	$PiPr_3$/Br	1806 / 1694[c]	1809 / 1710	1802 / 1765	112 / 99
25b-2	$PiPr_3$/Br	1794 / 1753[c]	1799 / 1776	1802 / 1765	41 / 23

DCM = dichloromethane. [a] Since compound **21b-2** was formed as a minor species, there is no analytical data except for X-ray diffraction analysis. [b] Being a non-minimum structure, the RuNO angles of compound **21b-2** were fixed during geometry optimisation and frequency analysis. [c] Frequencies measured on Nicolette 5700 FTIR device, which has a better resolution (2 cm^{-1}). Compound **26b** is not included due to the fact that X is not only iodine. Compounds adopting intermediate structures are also not included. No vibrational scaling factor was applied to the frequencies from calculations.

Table 2.4 Geometrical data. All data were taken from crystal structures. Only the τ_5-value was taken from both experiment and calculations.

Number	Compound (PR_3/X)	ΔRu–N–O / °	ΔRu–N / Å	τ_5-value exp / calc	CShM-values *VOC*-5	*TBPY*-5	*SPY*-5
1	THF/Cl[a]	54.4	0.188	—	—	—	—
6b	PPh_3/Cl	44.1	0.126	0.36 / 0.30	**2.588**	3.899	3.613
7b	PPh_3/Br	32.2	0.101	0.51 / 0.41	3.730	3.096	4.312
9b	PPh_2Bn/Cl	3.2	0.004	0.65 / 0.64	5.464	**2.124**	4.616
10b	PPh_2Bn/Br	5.4	0.004	0.64 / 0.68	5.419	**2.153**	4.618
18b	PCy_3/Cl	43.4	0.131	0.15 / 0.21	**1.804**	2.292	2.292
19b	PCy_3/Br	38.5	0.093	0.19 / 0.16	**1.851**	5.325	2.383
20b-1	PCy_3/I	4.8	0.021	0.79 / 0.76	6.205	**2.110**	5.467
20b-2	PCy_3/I	6.6	0.021	0.78 / 0.76	6.731	**2.193**	6.360
21b-1	$PCyp_3$/Cl	39.8	0.092	0.09 / 0.10	**1.555**	6.236	2.167
21b-2	$PCyp_3$/Cl	3.7	0.008	0.68 / 0.71	5.495	**2.075**	4.518
22b	$PCyp_3$/Br	2.1	0.001	0.66 / 0.63	5.618	**2.023**	4.955
23b	$PCyp_3$/I	3.4	0.008	0.65 / 0.68	4.941	**2.464**	4.518
24b	$PiPr_3$/Cl	29.2	0.092	0.26 / 0.27	**2.170**	4.590	2.454
25b-1	$PiPr_3$/Br	26.3	0.144	0.09 / 0.11	**1.999**	6.638	2.400
25b-2	$PiPr_3$/Br	0.0	0.000	0.69 / 0.68	6.518	**2.303**	4.975

[a] Included for better comparison; since the ruthenium atom is six-coordinated, no values are given for τ_5 and CShM. Bold: smallest CShM-value of the respective structure. Compound **26b** is not included due to the fact that X is not only iodine. Compounds adopting intermediate structures are also not included.

II) If the equal bonding situation for the two NO ligands is caused by a disorder according to Fig. 2.31 or Fig. 2.32, the wavenumber for the asymmetrical stretching frequency should be shifted to lower values when the disorder is broken by dissolving the compound. When frequencies for the symmetrical and asymmetrical stretching from the solid and liquid state are compared, it is obvious that no such change is observable. In contrast, the asymmetrical frequencies are slightly shifted to higher values. The mean deviation $\nu(NO)_{sym,liquid} - \nu(NO)_{sym,solid}$ is found to be 4.9 cm^{-1} while the mean deviation for $\nu(NO)_{asym,liquid} - \nu(NO)_{asym,solid}$ is found to be 10.4 cm^{-1}.

III) The measured frequencies in the solid and liquid state are in relatively good agreement with the calculated ones. If only the calculated frequencies and the frequencies derived from the solid state are compared, it is obvious that the asymmetrical vibration is always predicted a little bit too high with the mean deviation at +14.0 cm^{-1} ($\nu(NO)_{asym,calcd.} - \nu(NO)_{asym,solid}$), whereas the symmetrical vibration mode is predicted more reliably, the mean deviation being +2.3 cm^{-1} ($\nu(NO)_{sym,calcd.} - \nu(NO)_{sym,solid}$). In better agreement with the calculated frequencies are the frequencies from the liquid state, as expected, since intermolecular interactions are reduced for the liquid state compared to the solid state (calculations were performed for the gas phase): again, the asymmetrical vibration is predicted a little bit too high, the mean deviation is +6.6 cm^{-1} ($\nu(NO)_{asym,calcd.} - \nu(NO)_{asym,liquid}$), whereas the symmetrical vibration mode is predicted more reliably, the mean deviation being −3.2 cm^{-1} ($\nu(NO)_{sym,calcd.} - \nu(NO)_{sym,liquid}$).

Three frequencies in the ν(NO) range are found for solutions of compounds **6b, 19b** and **24b**. Presumably, the frequencies at intermediate values can be assigned to the formation of a second structure, namely a tbp one. If two species are detectable, one would expect four values for the NO stretching vibration. Thus, it is assumed that the resolution of the IR device is not sufficient to separate the symmetrical vibration mode for the two geometries (as is proved in the case of **25b**).

The CShM as well as the τ_5 value were calculated according to References [118] and [119] from the respective crystal structures and compared to the corresponding values derived from the geometry optimisation of the crystal structures by use of DFT. The τ_5-value from calculation and experiment are in good agreement with each other, the maximum deviation being 0.10 for compound **3**.
The two conformers of **25b** were both found as minimum structures during geometry optimisation. The energetic difference between the tbp structure (**25b-2**) and the sqp structure (**25b-1**) is only $\Delta E_{(tbp\text{-}sqp)} = 2.74$ kJ mol^{-1}.
Animations of the vibrations calculated from frequency analysis show a high degree of vibrational coupling for the tbp structures, whereas the magnitude of the vibrational coupling in the sqp structures is much lower. In the case of strong vibrational coupling, the symmetrical and the asymmetrical mode receive equal contributions from both nitrosyl ligands. In the case of weak vibrational coupling, the symmetrical mode is dominated by the vibrations of the linearly coordinated nitrosyl, whereas the asymmetrical mode is dominated by the vibrations of the bent nitrosyl ligand. These observations are consistent with a simplified physical model of a coupled pendulum with two equal or two different spring stiffnesses. The magnitude of coupling will be higher in the case of equal spring stiffness and lower in the case of unequal spring stiffness.

2.7.2 By investigations on the temperature dependence of ADPs

IV) In addition to quantum-chemical calculations in order to verify whether the crystal structure displays a global minimum on the PES, X-ray diffractional experiments were performed to check on disorder and dynamic processes. For this purpose, two crystal structures showing the approximation of the bonding situation of the two NO ligands were measured at five different temperatures to allow a statement on disorder and dynamic effects.
There are two possible scenarios for the formation of a potentially C_{2v}-symmetrical tbp structure with equal NO ligands from a potentially C_S-symmetrical sqp structure with unequal NO ligands, depicted in Fig. 2.31 and Fig. 2.32. In a disordered crystal an atom can have one equilibrium position in one unit cell and another position in the other unit cell. If the crystal is subjected to dynamic processes, the equilibrium position of an atom can be changed temporarily. If the distance between the two different equilibrium positions, resulting from disorder or motion, is small compared to the resolving power of the diffractometer, only a mean atomic position can be determined. Although disorder and motion lead to the same results—both are reflected in the magnitude of the anisotropic displacement parameters (ADPs)—they can be distinguished when the structure is measured at various temperatures.
In this context the behaviour of the ADPs upon successive cooling was investigated, and the mean-square atomic displacement was plotted against the temperature. In the case of a dynamic process, the anisotropic displacement parameters ideally should have a value of 0 Å^2 when extrapolated to zero Kelvin, since the expansion of the ellipsoids will decrease when thermal motion is minimised. According to Reference [132], with a value ≤ 0.005 Å^2 static disorder can be excluded. If the value is significantly higher than 0.005 Å^2, static disorder can be assumed. The value of the y intercept

corresponds to the length of the distance vector between the two alternative equilibrium positions, the mean atomic displacement (centre of the ellipsoid) corresponds to half the length of the distance vector. Fig. 2.33, Fig. 2.34 and Table 2.5 show the temperature dependence of the ADPs and the values for U_{11} for extrapolation against zero Kelvin for compound **22b** and **9b**, respectively.

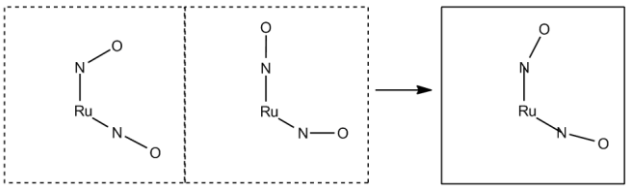

Fig. 2.31: Simplified model representation of static disorder as a cause for the equal bonding situation of the two NO ligands in the tbp structures. The X-ray beam "notices" a spatial superposition of two different equilibrium positions of the oxygen atom in different unit cells.

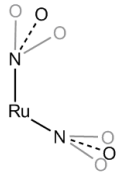

Fig. 2.32: Simplified model representation of a dynamic process as a cause for the equal bonding situation of the two NO ligands in the tbp structures. The X-ray beam "notices" a temporal superposition of different equilibrium orientations of the NO moieties.

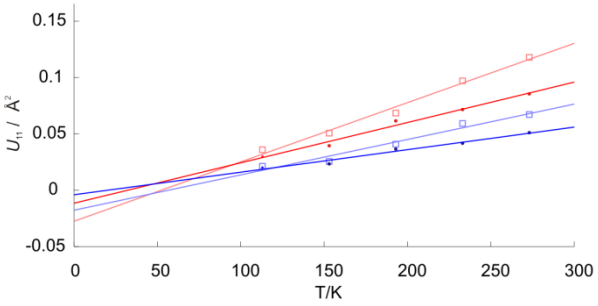

Fig. 2.33: MATLAB plot[133] of the temperature dependence of the ADPs of oxygen and nitrogen within $[RuBr(NO)_2(PCyp_3)_2]BF_4$ (**22b**). Boxes: red = O1, blue = N1, points: red = O2, blue = N2.

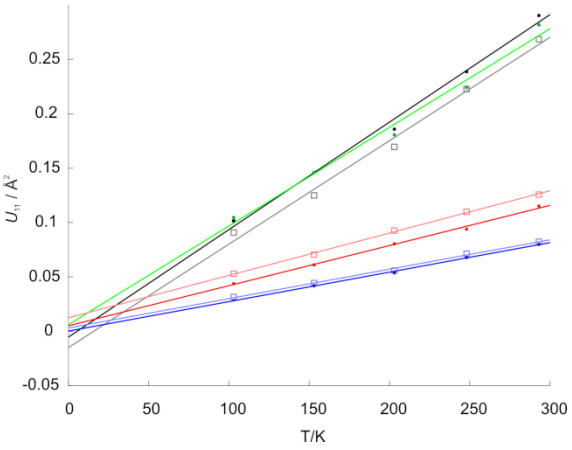

Fig. 2.34: MATLAB plot[133] of the temperature dependence of the ADPs of oxygen and nitrogen within $[RuCl(NO)_2(PPh_2Bn)_2]BF_4$ (**9b**). Boxes: red = O1, blue = N1, grey = C28, points: red = O2, blue = N2, black = C29, green = F4.

Table 2.5 Values of U_{11} (T = 0K).

Compound	**9b**	**22b**
U_{11}(O1) /Å^2	−0.02757	0.01235
U_{11}(O2)	−0.01152	0.00502
U_{11}(N1)	−0.01776	0.00296
U_{11}(N2)	−0.00407	0.00013
U_{11}(C28)	—	−0.01509
U_{11}(C29)	—	−0.00550
U_{11}(F4)	—	0.00596

Crystals of compound **22b** were measured at 273, 233, 193, 153 and 113 K.

All four ADPs (N1, N2, O1 and O2) reach values lower than 0 Å^2 when extrapolated against zero Kelvin, so that static disorder can be excluded (see Table 2.5). Nor can a dynamic process beyond normal thermic displacement be considered as a causal factor for the MNO geometry, since there is

no change towards an sqp structure upon cooling. Crystals of compound **9b** were measured at 293, 248, 203, 153 and 103 K. For the oxygen atom O2 of that NO ligand, which is bonded with an angle of 169°, static disorder can be excluded (see Table 2.5). For the oxygen atom O1 a slight static disorder seems to contribute to the slightly-too-high value of the ADP, which can be interpreted as a precession of the O1 atom around the N–O bond of that NO ligand, bound with an angle of 163°. For better comparison, the ADPs of the carbon atoms C28 and C29 (cyclopentyl ring) and F4 (counterion BF_4^-) were also investigated. The decrease in the magnitude of their ADPs is clearly a consequence of the decrease in displacement upon temperature reduction. (For the theoretical background to the applied method see EXPERIMENTAL PART, chapter 5.9)

2.8 Correlations between structure, co-ligands and spectroscopic properties

After having proven that the crystallographically determined structures are not the result of disorder or a dynamic process, it is valid to assume that the adopted structure is dependent from the only parameter in which the dinitrosyls vary: the co-ligands X and PR_3. A view on the shape map given in Fig. 2.11 already leads to the guess of a dependence from this parameter.

All structures which are clearly sqp (τ_5 = 0.09−0.36) can be described as vacant octahedrons (*VOC*-5) when Alvarez's shape rules are applied. This structure is found for all of the chlorido species (except for **9b**) and for two of the bromido species, namely compounds **19b** and **25b-1**. The compounds adopting tbp structure (τ_5 = 0.64−0.79) are all bromido or iodido species, except for compounds **9b** and **21b-2**. Thus, it is concluded that the adopted structure is dominated primarily by the halogenido ligand and, secondarily, by Tolman's electronic factor of the phosphane ligand (see Table 2.6). Upon viewing Table 2.6, compounds with an sqp structure are primarily found on the top left, compounds which adopt both structures in the middle, and compounds adopting a tbp structure on the bottom right. The extent to which the ligand X and the substituent R donate electron density to the metal centre has opposing effects with regard to the adopted structure. Thus it can be concluded that they have different sterical and/or electronical effects on the NO groups.

Since the tbp structure is associated with the equal NO ligands, whereas the sqp structures are associated with the unequal NO ligands it is expected that the structure is correlated to the *ν*(NO) frequencies. (Fig. 2.35, Fig. 2.36 and Fig. 2.37 show the adopted structure in dependence of the spectroscopic and structural parameters of the Ru–N–O moiety).

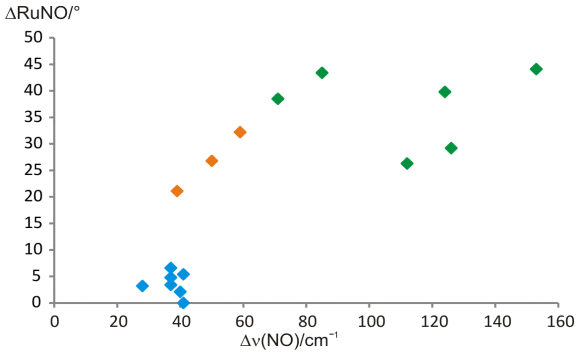

Fig. 2.35: Adopted structures (green: sqp, blue: tbp, orange: sqp/tbp) in dependence of the RuNO angle and the *ν*(NO) stretching frequency.

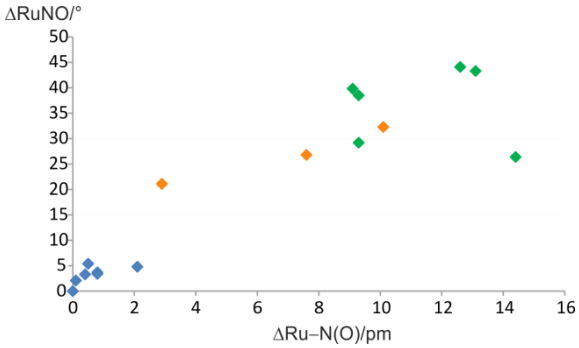

Fig. 2.37: Adopted structures (green: sqp, blue: tbp, orange: sqp/tbp) in dependence of the Ru–N(O) distance and the RuNO angle.

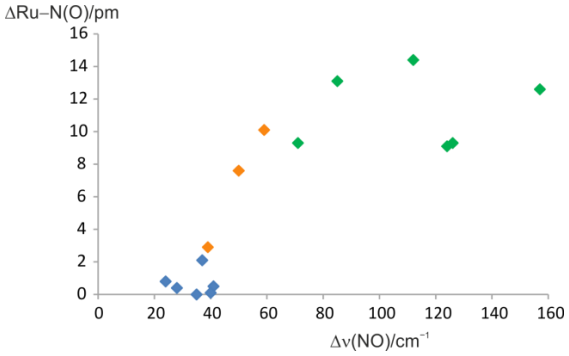

Fig. 2.36: Adopted structures (green: sqp, blue: tbp, orange: sqp/tbp) in dependence of the Ru–N(O) distance and the *ν*(NO) stretching frequency.

Table 2.6 Structures of the $[RuX(NO)(PR_3)_2]BF_4$ compounds in solid and liquid state in dependence of X and R.

	PPh_3	P^iPr_3	PCy_3	$PCyp_3$
Cl	sqp	sqp + tbp	sqp	sqp + tbp
Br	sqp/tbp	sqp + tpb only tbp	sqp + tbp	tbp
I	-	tbp	tbp	tbp

The electronic parameter of the phosphanes (*ν*(CO) according to Tolman) decreases from left to right. The π donor ability of the halides increases when going from top to bottom. Green: species which are detected in solution; sqp/tbp: structurally in between. Box: compounds which can adopt both structures.

2.9 [{Ru(NO)$_2$(P^{i}Pr$_3$)}$_2$(μ-I)]BF$_4$: a DNIC analogous bis-dinitrosyl

The reduction of product mixture **26a** with a zinc copper alloy in toluene at 85 °C and subsequent addition of ethanol and nitrosyl tetrafluoroborate at elevated temperatures (50–60 °C) resulted in the formation of reddish-brown crystals overnight.

Structure solution succeeded in the triclinic space group *P*1. The unit cell contains one formula unit. The complex cation and the counterion are shown in Fig. 2.38.

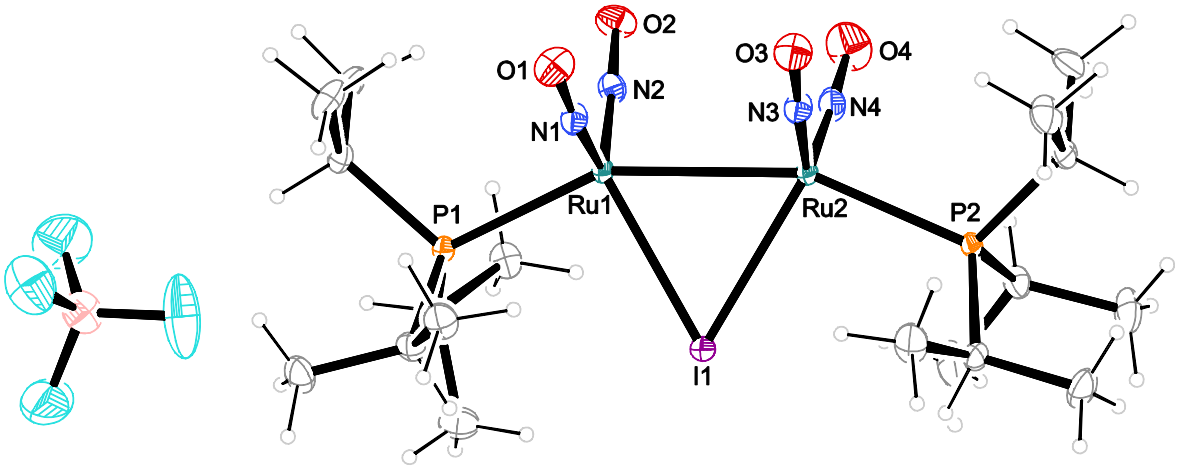

Fig. 2.38: ORTEP plot of the content of the unit cell in crystals of **26c**.·The thermal ellipsoids are drawn at 50% probability level at 123 K. Interatomic distances (Å) and angles (°), the standard deviation of the last decimal place is given in parentheses: Ru1–I 2.7247(11), Ru1–Ru2 2.7364(14), Ru1–P1 2.4102(13), Ru1–N1 1.7873(36), Ru1–N2 1.7702(35), O1–N1 1.1578(47), O2–N2 1.1714(45), Ru2–I 2.7364(14), Ru1–Ru2 2.7364(14), Ru2–P2 2.4133(13), Ru2–N3 1.7752(34), Ru2–N4 1.7805(36), O3–N3 1.1564(45), O4–N4 1.1592(50); O1–N1–Ru 165.80(33), O2–N2–Ru 169.50(32), O3–N3–Ru 169.53(33), O4–N4–Ru 169.01(37), I–Ru1–Ru2 60.43(3), Ru1–N1–N2 118.20(16), Ru1–P1–N2 100.58(12), Ru1–P1–N1 98.76(12), Ru1–I–N2 122.31(11), Ru1–I–N1 114.21(12), Ru1–I–P1 93.58(4), Ru1–Ru2–N2 91.67(11), Ru1–Ru2–N1 96.10(12), Ru1–Ru2–P1 153.29(3), Ru1–Ru2–I 59.99(3), Ru2–N3–N4 119.49(176), Ru2–P2–N3 100.32(12), Ru2–P2–N4 96.06(12), Ru2–I–N3 117.33(12), Ru2–I–N4 117.57(13), Ru2–I–P2 97.38(3), Ru2–Ru2–N3 92.00(12), Ru2–Ru2–N4 94.66(11), Ru2–Ru1–P2 156.95(3), Ru2–Ru1–I 59.57(2). Selected torsion angles: Ru1–I1–Ru2–P2 −179.27(3), I1–Ru1–Ru2–P2 1.86(7), N1–Ru1–N2–O2 4.32(1.78), N3–Ru2–N4–O 40.95(1.89).

The cation of the homodinuclear complex is a vertex-shared bitetrahedron (CShM$_{T\text{-}4}$ value of 2.887 and 2.902), wherein a pair of Ru(NO)$_2$ units are bridged by an iodido ligand. A phosphane ligand is additionally bound in a terminal way to each of the ruthenium atoms. Although the coordination cation might look symmetrical at first glance, the iodido bridge is not exactly symmetrical and the dinitrosyl moieties are not completely ecliptic. Otherwise, the complex cation would exhibit C_{2v} symmetry. The Ru–Ru distance of 2.73 Å indicates a metal–metal bond.[134] The Ru–N bond lengths vary by only 0.017 ($\Delta_{RuN1-RuN2}$) and 0.005 Å ($\Delta_{RuN4-RuN3}$), the RuNO angles by only 3.7° ($\Delta_{RuN1O1-RuN2O2}$) and 0.5° ($\Delta_{RuN4-RuN3}$). Thus, a determination in an NO$^+$ and an NO$^-$ ligand is not possible. The RuNO angles are 168.5° on average. The Ru–N bond lengths as well as the RuNO angles indicate the coordination of four NO$^+$ ligands. This is consistent with a Ru–Ru single bond since the valence electrons will then add up to 36 (2 · 8 + 4 · 3 (NO$^+$) + 1 · 3 + 2 · 2 – 1 + 2 = 36). The Enemark–Feltham notation is {Ru(NO)$_2$}^{9}–{Ru(NO)$_2$}^{9}. Thus, the compound is the ruthenium analogue of a dimeric DNIC. The structure, the oxidation state of the central

atom and the bonding mode of the nitrosyl units resemble those found in the ethyl ester of Roussin's red salt (depicted in Fig. 2.39).[135]

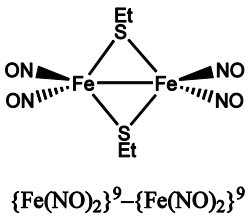

Fig. 2.39: The ethyl ester of Roussin's red salt, a dimeric DNIC. Data taken from Ref. [135].

The anion is an edge-shared bitetrahedron, the $Fe(NO)_2$ moieties are bridged by a pair of thiolato ligands. The Fe–NO bonds are only slightly deviating from linearity (168° and 167°) indicating that the nitrosyl ligands are acting as three electron donors. The diamagnetic compound (antiferromagnetic coupling) obeys the 18-electron rule when a metal-metal bond is assumed (Fe–Fe 2.72 Å).

The IR spectrum of **26c** showed three bands in the region assignable to coordinated NO at 1781, 1738, and 1704 cm^{-1}. The frequency at 1781 cm^{-1} is assigned to the fully symmetrical vibration mode (both the dinitrosyl moieties vibrate symmetrically and in phase to each other, see Fig. 2.40). The frequency at 1738 cm^{-1} is assigned to the fully asymmetrical vibration mode (both the dinitrosyl moieties vibrate asymmetrically and in phase to each other, see Fig. 2.40). The third frequency at 1704 cm^{-1} is assigned to the symmetrically vibration mode (both dinitrosyl moieties vibrate symmetrically but antiphasic to each other, see Fig. 2.40).

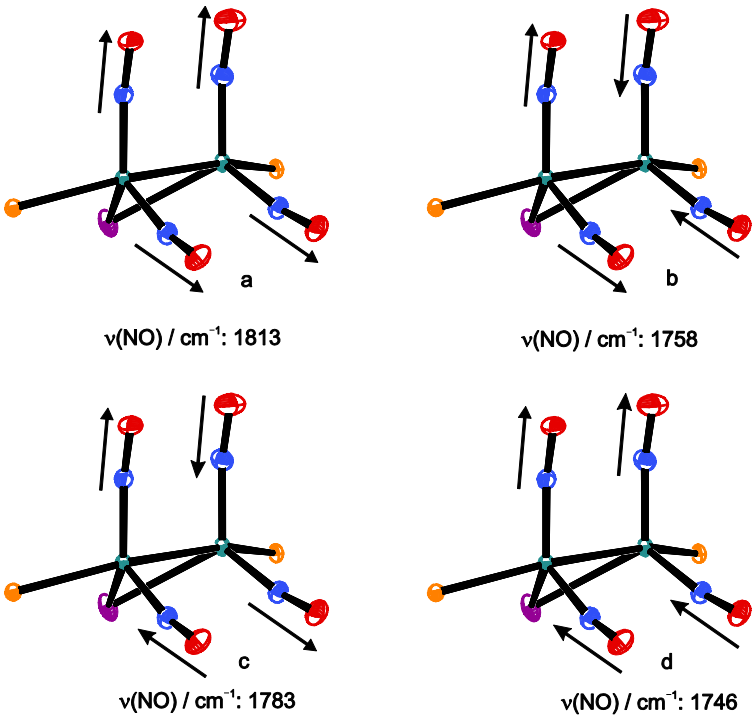

Fig. 2.40: The four symmetrically and asymmetrically coupled stretching vibrations of a bis-dinitrosyl. (a) Fully symmetrically coupled *ν*(NO) vibration. (b) Symmetrically coupled ν(NO) vibration. (c) Fully asymmetrically coupled *ν*(NO) vibration. (d) Asymmetrically coupled *ν*(NO) vibration, very low intensity. *ν*(NO) values were taken from quantum-chemical calculations, based on DFT.

The mass spectrum showed one peak for the complex cation $[M]^+$ at *m/z* = 770.4 and two peaks for the fragment cations $[M - NO]^+$ and $[M - 2\ NO]^+$ at *m/z* = 740.4 and 709.4, respectively. Two signals are detectable in the $^{31}P\{^1H\}$ NMR spectrum at 80.2 and 42.1 ppm with approximately same intensities. Purification of the raw product by recrystallisation from dichloromethane yielded an NMR spectrum in which the signal at 80.2 ppm has the eightfold intensity of that at 40.1 ppm. The results from elemental analysis of the purified product were consistent with the empirical formula $C_{18}H_{42}BF_4IN_4O_4P_2Ru_2$. Thus, the signal at 80.2 ppm was assigned to the complex.

If the Cambridge Structural Database is consulted (CSDS version 5.34, november 2012), the compound is the first structurally characterised ruthenium dinitrosyl with a metal–metal bond.

2.10 PLI measurements

As mentioned in the introduction, ruthenium nitrosyls of the $\{RuNO\}^6$ are known to be able to show PLI. This phenomenon had, so far, not been investigated for $\{Ru(NO)_2\}^8$ compounds, which were promising candidates for interesting PLI behaviour due to the two different kinds of nitrosyl ligands that some of them own. Since the detection and characterisation of PLI requires special technical equipment, the investigations were performed by a co-operation partner at the *Institut Jean Barriol* in Nancy, France. Photocrystallographic experiments were performed at the *Paul Scherrer Institut* in Villigen, Switzerland. The results of the photoinduced linkage isomerism for **6b**, **7b**, **9b**, **14b**, **18b**, **25b** and the results of photocrystallography of **6b** are discussed in the following.

2.10.1 $[RuCl(NO)_2(PPh_3)_2]BF_4$

To test under which conditions a maximum population of the metastable isomer is achievable, compound **6b** was irradiated with laser light of the wavelengths 405, 442, 660, 780, 980 and 1064 nm at 80 K. Maximal photo-excitation was gained at 405 nm. Fig. 2.41 shows an infrared spectrum in the *v*(NO) range of the ground state and the photo-excited state at 80 K. Upon illumination in the blue spectral range the two NO bands of the ground state (1866 and 1687 cm^{-1}) are shifted, the asymmetrical stretching mode is shifted into the lower-energy range by −34 cm^{-1}, the symmetrical stretching mode is shifted into the higher-energy range by +6 cm^{-1}. The novel bands appear at 1872 and 1653 cm^{-1}. The diminishment of the integral of the ground-state bands indicates a population of the photo-excited state of about 60%. As Fig. 2.42 and Fig. 2.43 show the photoswitching is reversible since irradiation with a wavelength, corresponding to the red spectral range, as well as gradual heating result in an increase of the integral of the ground-state bands until the original value is reached.

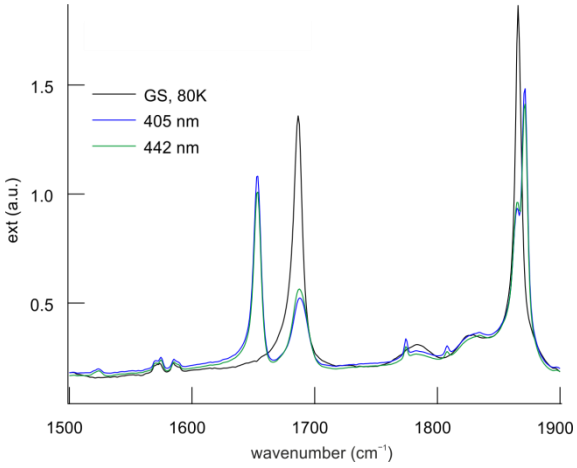

Fig. 2.41: IR spectrum of **6b** (black line corresponds to the ground state) in the *v*(NO) range after population by irradiation with light of the wavelengths 405 nm (blue line) and 442 nm (green line).

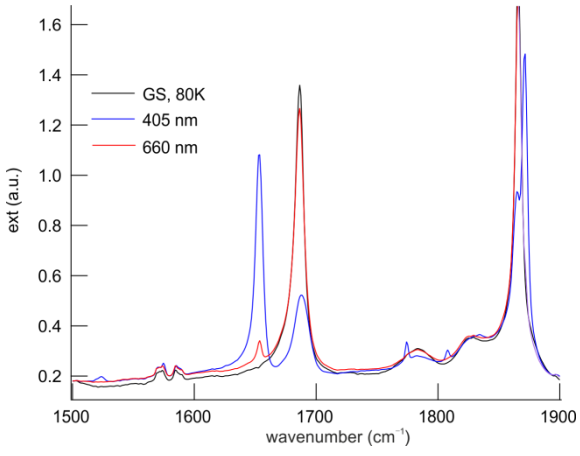

Fig. 2.42: IR spectrum of **6b** (black line corresponds to the ground state) in the *v*(NO) range after population (405 nm, blue line) and depopulation (660 nm, red line) by irradiation with light of the appropriate wavelengths.

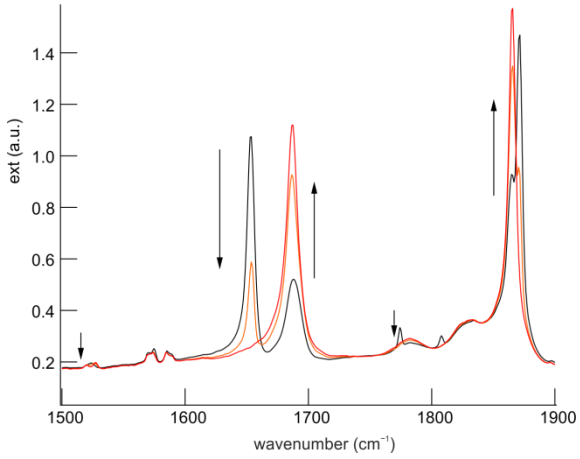

Fig. 2.43: IR spectrum of **6b** in the *ν*(NO) range after population by irradiation with light of the wavelength 405 nm (black line) and subsequent thermal depopulation by gradual heating (orange and red lines) until about 100–110 K.

Additionally, two less intense photoinduced bands at 1774 and 1808 cm^{-1} are detectable. Compared to the ground-state bands the shifts are +87 and −58 cm^{-1} (or +21 and −92 cm^{-1}). To elucidate the origin of these bands a series of experiments was performed using different irradiation wavelengths. In the near infrared spectral range the two smaller bands vanish and the integrals of the ground-state bands increase correspondingly. The bands at 1872 and 1653 cm^{-1} are not affected at these wavelengths. This clearly indicates that there are two distinct photo-induced states. The population of the second photo-excited state is only of the order of 4–5%. Regarding the photoswitching signature (shifts of the wavelengths of about 100 cm^{-1} and the spectral range used for the generation and erasure of this metastable state), which is comparable to those found for $\{RuNO\}^6$ isonitrosyls,[56, 58] this state may be assigned to an isonitrosyl species of the linear RuNO moiety.

2.10.2 $[RuBr(NO)_2(PPh_3)_2]BF_4$

To test under which conditions a maximum population of the metastable isomer is achievable, compound **7b** was irradiated with laser light of the wavelengths 325, 405 and 442 nm at 80 K. No clear maximum was detected due to heavy overlap of the bands, but the maximum population is much smaller than in the chloride analogue. Fig. 2.44 shows an infrared spectrum in the *ν*(NO) range of the ground state (bands at 1756, 1787 and 1834 cm^{-1}) and the photo-excited state at 80 K. Upon illumination in the blue spectral range novel bands appear at 1654 and 1872 cm^{-1}. The magnitude of the shift of the asymmetrical stretching vibration (−103 cm^{-1}) indicates the generation of an isonitrosyl species.[56, 58] As Fig. 2.44 shows, heating up to 115 K results in the re-establishment of the ground-state bands.

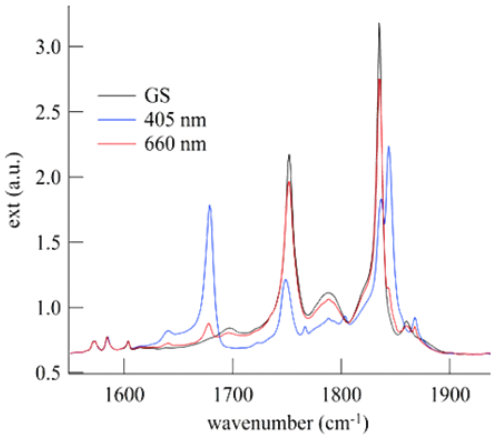

Fig. 2.44: IR spectrum of **7b** (black line corresponds to the ground state) in the *ν*(NO) range after population by irradiation with light of the wavelengths 405 nm (blue line) and depopulation at 660 nm (red line).

2.10.3 $[RuCl(NO)_2(PPh_2Bn)_2]BF_4$

To test under which conditions a maximum population of the metastable isomer is achievable, compound **9b** was irradiated with laser light of the wavelengths 405, 442, 476, 488 and 532 nm at 80 K. Maximum photo-excitation was gained at 405 and 442 nm. Fig. 2.45 shows an infrared spectrum in the *ν*(NO) range of the ground-state and the photo-excited state at 80 K.

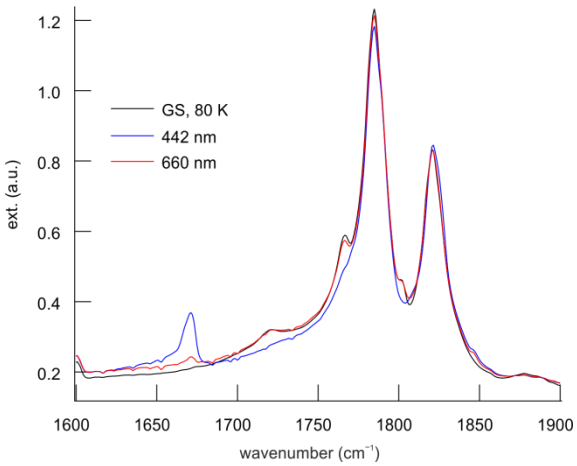

Fig. 2.45: IR spectrum of **9b** in the *ν*(NO) range after population (442nm) and depopulation (660 nm) by irradiation with light of the appropriate wavelengths.

Upon illumination in the blue spectral range the NO band corresponding to the asymmetrical stretching mode of **9b** (1821 and 1785 cm^{-1}, ground state) is shifted into the lower-energy range by −114 cm^{-1}. The novel band appears at 1671 cm^{-1}. The diminishment of the integral of the

ground-state band of **9b** indicates a population of the photo-excited state of about 6–7%. The magnitude of the shift indicates the generation of an isonitrosyl species.[56, 58] As Fig. 2.45 shows, the photoswitching is reversible since irradiation with a wavelength, corresponding to the red spectral range results in an increase of the integral of the ground-state bands until the original value is reached. The metastable state decomposes at temperatures above 115 K.

2.10.4 $[RuCl(NO)_2\{P(p\text{-tolyl})\}_2]BF_4$

To test under which conditions a maximum population of the metastable isomer is achievable, compound **14b** was irradiated with laser light of the wavelengths 325, 405, 442 and 476 nm at 80 K. Maximum photo-excitation was gained at 442 and 405 nm. Fig. 2.46 shows an infrared spectrum in the *v*(NO) range of the ground state (*v*(NO) at 1870, 1832, 1777, 1752 cm^{-1}) and the photo-excited state at 80 K. Upon illumination in the blue spectral range the NO band corresponding to the asymmetrical stretching mode of **14b** (1777/1752 cm^{-1}, ground state) is shifted into the lower-energy range by −136/111 cm^{-1}. The novel band appears at 1641 cm^{-1}. The magnitude of the shift indicates the generation of an isonitrosyl species.[56, 58] Upon heating, the band at 1641 cm^{-1} disappears at temperatures above 110 K (see Fig. 2.47).

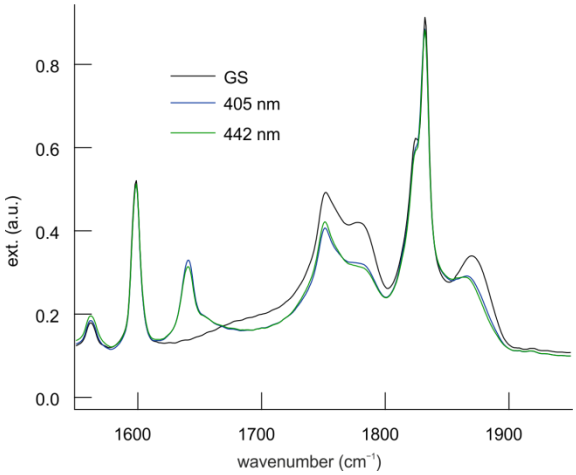

Fig. 2.46: IR spectrum of **14b** (black line corresponds to the ground state) in the *v*(NO) range after population by irradiation with light of the wavelengths 405 nm (blue line) and 442 nm (green line).

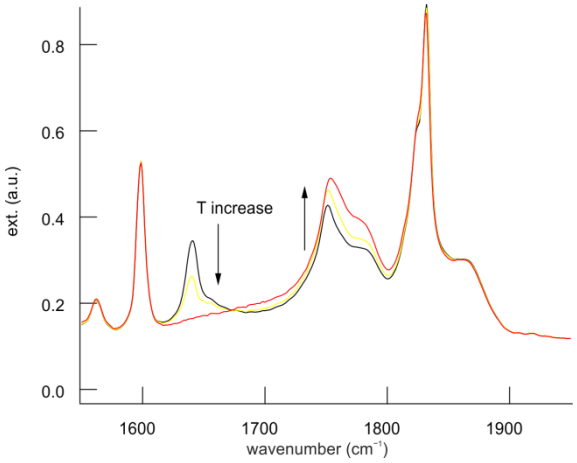

Fig. 2.47: IR spectrum of **14b** (black line corresponds to the ground state) in the *v*(NO) range after population (405nm, blue line) and depopulation (660 nm, red line) by irradiation with light of the appropriate wavelengths.

2.10.5 $[RuCl(NO)_2(PCy_3)_2]BF_4$

To test under which conditions a maximum population of the metastable isomer is achievable, compound **18a** was irradiated with laser light of the wavelengths 405 and 488 nm at 80 K. Maximum photo-excitation was gained at 405 nm. Fig. 2.48 shows an infrared spectrum in the *v*(NO) range of the ground state and the photo-excited state at 80 K. The ground-state spectrum shows three bands in the *v*(NO) range at 1710, 1760 and 1798 cm^{-1}. Upon illumination in the blue spectral range the asymmetric as well as the symmetric stretching vibration bands of the ground state (1710 and 1798 cm^{-1}) are shifted into the lower-energy range by −60 and −36cm^{-1}. The novel band appears at 1650 and 1762 cm^{-1}. The diminishment of the integral of the ground-state band of **18a** indicates a population of the photo-excited state of about 29%. At 980 nm the integral of the band at 1762 cm^{-1} diminishes while the other band remains unaffected. Upon heating, the band at 1762 cm^{-1} disappears around 120 K, whereas the band at 1650 cm^{-1} vanishes at about 160 K (see Fig. 2.49).

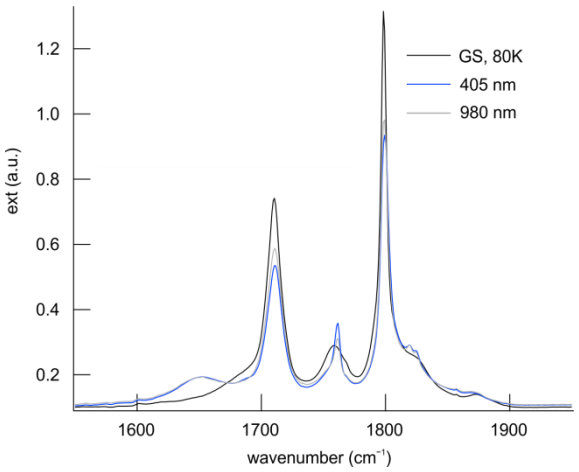

Fig. 2.48: IR spectrum of **18a** in the *v*(NO) range after population by irradiation with light of the wavelengths 405 nm and 980 nm.

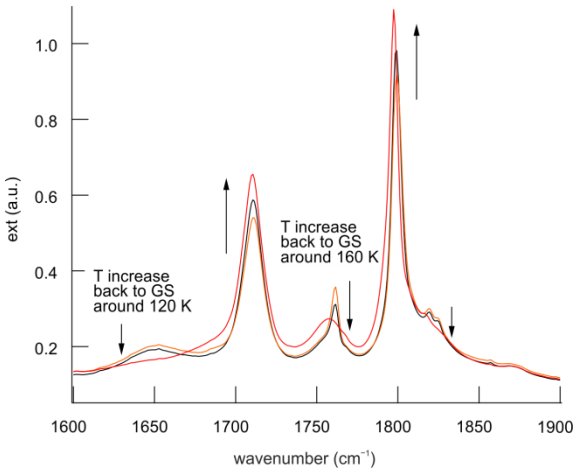

Fig. 2.49: IR spectrum of **18a** in the *v*(NO) range after population (405nm) and thermal depopulation by gradual heating.

2.10.6 $[RuBr(NO)_2(P^iPr_3)_2]BF_4$

Fig. 2.50 shows infrared spectra of the ground state at room temperature and 80 K, recorded on a *Nicolet 5700 FTIR spectrometer* having a resolution power of 2 cm^{-1}. Remarkable is the existence of four bands at 1801, 1794, 1750 and 1694 cm^{-1} (the two bands richest in energy overlap partially) when compared to the ground-state spectrum recorded on a *Jasco FT/IR-460 plus spectrometer* using a resolution power of 4 cm^{-1}, which only shows three bands at 1797, 1744 and 1689 cm^{-1}. Additionally, the Figure shows the temperature dependence of resolution (decrease of the *Full width at half maximum* with decreasing temperature) and wavelength (shift to higher wavelengths with decreasing temperature, bands at 1806, 1797, 1753 and 1694 cm^{-1}).

The assignment of the ground-state bands to the two isomers **a** and **b** was carried out by comparative quantum-chemical calculations, based on DFT. Therefore, the structures of the isomers derived from X-ray data were first subjected to a geometry optimisation and then to frequency analysis.

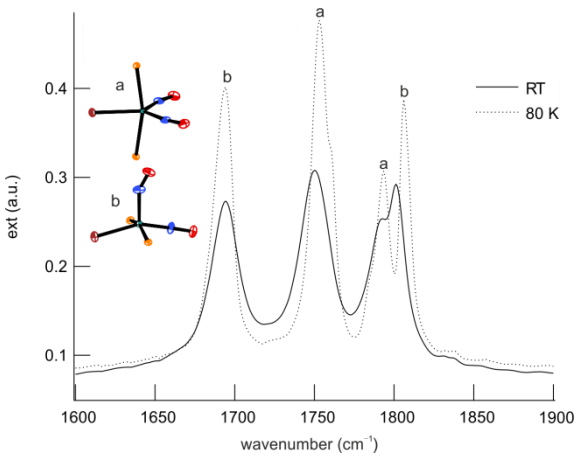

Fig. 2.50: IR spectrum of the ground state of the isomers a and b of **25b** in the *v*(NO) range at RT(solid line) and 80 K (dashed line).

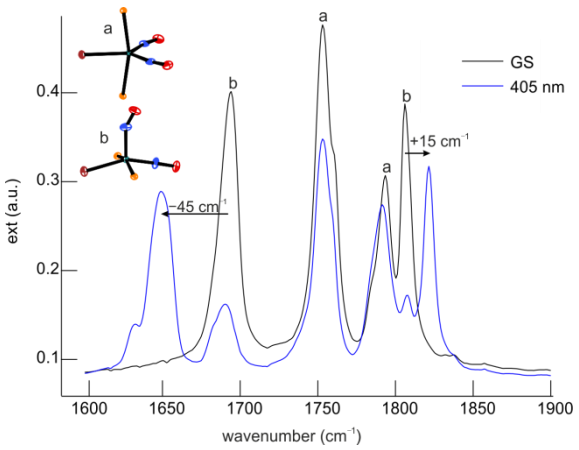

Fig. 2.51: IR spectrum of the isomers a and b of **25b** in the *v*(NO) range before (black line) and after (blue line) population by irradiation with light of the wavelength 405 nm at 80 K.

To test under which conditions a maximum population of the metastable isomer is achievable, compound **25b** was irradiated with laser light of the wavelengths 405, 445 and 476 nm at 80 K. Maximal photo-excitation was gained at 405 nm. Fig. 2.51 shows an infrared spectrum in the *v*(NO) range of the ground state and the photo-excited state at 80 K. Upon illumination in the blue spectral range the two NO bands of isomer **b** (1806 and 1694 cm^{-1}, ground state) are shifted, the asymmetrical stretching mode is shifted into the lower-energy range by −45 cm^{-1}, the symmetrical stretching mode is shifted into the higher-energy range by +15 cm^{-1}. The magnitude of the shifts is similar compared to those of compound **6b**. The novel bands appear at 1821 and 1649 cm^{-1}.

The diminishment of the integral of the ground-state bands of isomer **b** indicates a population of the photo-excited state of about 70%. The ground-state bands of isomer **a** stay relatively unaffected. As Fig. 2.52 and Fig. 2.53 show, the photoswitching is reversible since irradiation with a wavelength corresponding to the red spectral range, as well as gradual heating, result in an increase of the integral of the ground state-bands until the original value is reached.

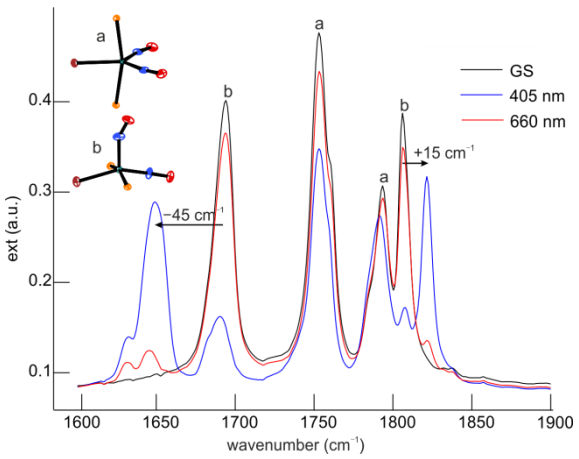

Fig. 2.52: IR spectrum of the isomers a and b of **25b** in the *ν*(NO) range before (black line) and after population (405 nm, blue line) and depopulation (606 nm, red line) by irradiation with light of the appropriate wavelength at 80 K.

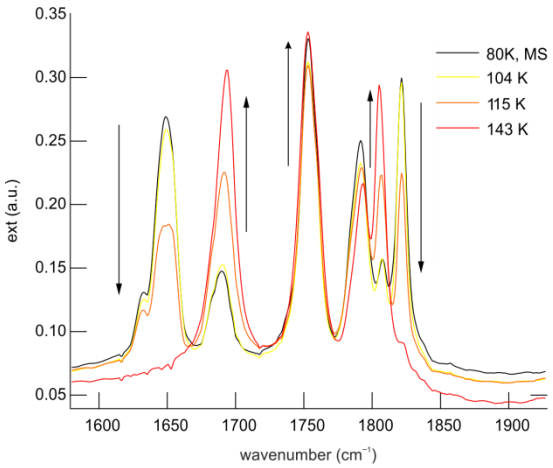

Fig. 2.53: IR spectrum of the isomers a and b of **25b** in the *ν*(NO) range after population at 80 K (black line) and subsequent thermal depopulation by gradual heating (yellow, orange and red line).

2.11 Photocrystallography of $[RuCl(NO)_2(PPh_3)_2]BF_4$

For theoretical background knowledge on photocrystallography see EXPERIMENTAL PART, chapter 5.10.

Since compound **6b** shows a high photo-excitability—according to IR data 70% of the ground state molecules can be transferred into a metastable state—photocrystallographic investigations were possible when using a helium-cryosystem (10K) and a wavelength of 405 nm.

Fig. 2.54 shows the electron density map of the ground state at 90 K.

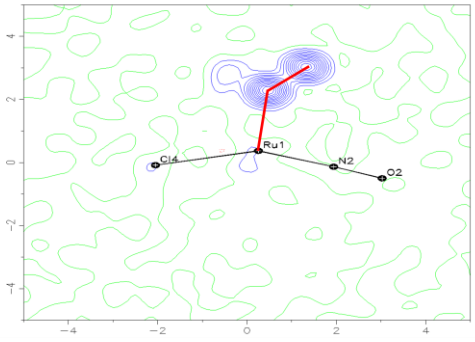

Fig. 2.54: Electron density map of the ground state in **6b** calculated in the Ru-N1-N2 plane, with contours of ±1.0 e Å^{-3} (blue: positive) at 90K.The lone electron pair at the nitrogen atom of the bent nitrosyl ligand can clearly be seen.

Fig. 2.55 and Fig. 2.56 show a three- and two-dimensional plot of the photo-difference map calculated from the Fourier transform of the $F_{photo\text{-}irradiated}(hkl) - F_{GS}(hkl)$ difference, using the structure factor phases of the refined ground-state model. As evidenced by electron-deficient regions on the heaviest atoms of the structure (P1, P2, Ru, Cl), the model of the irradiated state clearly shows a slight displacement of the whole structure upon illumination when compared to the ground-state model.

In order to deconvolute the structure of the GS and the PLI state, several refinement strategies were applied (see Fig. 2.57, Fig. 2.58, Fig. 2.59 and Fig. 2.60), which led to different agreement factors R_1 and wR_2 (see Table 2.7). Only that model, will be discussed in detail, which consists in refining the average structural parameters for all the atoms except the nitrogen and the oxygen atom of the bent NO group, which are described and refined by two configurations, the GS and the PLI one (Fig. 2.58, Fig. 2.59 and Fig. 2.61).

As already expected from infrared spectroscopic investigations, the calculated photo-difference map reveals the most striking structural reorganisation in the surrounding of the bent nitrosyl ligand (see Fig. 2.54), which is a clear indication for the existence of both GS- and PLI-molecular species. A strong electron-deficient region is located on the O atom of the bent nitrosyl group. Accordingly, a strong electron-excessive region is found on the other side of the Ru–N1-axes. This structural reorganisation can be described by the superposition of two configurations of the affected nitrosyl group (see Fig. 2.61): one corresponds to the ground-state configuration, where the bent NO ligand is inclined to the linear NO group (*syn*-configuration, Ru–N1A–O1A angle of 131.0°, Ru–N1A distance of 2.115 Å and N1A–O1A distance of 1.130 Å) with an occupancy factor much lower than unity. In the other configuration the bent NO group is inclined to the site opposite of the linear NO group (*anti*-configuration, Ru–N1B–O1B angle of 115.0°, Ru–N1B distance of 1.862 Å and N1B–O1B distance of 1.181 Å).

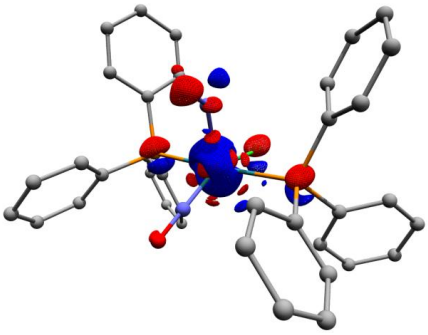

Fig. 2.55: Photo-difference map with isosurface of ±2.8 e Å^{-3} (red, negative; blue, positive) at 10K after irradiation with 405 nm. The map is based on all independent measured reflections.

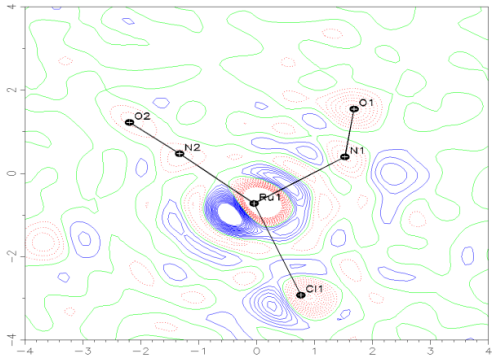

Fig. 2.56: Photo-difference map calculated in the Ru-N1-N2 plane, with contours of ±1.0 e Å^{-3} (red: negative, blue: positive) at 10K after irradiation with 405 nm.

The photo-induced *anti*-configuration can also be modelled by an isonitrosyl ligand (Ru–O1B–N1B angle of 114.8°, Ru–O1B distance of 1.856 Å and O1B–N1B distance of 1.215 Å).

In both cases (*anti*-configured nitrosyl, *anti*-configured isonitrosyl) the major structural feature of the PLI is a significant decrease in the RuN1O1 angle with respect to the ground-state structure and an inversion in the inclination angle relative to the Ru-N1 axis with regard to the ground-state structure. In the case of an N-bound PLI structure, the degree of population reaches up to 42.1%, whereas in the case of an O-bound PLI structure, the degree of population reaches up to 43%. Being equivalent, neither R-values nor residual electron-density maps for the nitrosyl and the isonitrosyl model allow for an unambiguous determination of the metastable state.

Even neutron-diffraction experiments did not allow for an unambiguous determination of the metastable state, due to the high neutron cross section of boron and inelastic scattering of the neutrons with the hydrogen atoms of PPh_3.

As affirmed by the photo-difference map and confirmed by the IR data, there is no remarkable change of the structure parameters of the linearly coordinated NO group. This can be due to a low degree of population, not detectable by photo-crystallography, or the linear NO group is not subjected to PLI.

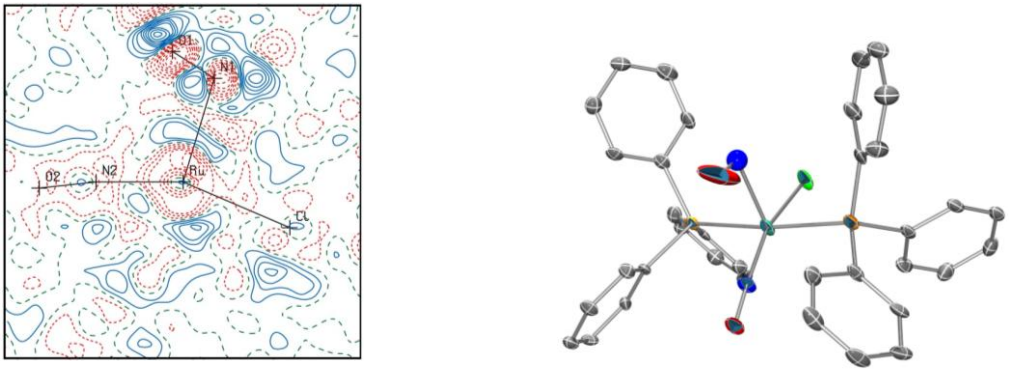

Fig. 2.57: Left: Residual electron density map calculated in the Ru-N1-N2 plane, with contours of ±0.25 e $Å^{-3}$ (red: negative, blue: positive) for the average refinement strategy. In this model the nitroxyl ligand is refined anisotropically. Thus, the resulting atomic positions correspond to an average of the GS and photo-irradiated positions, weighted by their respective population. The result is a heavy disorder of the N1O1 moiety, displayed by the elongated ellipsoids. There is no disorder on the N2O2 moiety (see *U* values in table 2.1). Right: ORTEP view, ellipsoids are plotted at the 50% probability level.

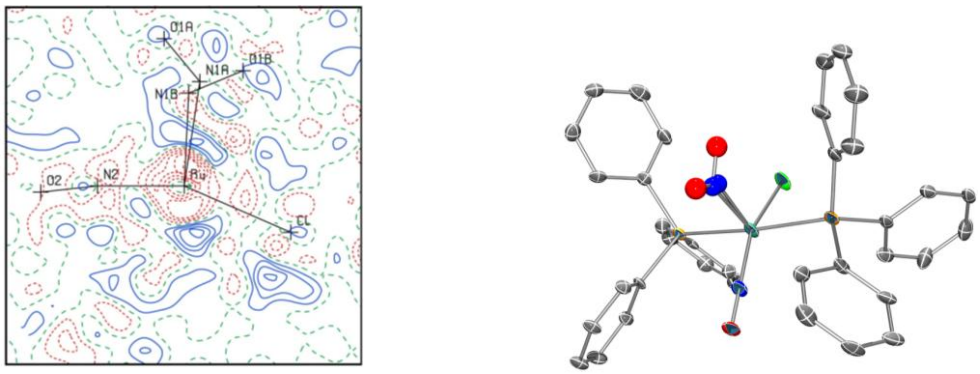

Fig. 2.58: Left: Residual electron density map calculated in the Ru-N1-N2 plane, with contours of ±0.25 e $Å^{-3}$ (red: negative, blue: positive) for the average + 2 N–O refinement strategy. Two configurations for the nitroxyl ligand were described in this refinement strategy, one corresponding to the GS structure, one to the PLI species. For this purpose, the two configurations were refined separately and isotropically with restraints for the N–O distance (1.16 A) and assuming a random spatial distribution. The agreement factors are better with respect to the average model (Fig 2.43) and the U values for the N1O1 and the N2O2 moiety are of the same magnitude, a further hint that this model is more appropriate. Right: ORTEP view, ellipsoids are plotted at the 50% probability level.

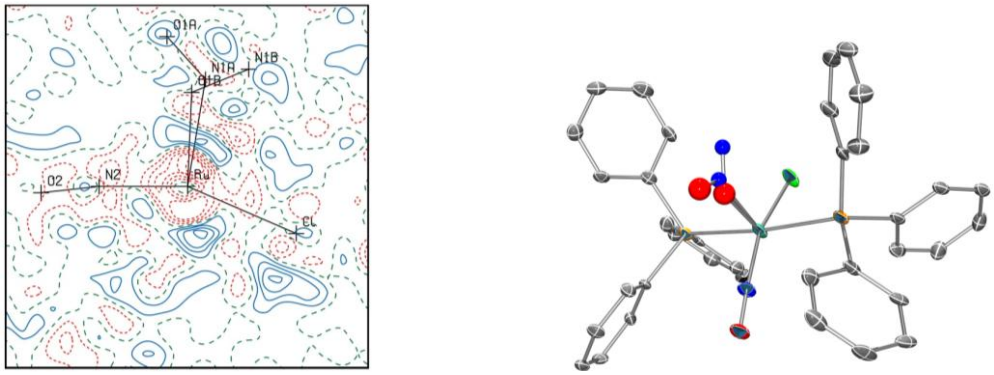

Fig. 2.59: Left: Residual electron density map calculated in the Ru-N1-N2 plane, with contours of ±0.25 e Å^{-3} (red: negative, blue: positive) for the average + 1 N–O and 1 O–N refinement strategy. As for model 2.44, two configurations were refined for the nitroxyl ligand, but in this case the second configuration is described as an isonitrosyl. The agreement factors are identical to those of model 2.44. Right: ORTEP view, ellipsoids are plotted at the 50% probability level.

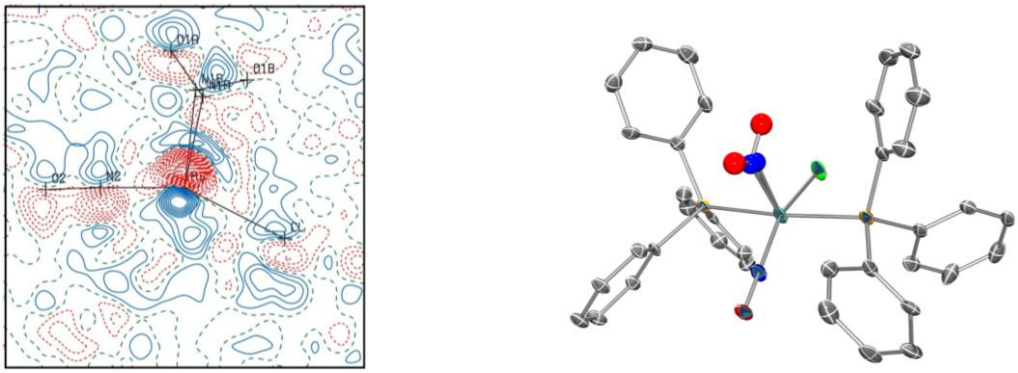

Fig. 2.60: Left: Residual electron density map calculated in the Ru-N1-N2 plane, with contours of ±0.25 e Å^{-3} (red: negative, blue: positive) for the rigid group refinement strategy. For this strategy the GS structure was treated as rigid group and changes in lattice parameters upon irradiation were taken into account. A second NO configuration was described for the PLI state. The agreement factors are even higher than in model 2.43. Right: ORTEP view, ellipsoids are plotted at the 50% probability level.

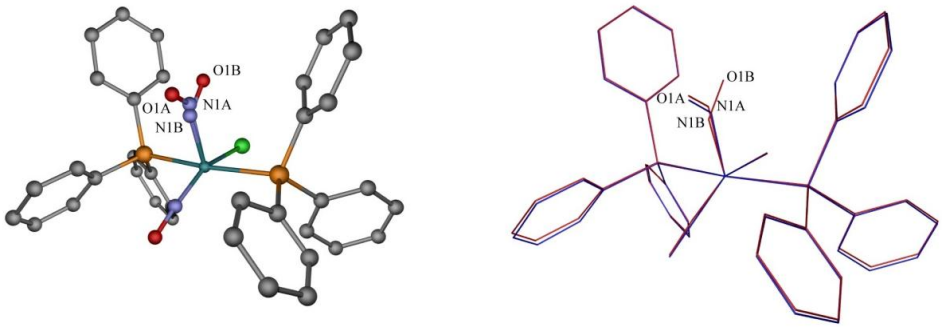

Fig. 2.61: Left: structural model of the PLI state upon photo-excitation. Right: superposition of the GS (blue) and PLI (red) molecular structure.

Table 2.7: Refinement details for $[RuCl(NO)_2(PPh_3)_2]BF_4$ (1) in the ground state (GS) and photo-irradiated state.

	Ground state	**Photo-irradiated state**			
Refinement strategy		Average	Average + 2 N–O	Average + 1 N–O and 1 O–N	GS Rigid group + N–O
No. of variables	442	442	439	439	314
No. of constraints					
$^{a}R_1$ [$F^2 > 2\sigma(F^2)$]	0.0816 [0.0522]	0.1238 [0.0728]	0.1174 [0.0664]	0.1173 [0.0664]	0.1477 [0.0955]
$^{b}wR_2$ [$F^2 > 2\sigma(F^2)$]	0.1174 [0.1013]	0.1707 [0.1404]	0.1485 [0.1213]	0.1490 [0.1219]	0.2570 [0.2160]
$^{c}GooF$	1.039	1.043	1.039	1.038	1.043
$\Delta\rho_{max,\ min}$ (eÅ^{-3})	2.542 / -1.251	1.919 / -1.821	1.310 / -0.989	1.334 / -1.002	3.465 / -2.954
Refined population of PLI (P_{PLI})	/	/	42.1(5)%	43.0(7)%	44(1) %
U_{eq}(Ru)	0.00820(7)	0.01812(14)	0.0180(1)	0.0180(1)	0.0183(2)
U_{eq}(N2)	0.0083(5)	0.021(1)	0.0211(9)	0.0211(9)	0.0204(14)
U_{eq}(O2)	0.0145(5)	0.0258(9)	0.0265(8)	0.0265(8)	0.0260(13)
U_{eq}(N1A)	0.0134(6)	0.135(6)	0.0206(13)	0.0171(16)	0.0260(17)
U_{eq}(O1A)	0.0279(6)	0.178(6)	0.0324(12)	0.0341(17)	0.033(2)
U_{eq}(N1B)	/	/	0.0206(13)	0.0171(16)	0.0260(17)
U_{eq}(O1B)			0.0324(12)	0.0341(17)	0.033(2)

$^{a}R_1 = \sum|Fo\text{-}Fc|/Fo$. $^{b}wR_2 = \{[\Sigma w(F_o^2\text{-}F_c^2)^2]/[\Sigma wF_o^2)^2]]\}^{1/2}$. ^{c}GooF= $\{[\Sigma w(F_o^2\text{-}F_c^2)^2]/(N_{obs}\text{-}N_{var})\}^{1/2}$.

3 Discussion

The chapter will, at first, deal with the observations—made from IR measurements in solution—that for some compounds additional bands occur when compared to the solid state. A sub chapter will follow which deals with the application of the Enemark–Feltham notation and ascertainment of oxidation states to the metal and the nitrosyl ligands from spectroscopic results. Next, spectroscopic and structural parameters of a $\{RuNO\}^6$, a $\{RuNO\}^8$ and a $\{Ru(NO)_2\}^8$ system will be compared. Subsequently, it will be discussed, using crystal field and MO theory, whether the sqp/*VOC*-5 dinitrosyls can be regarded as derivatives of $\{Ru^{II}/NO^+/NO^+\}^8$, whereas the tbp/*TBPY*-5 structures can be considered as derivatives of $\{Ru^0/NO^+/NO^+\}^8$. The aim is to answer this question by comparison with results from DFT. After having taken a closer look at the ground states, the photo-induced metastable states will be discussed and a possible mechanism will be presented.

3.1 Structural interconversion observed in solution

Chapter 2.7 dealt with the verification of the crystallographically determined Ru–N–O angles in the tbp structures. Tools for this purpose were IR measures of the dissolved state, comparative quantum-chemical calculations and temperature dependence of ADPs.

As mentioned in the INTRODUCTION, chapter 1.4.2 ^{15}N NMR spectroscopy (50-100% enrichment) can be used as a tool to differentiate between a nitrosyl ligand coordinated in a bent or linear fashion. Thus, ^{15}NMR could have served as a further tool, would it not be that costly and substance consuming.

Mingos *et al.* performed such an experiment for compound **6b**.[136] They observed one triplett ^{15}N NMR signal at 125.9 ppm (CD_2Cl_2, 293 K, $^2J(^{31}P^{15}N)$ = 2.5 Hz), whereas solid-state NMR investigations showed two signals at 26 and 303 ppm. Thus, they assumed a rapid intramolecular fluctuation process which leads to an equilibration of the nitrosyl ligands making them identical on the NMR time scale (see Fig. 3.1) with **6b-2** as the intermediate. This assumption is supported by IR data of the dissolved compound (see chapter 2.7.1).

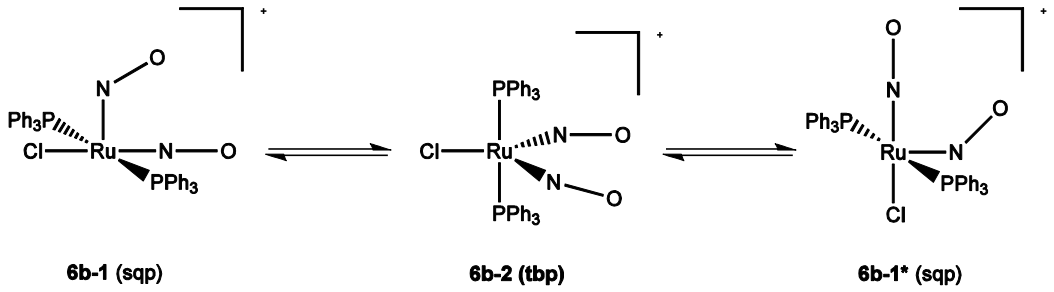

Fig. 3.1: Solution equilibrium of the sqp (square pyramid) and tbp (trigonal bipyramidal) isomers of **6b**. Since the nitrosyl ligands in **6b-1** and **6b-1*** can undergo a rapid intramolecular fluxional process *via* **6b-2** as intermediate, the ^{15}N NMR spectrum with 99% ^{15}N-enrichment shows only one signal.[136] The solid-state NMR spectrum of **6b** shows two signals, as expected from X-ray data.[136]

Not only **6b** but also **19b**, **21b-1**, **24b** and **25b-1**, all of which adopt sqp structure in the solid state, gave *ν*(NO) frequencies which indicate the interconversion to a tbp structure upon dissolving. The interconversion path most probably follows the Berry mechanism.

3.2 Electronic states and Enemark–Feltham notation

The following chapter will describe the application of the Enemark–Feltham notation (see INTRODUCTION, chapter 1.4.2) for the nitrosyl compounds of this work.

Compounds **2–5**: $K_2[Ru(NO_2)_4(OH)(NO)]$, $K_2[RuX_5(NO)]$, 18 VE

Ru^{II}/NO^+ (spectroscopic oxidation state)	6 d/0 π* electrons
$Ru^{III}/NO^{\cdot}$ (formal oxidation state, IUPAC)	5 d/1 π* electrons
Ru^{IV}/NO^-	4 d/2 π* electrons
	$\Sigma(n\ d + n\ \pi^*)e^- = 6 \rightarrow \{RuNO\}^6$

Compounds **6a–19a, 21a-24a**: $[RuX_3(NO)(PR_3)_2]$, 18 VE

Ru^{II}/NO^+ (spectroscopic oxidation state)	6 d/0 π* electrons
$Ru^{III}/NO^{\cdot}$ (formal oxidation state, IUPAC)	5 d/1 π* electrons
Ru^{IV}/NO^-	4 d/2 π* electrons
	$\Sigma(n\ d + n\ \pi^*)e^- = 6 \rightarrow \{RuNO\}^6$

Compounds **14a-26a**: $[RuX_2(NO)(PR_3)_2]$, 17 VE

Ru^{I}/NO^+ (spectroscopic oxidation state[a])	7 d/0 π* electrons
$Ru^{II}/NO^{\cdot}$ (formal oxidation state, IUPAC)	6 d/1 π* electrons
Ru^{III}/NO^-	4 d/2 π* electrons
	$\Sigma(n\ d + n\ \pi^*)e^- = 7 \rightarrow \{RuNO\}^7$

[a] Most probable electronic state. Comparative data from literature are missing.

Compounds **14a-26a**: $[RuX(NO)(PR_3)_2]$, 16 VE

Ru^{0}/NO^+ (spectroscopic oxidation state)	8 d/0 π* electrons
$Ru^{I}/NO^{\cdot}$ (formal oxidation state, IUPAC)	7 d/1 π* electrons
Ru^{II}/NO^-	6 d/2 π* electrons
	$\Sigma(n\ d + n\ \pi^*)e^- = 8 \rightarrow \{RuNO\}^8$

Compounds **6b-26b**: $[RuX(NO)_2(PR_3)_2]BF_4$, 18 VE

$Ru^{0}/NO^+/NO^+$ (spectroscopic oxidation state)	8 d/0 π*/0 π* electrons
$Ru^{I}/NO^{\cdot}/NO^+$	7 d/1 π*/0 π* electrons
$Ru^{II}/NO^{\cdot}/NO^{\cdot}$ (formal oxidation state, IUPAC)	6 d/1 π*/1 π* electrons
$Ru^{II}/NO^+/NO^-$ (spectroscopic oxidation state)	6 d/0 π*/2 π* electrons
$Ru^{III}/NO^{\cdot}/NO^-$	5 d/1 π*/2 π* electrons
$Ru^{IV}/NO^-/NO^-$	4 d/2 π*/2 π* electrons
	$\Sigma(n\ d + n\ \pi^*)e^- = 8 \rightarrow \{Ru(NO)_2\}^8$

Compounds **26c**: $[\{Ru(NO)_2(PR_3)\}_2(\mu\text{-}I)]BF_4$, 34 VE (36 VE Ru–Ru bond)

$Ru^0/NO^{\cdot}/NO^+$	8 d/1 π*/0 π* electrons
$Ru^I/NO^{\cdot}/NO^{\cdot}$ (formal oxidation state, IUPAC)	7 d/1 π*/1 π* electrons
$Ru^I/NO^+/NO^-$	7 d/0 π*/2 π* electrons
$Ru^{II}/NO^{\cdot}/NO^-$	6 d/1 π*/2 π* electrons
$Ru^{III}/NO^-/NO^-$	5 d/2 π*/2 π* electrons
	$\Sigma(n\ d + n\ \pi^*)e^- = 9 \rightarrow$
	$\{Ru(NO)_2\}^9$–$\{Ru(NO)_2\}^9$

Compounds **8c, 13c**: $[\{RuX_2(NO)(PR_3)\}_2(\mu\text{-}X)_2]$, 36 VE

Ru^{II}/NO^+	6 d/0 π* electrons
$Ru^{III}/NO^{\cdot}$ (formal oxidation state, IUPAC)	5 d/1 π* electrons
Ru^{IV}/NO^-	4 d/2 π* electrons
	$\Sigma(n\ d + n\ \pi^*)e^- = 6 \rightarrow$
	$\{Ru(NO)\}^6$–$\{Ru(NO)\}^6$

Compounds **2**–**5** and **6a**–**13a** can be described electronically as a d^6 metal centre coordinated to an NO^+ ligand, compounds **14a**–**26a** are product mixtures, whose products can be described as a d^6, d^7 and d^8 metal centres coordinated to an NO^+ ligand, respectively. The characterisation of the $\{RuNO\}^6$, $\{RuNO\}^8$ and $\{Ru(NO)_2\}^8$ compounds is accessible with standard NMR spectroscopy, since these compounds are diamagnetic low-spin complexes.

3.3 $\{RuNO\}^6$, $\{RuNO\}^8$, $\{Ru(NO)_2\}^8$: Structural and IR spectroscopic properties in comparison

As mentioned in chapter 1.9, one of the aims of this work is to contribute to a better understanding of the ruthenium-nitrosyl bond, on which various properties of the nitrosyl ligand, such as photoexcitability, structural and IR spectroscopic parameters, depend. The special focus lies on the comparison of two different bonding modes of the nitrosyl ligand (NO^+, NO^-) within one molecule and the distribution of the charge on the ruthenium central atom—which is heavily dependent on the co-ligands—towards the nitrosyl ligands. There are no better tools for this purpose than X-ray diffraction and IR spectroscopy, since they allow the determination of the Ru–N–O angle, Ru–N and N–O bond lengths (with limitations due to disorder and dynamic, see INTRODUCTION, chapter 1.4.2) as well as the assignment of spectroscopic oxidation states ($NO/NO^+/NO^-$) and charges on the NO ligand *via* IR spectroscopy (see INTRODUCTION, chapter 1.4.2).

The structures and IR data in the *ν*(NO) range of compounds **6a**, **6b** and **6c** offer an excellent possibility to study the changes of the metal nitrosyl bond upon reduction of the ruthenium central atom (see Fig. 3.2).

Since a spectroscopic oxidation state of +II (formal oxidation state +III) can be assigned to the ruthenium atom of compound **6a**, the central atom is a relatively weak π base and there is no noteworthy π backdonation. Accordingly, the *ν*(NO) stretching frequency is relatively high. As expected, upon reduction of the ruthenium central atom to a formal oxidation state of +I, the Ru–N

bond length decreases as the π basicity of the ruthenium increases, accordingly the N–O bond length increases since the increasing basicity of the ruthenium atom leads to a higher population of the π* orbitals of the NO ligand. Thus, the *ν*(NO) stretching frequency is lower than in the analogous $\{RuNO\}^6$ compound. It could have been expected that the reduction might have led to a Ru^{II}/NO^- complex. As discussed in the INTRODUCTION, chapter 1.5.1, there are two different possibilities for the localisation of the additional electrons: If the two additional electrons are localised on the metal atom (filling of the $4a_1$ level, see Fig. 1.14) the coordination number will be lowered and the RuNO fragment will maintain linearity. If the two additional electrons will be localised on the nitrosyl ligand bending of the RuNO fragment will result, according to Walsh's rules. Indeed, the first possibility described is realised by compound **6c**, which maintains the linear RuNO arrangement of **6a** by lowering the coordination number. It can thus be assumed that in compound **6c** the $4a_1$ level is energetically lying underneath the 3e level.

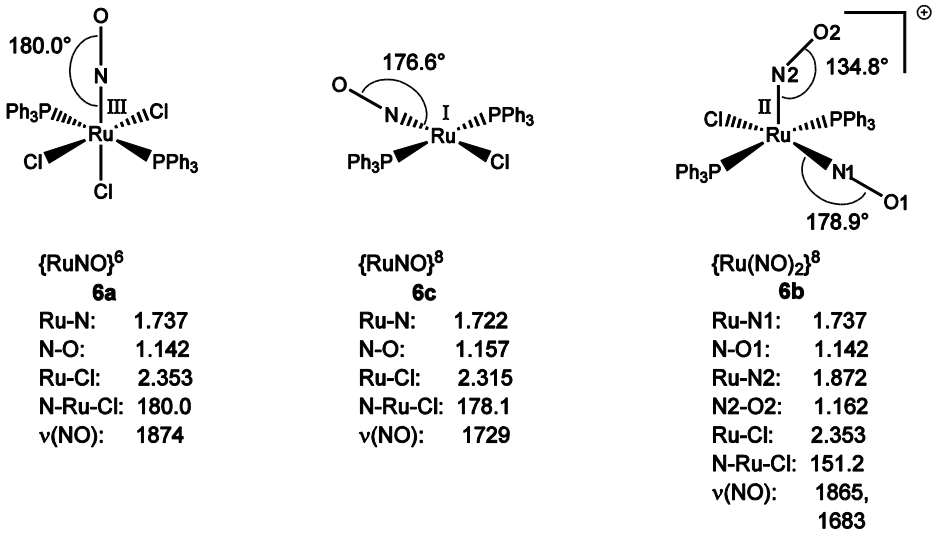

Fig. 3.2: Structural and spectroscopic parameters of $[RuCl_3(NO)(PPh_3)_2]$ (**6a**), $[RuCl(NO)(PPh_3)_2]$ (**6c**) and $[RuCl(NO)_2(PPh_3)_2]BF_4$ (**6b**) and their formal oxidation states. Distances are given in Å, frequencies in cm^{-1}. Structural data for **6a** were taken from Reference [137].

When an additional ligand is introduced and the coordination number is raised (**6c** → **6b**), the additional σ-bond will increase the electron density on the ruthenium atom. The already electron-rich ruthenium atom avoids the additional density by localizing the electrons onto one of the nitrosyl ligands, which thereupon reacts by bending. The low oxidation state of the ruthenium atom in **6c** will thus favour an oxidative nitrosylation (INTRODUCTION, chapter 1.4.2), giving rise to a bend NO^-, whose spectroscopic and structural parameters are clearly deviating from the other NO ligand, coordinated in a linear fashion: the Ru–N1 and N1–O1 bond length are identical to those of compound **6a**, whereas the Ru–N2 and N2–O2 bond lengths are greater since the electrons in the π* orbitals of the NO^- ligand will lower the NO bond order, reflected in the lower *ν*(NO) valence vibration. Additionally the lowered π acidity of an NO^- ligand will lead to a weaker π backdonation.

When the spectroscopic data is taken into account, the compounds can be classified as Ru^{II}/NO^{+} (**6a**), Ru^{0}/NO^{+} (**6c**) and $Ru^{II}/NO^{+}/NO^{-}$ (**6b**). This explains both, the similar Ru–Cl, Ru–N and N–O bond lengths of the linear NO in **6a** and **6b** and the deviating Ru–N, N–O and Ru–Cl bond lengths in **6c**. Compound **6c** is a good example for the danger of a misinterpretation when the bonding situation of the nitrosyl ligand is derived only from the *ν*(NO) value.

3.4 Description of $[RuX(NO)_2(PR_3)_2]BF_4$ compounds using MO theory

The argumentation used in the following chapters is based on qualitative MO and crystal-field theoretical considerations published by Enemark and Feltham and Hoffmann *et al*.[44, 138]

3.4.1 Pentacoordination and site preferences in $[RuX(NO)_2(PR_3)_2]^+$: crystal-field theoretical considerations

In compounds of the general formula $[RuX(NO)_2(PR_3)_2]BF_4$, the ruthenium central atom is pentacoordinated, possible structures are, thus, the trigonal bipyramid (tbp) or the square pyramid (sqp), which corresponds to a vacant octahedron (*VOC*-5) under a certain condition. Whether a tbp or a sqp structure is favoured depends on the number of d electrons. The adopted structure can easily be deduced from the left side of Fig. 3.3, which shows the correlations of the crystal-field splitting for tbp and sqp. For the electron configurations d^0, d^3-d^4, hs-d^6 and d^8-d^{10} the trigonal bipyramid is favoured while for the electron configuration ls-d^6 the square pyramid is favoured. Both geometries are found for the electron configurations ls-d^7 and d^8. This is due to the fact that the energetic difference between tbp and sqp for a d^7 or d^8 configuration is very small. In the case of d^0, the reason for the favouring of the tbp is a steric one (ligand-ligand repulsion is minimised).

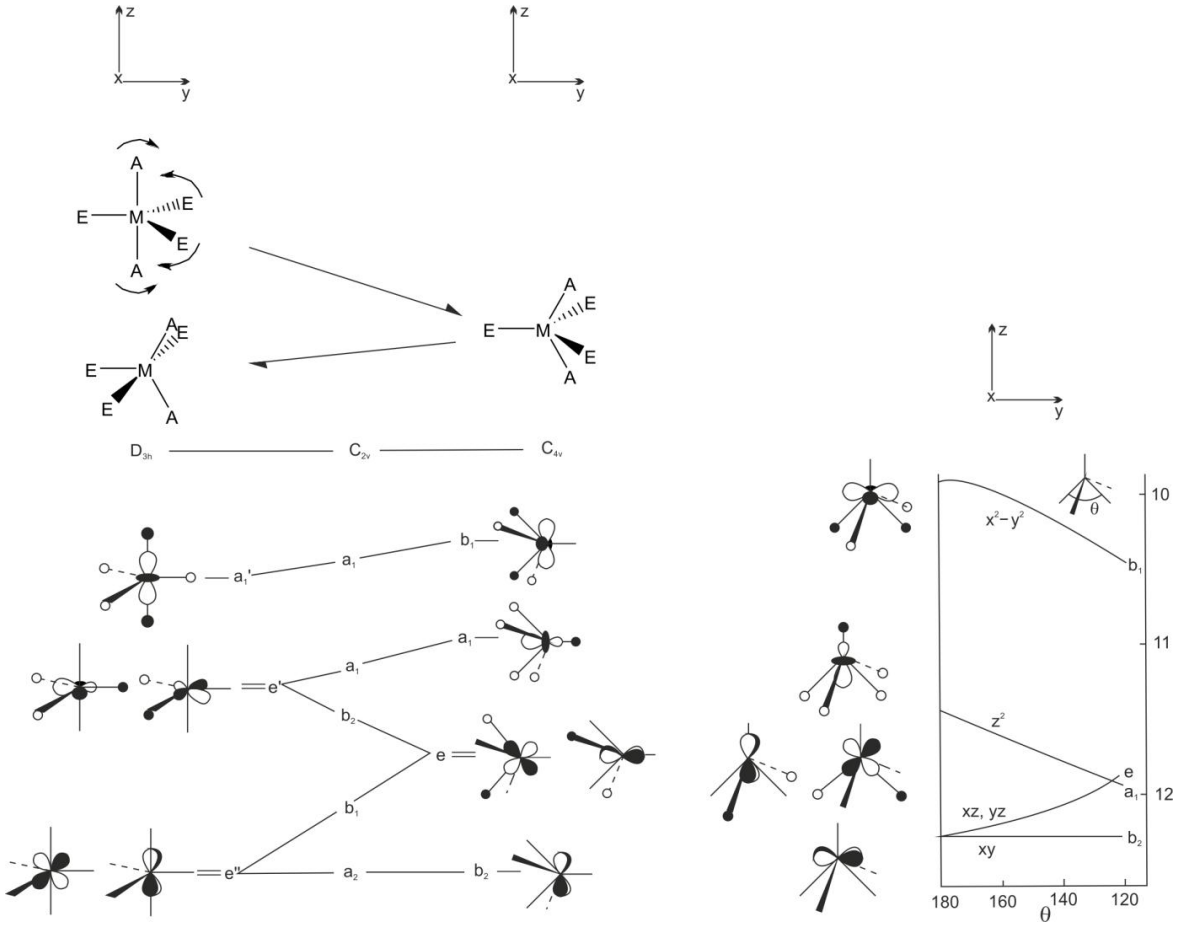

Fig. 3.3: Left: Molecular orbitals and energy changes along a Berry pseudorotation coordinate. Right: Calculated energy levels of ML_5 as a function of the L_E-M-L_E angle θ. The labels identify the primary character of the MO, even though these orbitals are, to various degrees, delocalised. The vertical energy scale is in electron volts. Redrawn from Ref. [138].

In the present case, the compounds **6b**, **18b**, **19b** and **24b** (all adopting sqp structure), can be regarded as low-spin complexes of d^6 configured ruthenium (see DISCUSSION, chapter 3.2). Thus, six electrons have to be filled in the relevant orbitals.

The energy is minimised when a sqp structure is adopted. But the energetic difference E_{sqp}-E_{tbp} should expectedly be small, since it is known that crystal-packing effects or ligand-field stabilisation can compensate this difference.[139] The low energetic difference is reflected in the ability of the compounds **21b** and **25b** to adopt both structures, sqp and tbp. Compounds **9b**, **10b**, **20b**, **22b** and **23b** adopt tbp structure and can be regarded as low-spin complexes of a d^8-configured ruthenium (see DISCUSSION, chapter 3.2). Thus, eight electrons have to be filled in the relevant orbitals. The energy is minimised when a tbp structure is adopted.

Both predictions (sqp is favoured for d^6 and tbp is favoured for d^8 with a small yield in energy) are consistent with the results of DFT-based calculations and the experimental data.

The energetic ordering of the orbitals in sqp depends on the L_E-M-L_E angle θ, the single degree of freedom left in C_{4v}. If θ is 180°, the square pyramid can be regarded as a vacant octahedron (*VOC*-5) and the energetic ordering of the d orbitals corresponds to that of a O_h symmetrical complex, the only difference is that the degeneracy of the e_g and t_{2g} orbitals is lifted since repulsion of one ligand in the z direction is missing. The order changes with a decreasing θ angle. For a d^6 low-spin configuration the optimal angle is 180°, for d^8 configuration the optimal angle is 164°.

The X-ray crystallographically determined L_E–M–L_E angles for the sqp structures have values of 144°–158° and thus deviate from the ideal value for a VOC. Shape measurements show the compounds to be nearer to a *VOC*-5 geometry than to an sqp one (lower CShM values for *VOC*-5 compared to *SPY*-5, see Table 2.4) as should be expected for a ls-d^6 configuration. The clear distortion from an ideal *VOC*-5 geometry might be the result of the strong heteroleptic character of these compounds.

Molecular orbital schemes and the shape of the orbitals involved in the respective bonding, allow the estimation of the preferred subsitution sites for acceptors and donors in both geometries.

First, the trigonal bipyramid will be examined. In the case of d^0, the axial bonds are weaker. This isn't changed for the configurations d^1–d^4 since the d_{xz} and d_{yz} molecular orbitals are pure metal d. Filling of the M-L_{eq} antibonding orbitals $d_{x^2-y^2}$ and d_{xy} (d^5-d^8) will lead to weaker bonds in the equatorial base and at d^8 the axial bonds are clearly stronger. Filling of the M-L_{ax} antibonding orbital d_{z^2} will lead to stronger equatorial bonds (see Fig. 3.4 upper row, left side). Corresponding considerations for the square pyramid lead to the right side of Fig. 3.4.

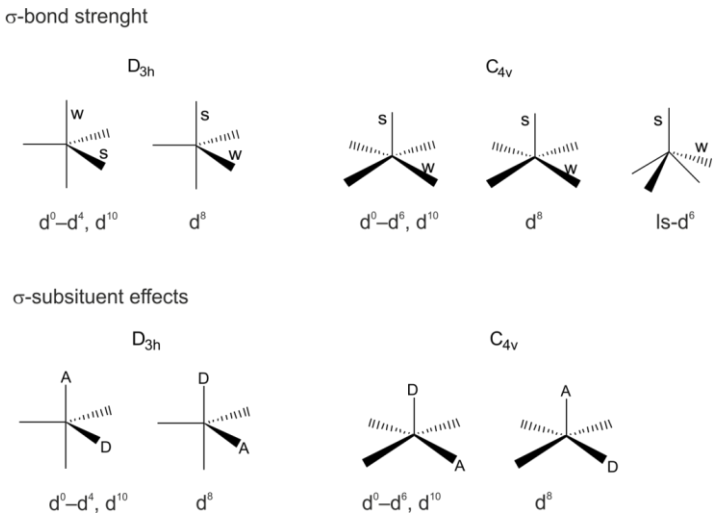

Fig. 3.4: σ-bond strengths and σ-substituent effects in tbp (D_{3h}) and sqp (C_{4v}), w = weaker, s = stronger, A = acceptor, D = donor. Redrawn from Ref. [138].

To estimate which position will be occupied by a σ-donor or σ-acceptor, the electron density along the respective M-L bond has to be considered. Acceptors will favour sites with electron excess, donors will favour sites with electron deficiency. This leads to the scheme depicted in Fig. 3.4 (row below).

π-Substituent effects for the trigonal bipyramid will shortly be analyzed. As can be seen from Fig. 3.5, the axial and the equatorial (parallell to C_3) interactions are identical. Thus, the position of the acceptor or donor will depend on the contribution of the equatorial interaction perpendicular to C_3 to the total equatorial interaction.

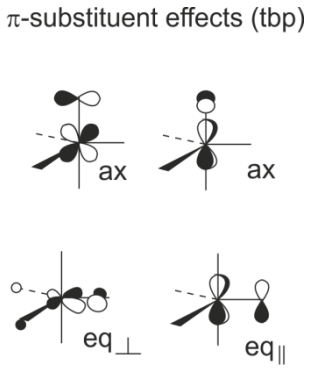

Fig. 3.5: Axial or equatorial substitution in a trigonal bipyramid, ax = axial, eq = equatorial (parallel or perpendicular to the C_3 axis. Redrawn from Ref. [138].

Since the orbital responsible for the equatorial interaction perpendicular to C_3 is hybridised towards the π-ligand, a strong interaction is formed. The equatorial π bond is stronger than the axial. π-acceptor ligands thus prefer equatorial sites over axial sites in a trigonal bipyramid. If coligands are also π-substituents, an ordering, obtained from experimental data, allows the estimation of which π-substituent will occupy the base:

$$NO^+ > CO > CN^- > Cl^- > PR_3 > CH_3^-$$

These theoretical and experimental considerations are consistent with the ligand-occupied sites in the compounds, adopting tbp structure. The strong σ-bonding phosphanes are *trans*-axial, the π-donating halogenido ligand and the nitrosyl ligands occupy the equatorial positions.

π-Substituent effects for the square pyramid will shortly be analyzed. A schematic representation for the relevant interactions is depicted in Fig. 3.6.

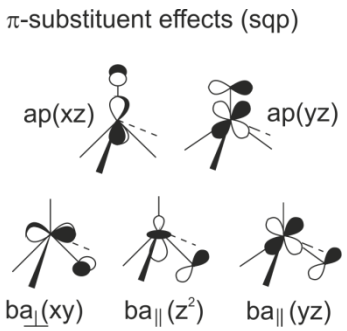

Fig. 3.6: Axial or equatorial substitution in a square pyramid, ap = apical, ba = basal (parallel or pependicular to the C_4 axis). Redrawn from Ref. [138].

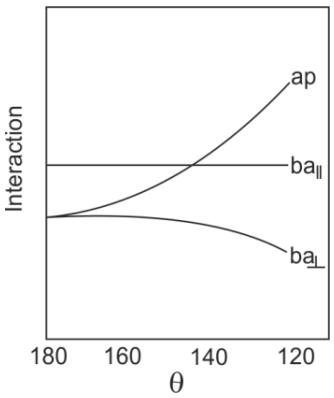

Fig. 3.7: Schematic representation of the degree of interaction between donor or acceptor orbitals and the framework molecular orbitals of a square pyramid as a function of the bending angle θ. Adapted from Ref. [138].

The magnitude of the interaction of the ligand π-orbitals with the metal d-orbitals depends on θ. At a θ value of 180° the degree of interaction is identical for the apical substitution and two of the basal substitutions (xy and yz). With decreasing θ value the apical substitution will gain in interaction whereas the overlap for the basal substitutions d_{xy} and d_{yz} will decrease. The interaction for the basal substitution d_{z^2} will increase in its overlap. The netto interaction for the basal substitution parallel to C_4 is approximately constant over θ. The reason for this is that one of these interactions decreases with decreasing θ, whereas the other increases with the same value. Fig. 3.7 shows the net interactions. For cylindrically symmetrical π acceptors and a θ value of 180°, the best interaction is found for basal substitution. At θ values lower than 145° apical substitution is favoured.

The way in which the sites in the tbp and sqp structures of the dinitrosyls of this work are occupied by the ligands corresponds relatively well to the predictions, made from the rules above.

In the sqp structure the good π-accepting NO^+ ligand is found in the base of the pyramid. The most electronegative element (Cl^-) is also found in the base, *trans* to the nitrosyl. The good σ-donor NO^- is at the apex of the pyramid and the bulky phosphanes are *trans* arranged, minimizing steric repulsion.

More detailed considerations and MO-based analysis on bond strengths and site preferences can be found in R. Hoffmann *et al.*, Ref. [138].

3.4.2 The $\{Ru(NO)_2\}^8$ moiety in the context of MO theory

In their review article from 1974 Enemark and Feltham tried a qualitative MO theoretical approach for the understanding of spectroscopic and X-ray crystallographic findings in relation to metal nitrosyls.[44] They regarded the MNO unity as a highly covalent entity and used Walsh's rules for triatomic species to deduce MO schemes for mono- and polynitrosyls, using not only symmetry and overlap criteria but also experimental data. The MO diagram for a hypothetic linear $\{M(NO)_2\}^x$ species is shown in Fig. 3.8.

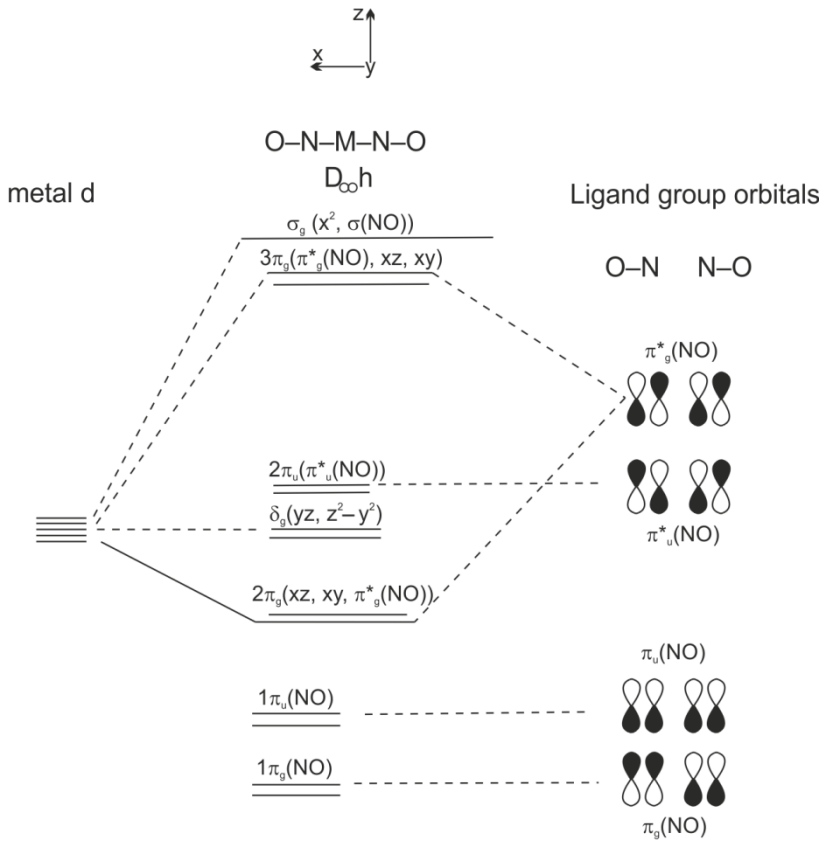

Fig. 3.8: Proposed molecular orbital scheme for a linear $M(NO)_2$ group. In this figure and in all subsequent figures z is defined as the bisector of the N–M–N angle. The metal d orbitals were obtained from the conventional d orbitals by the transformation x → z, y → y, z → x. There is a second set of ligand group orbitals not shown, which are parallel to the y axis. Redrawn from Ref. [44].

Upon the bending of the M–N–M angle, the orbital scheme is changed according to the highest symmetry possible, C_{2v}. Fig. 3.9 depicts the correlation diagram relating the molecular orbitals for a linear $M(NO)_2$ group with a bent $M(NO)_2$ group. Bending of the N–M–N angle will lead to a constructive interaction of the formerly non-bonding d_{yz} and $d_{z^2-y^2}$ orbitals with the formerly non-bonding $\pi^*_u(NO)$ orbitals. Whereas these orbitals are energetically stabilised with a decreasing N–M–N angle, the bonding interaction of the $2\pi_g$ orbitals is weakened and the respective orbitals are destabilised. If the angle reaches 90° the d_{xz} orbital and one of the π^*_g (NO) orbitals become non-bonding (shown in Fig. 3.9, right). Thus, the bending will lead from two bonding interactions in $D_{\infty h}$

($2\pi_g$) to three bonding interactions in C_{2v}: the ligand group orbitals π^*a_1 and π^*b_2 are derived from non-bonding orbitals of $D_{\infty h}$ and are bonding in C_{2v}. π^*a_2 is bonding in both symmetries and π^*b_1 is non-bonding in C_{2v} and is derived from a bonding orbital of $D_{\infty h.}$ Thus, diminishing of the angle in the xz plane will stabilise the π^*a_1 and π^*b_2 orbital and destabilise the π^*b_1 and π^*a_2 orbital. The M–N–O angle can y deviate slightly from linearity due to the fact that the π^*a_1 and π^*b_2 orbitals (which are both bonding with respect to the two N and the two O atoms of the nitrosyl ligands) can give rise to an additional interaction (shown in Fig. 3.9, right).

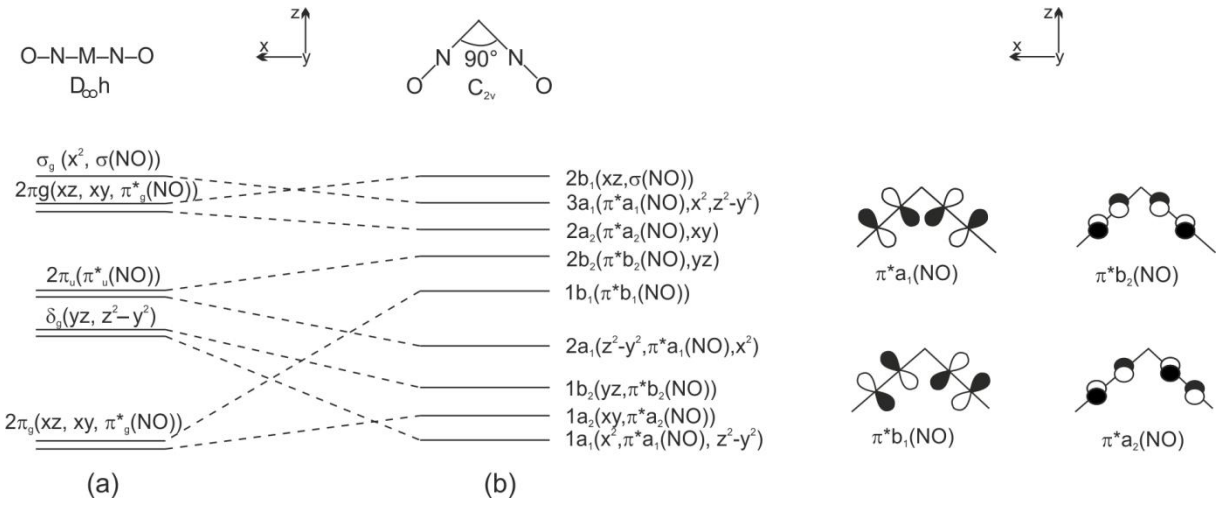

Fig. 3.9: Left: Correlation diagram relating the molecular orbitals for a linear $M(NO)_2$ group (a) with a bent $M(NO)_2$ group (b). The metal d orbitals are those of Fig. 3.18. Right: The ligand group orbitals in C_{2v} symmetry derived from the π^* orbitals of the two NO ligands. Adapted from Ref. [44].

A hypothetical $\{M(NO)_2\}^4$ complex has two bonding interactions for M–N in both geometries, but a linear arrangement will minimise steric repulsion of the two NO ligands. The complex will therefore adopt $D_{\infty h}$ symmetry.

A hypothetical $\{M(NO)_2\}^6$ complex has two bonding interactions for M–N and one non bonding in $D_{\infty h}$, but three bonding interactions in C_{2v}. The complex will thus adopt C_{2v} symmetry.

A hypothetical $\{M(NO)_2\}^8$ complex will adopt $D_{\infty h}$ symmetry if the $2\pi_u$ level is energetically much higher than the δ_g level. In this case, decreasing the angle would not lead to a sufficient interaction of δ_g and $2\pi_u$ to compensate the repulsion of the two nitrosyl ligands. In the normal case, $\{M(NO)_2\}^8$ complexes adopt C_{2v} symmetry. Fig. 3.10 shows the possible structures of a C_{2v}-symmetrical $M(NO)_2L_2X$ complex.

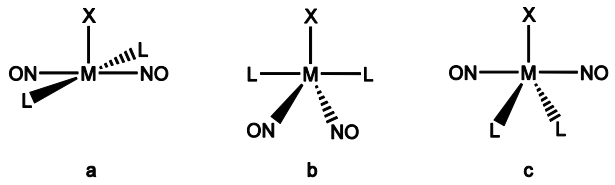

Fig. 3.10: The possible structures for an $M(NO)_2L_2X$ complex possessing C_{2v} symmetry. Adapted from Ref. [44].

It has now been shown qualitatively, that $\{Ru(NO)_2\}^8$ complexes will favour a *cis*-NO-geometry. The only structure which meets this restriction, and is C_{2v} symmetrical, is structure b.

This structure can be subjected to two possible modifications, depending on the energetic ordering of the $1b_1$ and the $2b_1$ orbital (see Fig. 3.11, below).

Since the $2a_1$ orbital is strongly σ anti bonding (y-axis corresponds to the C_3 axis), filling of the orbitals of Fig. 3.9(b) with eight electrons will lead to the electron configuration $(1a_2)^2\ (1a_1)^2\ (1b_2)^2\ (1b_1)^2$.

Thus, only the energetic ordering of the $1b_1$ (HOMO in Fig. 3.9 (b)) and $2b_1$ (LUMO in Fig. 3.9 (b)) orbital is relevant.

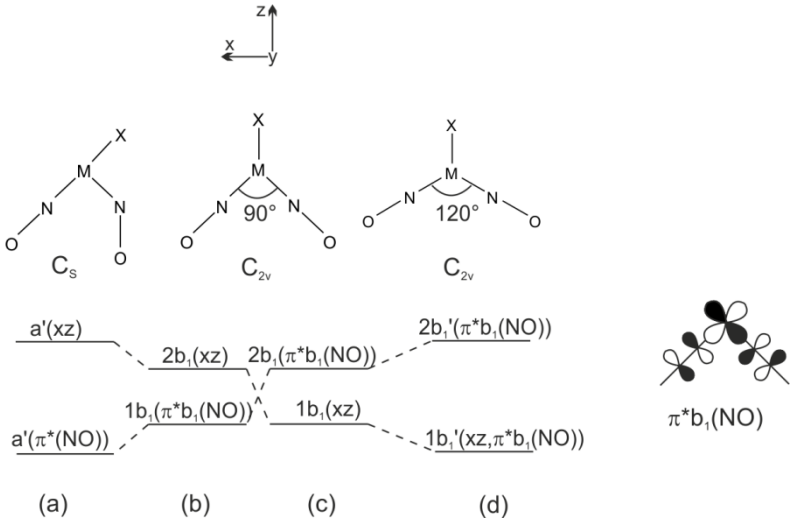

Fig. 3.11: Left: Correlation diagram showing the proposed behaviour of the $1b_1$ and $2b_1$ molecular orbitals in five-coordinate $\{M(NO)_2\}^8$ complexes with a $(1b_1)^2$ electron configuration. Scheme (b) has π^*b_1(NO) lower in energy than d_{xz} and leads to structure (a). Scheme (c) has d_{xz} lower in energy than π^*b_1(NO) and leads to (d). Adapted from Ref. [44]. Right: The relevant orbital (xz, π*b1(NO)) which is non bonding at an N–M–N angle of 90° since the lobs of the metal d_{xz} orbital points towards the nods of the π*(NO) orbitals.

If $1b_1$ is lower in energy than $2b_1$, two electrons will occupy a non bonding orbital of π*(NO) character, corresponding to a localisation of the two electrons as the lone pair of the nitrogen atom of an $^1NO^-$ ligand (which can be seen in the electron density maps, see Fig. 2.54 in RESULTS, chapter 2.11).

Concomitant with the transfer from (b) to (a), the coligand X is moved in such a way as to stabilise the d_{xz} orbital. The transformation from (b) to (a) is followed by symmetry reduction from C_{2v} to C_s, making the two nitrosyl ligands unequivalent.

If, on the contrary, $2b_1$ is lower in energy than $1b_1$, two electrons will occupy a non-bonding orbital of metal d character. An increasing N–M–N angle will make the non-bonding orbital weakly bonding. The N–M–N angle is thus expanded from 90° to 120°. This leads to an interaction of the d_{xz} orbital with the π^*b_1(NO) orbital. The symmetry remains C_{2v}, thus the nitrosyl ligands are still equivalent.

The linear MNO angles in C_s and C_{2v} might, for some degree, deviate from linearity since the occupied molecular orbitals $1a_1$ and $1b_2$, derived from the ligand group orbitals π^*a_1(NO) and π^*b_2(NO), are bonding with respect to the two N atoms and the two O atoms.

Enemark and Feltham predicted that structure (d) "would be favoured by the presence of good π-accepting ligands and by first-row transitions metals."[44]

Those compounds which adopt structure (d) are neither complexes of a first row transition metal nor of good π-accepting ligands.

Structure (a) is found for all the sqp structures, the average of the N–M–N angle is 103.8°. Structure (d) is found for all the tbp structures, and, indeed, the N–M–N angle is on average 117.4°.

The two conformers of compound **25b** were subjected to DFT-based calculations and the frontier orbitals were examined. All the orbitals of the frontier range (except for one orbital) describe metal to nitrosyl interactions. Fig. 3.12 shows selected frontier orbitals from these calculations for the C_{2v} (tbp/*TBPY*-5) and the C_s (sqp/*VOC*-5) conformer.

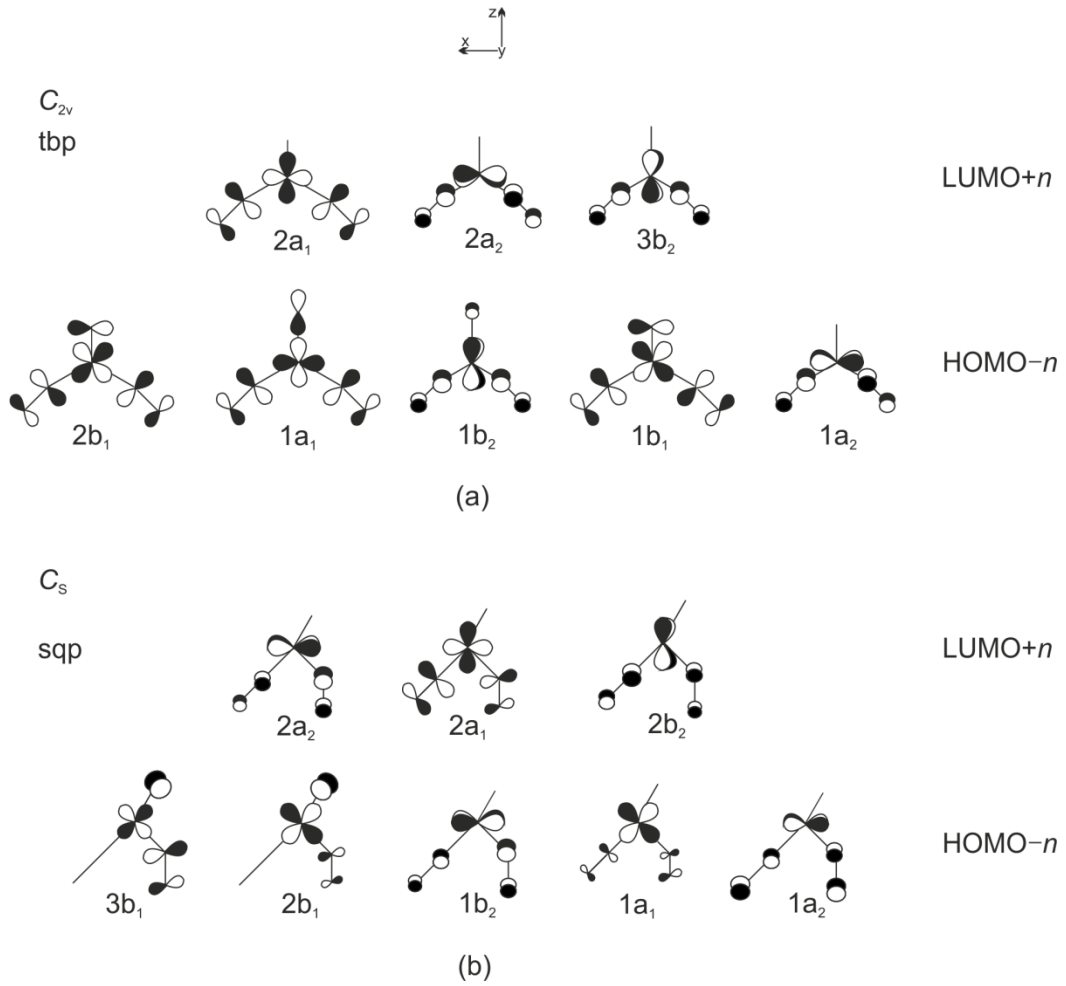

Fig. 3.12: Schematic representation of selected frontier orbitals for the C_{2v} (tbp) and the C_s (sqp) conformer calculated by a DFT-based method (BP/tzvp).

First, C_{2v} symmetry will be analyzed.

In the LUMO range, the kind of orbitals as well as their energetic order is consistent with the predictions made by Enemark and Feltham. In the bonding range the energetic order is a little bit different. The HOMO orbital has halide and d_{yz} character (not depicted in Fig. 3.12). The HOMO−1 is $2b_1$ in Fig. 3.12 (which is the highest M–NO orbital by Enemark and Feltham). Calculations show that this HOMO−1 orbital is comprised of the metal d_{xz} orbital and the π^*b_1(NO) group orbital with both nitrosyl ligands making the same contribution. Additionally, an anti-bonding metal to X interaction is

found for this orbital. Maybe, this interaction moves the d_{xz} orbital a little bit higher in energy so as to interact better with the energetically similar π^*b_1(NO) orbital. All the orbitals describing an M–NO interaction in the HOMO-range show equal contributions from the two nitrosyl ligands. The $1b_1$ orbital has, additionally, a bonding interaction with one of the π-orbitals of the co-ligand X, which stabilises this orbital.

In C_S symmetry the frontier orbitals look clearly different. For both the LUMO and the HOMO range, the kind of orbitals is consistent with the predictions made by Enemark and Feltham, only their energetic order is a bit different. In the LUMO range as well as in the HOMO range the contribution of the two nitrosyl ligands to the interactions with the metal displayed in the orbitals are obviously different. The HOMO orbital consists only of an interaction between the metal and the bent nitrosyl ligand where the contribution from the ligand is greater than from the metal, thus, the orbital has mainly NO^- character. The HOMO−1 orbital consists only of an interaction between the metal and the X atom with a small contribution from the bent nitrosyl ligand. In the third orbital of the b_n-kind the greater contribution to the nitrosyl-metal interaction is made by the nitroxyl ligand and a smaller contribution is found for the linear nitrosyl ligand. The bonding situation of the two nitrosyls is clearly unequal and suggests an interpretation of the bent nitrosyl ligand as $^1NO^-$ (nitroxyl) and of the linear nitrosyl ligand as NO^+ (nitrosonium).

In general, the tbp structures are found for X = Br, I, whereas the sqp structures are found for X = Cl. Consistent with this observation are the affected orbitals: the HOMO orbital in tbp is a bonding orbital, localised on the metal and in equal parts on the two nitrosyl ligands. There is a secondary interaction with the halide. Thus, the tbp structures will be favoured in the case of a strong π-donating ligand (Br, I), which will pass electron density towards the ruthenium centre and stabilise the $1b_1$ orbital. The increased electron density will strengthen the Ru–N π backdonation, giving rise to two nearly linearly coordinated NO^+ ligands. It can thus be concluded, that the tbp structures are derived from a Ru d^8 system with two nearly linear nitrosonium ligands.

The HOMO and HOMO−1 orbitals in sqp are very weakly or nonbonding orbitals with respect to the bent-NO-metal interaction, localised primarily on the N atom of the bent NO ligand and have weak contributions from the metal d_{xz}. There are relatively strong contributions from the ligand X and no contributions from the linear nitrosyl. Chlorine, which is found in the compounds adopting an sqp structure, is a weak π-base and can thus donate electron density towards the ruthenium centre not as well as bromine or iodine. Hence, strong π backdonation is only found for one Ru–N interaction: The sqp structures are derived from a ruthenium d^6 system with one nitrosonium (NO^+, strong π backdonation) and one nitroxyl ligand ($^1NO^-$ weak π backdonation).

The Lewis formalism for the described situation is depicted in Fig. 3.13.

For some compounds, sqp and tbp structures are found. Thus, it has to be assumed that the structure is primarily determined by halide X and, secondarily, by the phosphane PR_3.

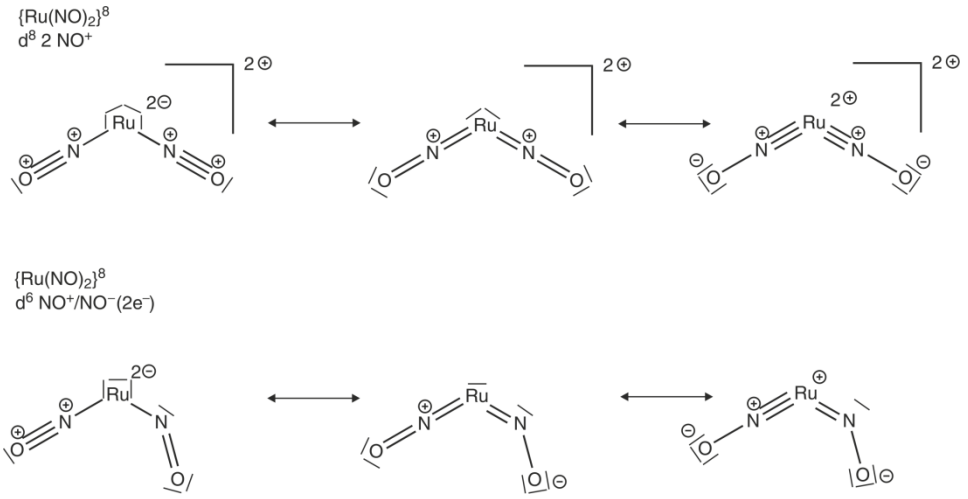

Fig. 3.13: Description of the bonding situation in the $\{Ru(NO)_2\}$ moiety in tbp/*TBPY*-5 (upper row) and sqp/*VOC*-5 (lower row) with application of the Lewis formalism.

3.5 Investigations of PLI behaviour by low-temperature IR spectroscopy and photocrystallography

*$[RuCl(NO)_2(PPh_3)_2]BF_4$ (**6b**)*

The low-temperature infrared spectrum of photo-irradiated crystals of **6b** showed two novel bands in the *v*(NO) range compared to the spectrum recorded under normal conditions, which were shifted by +6 and −34 cm^{-1} relative to the frequencies of the symmetric and asymmetric ground state stretching vibrations. The asymmetrically coupled stretching vibration is primarily dominated by the bent NO ligand. Since the frequency of this mode was more strongly shifted, it could be expected that the bent NO ligand is the nitrosyl group which is more affected by irradiation and is more "PLI-active".

This assumption is supported by the photo-difference map which showed that the bent NO ligand was most strongly affected by the structural reorganisations following photo-conversion: the angle with which the nitrosyl ligand is attached to the ruthenium centre was changed from 135° to 109° with a simultaneous transformation from a *syn* to an *anti* arrangement (see Fig. 3.14).

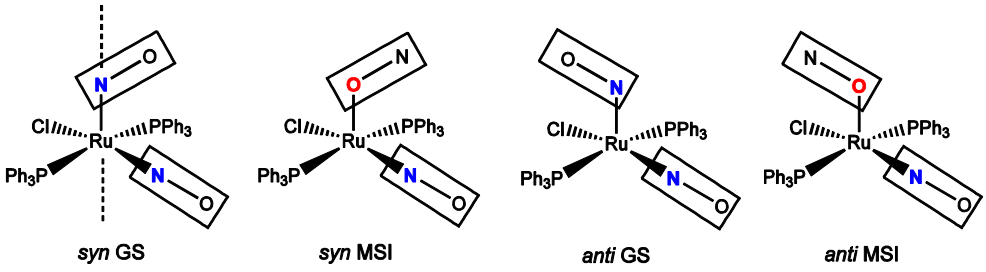

Fig. 3.14: Schematic representation of the various isomers of which the photo-irradiated state can be composed. The terms *anti* and *syn* refer to the orientation of the two nitrosyl groups towards a hypothetical axis, which is orthogonal to the square plane of the square pyramid.

Since the structural change would lead to an altered distribution of the electron density and the stretching modes are vibrationally coupled, the frequency of the symmetrical stretching mode, dominated by the linearly coordinated nitrosyl ligand, was also shifted (+6 cm^{-1}).

Whether the structural reorganisation of the bent nitrosyl group leads to an *anti*-GS state or a *syn*-MSI state cannot be determined unambiguously from the photocrystallographic experiment, since the corresponding agreement values (*R*, *wR*) were identical and the alteration in the distribution of the electron density is not as easy to interpret as would be the case if a MSII isomer were formed.

As the photo-difference map also elucidated, there were no significant changes on the linear nitrosyl ligand upon irradiation. From this, it could be concluded that the linear NO ligand is either not subjected to a PLI effect or the population reached was so low as not to be detectable by X-ray crystallography. A possible mechanism for the structural interconversion from a nitrosyl ground state to an isonitrosyl metastable state is shown in Fig. 3.15.

Table 3.1 summarises the observed PLI effects for compounds **6b**, **7b**, **9b**, **14b**, **18b** and **25b**.

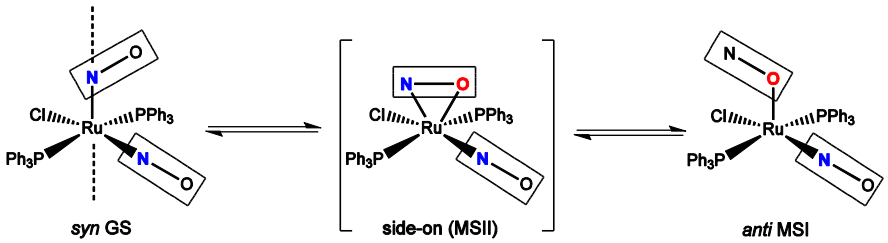

Fig. 3.15: Possible mechanism for the generation of an *anti*-MSI state from a *syn*-GS state *via* a side-on state (MS II).

Table 3.1 Degree of population of the metastable state (from IR data) and frequencies in the *v*(NO) range of the PLI-active compounds in their ground and photo-irradiated state.

Compound	*v*(NO) / cm^{-1} (GS)	*v*(NO) / cm^{-1} (MS)	$\Delta v(NO)_{MS-GS}$ / cm^{-1}	λ / nm excitation/erasure	% MS
6b	1866 / 1687	1872 / 1653	+6 / −34	405 / 660	60%
		1808 / 1774	−58 /+87	405 / 980	4–5%
7b	1756 / 1787 / 1834	1872 / 1654	+38 / −133/102[a]	442 / 660	10%
9b	1821 / 1785	1821 / 1671	0 / −114	442 / 660	6–7%
14b	1870 / 1832 / 1777 / 1752	1832 / 1641	0 / −136/111[b]	405 / –	–
18b	1798 / 1760 / 1710	1762 / 1650	−36 / −60	405 / –	29%
25b	1806 / 1694	1821 / 1649	+15 / −45	405 / 660	70%

[a] −133 with regard to the ground-state band of the asymmetrical stretching mode at 1787 and −102 with regard to the ground-state band of the asymmetrical stretching mode at 1756. [b] −136 with regard to the ground-state band of the asymmetric stretching mode at 1777 and −111 with regard to the ground-state band of the asymmetrical stretching mode at 1752.

Similar photo-signatures (absolute value and direction of the shifts, wavelength for generation and erasure of the metastable state) and a good photo-excitability (high degree of population) were found for the sqp shaped compounds **6b**, **18b** and **25b-2**. Bearing in mind the results of the photocrystallographic experiments on **6b**, the metastable state in these three compounds is most probably an *anti*-GS or an *anti*-MS (isonitrosyl) species with a highly irradiation-affected bent nitrosyl and an almost unaffected linear nitrosyl. PLI experiments also revealed that the tbp conformer in **25b** was not affected by photo-irradiation and showed no PLI.

Compounds **7b**, **9b** and **14b**, which adopt intermediate or tbp structure, show a similar photo-signature as the MSI state in $\{RuNO\}^6$ compounds. Thus, they can most probably be regarded as isonitrosyl states of the linear NO.

Compound **6b** has two distinct photo-induced states, one which was investigated by X-ray crystallography and one which has no clear X-ray signature. The shifts are either −58 and +87 or −92 and +121 cm^{-1}, depending on which symmetrical and asymmetrical modes are compared and used for the calculation of the difference (shift). The photo-signature suggests the generation of an isonitrosyl state of the linear NO group.

The results, gained from PLI experiments, could support the assumption, that in the case of $\{Ru(NO)_2\}^8$ compound possessing a bent nitrosyl with a weaker metal to ligand backdonation, a high degree of photoexcitability of this NO group is possible. In the case of the symmetrical tbp structures, a light-induced state with low photoexcitability corresponding to the isonitrosyls of the $\{RuNO\}^6$ compounds can be expected, which possess a linearly attached NO group.

Unfortunately, comparative data for the PLI behaviour of $\{Ru(NO)_2\}^8$ compounds with a bent nitrosyl ligand are missing in literature. Two examples of $\{PtNO\}^8$ complexes owning a bent NO ligand and showing PLI can be found in literature.[140] Both compounds can be transferred to the MSI state by irradiation with light of the red spectral range. The photo-isomerisation process is very fast since the photo-conversion is a one step process, leaving out the MSII state. The *ν*(NO) frequencies are shifted into the higher-energy range by 71 and 100 cm^{-1}, respectively. The only dinitrosyl tested for PLI, so far, is the compound $[Fe(NO)_2(CO)_2]$.[141] This $\{FeNO\}^{10}$ compound possesses two identical NO ligands. Irradiation with light of the appropriate wave length leads to shifts of the symmetrical and asymmetrical ν(NO) vibration of −30 cm^{-1}. Due to the fact that photocrystallographic data for this system are missing, the nature of the photo-irradiated state is, so far, unknown.

The shifts for **6b**, **18b** and **25b** are comparable to the one found in $[Fe(CO)_2(NO)_2]$. Thus, the photo-irradiated state might be the same. The shifts found for the second photo-irradiated state of **6b** are similar to those found in the two platinum complexes. Since all three compounds have a bent NO ligand and a similar magnitude of the *ν*(NO) shift, it is imaginable that the photo-irradiated states are the same. Nevertheless, it should be mentioned, that the photo-signature is not identical since the platinum compounds show PLI in the red spectral range whereas the second photo-irradiated state in **6b** is generated by laser light of the blue spectral range.

In this context, the PLI data of compound **6b** suggest that the various isomers, shown in Fig. 3.14, might all exist at the same time, making the data from photo-crystallographic experiments very hard to interpret.

4 Summary

Up to now there have been only qualitative, hypothetical considerations about the structure of $S = 0$ $\{Ru(NO)_2\}^8$ compounds of the general formula $[RuX(NO)_2L_2]^+$ with X = Br, I. This is the first report on the synthesis and characterisation of such compounds (and corresponding ones with X = Cl) together with their photoexcitability. Twenty novel compounds of the $S = 0$ $\{Ru(NO)_2\}^8$ type were synthesised by a slightly modified combination of the procedures adopted from Townsend *et al.*[142] and Ibers *et al.*[143]

The second step, the substitution of X by phosphane ligands PR_3, the reaction took either place as a simple ligand substitution (**6a**–**13a**), yielding the respective $\{RuNO\}^6$ compounds, or as both a substitution and a redox reaction (**14a**–**26a**), yielding the respective $\{RuNO\}^n$ product mixtures with n = 6, 7, 8. These $\{RuNO\}^n$ mixtures were reduced to the respective $\{RuNO\}^8$ compound as completely as possible using a zinc-copper alloy. The reduction is a necessary condition for an oxidative nitrosylation in the next step in order to finally gain both a linear (NO^+) and a bent NO (NO^-) ligand.

The reaction of $[RuI(NO)(P^iPr_3)_2]$ with $NOBF_4$ took place not only by an oxidative addition reaction, resulting in the desired dinitrosyl, but also took place in a reductive coupling of two equivalents of the nitrosyl precursor, resulting in $[\{Ru(NO)_2(P^iPr_3)\}_2(\mu\text{-}I)]BF_4$, a dinuclear DNIC-analogue $\{Ru(NO)_2\}^9$–$\{Ru(NO)_2\}^9$ species. Fourteen of the twenty dinitrosyls of the general formula $[RuX(NO)_2(PR_3)_2]BF_4$ (X = Cl, Br, I; PR_3 = PPh_3, PPh_2Bn, PBn_3, P^tBuPh_2, P(*p*-tolyl)$_3$, P(*p*-anisyl)$_3$, PCy_3, $PCyp_3$, P^iPr_3), synthesised in this work, could be characterised by single-crystal X-ray diffraction. Two dinitrosyls (**21b**, **25b**) crystallised in two different conformations, denominated as **xb-1** and **xb-2** (for an overview of the adopted conformers see Fig. 4.1).

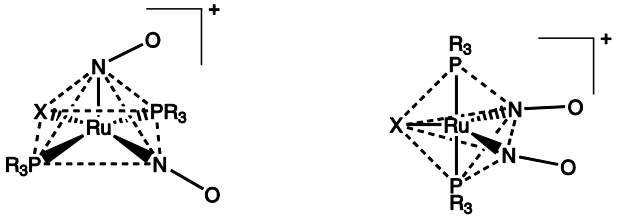

sqp, VOC

	PR_3/X
6b	PPh_3/Cl
18b	PCy_3/Cl
19b	PCy_3/Br
21b-1	$PCyp_3$/Cl
24b	P^iPr_3/Cl
25b-1	P^iPr_3/Br

tbp, TBPY

	PR_3/X
9b	PPh_2Bn/Cl
10b	PPh_2Bn/Br
20b	PCy_3/I
21b-2	$PCyp_3$/Cl
22b	$PCyp_3$/Br
23b	$PCyp_3$/I
25b-2	P^iPr_3/Br

Fig. 4.1: Overview of the structures, adopted by $S = 0$ $\{Ru(NO)_2\}^8$ compounds of the general formula $[RuX(NO)_2(PR_3)_2]BF_4$. Compounds **7b**, **14b** and **15b** cannot be assigned to one of these ideal geometries, since the τ_5-values are within 0.40–0.60. Compounds **11b**–**13b** and **16b**–**17b** are not enlisted, since attempts of an X-ray spectroscopic characterisation failed. Compound **26b** is not enlisted since X is not clearly determinable as iodine.

X-ray studies of the dinitrosyls revealed that they adopt two different structures (see Fig. 4.1): one which is already known for $\{Ru(NO)_2\}^8$ compounds, and one which has, so far, been unknown for these types of compounds. The known structure can be described as sqp or *VOC*-5 and shows two clearly distinct bonding modes for the two NO ligands, indicating that a formal NO^+ and a formal NO^- ligand are coordinated (maximum symmetry is C_s). The bent nitrosyl forms the apex of the square pyramid, the bulky phosphanes are *trans*-arranged and comprise the base together with the also *trans*-arranged halogenido and the linear nitrosyl ligand. The bent nitrosyl ligand is inclined to the linear nitrosyl ligand. The second part of the compounds shows an alternative, unexpected arrangement in which the two NO groups seem to adopt equal bonding situations and the structure is changed to a trigonal bipyramid (tbp or *TBPY*-5). Identical structural parameters for the RuNO moiety as well as the equivalence of the positions of the NO ligands within the tbp structure enable the complex cation to reach C_{2v}-symmetry. The phosphanes occupy *trans*-axial positions, both nitrosyl ligands and the halogenido ligand are found in the equatorial positions. The nitrosyl ligands, themselves, are slightly bent (13.5° on average) in a *cisoid* fashion. This structure, predicted in a review article by Enemark and Feltham (see Ref. 44) for five-coordinated $\{M(NO)_2\}^8$ compounds of third-row transitions metals and good π-accepting ligands X, is known for M = Re, Mn and X = Cl, CO.
The geometries and the adjustment of the ligands within the respective geometries, found in the crystal structures, are consistent with crystal-field theoretical considerations and derived site preferences.[140]
Compounds **7b**, **14b** and **15b** adopt an intermediate structure.
To exclude that the RuNO angles of ca. 165° in the tbp structures arise as a temporal or spatial superposition of a linear and a bent NO ligand (see Fig. 2.31 and Fig. 2.32 in RESULTS, chapter 2.7.2), investigations on the temperature dependency of the atomic displacement parameters, IR studies in the dissolved state and comparative quantum chemical calculations were performed (see Table 4.2). It was shown that this unexpected structure of $\{Ru(NO)_2\}^8$ compounds is not the result of a dynamic process or the disorder of the two oxygen atoms of the NO groups, but is caused primarily by the nature of X, and, secondarily, by the substituent R on the phosphane group (see Table 2.6, DISCUSSION, chapter 2.8).
The structures were characterised by means of continuous shape measures and τ_5-value analysis and were additionally compared to predictions derived from calculations based on density functional theory. The same compound-specific structure was obtained from measurement and calculation.
Orbital analyses of the frontier orbitals of the two conformers of **25b**, calculated with DFT methods, were compared to the predictions made by Enemark and Feltham for sqp- and tbp-shaped $\{Ru(NO)_2\}^8$ compounds of the general formula $[RuX(NO)_2(PR_3)_2]^+$. Although tbp-shaped compounds of this type were not known at this time, and the predictions were, thus, based only on symmetry and overlap criteria, the energetic order as well as the type of orbitals involved are, to a great deal, consistent to the DFT derived ones for both sqp and tbp structures. There is one interaction in the frontier orbital range which explains why the predictions made by Enemark and Feltham, that tbp structures should "be favoured by the presence of good π-accepting ligands and by first row transitions metals", are not prooved by the experimental findings but have to be refuted. The mentioned interaction is

described by two orbitals of metal d_{xz} type. The first orbital is composed of a bonding interaction between the nitrosyl ligands and the d_{xz} orbital and an antibonding interaction of π character between the p orbital of the halogenido ligand X and the metal. The second orbital possesses the same type of interactions between the metal and the nitrosly ligands but a bonding interaction between the metal and X. This interaction is responsible for an increasing electron density on the metal and is thus strengthening the π backdonation to the nitrosyls which turns out the stronger, the better the π basicity of the ligand X is. Thus, these C_{2v} symmetrical structures are only found for X = Br, I. The strong π backdonation leads to two nearly linearly coordinated NO groups. Compounds of this type can, therefore, be regarded as derivatives of Ru d^8 coordinating to two nitrosonium (NO^+) ligands ($\{Ru^0/NO^+/NO^+\}^8$). The slight deviation from linearity can be explained by the presence of two filled orbitals whose bonding interaction with respect to the two nitrogen and the two oxygen atoms is increased upon bending.

In the case of X = Cl, the π basicity is not high enough to stabilise two NO^+ ligands and the coordination mode of one nitrosyl ligand is changed to a bent coordination, which corresponds to a coordinated nitroxyl (NO^-) ligand. Concomitant to a change in the coordination mode is the reduction in symmetry from C_{2v} to C_s. These, in the ideal case, C_s-symmetrical compounds can be regarded as derivatives of Ru d^6 coordinating to one nitrosonium (NO^+) and one nitroxyl (NO^-) ligand ($\{Ru^{II}/NO^+/^1NO^-\}^8$). Compounds of this structure are not only found when X = Cl but, in a few cases, also when X = Br. Thus, the adopted structure is dominated primarily by the halide and, secondarily, by the substituent R of the phosphane.

The dinitrosyls of the general formula $[RuX(NO)_2(PR_3)_2]BF_4$ were further characterised by various spectroscopic analyses (NMR, IR, see Fig. 2.8 and Table 4.1), mass spectrometry (see Fig. 2.7 and Table 4.1) as well as elemental analysis. All IR spectra showed one band which is higher in energy for the symmetrically coupled stretching vibration of the nitrosyl ligands and one which is lower in energy for the asymmetrically coupled stretching vibration (see Fig. 2.8). As mentioned above, part of the compounds possess one linearly and one bently coordinated NO group and exhibit a vacant octahedral structure, known from literature. Animations of the calculated *ν*(NO) vibrations revealed that the symmetrically coupled vibration is dominated by the linearly coordinated nitrosyl, the asymmetrically coupled vibration by the nitrosyl ligand coordinated in a bent way. The magnitude of the vibrational coupling is lower than in the tbp structures. Animations of the calculated *ν*(NO) vibrations of compounds of this structure revealed that the symmetrically coupled and the asymmetrically coupled vibration are dominated in equal parts by the two NO ligands. The magnitude of the vibrational coupling is higher than in the sqp structures.

All mass spectra showed the $[M]^+$ and $[M - NO]^+$ peak (see Fig. 2.7), separated by 30 *m/z* (according to the mass of nitric oxide), with the typical Ru_1-isotope pattern.

Table 4.2 gives an overview of the DFT-based characterisation of the $\{Ru(NO)_2\}^8$ compounds and comparison with the experimental results.

Table 4.1: Overview of the analytic characterisation of the $\{Ru(NO)_2\}^8$ compounds and of the $\{RuNO\}^9$–$\{RuNO\}^9$ dimer.

number	**PR_3/X** $[RuX(NO)_2(PR_3)_2]^+$	**X-ray** Ru–N1–O1 / °, Ru–N2–O2 / °	**IR** (solid) $\nu(NO)_{sym}$ / cm^{-1}, $\nu(NO)_{asym}$ / cm^{-1}	**IR** (DCM) $\nu(NO)_{sym}$ / cm^{-1}, $\nu(NO)_{asym}$ / cm^{-1}	**MS** $[M]$ / $m\,z^{-1}$, $[M–NO]^+$ / $m\,z^{-1}$	**NMR** $\delta(^{31}P)$ / ppm	τ_5 $(\alpha-\beta)/60°$
6b*	PPh_3/Cl	178.9, 134.8	1842, 1685	1823, 1776, 1720	721.0, 691.0	30.8	0.36
7b*	PPh_3/Br	175.3, 143.1	1824, 1765	1813, 1778	765.1, 735.1	27.3	0.51
9b*	PPh_2Bn/Cl	167.2, 164.0	1799, 1771	1818, 1776	749.1, 719.1	42.9	0.65
10b*	PPh_2Bn/Br	168.2, 162.8	1817, 1776	1815, 1778	793.0, 763.0	39.4	0.64
11b	PBn_3/Cl	—	1811, 1775	1821, 1783	805.2, 775.1	50.6	—
12b	PBn_3/Br	—	1812, 1776	1822, 1787	851.4, 821.4	45.0	—
13b	P^tBuPh_2/Cl[a]	—	1813, 1714	—	681.2, 651.2	—	—
14b*	P(*p*-tolyl)/Cl	178.0, 151.2	1816, 1766	—	805.2, 775.1	29.8	0.55
15b*	P(*p*-tolyl)/Br	177.8, 156.7	1815, 1776	—	851.2, 821.1	25.9	0.60
16b	P(*p*-anisyl)/Cl	—	1811, 1770	—	901.3, 871.5	28.1	—
17b	P(*p*-anisyl)/Br	—	1809, 1773	—	947.4, 917.4	23.8	—
18b*	PCy_3/Cl	179.9, 136.5	1789, 1704	1812, 1706	758.0, 728.0	51.3	0.15
19b*	PCy_3/Br	178.0, 139.5	1785, 1714	1800, 1760, 1716	804.1, 774.0	50.4	0.19
20b-1*	PCy_3/I	170.7, 156.9	1788, 1751	1797, 1765	849.9, 819.9	45.8	0.79
20b-2*	PCy_3/I	169.9, 163.3	1788, 1751	1797, 1765	849.9, 819.9	45.8	0.78
21b-1*	$PCyp_3$/Cl	176.8, 137.0	1807, 1681	1834, 1797, 1754, 1710	673.2, 643.2	48.2	0.09
21b-2*	$PCyp_3$/Cl[b]	168.1, 164.4	—	—	673.2, 643.2	48.2	0.68
22b*	$PCyp_3$/Br	168.7, 166.6	1810, 1770	1795, 1759	719.8, 689.9	43.7	0.66
23b*	$PCyp_3$/I	168.9, 165.5	1809, 1772	1794, 1759	765.2, 735.2	34.2	0.65
24b*	P^iPr_3/Cl	177.0, 142.0	1808, 1682	1809, 1759, 1714	517.2, 487.2	61.7	0.26
25b-1*	P^iPr_3/Br	177.2, 150.9	1806, 1694	[c]	563.1, 531.1	59.8, 41.9	0.09
25b-2*	P^iPr_3/Br	165.0, 165.0	1794, 1753	1802, 1765	563.1, 531.1	59.8, 41.9	0.69
	Dimer						
26b-2*	P^iPr_3/I	165.8, 169.5, 169.5, 169.0	1781, 1738, 1704	1797, 1756, 1734	770.4, 740.4	80.2	—

*Compounds could be isolated as crystals. [a]**13b** could only be isolated as an oily product, [b]**21b-2** is a minor species, no analytic data, except for X-ray diffraction, [c]In solution, **25b-1** and **26b-1** are quantitatively transformed in **25b-2** and **26b-2**.

Table 4.2: Overview of the DFT-based characterisation of the $\{Ru(NO)_2\}^8$ compounds and comparison with the experimental results.

number	PR_3/X $[RuX(NO)_2(PR_3)_2]^+$	optimisation τ_5 (α-β)/60°	$\Delta\tau_{5calc-exp}$ τ_5 (α-β)/60°	Frequency analysis $\nu(NO)_{sym}$ / cm^{-1}, $\nu(NO)_{asym}$ / cm^{-1}	$\Delta\nu(NO)_{calc-exp}$ $\Delta\nu(NO)_{sym}$ / cm^{-1}, $\Delta\nu(NO)_{asym}$ / cm^{-1}	$\Delta\nu(NO)_{calc-exp}$ $\Delta\nu(NO)_{sym}$ / cm^{-1}, $\Delta\nu(NO)_{asym}$ / cm^{-}
6b*	PPh_3/Cl	0.30	−0.06	1830, 1724	−11, +39	+7, +4
7b*	PPh_3/Br	0.41	−0.10	1819, 1736	−5, −29	+6, −42
9b*	PPh_2Bn/Cl	0.64	−0.01	1811, 1788	+12, +17	−7, +12
10b*	PPh_2Bn/Br	0.68	+0.04	1809, 1787	−8, +11	−6, +9
14b*	P(*p*-tolyl)/Cl	—	—	1797, 1739	−19, −27	—
15b*	P(*p*-tolyl)/Br	—	—	1798, 1763	−17, −13	—
18b*	PCy_3/Cl	0.21	+0.06	1806, 1709	+17, +5	−6, +3
19b*	PCy_3/Br	0.16	−0.03	1899, 1709	+5, −5	0, −7
20b-1*	PCy_3/I	0.76	−0.03	1791, 1768	+3, +17	−6, +3
20b-2*	PCy_3/I	0.76	−0.02	1791, 1768	+3, +17	−6, +3
21b-1*	$PCyp_3$/Cl	0.10	+0.01	1809, 1710	+5, +29	[a]
21b-2*	$PCyp_3$/Cl[b]	0.71	+0.03	1788, 1763	[b]	−9, +7
22b*	$PCyp_3$/Br	0.63	−0.03	1791, 1766	−19, +4	−4, 7
23b*	$PCyp_3$/I	0.68	+0.03	1809, 1783	0, +11	−1,+10
24b*	P^iPr_3/Cl	0.27	+0.01	1815, 1717	+9, +35	+6, +3
25b-1*	P^iPr_3/Br	0.11	+0.02	1809, 1710	+3, +16	[c]
25b-2*	P^iPr_3/Br	0.68	−0.01	1799, 1776	+5, +23	−3, +11

[a] **21b-1** No value given since the configuration of the compound is transformed in solution. [b] No value given since **21b-2** is a minor species. [c] No value given since the configuration of the compound is transformed in solution. Green: Experimental IR values from measurements in dichloromethane. Red: Experimental IR values from measurements in the solid state.

The structures and frequencies predicted from calculations correspond well to the experimentally measured ones (see Table 4.2). The fact that there are two X-ray crystallographically detectable structures for the complex cations of compound **25b** $[RuBr(NO)_2(P^iPr_3)_2]BF_4$ (**25b-1** and **25b-2** crystallised in different crystal habiti) and **21** $[RuCl(NO)_2(PCyp_3)_2]BF_4$ (**21b-1** and **21b-2** crystallised within one crystal), as well as the data from computational calculations and IR spectroscopy of the liquid state (see Table 4.2) indicate that the PES for the transformation from one structure to the other and the concomitant change of bond lengths and angles in the RuNO moiety is very flat. The energetic difference between the tbp (**25b-2**) and the sqp (**25b-1**) structure of compound **25b** is only $\Delta E_{(tbp\text{-}sqp)}$ = 2.74 kJ mol^{-1}. Thus, it is imaginable that the tbp structures are easily interconverted *via* intermediate structures to sqp structures and *vice versa,* maybe following the Berry pathway. Investigations on the photoexcitability of the compounds revealed that those dinitrosyls which possess a strongly bent NO ligand gave rise to a higher degree of population of the metastable state upon photo-irradiation.

The photocrystallography of compound **6b** unambiguously showed that the bent NO ligand was much more strongly affected by the excitation with laser light than the linearly coordinated one. This result was somewhat astonishing, since it was expected that the linear NO ligand would show a PLI behaviour comparable to that of PLI-active $\{RuNO\}^6$ compounds, which are well characterised with regard to PLI. This might suggest that a sufficient „activation“ of the NO ligand is necessary to evoke this effect. This „activation“ is reflected in the strength of the Ru–N bond, since this bond has to be cleaved to generate the MS1 or MS2 state. As the bent NO ligand can formally be interpreted as a NO^- ligand (a weaker π acid than NO or NO^+), the π backdonation from the metal should be weaker. This connection is reflected in the Ru–N bond length. All compounds with a clearly bent NO ligand (N2O2) showed a larger value for the Ru–N2 bond length than for the Ru–N1 bond length (N1O1 = linearly coordinated NO ligand). This might explain the better photoexcitability of those structures which have bent NO ligands. Since the necessary energy is also available (a green laser has approximately 3 eV) for the activation of the linear NO ligand, the reason cannot be found in a better “activation” of the bent NO ligand. Maybe, photo-excitation is more effective (higher population) for a bent NO ligand because it is already less tightly coordinated to the metal. Knowledge of the excitation pathway would help to understand these results in a better way.

It has not yet been proved that the metastable state in **6b** is indeed the MS1 state. The MS1 state is not unambiguously distinguishable from the GS state by means of X-ray photocrystallography. Further experiments using neutron diffraction, which are currently in progress, might elucidate the nature of the metastable state.

It can be concluded that the ground state structures are well understood, whereas the structures of the metastable states still raise various questions.

5 Experimental Part

5.1 Common working techniques

All reactions—as far as not explicitly described otherwise—were carried out under inert gas atmosphere using standard Schlenk techniques.

The syringes, cannulas and pipettes for the dosage of the solvents were flushed three times with argon before use. Ethanol (used for the dissolving of $NOBF_4$) was dried over a molecular sieve and degassed by refluxing and cooling the solvent under argon atmosphere. Water and ethanol (used for the preparation of the phosphane containing mononitrosyl ruthenium compounds) were degassed by the same procedure. The solvents, as well as the zinc-copper alloy, were kept under argon atmosphere. The nitrosyl tetrafluoroborate was stored in a Schlenk tube at 4 °C under argon atmosphere.

For crystallisation, various techniques were applied: dinitrosyls, containing trialkylphosphanes as ligands, were crystallised directly from the reaction solution by means of adjusting different concentrations. Other attempts—for example by diffusing diethyl ether or *n*-hexane into solutions of powders in dichloromethane or by covering these solutions with the mentioned solvents—often resulted in oily products. Those dinitrosyls which bear triarylphosphanes as ligands can easily be prepared as powders and recrystallised in dichloromethane, covered with *n*-hexane or diethyl ether.

In those cases where no date of elemental analysis is given, high resolution mass spectra were recorded.

5.2 Analytic methods

Elemental analysis:	*Elementar* vario EL (C, H, N content)
	Metrohm 888 Titrando (Cl, Br, I content)
	Varian Vista RL CCD simultaneous ICP-AES (Ru, K, P content)
Infrared spectrometer:	*Jasco* FT/IR-460Plus with ATR Diamond Plate
Crystal selection:	microscope Leica MZ6 with polarisation filter
NMR spectrometer:	*Jeol* GSX 270
	Jeol Eclipse 400
	Jeol EX 400
X-ray diffraction experiments:	Bruker-*Nonius* Kappa CCD
	Oxford XCalibur 3
	Bruker D8 Quest
	Bruker D8 Venture
UV/VIS spectrophotometer:	*Varian* Cary 50
Scales:	*Sartorius* BP410S
	Sartorius ED124S
Mass spectrometer:	*Jeol* JMS 700, *Thermo* Finnigan MAT 95, FAB
	Thermo Finnigan LTQ FT, IonMax ion source, ESI

5.3 Reagents and solvents

amidosulfonic acid	≥ 99.9 %, purum p.a.	Fluka
benzyldiphenylphosphane	99 %	ABCR
tert-butyldiphenylphosphane	97 %	Aldrich
d-chloroform	99.8% (H_2O < 0.01 %)	EURISO-top
diethyl ether	99.9%	VWR
d_2-dichloromethane	99.9 % (H_2O < 0.01 %)	EURISO-top
ethanol	abs.	BfB
n-hexane	puriss.	Grüssing
hydrobromic acid	48 wt %	Acros
hydrochloric acid (1 M)	Standard solution	AppliChem
hydrochloric acid	37 wt %	Merck
hydroiodic acid	57 wt %	Merck
molecular sieve 4A	8–12 mesh	Acros
nitrosyl tetrafluoroborate	95 %	Aldrich
potassium nitrite	≥ 98 %, puriss. p.a.	Fluka
α-phellandrene	–	Aldrich
ruthenium(III) chloride hydrate	99.9 %, 36 % Ru	ABCR
ruthenium(III) chloride hydrate	40.3 % Ru	Alfa Aesar
ruthenium(III) nitrosyl chloride hydrate	39.60 % Ru	ChemPur
toluene (over molecular sieve)	99.7 %	Aldrich
tribenzylphosphane	–	ABCR
tricyclohexylphosphane	97 %	ABCR
tricyclopentylphosphane	97 %	Aldrich
triethylphosphane	–	Acros
triphenylphosphane	99 %	Acros
tri(*iso*-propyl)phosphane	90 %	ABCR
tri(*para*-tolyl)phosphane	98 %	ABCR
water	de-ionised	house installation
zinc-copper couple	–	Acros

5.4 Preparation of the precursor compounds

5.4.1 $RuCl_3(NO) \cdot x\ H_2O$

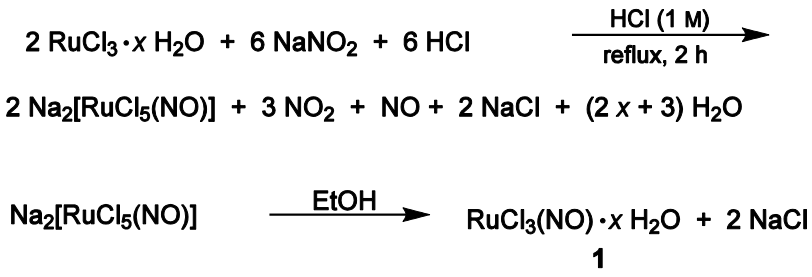

Literature: J.M. Fletcher, I.L. Jenkins, F.M. Lever, F.S. Martin, A.R. Powell, R. Todd, *J. Inorg. Nucl. Chem.* **1955**, *1*, 378–401.

Starting material: Ruthenium(III) chloride hydrate, sodium nitrite, water, hydrochloric acid (1M), diethyl ether.

Procedure: Ruthenium(III) chloride hydrate (2.71 g, 36% Ru, 7.12 mmol) was dissolved in hydrochloric acid (18 mL, 1 M) and heated to reflux. A saturated solution of sodium nitrite (2.06 g, 29.9 mmol) in water was added dropwise during one hour. Nitric oxides were disposed of in amidosulfonic acid. The reaction solution was heated for another hour before the water was evaporated *in vacuo*. The resulting solid was dissolved in ethanol, precipitating sodium chloride was filtered off and the solvent was removed *in vacuo*. The solid was redissolved in ethanol (20 mL) and precipitated with diethyl ether (40 mL) as a dark violet powder which was freed from all volatile components *in vacuo*.

Empirical formula: $RuCl_3(NO) \cdot x\ H_2O$ (**1**).

Yield: 1.88 g, purple powder.

MS (H_2O/CH_3CN, M = Cl_3NORu): ESI^+: *m/z* = 377.7123 (Ru_1-pattern $[M + 2Cl + 3Na]^+$, calcd. 377.7130); ESI^-: *m/z* = 206.8114 (Ru_1-pattern, $[M - NO]^-$, calcd. 206.8109), 243.7774 (Ru_1-pattern $[M + Cl - NO]^-$, calcd. 243.7768), 273.7754 (Ru_1-pattern, $[M + Cl]^-$, calcd. 273.7748).

IR spectroscopy (RT, solid), (intensity): *v* = 3575 (w), 3466 (w), 1904 (s, NO), 1612 (w), 1036 (w), 618 (w) cm^{-1}.

5.4.2 $K_2[RuCl_5(NO)]$

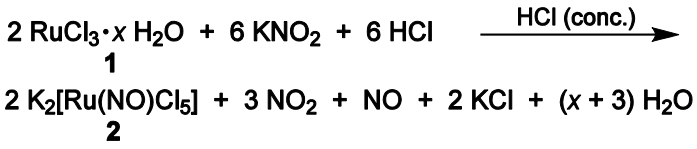

Literature: J.R. Durig, W.A: McAllister, J.N. Willis, E.E. Mercer, *Spectrochim. Acta.* **1966**, *22*, 1091–1100.

Starting material Ruthenium(III) chloride hydrate (36%, 40.31% Ru), water, potassium nitrite, hydrochloric acid (conc.), amidosulfonic acid, diethyl ether.

Procedure: Ruthenium(III) chloride hydrate (0.510 g, 36.0% Ru; 6.83 g, 40.3% Ru; 29.0 mmol) was dissolved in water (60 mL) at 80 °C. Subsequently, small portions of solid potassium nitrite (7.41 g, 87.1 mmol) were added during a period of one hour. Upon the dropwise addition of concentrated hydrochloric acid (60 mL) nitrogen oxides evolved, which were passed into a system of washing bottles (amidosulfonic acid / amidosulfonic acid) for disposal. After stirring the reaction mixture for another 75 minutes at 80 °C, the solution was concentrated *in vacuo* to a volume of 10 mL. The resulting dark violet solid was separated by filtration and washed several times with iced water until no white solid could be seen. After being washed with diethyl ether, the compound was dried *in vacuo.* The yield could be increased by concentrating the filtrate *in vacuo* again. The resulting solid was purified by the same procedure as described above.

Empirical formula: Cl_5K_2NORu (386.54 g mol^{-1}, **2**).

Yield: 5.33 g (13.8 mmol), 47.5% of th., violet crystals.

Elemental analysis: (calcd. for Cl_5K_2NORu, 386.54 g mol^{-1}), found (calcd.): N 3.29% (3.62%).

MS (H_2O/CH_3CN, M = Cl_5K_2NORu): ESI^+: m/z = 425.6342 (Ru_1-pattern $[M + K]^+$, calcd. 425.6345); ESI^-: m/z = 243.7775 (Ru_1-pattern $[M - Cl - 2K - NO]^-$, calcd. 243.7781), 273.7756 (Ru_1-pattern, $[M - Cl - 2K]^-$, calcd. 273.7761), 347.7083 (Ru_1-pattern, $[M - K]^-$, calcd. 347.7082).

IR spectroscopy (RT, solid), (intensity): ν = 1880 (s, NO) cm^{-1}.

5.4.3 $K_2[Ru(OH)(NO_2)_4(NO)]$

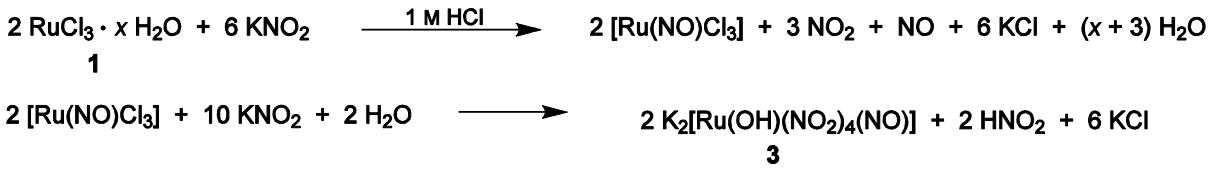

Literature: J.M. Fletcher, I.L. Jenkins, F.M. Lever, F.S. Martin, A.R. Powell, R. Todd, *J. Inorg. Nucl. Chem.* **1955**, *1*, 378–401.

Starting material: Ruthenium(III) chloride hydrate (40.31% Ru), hydrocloric acid (1 M), potassium nitrite, amidosulfonic acid, diethyl ether, water.

Procedure: Ruthenium(III) chloride hydrate (15.6 g, 58.1 mmol) was added to 60 mL of hydrochloric acid and the resulting suspension heated until boiling. Subsequently, small portions of solid potassium nitrite (14.9 g, 175 mmol) were added over a period of one hour. Evolving nitrogen oxides were passed into a system of washing bottles (amidosulfonic acid/ amidosulfonic acid) for disposal. After completing the addition, the solution was cooled to 80 °C and, again, small portions of potassium nitrite (24.8 g, 291 mmol) were added over a period of four hours. Hereupon the red-orange reaction mixture was filtered into a crystallisation dish and covered with a watch glass. Orange crystals, which formed over night, were washed with iced water (5 mL) and diethyl ether (50 mL). The solid was freed from all volatile components *in vacuo*.

Empirical formula: $HK_2N_5O_{10}Ru$ (410.30 g mol^{-1}, **3**).

Yield: 13.7 g (33.3 mmol), 57.3% of th., orange crystals.

Elemental analysis: (calcd. for $HK_2N_5O_{10}Ru$, 410.30 g mol^{-1}), found (calcd.): H 0.32% (0.25%), K 20.92% (19.06%), N 16.56% (17.07%), Ru 23.84% (24.63%).

MS (H_2O/CH_3CN, M = Cl_5K_2NORu): ESI^+: m/z = 449.7669 (Ru_1-pattern $[M + K]^+$, calcd. 449.7671)

IR spectroscopy (RT, solid), (intensity): ν = 3529 (vw), 1880 (m, NO), 1398 (s), 1330 (vs), 956 (m), 829 (s) cm^{-1}.

5.4.4 $K_2[RuBr_5(NO)]$

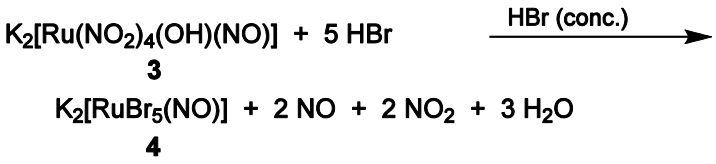

Literature: M.J. Cleare, W.P. Griffith, *J. Chem. Soc. A* **1967**, *7*, 1144–1147.

Starting material: Dipotassium hydroxido tetranitrito nitrosyl ruthenate, hydrobromic acid (conc.), amidosulfonic acid, diethyl ether, water.

Procedure: Dipotassium hydroxide tetranitrito nitrosyl ruthenate (6.07 g, 14.8 mmol) was dissolved in water (30 mL) at 80 °C. As soon as the educt was in solution, hydrobromic acid (70 mL) was added dropwise under vigorous stirring. The evolving nitrogen oxides were passed into a system of washing bottles (amidosulfonic acid/ amidosulfonic acid) for disposal. After the addition was completed, the solution was stirred for another 2 h at 80 °C and was then concentrated *in vacuo* to 10 mL. Thus a solid precipitated which was washed with hydrobromic acid (5 mL, 6 M) and diethyl ether (50 mL) and dried *in vacuo*.

Empirical formula: Br_5K_2NORu (608.79 g mol^{-1}, **4**).

Yield: 7.84 g, 87.2% of th., dark purple crystals.

Elemental analysis: (calcd. for Br_5K_2NORu 608.79 g mol^{-1}), found (calcd.): Br 65.57% (65.63%), N 2.01% (2.30%), K 12.98% (12.84%), Ru 14.71% (16.60%)

MS (H_2O/CH_3CN, M = Cl_5K_2NORu): ESI^+: *m/z* = 649.3779 (Ru_1-pattern $[M + K]^+$, calcd. 649.3791); ESI^-: *m/z* 451.5724 (Ru_1-pattern $[M - Br - 2K]^-$, calcd. 451.5725), 687.0755 (Ru_1-pattern $[M + Br]^-$, calcd. 689.3345).

IR spectroscopy (RT, solid), (intensity): ν = 1875 (s, NO) cm^{-1}.

5.4.5 $K_2[RuI_5(NO)]$

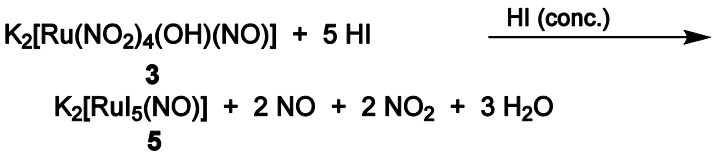

Literature: M.J. Cleare, W.P. Griffith, *J. Chem. Soc. A* **1967**, *7*, 1144–1147.

Starting material: Dipotassium hydroxido tetranitrito nitrosyl ruthenate, hydroiodic acid (conc.), amidosulfonic acid, diethyl ether, water.

Procedure: Dipotassium hydroxido tetranitro nitrosyl ruthenate (4.96 g, 12.1 mmol) was dissolved in water (30 mL) at 50 °C. As soon as the educt was in solution, hydroiodic acid (70 mL) was added dropwise under vigorous stirring. The evolving nitrogen oxides were passed into a system of washing bottles (amidosulfonic acid/ amidosulfonic acid) for disposal. After the addition was completed, the solution was stirred for another 90 minutes at 80 °C and was then concentrated *in vacuo* to 15 mL. Thus a solid precipitated which was washed with diethyl ether (100 mL) and dried *in vacuo*.

Empirical formula: I_5K_2NORu (843.79 g mol^{-1}, **5**).

Yield: 8.73 g, 85.1% of th., crystals of anthracite colour.

Elemental analysis: (calcd. for I_5K_2NORu 843.79 g mol^{-1}), found (calcd.): I 74.94% (75.2%), K 9.44% (9.27%), N 1.76% (1.66%), Ru 11.02% (11.98%).

MS (H_2O/CH_3CN, M = I_5K_2NORu): ESI$^+$: *m/z* = 758.4741 (Ru_1-pattern $[M - I]^+$, calcd. 758.4124), 883.3162 (Ru_1-pattern $[M + K]^+$, calcd. 767.3158), 1049.1839 ($[M + I + 2K]^+$, calcd. 1049.1840); ESI$^-$: *m/z* = 639.5222 (Ru1-pattern $[M - I - 2K]^-$, calcd. 639.5202).

IR spectroscopy (RT, solid), (intensity): ν = 1840 cm^{-1} (s, NO).

5.4.6 $[RuCl_3(NO)(PPh_3)_2]$

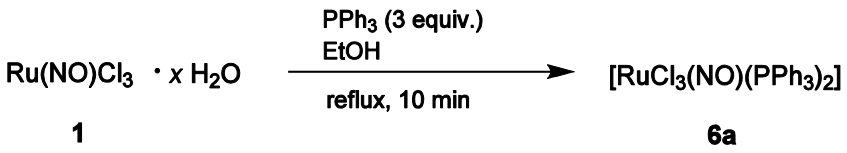

Literature: J. Chatt, B.L. Shaw, *J. Chem. Soc. A* **1966**, 1811–1812.

Starting material: Ruthenium(III) nitrosyl chloride hydrate, triphenylphosphane, ethanol, diethyl ether, toluene.

Procedure: Triphenylphosphane (3.14 g, 12.0 mmol), dissolved in hot ethanol (15 mL), was added to a hot ethanolic solution (10 mL) of ruthenium(III) nitrosyl chloride hydrate (1.00 g, 4.00 mmol) and was then kept under refluxing conditions for 10 minutes. During the reaction a chartreuse solid was formed, which was filtered off after cooling to room temperature. Subsequently the raw product was washed with ethanol and diethyl ether and dried *in vacuo*.

An analytically pure, yellow product could be obtained by refluxing the raw product in toluene, washing with ethanol and drying *in vacuo*.

Empirical formula: $C_{36}H_{30}Cl_3NOP_2Ru$ (762.01 g mol^{-1}, **6a**).

Yield: 2.79 g (3.66 mmol), 92.0% of th., chartreuse powder.

Elemental analysis: (calcd. for $C_{36}H_{30}Cl_3NOP_2Ru$, 762.01 g mol^{-1}), found. (calcd.): C 57.01% (56.74%), H 3.98% (3.97%), Cl 13.40% (13.96%), N 1.86% (1.84%).

$^{31}P\{^1H\}$ NMR spectroscopy (toluene, 109 MHz): δ = 25.0 (s) ppm.

MS: Not possible, both FIB/FAB and DEI were unsuccessful.

IR spectroscopy (RT, solid), (intensity): *v* = 1874 (s, NO), 1481(w), 1435 (m), 1192 (vw), 1092 (m), 997 (vw), 742 (m), 704 (m), 688 (vs) cm^{-1}.

5.4.7 $[RuBr_3(NO)(PPh_3)_2]$

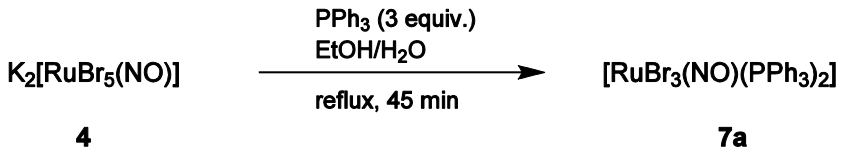

Starting material: Dipotassium pentabromido nitrosyl ruthenate, triphenylphosphane, ethanol, water, diethyl ether, toluene.

Procedure: Triphenylphosphane (1.57 g, 6.00 mmol), dissolved in hot ethanol (10 mL), was added to a water / ethanol solution (1 : 1-mixture, 20 mL) of dipotassium pentabromido nitrosyl ruthenate (1.22 g, 2.00 mmol) and was heated under refluxing conditions for 45 min. During the reaction a green solid was formed, which was filtered off after cooling to room temperature. Subsequently the raw product was washed with ethanol and diethyl ether and dried *in vacuo*.

An analytically pure, orange brown product could be obtained by refluxing the raw product in toluene, washing with ethanol and drying *in vacuo*.

Empirical formula: $C_{36}H_{30}Br_3NOP_2Ru$ (895.36 g mol^{-1}, **7a**).

Yield: 1.46 g (1.64 mmol), 81.8% of th., green powder.

Elemental analysis: (calcd. for $C_{36}H_{30}Br_3NOP_2Ru$ 895.36 g mol^{-1}) found (calcd.): C 48.79% (48.29%), H 3.40% (3.38%), N 1.61% (1.56%).

$^{31}P\{^1H\}$ NMR spectroscopy (toluene, 109 MHz): δ = 25.0 (s) ppm.

MS: Not possible, both FIB/FAB and DEI were unsuccessful.

IR spectroscopy (RT, solid), (intensity): *v* = 1870 (s, NO), 1480 (m), 1435 (s), 1192 (w), 1163 (w), 1090 (s), 997 (w), 741 (s), 703 (s), 688 (vs) cm^{-1}.

5.4.8 $[RuI_3(NO)(PPh_3)_2]$

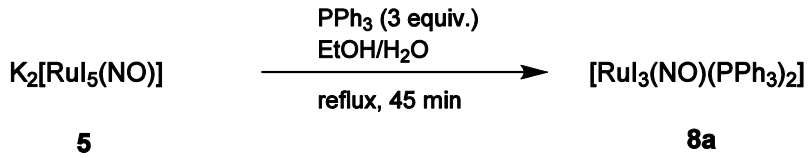

Starting material: Dipotassium pentaiodido nitrosyl ruthenate, triphenylphosphane, ethanol, diethyl ether.

Procedure: Triphenylphosphane (1.57 g, 6.00 mmol), dissolved in hot ethanol (8 mL), was added to a solution of dipotassium pentaiodido nitrosyl ruthenate (1.69 g, 2.00 mmol) in ethanol (10 mL) and was heated under refluxing conditions for 1 hour. During the reaction a reddish brown solid was formed, which was filtered off after cooling to room temperature. Subsequently the raw product was washed with ethanol and diethyl ether and dried *in vacuo*.

Empirical formula: $C_{36}H_{30}I_3NOP_2Ru$ (1036.36 g mol^{-1}, **8a**).

Yield: 1.46 g (1.91 mmol), 95.7% d. Th., reddish brown powder.

Elemental analysis: (calcd. for $C_{36}H_{30}Br_3NOP_2Ru$ 895.36 g mol^{-1}) found (calcd.): C 41.72% (42.58%), H 3.08% (2.92%), N 1.32% (1.35%).

MS: Not possible, both FIB/FAB and DEI were unsuccessful.

IR spectroscopy (RT, solid), (intensity): *v* = 1858 (s, NO), 1479 (m), 1434 (s), 1086 (s), 740 (s), 688 (vs) cm^{-1}.

5.4.9 $[RuCl_3(NO)(PPh_2Bn)_2]$

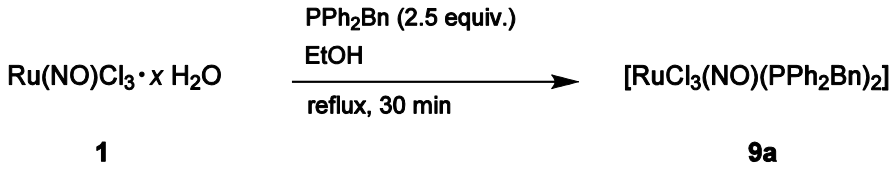

Starting material: Ruthenium(III) nitrosyl chloride hydrate, benzyldiphenylphosphane, ethanol, diethyl ether, dichloromethane, *n*-hexane.

Procedure: An ethanolic solution (5 mL) of ruthenium nitrosyl chloride hydrate (0.453 g, 1.78 mmol) was added to benzyldiphenylphosphane (1.23 g, 4.44 mmol), dissolved in hot ethanol (5 mL), and heated under reflux for 20–30 minutes. A yellow orange solid was formed during the reaction which was separated by filtration, washed with a 1:1:2-mixture of dichloromethane / ethanol / *n*-hexane (12 mL) and dried *in vacuo*.

Empirical formula: $C_{38}H_{34}Cl_3NOP_2Ru$ (790.06 g mol^{-1}, **9a**).

Yield: 1.26 g (1.59 mmol), 89.3% of th., yellow orange.

Elemental analysis: (calcd. for $C_{38}H_{34}Cl_3NOP_2Ru$, 790.06 g mol^{-1}), found (calcd.): C 58.05% (57.77%), H 4.44% (4.34%), Cl 13.13% (13.46%), N 1.64% (1.77%).

$^{31}P\{^1H\}$ NMR spectroscopy (toluene, 109 MHz): δ = 19.6 (s) ppm.

MS (NBA, *M* = $C_{38}H_{34}Cl_3NOP_2Ru$): FAB$^+$: *m/z* = 754 (Ru_1-pattern $[M - Cl]^+$, calcd. 754.1).

IR spectroscopy (RT, solid), (intensity): *v* = 1850 (s, NO), 1599 (vw), 1495 (w), 1482 (w), 1453 (w), 1433 (m), 1408 (w), 1330 (w), 1185 (w), 1143 (w), 1094 (w), 1096 (w), 1030 (w), 1000 (w), 914 (w), 831 (m), 773 (m), 752 (m), 740 (s), 697 (s) cm^{-1}.

5.4.10 $[RuBr_3(NO)(PPh_2Bn)_2]$

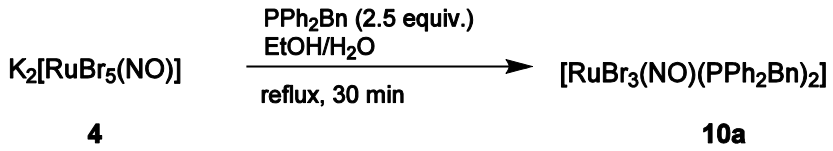

Starting material: Dipotassium pentabromido nitrosyl ruthenate, benzyldiphenylphosphane, ethanol, diethyl ether, dichloromethane, *n*-hexane.

Procedure: Benzyldiphenylphosphane (0.481 g, 1.74 mmol), dissolved in hot ethanol (5 mL), was treated with a solution of dipotassium pentabromido nitrosyl ruthenate (0.424 g, 0.696 mmol) in ethanol / water (3 : 1, 10 mL) and heated under reflux for 30 minutes. In the course of the reaction a yellow orange solid precipitated which, after cooling to room temperature, was filtered off and washed with a mixture of ethanol / dichloromethane / *n*-hexane (1 : 1 : 2, 8 mL). The product was freed from all volatile components *in vacuo*.

Empirical formula: $C_{38}H_{34}Br_3NOP_2Ru$ (923.41 g mol^{-1}, **10a**).

Yield: 0.610 g (0.661 mmol), 94.3% of th., yellow orange powder.

Elemental analysis: (calcd. for $C_{38}H_{34}Br_3NOP_2Ru$, 923.41 g mol^{-1}), found (calcd.): C 50.58% (49.43 %), H 3.83% (3.71 %), N 1.30% (1.52 %).

$^{31}P\{^1H\}$ NMR spectroscopy (toluene, 109 MHz): δ = 12.9 (s) ppm.

MS (NBA, *M* = $C_{38}H_{34}Br_3NOP_2Ru$): FAB$^+$: *m/z* = 844 (Ru_1-pattern $[M - Cl]^+$, calcd. 844.0).

IR spectroscopy (RT, solid), (intensity): ν = 1847 (s, NO), 1494 (vw), 1453 (vw), 1432 (w), 1408 (vw), 1143 (vw), 1099 (vw), 1069 (vw), 1030 (vw), 830 (m), 772 (m), 750 (m), 739 (s), 697 (vs) cm^{-1}.

5.4.11 $[RuCl_3(NO)(PBn_3)_2]$

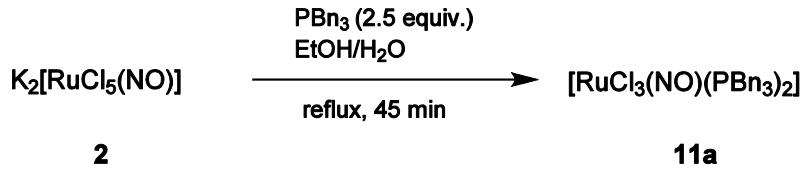

Starting material: Dipotassium pentachlorido nitrosyl ruthenate, tribenzylphosphane, ethanol, water, diethyl ether, dichloromethane, *n*-hexane.

Procedure: Dipotassium pentachlorido nitrosyl ruthenate (0.255 g, 0.660 mmol), dissolved in ethanol / water (1 : 1, 14 mL), was added to a solution of tribenzylphosphane (0.498 g, 1.64 mmol) in hot ethanol (20 mL). The reaction mixture was kept under refluxing conditions for 45 minutes. After cooling the mixture to ambient temperature a cream-coloured solid precipitated which was collected by filtration. The product was washed with dichloromethane / ethanol / *n*-hexane (1 : 1 : 2, 12 mL) and dried *in vacuo*.

Empirical formula: $C_{42}H_{42}Cl_3NOP_2Ru$ (846.17 g mol^{-1}, **11a**).

Yield: 0.432 g (0.511 mmol), 77.3% of th., cream-coloured powder.

Elemental analysis: (calcd. for $C_{42}H_{42}Cl_3NOP_2Ru$, 846.17 g mol^{-1}), found (calcd.): C 59.63% (59.62%), H 4.91% (5.00%), Cl 12.58% (12.57%), N 1.66% (1.66%).

$^{31}P\{^1H\}$ NMR spectroscopy (toluene, 109 MHz): δ = 14.3 (s) ppm.

MS (NBA, *M* = $C_{42}H_{42}Cl_3NOP_2Ru$): FAB$^+$: *m/z* = 847 (Ru_1-pattern $[M]^{\cdot+}$, calcd. 847.1), 810.2 (Ru_1-pattern $[M - Cl]^+$, calcd. 810.1); FAB$^-$: *m/z* = 847.0 (Ru_1-pattern $[M]^{\cdot-}$, calcd. 847.1).

IR spectroscopy (RT, solid), (intensity): *v* = 1867 (s, NO), 1600 (w), 1494 (s), 1452 (m), 1406 (w), 1225 (w), 1148 (w), 1069 (m), 1031 (w), 1000 (w), 913 (w), 854 (w), 833 (m), 775 (s), 694 (vs) cm^{-1}.

5.4.12 $[RuBr_3(NO)(PBn_3)_2]$

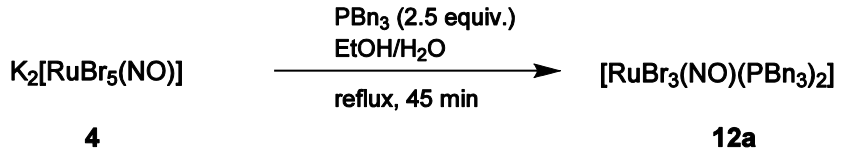

Starting material: Dipotassium pentabromido nitrosyl ruthenate, tribenzylphosphane, ethanol, water, diethyl ether, dichloromethane, *n*-hexane.

Procedure: Dipotassium pentabromido nitrosyl ruthenate (0.432 g, 0.710 mmol), dissolved in ethanol / water (1 : 1, 12 mL), was added to a solution of tribenzylphosphane (0.540 g, 1.77 mmol) in hot ethanol (20 mL). The reaction mixture was kept under refluxing conditions for 45 minutes. After cooling the mixture to ambient temperature an orange brown solid precipitated which was collected by filtration. The product was washed with dichloromethane / ethanol / *n*-hexane (1 : 1 : 2, 8 mL) and dried *in vacuo*.

Empirical formula: $C_{42}H_{42}Br_3NOP_2Ru$ (979.52 g mol^{-1}, **12a**).

Yield: 0.570 g (0.582 mmol), 82.0% of th., orange brown powder.

Elemental analysis: (calcd. for $C_{42}H_{42}Br_3NOP_2Ru$, 979.52 g mol^{-1}), found (calcd.): C 51.54% (51.50%), H 4.32% (4.32%), Br 23.57% (24.47%), N 1.42% (1.43%).

$^{31}P\{^1H\}$ NMR spectroscopy (toluene, 109 MHz): δ = 5.4 (s) ppm.

MS (NBA, *M* = $C_{42}H_{42}Br_3NOP_2Ru$): FAB$^+$: *m/z* = 981.0 (Ru_1-pattern, $[M]^{\cdot+}$, calcd. 980.9316), 900.1 (Ru_1-pattern $[M - Br]^{\cdot+}$, calcd. 900.0146); FAB$^-$: *m/z* = 979.3.0 (Ru_1-pattern, $[M]^{\cdot-}$, calcd. 978.9325).

IR spectroscopy (RT, solid), (intensity): *v* = 1845 (s, NO), 1599 (w), 1493 (m), 1452 (m), 1396 (w), 1234 (w), 1146 (w), 1070 (m), 1028 (w), 915 (w), 837 (m), 822 (m), 770 (s), 695 (vs) cm^{-1}.

5.4.13 $[RuCl_3(NO)(P^tBuPh_2)_2]$

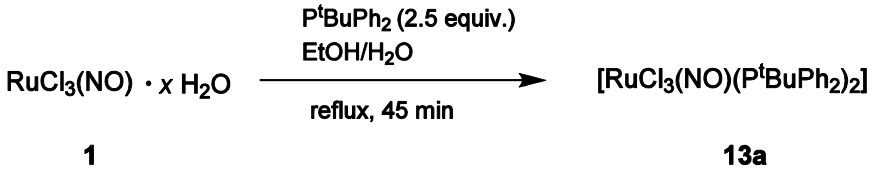

Starting material: Ruthenium nitrosyl chloride hydrate, *tert*-butyldiphenylphosphane, ethanol, water, diethyl ether, dichloromethane, *n*-hexane.

Procedure: Ruthenium nitrosyl chloride hydrate (0.421 g, 1.65 mmol), dissolved in ethanol (20 mL), was added to a solution of *tert*-butyldiphenylphosphane (1.00 g, 4.13 mmol) in hot ethanol (10 mL). The reaction mixture was kept under refluxing conditions for 45 minutes. After cooling the mixture to ambient temperature a red orange solid precipitated which was collected by filtration. The residue was washed with dichloromethane / ethanol / *n*-hexane (1 : 1 : 2, 16 mL) and dried *in vacuo*.

Empirical formula: $C_{32}H_{38}Cl_3NOP_2Ru$ (722.03 g mol^{-1}, **13a**).

Yield: 0.570 g (0.582 mmol), 82.0% of th., light orange powder.

Elemental analysis: (calcd. for $C_{32}H_{38}Cl_3NOP_2Ru$, 722.03 g mol^{-1}), found (calcd.): C 53.09% (53.23%), H 5.34% (5.30%), Cl 14.82% (14.73%), N 1.93% (1.94%).

$^{31}P\{^1H\}$ NMR spectroscopy (toluene, 109 MHz): δ = 25.2 (s) ppm.

MS (NBA, M = $C_{32}H_{38}Cl_3NOP_2Ru$, 722.03 g mol^{-1}): FAB$^+$: *m/z* = 686 (Ru_1-pattern, $[M - Cl]^+$, calcd. 686.1), 651 (Ru_1-pattern $[M - 2Cl]^{\cdot+}$, calcd. 651.1).

IR spectroscopy (RT, solid), (intensity): *v* = 1828 (s, NO), 1481 (vw), 1431 (m), 1396 (w), 1168 (w), 1088 (w), 1012 (w), 933 (w), 802 (vw), 740 (m), 691 (vs) cm^{-1}.

5.4.14 $[RuCl_{1-3}(NO)\{P(p\text{-tolyl})_3\}_2]$

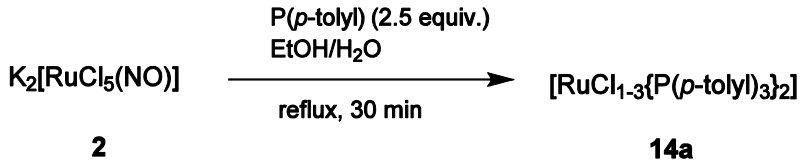

Starting material: Dipotassium pentachlorido nitrosyl ruthenate , tri(*para*-tolyl)phosphane, ethanol, water, diethyl ether, dichloromethane, *n*-hexane.

Procedure: Dipotassium pentachlorido nitrosyl ruthenate (0.538 g, 1.39 mmol), dissolved in ethanol/water (1 : 1, 24 mL), was added to a solution of tri(*para*-tolyl)phosphane (1.07 g, 3.52 mmol) in hot ethanol (30 mL). The reaction mixture was kept under refluxing conditions for 30 minutes. After cooling the mixture to ambient temperature an ochre solid precipitated which was collected by filtration. The residue was washed with dichloromethane : ethanol : *n*-hexane (1 : 1 : 2, 12 mL) and dried *in vacuo*.

Empirical formula: $C_{42}H_{42}ClNOP_2Ru$ (775.26 g mol^{-1}), $C_{42}H_{42}Cl_2NOP_2Ru$ (810.71 g mol^{-1}), $C_{42}H_{42}Cl_3NOP_2Ru$ (846.17 g mol^{-1}) **14a**.

Yield: 0.709 g (0.838 mmol), 60.0 % of th., ochre powder.*

Elemental analysis: (calcd. for $C_{42}H_{42}Cl_3NOP_2Ru$, 846.17 g mol^{-1}), found (calcd.): C 60.36% (59.62%), H 5.09% (5.00%), N 1.52% (1.66%).

$^{31}P\{^1H\}$ NMR spectroscopy (toluene, 109 MHz): δ = 24.9 (s), 11.3 (s) ppm.

MS (NBA, M = $C_{42}H_{42}Cl_3NOP_2Ru$, 846.17 g mol^{-1}): FAB$^+$: *m/z* = 812.2 (Ru_1-pattern, $[M - Cl]^+$, calcd. 812.1), 775.1 (Ru_1-pattern $[M - 2Cl]^{\cdot+}$, calcd. 775.2).

IR spectroscopy (RT, solid), (intensity): ν = 1863 (m, NO), 1823 (vs, NO), 1763 (NO, vw), 1598 (w), 1498 (w), 1398 (w), 1314 (vw), 1194 (m), 1089 (s), 1020 (w), 806 (s), 709 (w) cm^{-1}.

*In the present case a yield can be specified, as the elemental analysis of the product is in accordance with a formulation as a pure $\{RuNO\}^6$-compound.

5.4.15 $[RuBr_{1-3}(NO)\{P(p\text{-tolyl})_3\}_2]$

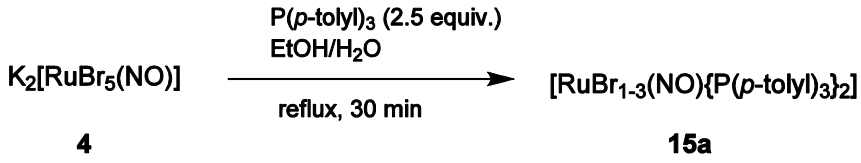

Starting material: Dipotassium pentabromido nitrosyl ruthenate, tri(*para*-tolyl)phosphane, ethanol, water, diethyl ether, dichloromethane, *n*-hexane.

Procedure: Dipotassium pentabromido nitrosyl ruthenate (0.882 g, 1.45 mmol), dissolved in ethanol/water (1:1, 22 mL), was added to a solution of tri(*para*-tolyl)phosphane (1.10 g, 3.62 mmol) in hot ethanol (30 mL). The reaction mixture was kept under refluxing conditions for 30 minutes. After cooling the mixture to ambient temperature the resulting solid was collected by filtration. The residue was washed with dichloromethane : ethanol : *n*-hexane (1 : 1 : 2, 12 mL) and dried *in vacuo*.

Empirical formula: $C_{42}H_{42}BrNOP_2Ru$ (819.71 g mol^{-1}), $C_{42}H_{42}Br_2NOP_2Ru$ (899.61 g mol^{-1}), $C_{42}H_{42}Br_3NOP_2Ru$ (979.52 g mol^{-1}) **15a**.

Yield: 1.136 g, greenish brown powder.

Elemental analysis: (calcd. for $C_{42}H_{42}Br_3NOP_2Ru$, 979.52 g mol^{-1}), found (calcd.): C 54.63% (51.50%), H 4.65% (4.32%), N 1.38% (1.43%).

$^{31}P\{^1H\}$ NMR spectroscopy (toluene, 109 MHz): δ = 39.5 (s), 25.7 (s), 24.6 (s), 4.2 (s) ppm.

MS (NBA, *M* = $C_{42}H_{42}Br_3NOP_2Ru$, 979.52 g mol^{-1}): FAB$^+$: *m/z* = 900.02 (Ru_1-pattern, $[M - Br]^+$, calcd. 900.01), 819.12 (Ru_1-pattern $[M - 2Cl]^+$, calcd. 819.10).

IR spectroscopy (RT, solid), (intensity): *v* = 1860 (vs, NO), 1738 (w, NO), 1596 (m), 1496 (m), 1442 (w), 1397 (m), 1312 (vw), 1192 (s), 1087 (s), 1017 (w), 804 (s), 731 (w), 706 (m) cm^{-1}.

5.4.16 $[RuCl_{2-3}(NO)\{P(p\text{-anisyl})_3\}_2]$

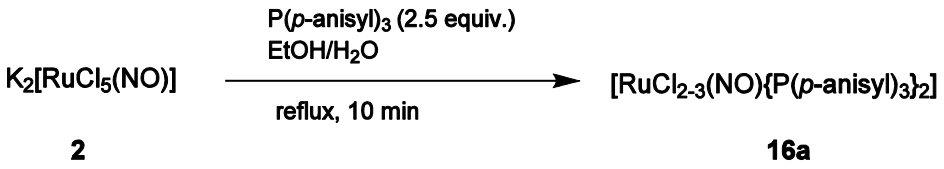

Starting material: Ruthenium nitrosyl chloride hydrate, tri(4-methoxyphenyl)phosphane, ethanol, water, diethyl ether, dichloromethane, *n*-hexane.

Procedure: Ruthenium nitrosyl chloride hydrate (0.153 g, 0.600 mmol), dissolved in ethanol (10 mL), was added to a solution of tri(4-methoxyphenyl)phosphane (0.529 g, 1.50 mmol) in hot ethanol (20 mL). The reaction mixture was kept under refluxing conditions for 10 minutes. After cooling the mixture to ambient temperature the resulting solid was collected by filtration. The residue was washed with dichloromethane : ethanol : *n*-hexane (1 : 1 : 2, 8 mL) and dried *in vacuo*.

Empirical formula: $C_{42}H_{42}Cl_2NO_7P_2Ru$ (906.70 g mol^{-1}), $C_{42}H_{42}Cl_3NO_7P_2Ru$ (942.16 g mol^{-1}) **16a**.

Yield: 0.307 g (0.326 mmol), 54.3 % of th., orange brown powder.*

Elemental analysis: (calcd. for $C_{42}H_{42}Cl_3NO_7P_2Ru$, 942.16 g mol^{-1}), found (calcd.): C 53.31% (53.54%), H 4.43% (4.49%), Cl 11.22% (11.29%), N 1.53% (1.49%).

$^{31}P\{^1H\}$ NMR spectroscopy (toluene, 109 MHz): δ = 10.2 (s) ppm.

MS (NBA, M = $C_{42}H_{42}Cl_3N_7OP_2Ru$, 942.16 g mol^{-1}): FAB$^+$: m/z = 906.0 (Ru_1-pattern, $[M - Cl]^+$, calcd. 906.09).

IR spectroscopy (RT, solid), (intensity): ν = 1865 (m, NO), 1834 (w, NO), 1591 (s), 1566 (m), 1497 (vs), 1462 (m), 1406 (w), 1282 (m), 1252 (vs), 1180 (vs), 1091 (vs), 1023 (s), 825 (s), 798 (vs), 716 (w) cm^{-1}.

*In the present case a yield can be specified, as the elemental analysis of the product is in accordance with a formulation as a pure $\{RuNO\}^6$-compound.

5.4.17 [RuBr$_{1-3}$(NO){P(*p*-anisyl)$_3$}$_2$]

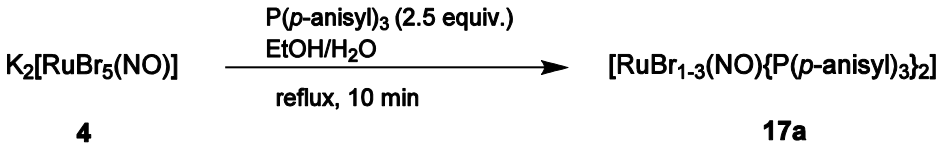

Starting material: Dipotassium pentabromido nitrosyl ruthenate , tri(4-methoxyphenyl)-phosphane, ethanol, water, diethyl ether, dichloromethane, *n*-hexane.

Procedure: Dipotassium pentabromido nitrosyl ruthenate (0.677 g, 1.11 mmol), dissolved in ethanol : water (1 : 1, 12 mL), was added to a solution of tri(4-methoxyphenyl)phosphane (1.00 g, 2.78 mmol) in hot ethanol (45 mL). The reaction mixture was kept under refluxing conditions for 45 minutes. After cooling the mixture to ambient temperature the resulting solid was collected by filtration. The residue was washed with dichloromethane : ethanol : *n*-hexane (1 : 1 : 2, 16 mL) and dried *in vacuo*.

Empirical formula: $C_{42}H_{42}BrNO_7P_2Ru$ (915.70 g mol^{-1}), $C_{42}H_{42}Br_2NO_7P_2Ru$ (995.61 g mol^{-1}), $C_{42}H_{42}Br_3NO_7P_2Ru$ (1075.51 g mol^{-1}), **17a**.

Yield: 0.749 g, greenish brown powder.

Elemental analysis: (calcd. for $C_{42}H_{42}Br_3NOP_2Ru$, 1075.51 g mol^{-1}), found (calcd.): C 47.68% (46.90%), H 4.16% (3.94%), N 1.33% (1.30%).

^{31}P{^{1}H} NMR spectroscopy (toluene, 109 MHz): δ = 22.2 (s), 18.9 (s), 2.9 (s) ppm.

MS (NBA, *M* = $C_{42}H_{42}Br_3N_7OP_2Ru$, 1075.51 g mol^{-1}): FAB$^+$: *m/z* = 996.2 (Ru_1-pattern, [*M* − Br]$^+$, calcd. 995.7).

IR spectroscopy (RT, solid), (intensity): *v* = 1859 (m, NO), 1719 (m, NO), 1591 (s), 1567 (m), 1497 (vs), 1458 (m), 1438 (m), 1405 (m), 1287 (s), 1252 (vs), 1177 (vs), 1096 (vs), 1024 (s), 823 (s), 798 (s), 715 (w) cm^{-1}.

5.4.18 $[RuCl_{1-3}(NO)(PCy_3)_2]$

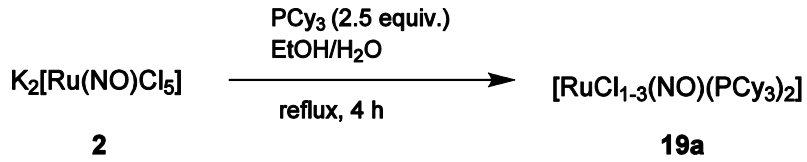

Starting material: Dipotassium pentachlorido nitrosyl ruthenate, tricyclohexylphosphane, ethanol, water.

Procedure: Dipotassium pentachlorido nitrosyl ruthenate (1.14 g, 2.94 mmol), dissolved in ethanol/water (1 : 1, 60 mL), was added to a solution of tricyclohexylphosphane (2.06 g, 7.35 mmol) in hot ethanol (55 mL). The reaction mixture was kept under refluxing conditions for 4 hours. The resulting solid was collected by filtration and dried *in vacuo.*

Empirical formula: $C_{36}H_{66}ClNOP_2Ru$ (798.29 g mol^{-1}), $C_{36}H_{66}Cl_2NOP_2Ru$ (762.84 g mol^{-1}), $C_{36}H_{66}Cl_3NOP_2Ru$ (727.39 g mol^{-1}) **18a**.

Yield: 1.67 g, light green powder.

Elemental analysis: (calcd. for $C_{36}H_{66}Cl_3NOP_2Ru$, 798.29 g mol^{-1}), found (calcd.): C 55.62% (54.16%), H 8.41% (8.33%), N 1.72% (1.75%).

$^{31}P\{^1H\}$ NMR spectroscopy (toluene, 109 MHz): δ = 38.8 (s), 25.2 (s), 17.6 (s) ppm.

MS (NBA, M = $C_{36}H_{66}Cl_2NOP_2Ru$, 762.84 g mol^{-1}): FAB$^+$: m/z = 727.8 (Ru_1-pattern, $[M - Cl]^+$, calcd. 727.3).

IR spectroscopy (RT, solid), (intensity): ν = 2921 (vs), 2846 (vs), 1826 (vs, NO), 1802 (w, NO), 1712 (vs, NO), 1442 (s), 1264 (m), 1195 (m), 1173 (s), 1127 (w), 1002 (s), 899 (m), 847 (s), 734 (m) cm^{-1}.

5.4.19 $[RuBr_{1-3}(NO)(PCy_3)_2]$

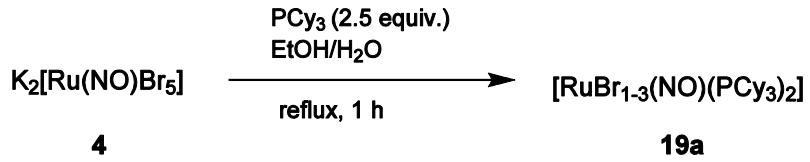

Starting material: Dipotassium pentabromido nitrosyl ruthenate, tricyclohexylphosphane, ethanol, water, dichloromethane, *n*-hexane.

Procedure: Dipotassium pentabromido nitrosyl ruthenate (1.00 g, 1.64 mmol), dissolved in ethanol/water (1 : 1, 70 mL), was added to a solution of tricyclohexylphosphane (1.15 g, 4.11 mmol) in hot ethanol (50 mL). The reaction mixture was kept under refluxing conditions for 1 hour. The resulting green solid was collected by filtration, washed with ethanol : dichloromethane : *n*-hexane (1 : 1 : 2, 28 mL) and dried *in vacuo.*

Empirical formula: $C_{36}H_{66}BrNOP_2Ru$ (771.84 g mol^{-1}), $C_{36}H_{66}Br_2NOP_2Ru$ (851.74 g mol^{-1}), $C_{36}H_{66}Br_3NOP_2Ru$ (931.64 g mol^{-1}) **19a**.

Yield: 1.00 g, green powder.

Elemental analysis: (calcd. for $C_{36}H_{66}Br_2NOP_2Ru$, 851.74 g mol^{-1}), found (calcd.): C 51.85% (50.76%), H 7.31% (7.81%), N 1.75% (1.64%).

$^{31}P\{^1H\}$ NMR spectroscopy (toluene, 109 MHz): δ = 73.7 (s), 36.5 (s), 24.8 (s), 16.2 (s), 9.3 (s) ppm.

MS (NBA, *M* = $C_{36}H_{66}Br_2NOP_2Ru$, 851.74 g mol^{-1}): FAB$^+$: *m/z* = 771.7 (Ru_1-pattern, $[M - Br]^+$, calcd. 771.3); FAB$^-$: *m/z* = 852.7 (Ru_1-pattern, $[M]^-$, calcd. 852.2).

IR spectroscopy (RT, solid), (intensity): *v* = 2922 (vs), 2846 (m), 1825 (w, NO), 1802 (m, NO), 1752 (w, NO), 1709 (s, NO), 1442 (m), 1265 (vw), 1172 (m), 1127 (vw), 1001 (m), 886 (w), 846 (m), 732 (m) cm^{-1}.

5.4.20 $[RuI_{1-3}(NO)(PCy_3)_2]$

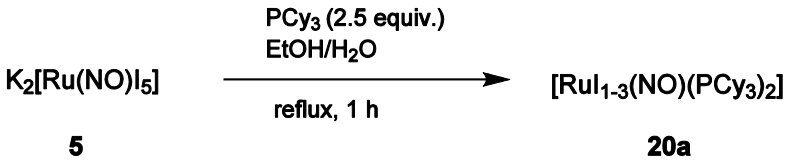

Starting material: Dipotassium pentaiodido nitrosyl ruthenate, tricyclohexylphosphane, ethanol, water, dichloromethane, *n*-hexane.

Procedure: Dipotassium pentaiodido nitrosyl ruthenate (0.72 g, 0.85 mmol), dissolved in ethanol/water (2 : 1, 24 mL), was added to a solution of tricyclohexylphosphane (0.62 g, 2.2 mmol) in hot ethanol (17 mL). The reaction mixture was kept under refluxing conditions for 1 hour. The resulting green solid was collected by filtration, washed with ethanol : dichloromethane : *n*-hexane (1 : 1 : 2, 28 mL) and dried *in vacuo.*

Empirical formula: $C_{36}H_{66}INOP_2Ru$ (818.84 g mol^{-1}), $C_{36}H_{66}I_2NOP_2Ru$ (945.74 g mol^{-1}), $C_{36}H_{66}I_3NOP_2Ru$ (1072.64 g mol^{-1}) **20a**.

Yield: 0.231 g, dark green powder.

Elemental analysis: (calcd. for $C_{36}H_{66}I_2NOP_2Ru$, 945.74 g mol^{-1}), found (calcd.): C 48.33% (45.72%), H 7.43% (7.03%), N 1.51% (1.48%).

$^{31}P\{^1H\}$ NMR spectroscopy (toluene, 109 MHz): δ = 45.8 (s), 34.1 (s), 25.6 (s), 16.9 (s), 11.3 (s) ppm.

MS (NBA, *M* = $C_{36}H_{66}I_2NOP_2Ru$, 945.74 g mol^{-1}): FAB$^+$: *m/z* = 820.0 (Ru_1-pattern, $[M - I]^+$, calcd. 819.3).

IR spectroscopy (RT, solid), (intensity): *v* = 2923 (m), 2846 (m), 1798 (m, NO), 1756 (m, NO), 1706 (vs, NO), 1442 (m), 1297 (vw), 1264 (w), 1172 (m), 1002 (m), 886 (w), 845 (m), 814 (w), 731 (m), 652 (w) cm^{-1}.

5.4.21 $[RuCl_{1-3}(NO)(PCyp_3)_2]$

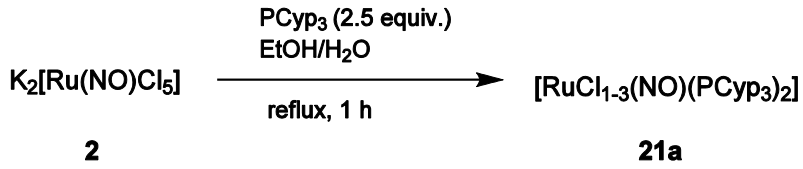

Starting material: Dipotassium pentachlorido nitrosyl ruthenate, tricyclopentylphosphane, ethanol, water.

Procedure: Dipotassium pentachlorido nitrosyl ruthenate (0.675 g, 1.75 mmol), dissolved in ethanol/water (1 : 1, 70 mL), was added to a solution of tricyclopentylphosphane (1.00 g, 4.20 mmol) in hot ethanol (10 mL). The reaction mixture was kept under refluxing conditions for 1 hour. The resulting solid was collected by filtration and dried *in vacuo.*

Empirical formula: $C_{36}H_{66}ClNOP_2Ru$ (643.23 g mol^{-1}), $C_{36}H_{66}Cl_2NOP_2Ru$ (678.68 g mol^{-1}), $C_{36}H_{66}Cl_3NOP_2Ru$ (714.13 g mol^{-1}) **21a**.

Yield: 1.199 g, light green powder.

Elemental analysis: (calcd. for $C_{36}H_{66}Cl_2NOP_2Ru$, 678.68 g mol^{-1}), found (calcd.): C 53.55% (53.09%), H 8.20% (8.02%), N 1.82% (2.06%).

$^{31}P\{^1H\}$ NMR spectroscopy (toluene, 109 MHz): δ = 38.2 (s), 19.8 (s), 19.3 (s), 16.9 (s), 4.0 (s) ppm.

MS (NBA, M = $C_{36}H_{66}ClNOP_2Ru$, 643.23 g mol^{-1}): FAB$^+$: m/z = 727.8 (Ru_1-pattern, $[M - Cl]^+$, calcd. 727.4).

IR spectroscopy (RT, solid), (intensity): $\tilde{\nu}$ = 2947 (m), 2863 (m), 1830 (m NO), 1803 (m, NO), 1703 (vs, NO), 1447 (w), 1299 (w), 1230 (w), 1120 (w), 1011 (vw), 906 (w), 724 (vw), 619 (vw) cm^{-1}.

5.4.22 $[RuBr_{1-3}(NO)(PCyp_3)_2]$

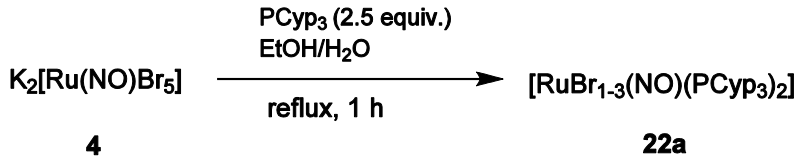

Starting material: Dipotassium pentabromido nitrosyl ruthenate, tricyclopentylphosphane, ethanol, water.

Procedure: Dipotassium pentabromido nitrosyl ruthenate (1.06 g, 1.75 mmol), dissolved in ethanol/water (1 : 1, 70 mL), was added to a solution of tricyclopentylphosphane (1.00 g, 4.20 mmol) in hot ethanol (10 mL). The reaction mixture was kept under refluxing conditions for 1 hour. The resulting green solid was collected by filtration and dried *in vacuo.*

Empirical formula: $C_{30}H_{54}BrNOP_2Ru$ (847.49 g mol^{-1}), $C_{30}H_{54}Br_2NOP_2Ru$ (767.58 g mol^{-1}), $C_{30}H_{54}Br_3NOP_2Ru$ (687.68 g mol^{-1}) **22a**.

Yield: 0.965 g (1.14 mmol), 65% of th., green powder.*

Elemental analysis: (calcd. for $C_{30}H_{54}Br_2NOP_2Ru$ 767.58 g mol^{-1}), found (calcd.): C 46.73% (46.94%), H 6.80% (7.09%), N 1.80% (1.82%).

$^{31}P\{^1H\}$ NMR spectroscopy (toluene, 109 MHz): δ = 36.9 (s), 27.1 (s), 15.4 (s), 15.0 (s) ppm.

MS (NBA, M = $C_{36}H_{66}Br_2NOP_2Ru$, 767.58 g mol^{-1}): FAB$^+$: m/z = 689.7 (Ru_1-pattern, $[M - Br]^+$, calcd. 689.19).

IR spectroscopy (RT, solid), (intensity): ν = 2954 (m), 2864 (w), 1828 (w, NO), 1806 (m, NO), 1762 (w), 1703 (m, NO), 1447 (vw), 1298 (vw), 1259 (m), 1013 (s), 906 (w), 861 (w), 795 (vs), 703 (w) cm^{-1}.

*In the present case a yield can be specified, as the elemental analysis of the product is in accordance with a formulation of the product as a pure $\{RuNO\}^7$ compound.

5.4.23 $[RuI_{1-3}(NO)(PCyp_3)_2]$

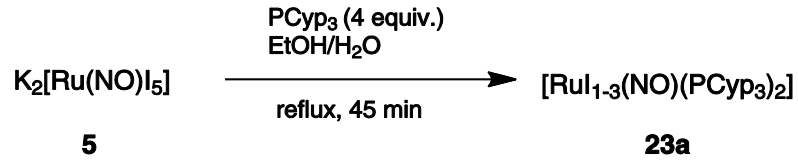

5 **23a**

Starting material: Dipotassium pentaiodido nitrosyl ruthenate, tricyclopentylphosphane, ethanol, water.

Procedure: Dipotassium pentaiodido nitrosyl ruthenate (1.90 g, 1.06 mmol), dissolved in ethanol/water (5 : 1, 30 mL), was added to a solution of tricyclopentylphosphane (1.00 g, 4.20 mmol) in hot ethanol (10 mL). The reaction mixture was kept under refluxing conditions for 45 minutes. The resulting dark green solid was collected by filtration and dried *in vacuo.*

Empirical formula: $C_{30}H_{54}INOP_2Ru$ (734.68 g mol^{-1}), $C_{30}H_{54}I_2NOP_2Ru$ (861.58 g mol^{-1}), $C_{30}H_{54}I_3NOP_2Ru$ 1000.49 g mol^{-1}), **23a**.

Yield: 1.02 g, dark green powder.

Elemental analysis: (calcd. for $C_{30}H_{54}I_2NOP_2Ru$, 861.58 g mol^{-1}), found (calcd.): C 46.53% (45.72%), H 7.10% (7.03%), N 1.68% (1.48%).

$^{31}P\{^1H\}$ NMR spectroscopy (toluene, 109 MHz): δ = 49.9 (s), 34.2 (s), 19.2 (s), 16.8 (s), 4.9 (s) ppm.

MS (NBA, M = $C_{30}H_{54}I_2NOP_2Ru$, 861.58 g mol^{-1}): FAB$^+$: *m/z* = 735.4 (Ru_1-pattern, $[M - I]^+$, calcd. 735.18).

IR spectroscopy (RT, solid), (intensity): ν = 2943 (m), 2864 (m), 2359 (w), 1750 (vs, NO), 1707 (vs, NO), 1446 (w), 1299 (vw), 1260 (vw), 1119 (w), 904 (m), 875 (m), 662 (vw) cm^{-1}.

5.4.24 $[RuCl_{1-3}(NO)(P^iPr_3)_2]$

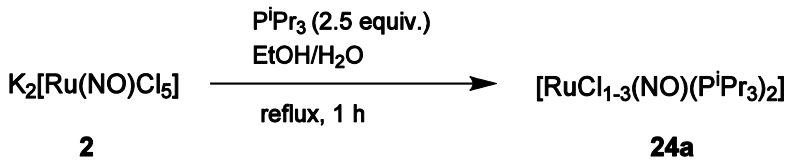

Starting material: Dipotassium pentachlorido nitrosyl ruthenate, tri-isopropylphosphane, ethanol, water.

Procedure: Dipotassium pentachlorido nitrosyl ruthenate (1.48 g, 3.83 mmol), dissolved in ethanol/water (1 : 1, 60 mL), was added to a solution of tri-isopropylphosphane (1.50 g, 9.36 mmol) in hot ethanol (15 mL). The reaction mixture was kept under refluxing conditions for 1 hour. The resulting solid was collected by filtration and dried *in vacuo.*

Empirical formula: $C_{18}H_{42}ClNOP_2Ru$ (487.00 g mol^{-1}), $C_{18}H_{42}Cl_2NOP_2Ru$ (522.46 g mol^{-1}), $C_{18}H_{42}Cl_3NOP_2Ru$ (557.91 g mol^{-1}) **24a**.

Yield: 1.17 g (2.23 mmol), 58.3 % of th., light green powder.*

Elemental analysis: (calcd. for $C_{18}H_{42}Cl_2NOP_2Ru$, 522.46 g mol^{-1}), found (calcd.): C 41.45% (41.38%), H 8.29% (8.10%), N 2.61% (2.68%).

$^{31}P\{^1H\}$ NMR spectroscopy (toluene, 109 MHz): δ = 33.2 (s), 29.6 (s), 27.1 (s) ppm.

MS (NBA, *M* = $C_{18}H_{42}Cl_2NOP_2Ru$, 522.46 g mol^{-1}): FAB$^+$: *m/z* = 522.4 (Ru_1-pattern, $[M]^{\cdot+}$, calcd. 522.12), 487.4 (Ru_1-pattern, $[M - Cl]^+$, calcd. 487.15).

IR spectroscopy (RT, solid), (intensity): *v* = 2958 (w), 1841 (m, NO), 1804 (s, NO), 1707 (vs, NO), 1455 (m), 1366 (w), 1240 (m), 1061 (m), 882 (m), 655 (vs) cm^{-1}.

*In the present case a yield can be specified, as the elemental analysis of the product is in accordance with a formulation of the product as a pure $\{RuNO\}^7$-compound.

5.4.25 $[RuBr_{1-2}(NO)(P^iPr_3)_2]$

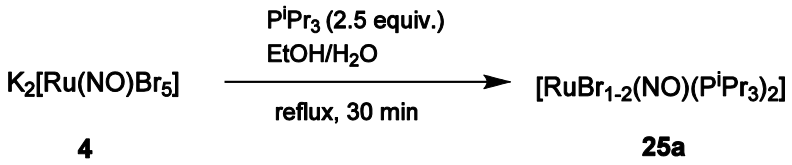

Starting material: Dipotassium pentabromido nitrosyl ruthenate, tri-isopropylphosphane, ethanol, water.

Procedure: Dipotassium pentabromido nitrosyl ruthenate (2.95 g, 4.84 mmol), dissolved in ethanol/water (1 : 1, 70 mL), was added to a solution of tri-isopropylphosphane (2.00 g, 12.5 mmol) in hot ethanol (20 mL). The reaction mixture was kept under refluxing conditions for 30 minutes. The resulting green solid was collected by filtration and dried *in vacuo.*

Empirical formula: $C_{18}H_{42}BrNOP_2Ru$ (531.45 g mol^{-1}), $C_{18}H_{42}Br_2NOP_2Ru$ (611.36 g mol^{-1}) **25a**.

Yield: 2.30 g, green powder.

Elemental analysis: (calcd. for $C_{18}H_{42}BrNOP_2Ru$, 531.45 g mol^{-1}), found (calcd.): C 39.31% (40.68%), H 7.55% (7.97%), N 2.55% (2.64%).

$^{31}P\{^1H\}$ NMR spectroscopy (toluene, 109 MHz): δ = 48.1 (s) ppm.

MS (NBA, *M* = $C_{18}H_{42}Br_2NOP_2Ru$, 611.36 g mol^{-1}): FAB$^+$: *m/z* = 533.3 (Ru_1-pattern, $[M - Br]^+$, calcd. 533.09).

IR spectroscopy (RT, solid), (intensity): *v* = 2955 (w), 1756 (m, NO), 1705 (m, NO), 1455 (w), 1365 (w), 1240 (w), 1060 (w), 1028 (w), 930 (w), 883 (m), 655 (vs), 624 (w) cm^{-1}.

5.4.26 $[RuI_{1-2}(NO)(P^iPr_3)_2]$

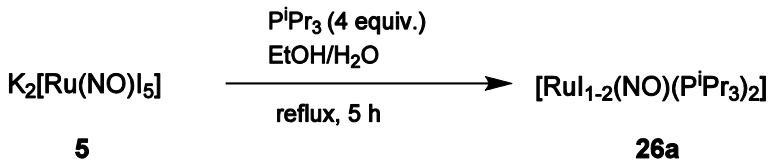

Starting material: Dipotassium pentaiodido nitrosyl ruthenate, tri-isopropylphosphane, ethanol, water.

Procedure: Dipotassium pentaiodido nitrosyl ruthenate (1.87 g, 2.22 mmol), dissolved in ethanol/water (3 : 1, 24 mL), was added to a solution of tri-isopropylphosphane (1.50 g, 9.36 mmol) in hot ethanol (10 mL). The reaction mixture was kept under refluxing conditions for 5 hours. The resulting dark green solid was collected by filtration and dried *in vacuo.*

Empirical formula: $C_{18}H_{42}INOP_2Ru$ (578.45 g mol^{-1}), $C_{18}H_{42}I_2NOP_2Ru$ (705.36 g mol^{-1}) **26a**.

Yield: 0.682 g, dark green, nearly black powder.

Elemental analysis: (calcd. for $C_{18}H_{42}I_2NOP_2Ru$, 705.36 g mol^{-1}), found (calcd.): C 28.50% (30.65%), H 5.49% (6.00%), N 2.12% (1.99%).

$^{31}P\{^1H\}$ NMR spectroscopy (toluene, 109 MHz): δ = 46.1 (s), 33.2 (s) ppm.

MS (NBA, M = $C_{18}H_{42}I_2NOP_2Ru$, 705.36 g mol^{-1}): FAB$^+$: m/z = 579.6 (Ru_1-pattern, $[M - I]^+$, calcd. 579.08).

IR spectroscopy (RT, solid), (intensity): ν = 2956 (w), 1755 (w, NO), 1702 (s, NO), 1455 (m), 1365 (w), 1240 (w), 1059 (m), 1028 (m), 881 (m), 652 (vs) cm^{-1}.

5.5 Synthesis of products of the $\{Ru(NO)_2\}^8$-type

5.5.1 $[RuCl(NO)_2(PPh_3)_2]BF_4$

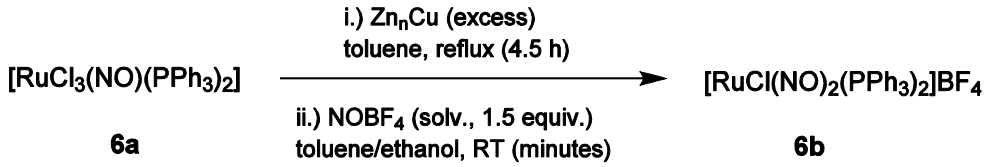

Literature: L. K. Bell, J. Mason, D. M. P. Mingos, D. G. Tew, *Inorg. Chem.* **1983**, *22*, 3497–3502.

Starting materials: 6a ($[RuCl_3(NO)(PPh_3)_2]$), zinc-copper couple, toluene, nitrosyl tetrafluoroborate, *n*-hexane.

Procedure: Compound **6a** (0.23 g, 0.30 mmol) and an alloy of zinc-copper (1.6 g) were suspended in toluene (20 mL) and heated under refluxing conditions for 4.5 h. The initially chartreuse suspension turned green during the course of the reaction. For removal of excess alloy the suspension was filtered. Afterwards a solution of $NOBF_4$ (0.053 g, 0.45 mmol) in toluene : ethanol (10 mL : 1.3 mL) was added, whereupon a rapid colour change from emerald-green to red orange occurred. Crystals were formed on cooling to ambient temperature. The yield could be increased by storage at 4 °C. The solid was filtered off, washed with *n*-hexane (5 mL) and dried *in vacuo*.

Empirical formula: $C_{36}H_{30}BClF_4N_2O_2P_2Ru$ (807.91 g mol^{-1}, **6b**).

Yield: 0.059 g (0.073 mmol), 24% of th., ruby red crystals, soluble in CH_2Cl_2.

Elemental analysis: (calcd. for $C_{36}H_{30}BClF_4N_2O_2P_2Ru$, 807.91 g mol^{-1}), found (calcd.): C 52.95% (53.52%), H 3.74% (3.74%), N 3.40% (3.47%).

$^{31}P\{^1H\}$ NMR spectroscopy (CH_2Cl_2, 109 MHz): δ = 30.8 (s) ppm.

MS: ($M^+ = C_{36}H_{30}ClN_2O_2P_2Ru^+$, 721.05 g mol^{-1}): FAB$^+$: *m/z* = 721.0 (Ru_1-pattern, $[M]^+$, calcd. 721.05), 691.0 (Ru_1-pattern, $[M - NO]^+$, calcd. 691.05).

IR spectroscopy (RT, solid), (intensity): *v* = 1842 (m, NO), 1685 (m, NO), 1482 (w), 1435 (m), 1191 (vw), 1095 (m), 1058 (vs), 997 (m), 747 (s), 713 (m), 689 (vs) cm^{-1}.

IR spectroscopy (RT, in CH_2Cl_2): *v*(NO) = 1823, 1776 and 1720 cm^{-1}.

X-ray structure analysis: pn320 (see Fig. 2.12).

5.5.2 $[RuBr(NO)_2(PPh_3)_2]BF_4$

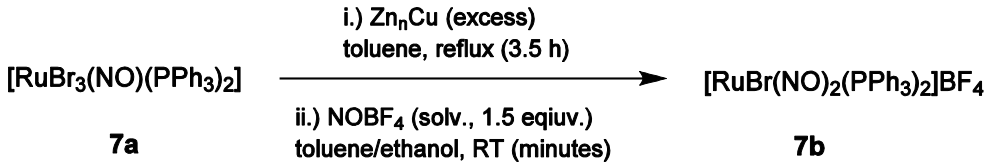

Starting material: 7a ($[RuBr_3(NO)(PPh_3)_2]$), zinc-copper couple, toluene, nitrosyl tetrafluoroborate, *n*-hexane.

Procedure: Compound **7a** (0.27 g, 0.30 mmol) and zinc-copper couple (1.6 g) were suspended in toluene (25 mL) and heated under refluxing conditions for 3.5 h. The initially green suspension turned dark green. For removal of excess alloy the suspension was filtered. Afterwards a solution of $NOBF_4$ (0.056 g, 0.48 mmol) in toluene : ethanol (10 mL : 1.3 mL) was added, whereupon a rapid colour change from dark green to dark red orange occurred. Red orange crystals in the shape of blocks formed over night. After keeping the solution at 4 °C for several days, the product was filtered off and washed with *n*-hexane (6 mL). It was freed from all volatile components *in vacuo*.

Empirical formula: $C_{36}H_{30}BBrF_4N_2O_2P_2Ru$ (852.36 g mol^{-1}, **7b**).

Yield: 0.14 g (0.16 mmol), 55% of th., garnet red crystals, soluble in CH_2Cl_2.

Elemental analysis: (calcd. for $C_{36}H_{30}BBrF_4N_2O_2P_2Ru$, 852.36 g mol^{-1}), found (calcd.): C 50.53% (50.73%), H 3.64% (3.55 %), N 3.22% (3.29%).

$^{31}P\{^1H\}$ NMR spectroscopy (CH_2Cl_2, 109 MHz): δ = 27.3 ppm.

MS: ($M^+ = C_{36}H_{30}BrN_2O_2P_2Ru^+$, 765.56 g mol^{-1}): FAB$^+$: *m/z* = 765.1 (Ru_1-pattern, $[M]^+$, calcd. 765.00), 735.1 (Ru_1-pattern, $[M - NO]^+$, calcd. 735.00).

IR spectroscopy (RT, solid), (intensity): *v* = 1824 (w, NO), 1765 (m, NO), 1480 (vw), 1435 (m), 1312 (w), 1187 (w), 1092 (m), 1050 (vs), 997 (m), 751 (m), 736 (m), 689 (s) cm^{-1}.

IR spectroscopy (RT, in CH_2Cl_2): ν(NO) = 1813, 1778 cm^{-1}.

X-ray structure analysis: pn390 (see Fig. 2.14).

5.5.3 $[RuCl(NO)_2(PPh_2Bn)_2]BF_4$

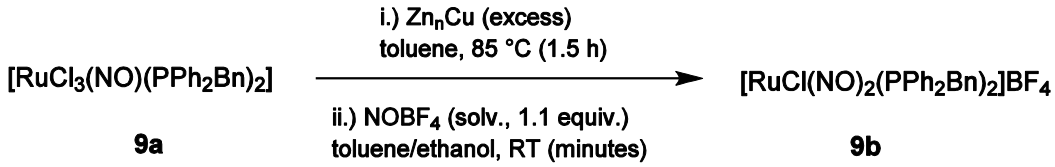

Starting substances: **9a** ($[RuCl_3(NO)(PPh_2Bn)_2]$), zinc-copper couple, toluene, ethanol, nitrosyl tetrafluoroborate, *n*-hexane.

Procedure: Compound **9a** (0.24 g, 0.30 mmol) and zinc-copper couple (1.4 g) were suspended in toluene (20 mL) and heated at 85 °C for 1.5 h. During the reaction the initially orange suspension turned into an emerald green solution. For removal of excess alloy the suspension was filtered under an inert gas atmosphere. After addition of the green ruthenium solution to a solution of $NOBF_4$ (47 mg, 0.40 mmol) in toluene/ethanol (15 mL / 1.3 mL), a rapid colour change from green to red orange occurred. Within a few days ruby red crystals could be detected at the bottom of the flask, which were separated by filtration and washed with *n*-hexane. The solid was then freed from all volatile components *in vacuo*.

Empirical formula: $C_{38}H_{34}BClF_4N_2O_2P_2Ru$ (835.96 g·mol^{-1}, **9b**).

Yield: 0.087 g (0.10 mmol), 34% of th., red crystals, soluble in CH_2Cl_2.

Elemental analysis: (calcd. for $C_{38}H_{34}BClF_4N_2O_2P_2Ru$, 835.96 g mol^{-1}), found (calcd.): C 54.32% (54.60%), H 4.07% (4.10%), N 3.32% (3.35%), Cl 4.37% (4.24%).

$^{31}P\{^1H\}$ NMR spectroscopy (CH_2Cl_2, 109 MHz): δ = 42.9 ppm.

MS: ($M^+ = C_{38}H_{34}ClN_2O_2P_2Ru^+$, 749.16 g mol^{-1}): FAB$^+$: *m/z* = 749.1 (Ru_1-pattern, $[M]^+$, calcd. 749.16), 719.1 (Ru_1-pattern, $[M - NO]^+$, calcd. 719.15).

IR spectroscopy (RT, solid), (intensity): *v* = 1799 (m, NO), 1771 (s, NO), 1583 (vw), 1484 (vw), 1455 (vw), 1436 (m), 1406 (vw), 1312 (vw), 1185 (vw), 1130 (vw), 1197 (m), 1046 (vs), 997 (m), 917 (vw), 829 (m), 774 (m), 740 (m), 700 (s), 688 (s) cm^{-1}.

IR spectroscopy (RT, in CH_2Cl_2): *v*(NO) = 1818, 1776 cm^{-1}.

X-ray structure analysis: qo093 (see Fig. 2.15).

5.5.4 $[RuBr(NO)_2(PPh_2Bn)_2]BF_4$

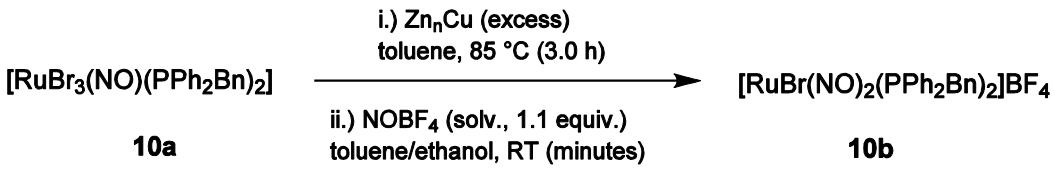

Starting substances: 10a ($[RuBr_3(NO)(PPh_2Bn)_2]$), zinc-copper couple, toluene, ethanol, nitrosyl tetrafluoroborate, *n*-hexane.

Procedure: Compound **10a** (0.28 g, 0.31 mmol) and zinc-copper couple (1.5 g) were suspended in toluene (20 mL) and heated at 85 °C for 3 h. The initially orange suspension turned dark green. For removal of excess alloy the suspension was filtered under an inert atmosphere. A solution of $NOBF_4$ (0.040 g, 0.34 mmol) in toluene/ethanol (10 mL/1.3 mL) was added, whereupon a rapid colour change from dark green to dark red orange occurred. Dark red crystals formed over night. After keeping the solution at 4 °C for several days, the product was filtered off, washed with diethyl ether (5 mL) and dried *in vacuo*.

Empirical formula: $C_{38}H_{34}BBrF_4N_2O_2P_2Ru$ (880.41 g mol^{-1}, **10b**).

Yield: 14 mg (0.016 mmol), 5.3% of th., garnet-red crystals, soluble in CH_2Cl_2.

Elemental analysis: (calcd. for $C_{38}H_{34}BBrF_4N_2O_2P_2Ru$, 880.41 g·mol^{-1}), found (calcd.): C 51.68% (51.84%), H 3.90% (3.89%), N 3.19% (3.18%), Br 9.00% (9.08%).

$^{31}P\{^1H\}$ NMR spectroscopy (CH_2Cl_2, 109 MHz): δ = 39.4 ppm.

MS: (M^+ = $C_{38}H_{34}BrN_2O_2P_2Ru^+$, 793.61 g mol^{-1}): FAB$^+$: *m/z* = 793.0 (Ru_1-pattern, $[M]^+$, calcd. 793.03), 763.0 (Ru_1-pattern, $[M - NO]^+$, calcd. 763.03).

IR spectroscopy (RT, solid), (intensity): *v* = 1817 (m, NO), 1776 (s, NO), 1495 (w), 1455 (w), 1435 (m), 1406 (w), 1312 (w), 1097 (s), 1046 (vs), 997 (s), 917 (w), 830 (s), 775 (s), 741 (s), 701 (s) cm^{-1}.

IR spectroscopy (RT, in CH_2Cl_2): *v*(NO) = 1815, 1778 cm^{-1}.

X-ray structure analysis: qn031 (see Fig. 2.16).

5.5.5 $[RuCl(NO)_2(PBn_3)_2]BF_4$

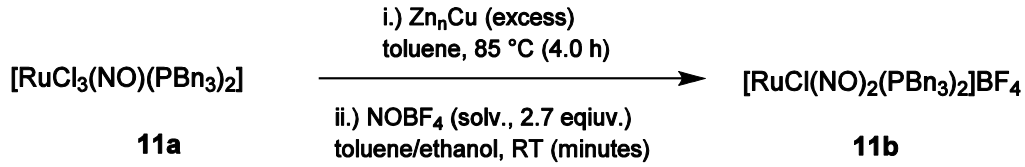

Starting substances: 11a ($[RuCl_3(NO)(PBn_3)_2]$), zinc-copper couple, toluene, ethanol, nitrosyl tetrafluoroborate, *n*-hexane, dichloromethane, *n*-pentane.

Procedure: Compound **11a** (0.25 g, 0.30 mmol) and zinc-copper (1.3 g) were suspended in toluene (20 mL) and heated at 85 °C for 4 hours. The initially orange suspension turned emerald green. For removal of excess alloy the suspension was filtered. Afterwards a solution of $NOBF_4$ (0.093 g, 0.80 mmol) in toluene : ethanol (10 mL : 1.3 mL) was added, whereupon an instantaneous colour change from green to orange occurred. After half an hour a bright orange precipitate formed which was filtered off and washed with *n*-hexane.

By means of recrystallisation from CH_2Cl_2/*n*-pentane small, orange needles could be obtained, which were too weak in scattering for single-crystal X-ray diffraction.

Empirical formula: $C_{42}H_{42}BClF_4N_2O_2P_2Ru$ (892.07 g mol^{-1}, **11b**).

Yield: 0.10 g (0.11 mmol), 38% of th., bright orange solid.

Elemental analysis (calcd. for $C_{42}H_{42}BClF_4N_2O_2P_2Ru$, 892.07 g mol^{-1}), found (calcd.): C 56.31% (56.55%), H 4.92% (4.75%), N 2.98% (3.14%), Cl 4.35% (3.97%).

$^{31}P\{^1H\}$ NMR spectroscopy (CH_2Cl_2, 109 MHz:): δ = 50.6 ppm.

MS: (M^+ = $C_{42}H_{42}ClN_2O_2P_2Ru^+$, 805.27 g·mol^{-1}): FAB$^+$: *m/z* = 805.2 (Ru_1-pattern, $[M]^+$, calcd. 805.27), 775.1 (Ru_1-pattern, $[M - NO]^+$, calcd. 775.26).

IR spectroscopy (RT, solid), (intensity): *v* = 1864 (vw, NO), 1811 (m, NO), 1775 (s, NO), 1496 (w), 1454 (w), 1406 (vw), 1231 (vw), 1054 (s), 914 (vw), 861 (m), 840 (m), 769 (m), 740 (w), 698 (vs) cm^{-1}.

IR spectroscopy (RT, in CH_2Cl_2): *v* (NO) = 1821, 1783 cm^{-1}.

5.5.6 $[RuBr(NO)_2(PBn_3)_2]BF_4$

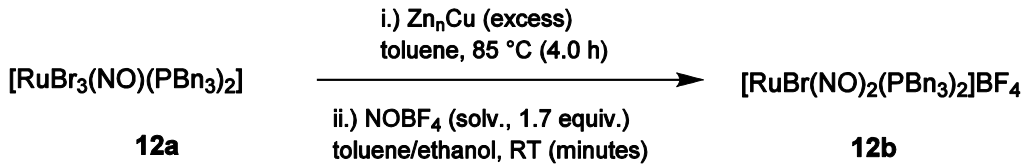

Starting substances: 12a ($[RuBr_3(NO)(PBn_3)_2]$), zinc-copper couple, toluene, ethanol, nitrosyl tetrafluoroborate, *n*-hexane.

Procedure: Compound **12a** (0.29 g, 0.30 mmol) and zinc-copper couple (2.0 g) were suspended in toluene (20 mL) and heated at 85 °C for 4 hours. The initially orange suspension turned dark-green. After cooling to ambient temperature, the suspension was filtered in order to remove excess alloy. Afterwards a solution of $NOBF_4$ (0.059 g, 0.51 mmol) in toluene/ethanol (10 mL/1.3 mL) was added, whereupon an instantaneous colour change from green to brown occurred. After half an hour a bright orange precipitate formed which was filtered off and washed with *n*-hexane.

Empirical formula: $C_{42}H_{42}BBrF_4N_2O_2P_2Ru$ (936.52 g mol^{-1}, **12b**).

Yield: 0.046 g (0.049 mmol), 16% of th., bright orange solid.

Elemental analysis (calcd. for $C_{42}H_{42}BBrF_4N_2O_2P_2Ru$, 936.52 g mol^{-1}), found (calcd.): C 51.69% (53.86%), H 4.84% (4.52%), N 2.74% (2.99%), Br (8.53%).

$^{31}P\{^1H\}$ NMR spectroscopy (CH_2Cl_2, 109 MHz): δ = 45.0 ppm.

MS: (M^+ = $C_{42}H_{42}BrN_2O_2P_2Ru$, 849.72 g mol^{-1}): FAB$^+$: *m/z* = 851.4 (Ru_1-pattern, $[M]^+$, calcd. 849.72), 821.4 (Ru_1-pattern, $[M - NO]^+$, calcd. 819.71).

IR spectroscopy (RT, solid), (intensity): *v* = 1812 (m, NO), 1776 (s, NO), 1601 (vw), 1496 (w), 1454 (w), 1407 (w), 1232 (vw), 1053 (s), 914 (w), 860 (m), 841 (m), 823 (w), 769 (m), 741 (m), 698 (vs) cm^{-1}.

IR spectroscopy (RT, in CH_2Cl_2): *v*(NO) = 1822, 1787 cm^{-1}.

5.5.7 $[RuCl(NO)_2(^tBuPPh_2)_2]BF_4$

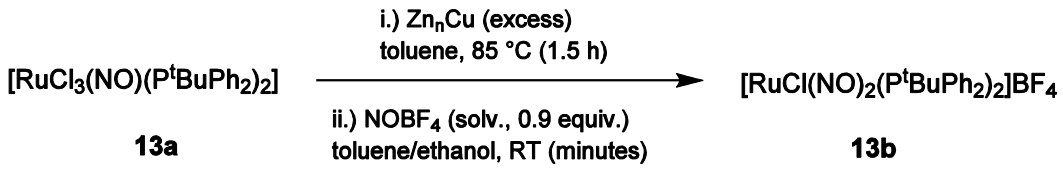

Starting substances: 13a ($[RuCl_3(NO)(PPh_2{}^tBu_3)_2]$), zinc-copper couple, toluene, ethanol, nitrosyl tetrafluoroborate, *n*-hexane.

Procedure: Compound **13a** (0.22 g, 0.38 mmol) and zinc-copper couple (1.1 g) were suspended in toluene (20 mL) and heated at 85 °C for 1.5 hours. The initially orange suspension turned dark green. After cooling to ambient temperature, the suspension was filtered in order to remove excess alloy. Afterwards a solution of $NOBF_4$ (0.040 g, 0.34 mmol) in toluene : ethanol (15 mL : 1.3 mL) was added, whereupon an instantaneous colour change from green to dark red occurred. *n*-Hexane was allowed to diffuse slowly into the solution via the gaseous phase. Thereby the solution turned bright yellow and a dark red oil could be detected at the bottom of the flask.

Empirical formula: $C_{32}H_{38}BClF_4N_2O_2P_2Ru$ (767.93 g mol^{-1}, **13b**).

MS: ($M^+ = C_{32}H_{38}ClN_2O_2P_2Ru$, 681.13 g mol^{-1}): FAB^+: *m/z* = 681.2 (Ru_1-pattern, $[M]^+$, calcd. 681.1), 651.2 (Ru_1-pattern, $[M - NO]^+$, calcd. 651.1).

IR spectroscopy (RT, solid), (intensity): *v* = 1813 (m, NO), 1714 (m, NO), 1474 (w), 1436 (m), 1401 (w), 1370 (w), 1282 (w), 1164 (m), 1052 (vs), 998 (s), 802 (m), 732 (s), 694 (vs) cm^{-1}.

5.5.8 $[RuCl(NO)_2\{P(p\text{-tolyl})_3\}_2]BF_4 \cdot C_7H_8$

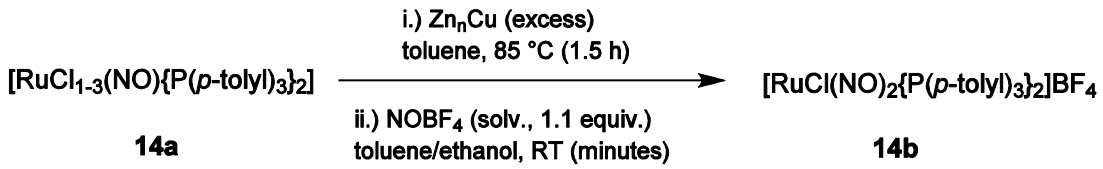

Starting substances: 14a [$RuCl_{1–3}(NO)\{P(p\text{-tolyl})_3\}_2$]), zinc-copper couple, toluene, ethanol, nitrosyl tetrafluoroborate, *n*-hexane.

Procedure: Compound **14a** (0.26 g, 0.31 mmol) and zinc-copper couple (1.4 g) were suspended in toluene (20 mL) and heated at 85 °C for 4 hours. The initially chartreuse suspension turned emerald green. After cooling to ambient temperature, the suspension was filtered in order to remove excess alloy. Afterwards a solution of $NOBF_4$ (0.040 g, 0.34 mmol) in toluene/ethanol (10 mL/1.3 mL) was added, whereupon an instantaneous colour change from green to brown occurred. Dark red crystals formed over night at room temperature, which were separated by filtration.

Empirical formula: $C_{42}H_{42}BClF_4N_2O_2P_2Ru \cdot C_7H_8$ (984.21 g mol^{-1}, **14b** $\cdot C_7H_8$)

Yield: 0.11 g (0.11 mmol), 35% of th., dark red crystals.

$^{31}P\{^1H\}$-NMR spectroscopy (CH_2Cl_2, 109 MHz): δ = 29.8 ppm.

MS: (M^+ = $C_{42}H_{42}ClN_2O_2P_2Ru$, 805.27 g mol^{-1}): FAB$^+$: *m/z* = 805.2 (Ru_1-pattern, $[M]^+$, calcd. 805.15), 775.1 (Ru_1-pattern, $[M - NO]^+$, calcd. 775.15).

IR spectroscopy (RT, solid), (intensity): *v* = 1816 (m, NO), 1766 (s, NO), 1596 (m), 1496 (w), 1445 (w), 1398 (w), 1310 (w), 1195 (w), 1094 (s), 1057 (vs), 1011 (s), 801 (s), 736 (m), 706 (w) cm^{-1}.

X-ray structure analysis: qn102 (see Fig. 2.17).

5.5.9 $[RuBr(NO)_2\{P(p\text{-tolyl})_3\}_2]BF_4$

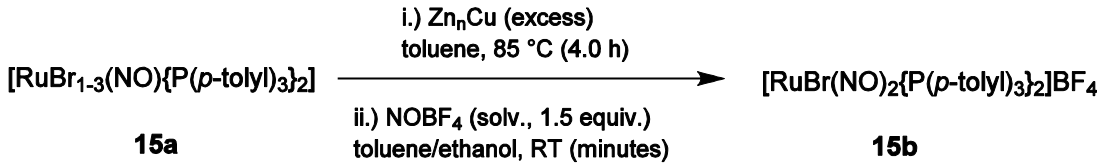

Starting substances: **15a** ($[RuBr_{1-3}(NO)\{P(p\text{-tolyl})_3\}_2]$, zinc-copper couple, toluene, ethanol, dichloromethane, nitrosyl tetrafluoroborate, dichloromethane, *n*-hexane.

Procedure: Compound **15a** (0.31 g, 0.31 mmol) and zinc-copper (1.8 g) were suspended in toluene (20 mL) and heated at 85 °C for 4 hours. The initially orange suspension turned dark green. After cooling to ambient temperature, the suspension was filtered in order to remove excess alloy. A solution of $NOBF_4$ (0.055 g, 0.47 mmol) in toluene : ethanol (10 mL : 1.3 mL) was added. A dark red crystalline solid and an orange powder precipitated immediately. The mixture was filtered off and recrystallised in dichloromethane and *n*-hexane. After several days, dark red crystals separated.

Empirical formula: $C_{42}H_{42}BBrF_4N_2O_2P_2Ru \cdot 0.3\ C_7H_8$ (936.52 g mol^{-1}, **15b** $\cdot 0.3\ C_7H_8$).

Yield: 0.16 g (0.18 mmol), 56% of th., dark red crystals, soluble in dichloromethane.

Elemental analysis (calcd. for $C_{42}H_{42}BBrF_4N_2O_2P_2Ru \cdot 0.3\ C_7H_8$ [1], 936.52 g mol^{-1}), found (calcd.): C 54.84% (54.94%), H 4.62 % (4.64%), N 2.99% (2.91%).

$^{31}P\{^1H\}$ NMR spectroscopy (CH_2Cl_2, 109 MHz): δ = 25.9 (s) ppm.

MS: ($M^+ = C_{42}H_{42}BrN_2O_2P_2Ru$, 849.72 g mol^{-1}): FAB$^+$: *m/z* = 851.2 (Ru_1-pattern, $[M]^+$, calcd. 851.09), 821.2 (Ru_1-pattern, $[M - NO]^+$, calcd. 821.10).

IR spectroscopy (RT, solid), (intensity): *v* = 1815 (s, NO), 1776 (vs, NO), 1596 (m), 1496 (w), 1454 (w), 1398 (w), 1195 (w), 1057 (vs), 1033 (vs), 1011 (vs), 801 (s), 736 (m), 697 (w) cm^{-1}.

X-ray structure analysis: qo067 (see Fig. 2.18).

[1]Contamination with toluene was calculated using Jasper v2.0; http://www.chem.yorku.ca/profs/potvin/Jasper/jasper2.htm

5.5.10 $[RuCl(NO)_2\{P(p\text{-anisyl})_3\}_2]BF_4$

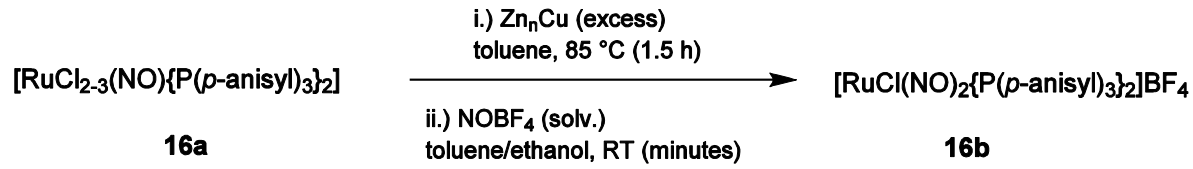

Starting substances: 16a ($[RuCl_{1-3}(NO)\{P(p\text{-anisyl})_3\}_2]$, zinc-copper couple, toluene, ethanol, dichloromethane, nitrosyl tetrafluoroborate, *n*-hexane.

Procedure: Compound **16a** (0.28 g) and zinc-copper (1.2 g) were suspended in toluene (20 mL) and heated at 85 °C for 1.5 hours. The initially orange suspension turned dark green. After cooling to ambient temperature, the suspension was filtered in order to remove excess alloy. A solution of $NOBF_4$ (0.051 g, 0.44 mmol) in toluene/ethanol (20 mL/1.3 mL) was added. The orange red solution was reduced *in vacuo* to a volume of 32 mL and stored at 4 °C. After several days a red oil formed, which was characterised by mass spectrometry as well as IR and NMR spectroscopy.

Empirical formula: $C_{42}H_{42}BClF_4N_2O_8P_2Ru$ (988.07 g mol^{-1}, **16b**).

$^{31}P\{^1H\}$-NMR spectroscopy (CH_2Cl_2, 109 MHz): δ = 28.1 (s) ppm.

MS: (M^+ = $C_{42}H_{42}ClN_2O_8P_2Ru$, 901.26 g mol^{-1}): FAB$^+$: *m/z* = 901.3 (Ru_1-pattern, $[M]^+$, calcd. 901.11), 871.5 (Ru_1-pattern, $[M - NO]^+$, calcd. 871.12).

IR spectroscopy (RT, solid), (intensity): *v* = 1811 (w, NO), 1770 (w, NO), 1591 (s), 1566 (m), 1498 (s), 1459 (m), 1442 (w), 1409 (w), 1291 (m), 1258 (s), 1182 (s), 1097 (s), 1056 (s) 1019 (s), 829 (s), 801 (s), 732 (s), 696 (m) cm^{-1}.

5.5.11 $[RuBr(NO)_2(P(p\text{-anisyl})_3)_2]BF_4$

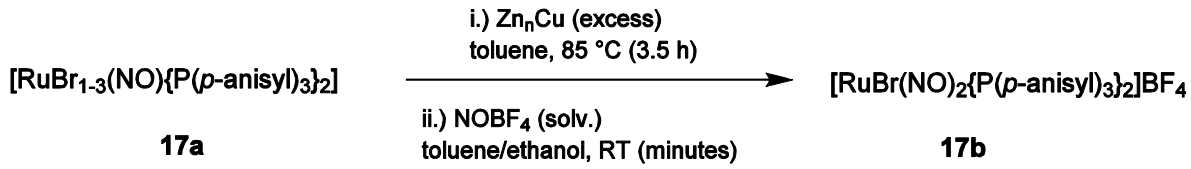

Starting substances: 17a ($[RuBr_{1-3}(NO)\{P(p\text{-anisyl})_3\}_2]$, zinc-copper couple, toluene, ethanol, dichloromethane, nitrosyl tetrafluoroborate.

Procedure: Compound **17a** (0.38 g) and zinc-copper (3.3 g) were suspended in toluene (25 mL) and heated at 85 °C for 3.5 hours. The initially orange suspension turned dark green. After cooling to ambient temperature, the suspension was filtered in order to remove excess alloy. A solution of $NOBF_4$ (0.071 g, 0.61 mmol) in toluene : ethanol (12.5 mL : 1.6 mL) was added. The brown solution was reduced *in vacuo* to a volume of 24 mL and stored at 4 °C. After several days, a brown oil formed, which was characterised by mass spectrometry as well as IR and NMR spectroscopy.

Empirical formula: $C_{42}H_{42}BBrF_4N_2O_8P_2Ru$ (1032.52 g mol^{-1}, **17a**).

$^{31}P\{^1H\}$-NMR spectroscopy (CH_2Cl_2, 109 MHz): δ = 23.8 (s) ppm.

MS: ($M^+ = C_{42}H_{42}BrN_2O_8P_2Ru$, 945.72g mol^{-1}): FAB$^+$: *m/z* = 947.4 ($Ru_1$-pattern, $[M]^+$, calcd. 945.72), 917.4 (Ru_1-pattern, $[M - NO]^+$, calcd. 915.71).

IR spectroscopy (RT, solid), (intensity): *v* = 1868 (vw, NO), 1809 (vw, NO), 1773 (w, NO), 1591 (s), 1566 (w), 1498 (s), 1459 (w), 1442 (w), 1409 (vw), 1290 (m), 1258 (s), 1182 (s), 1121 (m), 1094 (s), 1054 (m) 1019 (vs), 879 (w), 828 (m), 800 (m), 731 (s), 695 (m), 674 (m) cm^{-1}.

5.5.12 $[RuCl(NO)_2(PCy_3)_2]BF_4$

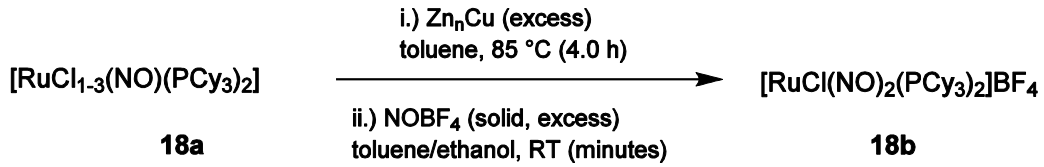

Starting substances: **18a** ($[RuCl_{1-3}(NO)(PCy_3)_2]$), zinc-copper couple, toluene, ethanol, dichloromethane, nitrosyl tetrafluoroborate.

Procedure: Compound **18a** (0.33 g) and zinc-copper couple (2.8 g) were suspended in toluene (57 mL) and heated at 85°C for 4 hours. The initially orange suspension turned dark green. After cooling to 50°C, the suspension was filtered in order to remove excess alloy. To the resulting solution first ethanol (1.3 mL) and then $NOBF_4$ (in small quantities) were added until the colour changed from dark green to red-orange. Overnight red-orange crystals could be obtained.

Empirical formula: $C_{36}H_{66}BClF_4N_2O_2P_2Ru$ (844.20 g mol^{-1}, **18b**).

Yield: 0.080 g (0.095 mmol), red-orange crystals, soluble in dichloromethane.

Elemental analysis (calcd. for $C_{36}H_{66}BClF_4N_2O_2P_2Ru$, 844.20 g mol^{-1}), found (calcd.): C 51.06% (51.22%), H 7.30% (7.88%), N 3.28% (3.32%).

$^{31}P\{^1H\}$ NMR spectroscopy (CH_2Cl_2, 270 MHz): δ = 51.3 (s) ppm.

MS: ($M^+ = C_{36}H_{66}ClN_2O_2P_2Ru^+$, 757.39 g mol^{-1}): FAB$^+$: *m/z* = 758.0 (Ru_1-pattern, $[M]^+$, calcd. 758.34), 728.0 (Ru_1-pattern, $[M - NO]^+$, calcd. 728.34).

IR spectroscopy (RT, solid), (intensity): *v* = 2928 (w), 2849 (w), 1789 (m, NO), 1704 (m, NO), 1445 (w), 1176 (vw), 1046 (s), 889 (vw), 851 (w), 732 (w), 636 (w), 620 (vw) cm^{-1}.

IR spectroscopy (RT, in CH_2Cl_2): *v*(NO) = 1812, 1706 cm^{-1}.

X-ray structure analysis: qv027 (see Fig. 2.19).

5.5.13 $[RuBr(NO)_2(PCy_3)_2]BF_4$

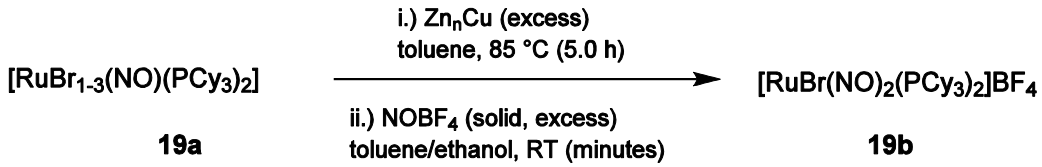

Starting substances: **19a** ($[RuBr_{1-3}(NO)(PCy_3)_2]$ zinc-copper couple, toluene, ethanol, dichloromethane, nitrosyl tetrafluoroborate, *n*-hexane.

Procedure: Compound **19a** (0.556 g) and zinc-copper couple (3.11 g) were suspended in toluene (40 mL) and heated at 85°C for 5 hours. The initially orange suspension turned dark green. After cooling to ambient temperature, the suspension was filtered in order to remove excess alloy. First ethanol (1.3 mL) and then $NOBF_4$ (s) were added to the solution at 50 °C. Overnight an orange-red precipitate formed which was filtered off and recrystallised in dichloromethane and *n*-hexane.

Empirical formula: $C_{36}H_{66}BBrF_4N_2O_2P_2Ru \cdot CH_2Cl_2$(888.65 g mol^{-1}, **19b**·CH_2Cl_2).

Yield: 0.419 g (0.426 mmol), orange-red powder, soluble in dichloromethane.

Elemental analysis (calcd. for $C_{38}H_{66}BBrCl_2F_4N_2O_2P_2Ru$, 983.57 g mol^{-1}), found (calcd.): C 45.51% (45.65%), H 7.14% (7.04%), N 2.97% (2.88%).

$^{31}P\{^1H\}$ NMR spectroscopy (CH_2Cl_2, 270 MHz): δ = 50.4 (s) ppm.

MS: ($M^+ = C_{36}H_{66}BrN_2O_2P_2Ru^+$, 888.65 g mol^{-1}): FAB$^+$: *m/z* = 804.1 (Ru_1-pattern, $[M]^+$, calcd. 803.28), 774.0 (Ru_1-pattern, $[M - NO]^+$, calcd. 773.28).

IR spectroscopy (RT, solid), (intensity): *v* = 2925 (w), 2851 (w), 1785 (m, NO), 1714 (m, NO), 1445 (w), 1270 (vw), 1177 (vw), 1047 (vs), 1003 (m), 889 (vw), 851 (w) cm^{-1}.

IR spectroscopy (RT, in CH_2Cl_2): *v*(NO) = 1800, 1760, 1716 cm^{-1}.

X-ray structure analysis: qq031 (see Fig. 2.20).

5.5.14 $[RuI(NO)_2(PCy_3)_2]BF_4$

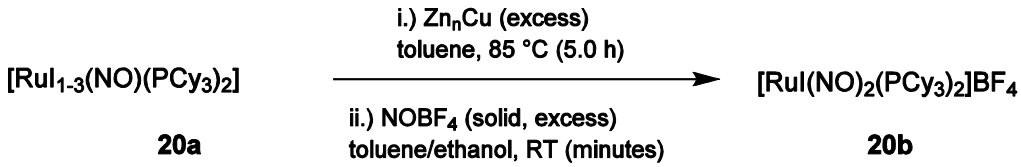

Starting substances: 20a [$RuI_{1-3}(NO)(PCy_3)_2$], zinc-copper couple, toluene, ethanol, dichloromethane, nitrosyl tetrafluoroborate, diethyl ether.

Procedure: Compound **20a** (0.11 g) and zinc-copper couple (2.7 g) were suspended in toluene (17 mL) and heated at 85°C for 5 hours. The initially orange suspension turned dark green. After cooling to ambient temperature, the suspension was filtered in order to remove excess alloy. Ethanol (1 mL) was added to the solution at 40°C. Solid nitrosyl tetrafluoroborate was added at the same temperature. Overnight reddish brown crystals separated which were washed with diethyl ether and dried *in vacuo*.

Empirical formula: $C_{36}H_{66}BF_4IN_2O_2P_2Ru$ (935.65 g mol^{-1}, **20b**).

Yield: 0.097 g (0.10 mmol), reddish brown crystals, soluble in dichloromethane.

Elemental analysis (calcd. for $C_{36}H_{66}BF_4IN_2O_2P_2Ru$, 935.65 g·$mol^{-1}$), found (calcd.): C 45.01% (46.21%), H 6.84% (7.11%), N 2.86% (2.99 %).

$^{31}P\{^1H\}$ NMR spectroscopy (CH_2Cl_2, 270 MHz): δ = 45.8 (s) ppm.

MS: ($M^+ = C_{36}H_{66}BF_4IN_2O_2P_2Ru^+$, 935.65 g mol^{-1}): FAB^+: *m/z* = 849.9 (Ru_1-pattern, $[M]^+$, calcd. 849.27), 819.9 (Ru_1-pattern, $[M - NO]^+$, calcd. 819.27).

IR spectroscopy (RT, solid), (intensity): *v* = 2928 (m), 2855 (w), 1788 (m, NO), 1751 (m, NO), 1445 (m), 1271 (vw), 1213 (vw), 1174(vs), 1118 (w), 1049 (m), 889 (w), 851 (w), 744 (w) cm^{-1}.

IR spectroscopy (RT, in CH_2Cl_2): *v*(NO) = 1797, 1765 cm^{-1}.

X-ray structure analysis: qo129 (see Fig. 2.21).

5.5.15 $[RuCl(NO)_2(PCyp_3)_2]BF_4$

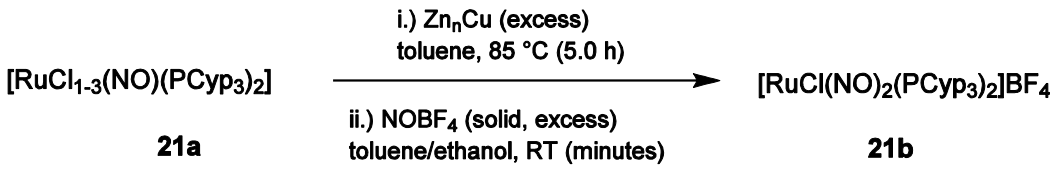

Starting substances: **21a** ($[RuCl_{1–3}(NO)(PCyp_3)_2]$), zinc-copper couple, toluene, ethanol, dichloromethane, nitrosyl tetrafluoroborate, diethyl ether.

Procedure: Compound **21a** (0.504 g) and zinc-copper couple (1.55 g) were suspended in toluene (54 mL) and heated at 85°C for 5 hours. The initially orange suspension turned dark green. After cooling to 50°C, the suspension was filtered in order to remove excess alloy. To the resulting solution first ethanol (1.8 mL) and then $NOBF_4$ (in small quantities) were added until the colour changed from dark green to red-orange. Overnight orange crystals could be obtained which were filtered off, washed with diethyl ether and dried *in vacuo*.

Empirical formula: $C_{30}H_{54}BClF_4N_2O_2P_2Ru$ (760.04 g mol^{-1}, **21b**).

Yield: 0.112 g, orange crystals, soluble in dichloromethane.

$^{31}P\{^1H\}$ NMR spectroscopy (CH_2Cl_2, 270 MHz): δ = 48.2 (s) ppm.

MS: ($M^+ = C_{30}H_{54}ClN_2O_2P_2Ru^+$, 673.23 g mol^{-1}): FAB$^+$: *m/z* = 673.2436 (Ru_1-pattern, $[M]^+$, calcd. 673.2398), 643.2435 (Ru_1-pattern, $[M - NO]^+$, calcd. 643.2418).

IR spectroscopy (RT, solid), (intensity): *v* = 2954 (w), 2870 (w), 1805 (m, NO), 1681 (m, NO), 1449 (w), 1087 (m), 1044 (vs), 714 (m) cm^{-1}.

IR spectroscopy (RT, in CH_2Cl_2): *v*(NO) = 1834, 1797, 1754, 1710 cm^{-1}.

X-ray structure analysis: qq041 (block, Fig. 2.23), rv021 (rod, Fig. 2.22).

5.5.16 $[RuBr(NO)_2(PCyp_3)_2]BF_4$

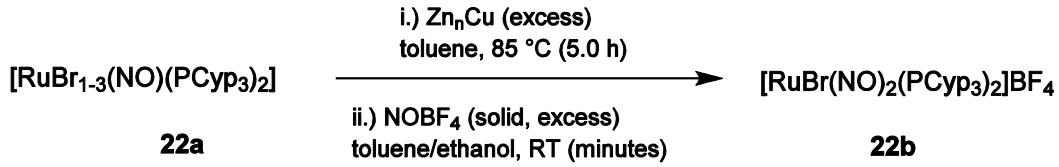

Starting substances: 22a ($[RuBr_{1-3}(NO)(PCyp_3)_2]$), zinc-copper couple, toluene, ethanol, dichloromethane, nitrosyl tetrafluoroborate, diethyl ether.

Procedure: Compound **22a** (0.588 g) and zinc-copper couple (1.30 g) were suspended in toluene (44 mL) and heated at 85°C for 5 hours. The initially orange suspension turned dark green. After cooling to 40°C, the suspension was filtered in order to remove excess alloy. To the resulting solution first ethanol (1.3 mL) and then $NOBF_4$ (in small quantities) were added until the colour changed from dark green to red-orange. Overnight red-orange crystals could be obtained which were washed with diethyl ether and dried *in vacuo*.

Empirical formula: $C_{30}H_{54}BBrF_4N_2O_2P_2Ru$ (804.49 g mol^{-1}, **22b**).

Yield: 0.156 g, red crystals, soluble in dichloromethane.

Elemental analysis (calcd. for $C_{36}H_{66}BBrF_4N_2O_2P_2Ru$, 804.49 g mol^{-1}), found (calcd.): C 44.60% (44.79%), H 6.47% (6.77%), N 3.45% (3.48%).

$^{31}P\{^1H\}$ NMR spectroscopy (CH_2Cl_2, 270 MHz): δ = 43.7 (s) ppm.

MS: ($M^+ = C_{36}H_{66}BrN_2O_2P_2Ru^+$, 717.68 g mol^{-1}): FAB$^+$: *m/z* = 719.8 (Ru_1-pattern, $[M]^+$, calcd. 719.19), 689.9 (Ru_1-pattern, $[M - NO]^+$, calcd. 689.19).

IR spectroscopy (RT, solid), (intensity): *v* = 2958 (w), 2867 (w), 1810 (w, NO), 1770 (m, NO), 1448 (vw), 1299 (vw), 1245 (vw), 1137 (vw), 1085 (m), 1045 (vs), 906 (w), 193 (w) cm^{-1}.

IR spectroscopy (RT, in CH_2Cl_2): *v*(NO) = 1795, 1759 cm^{-1}.

X-ray structure analysis: qo145 (see Fig. 2.24).

5.5.17 $[RuI(NO)_2(PCyp_3)_2]BF_4$

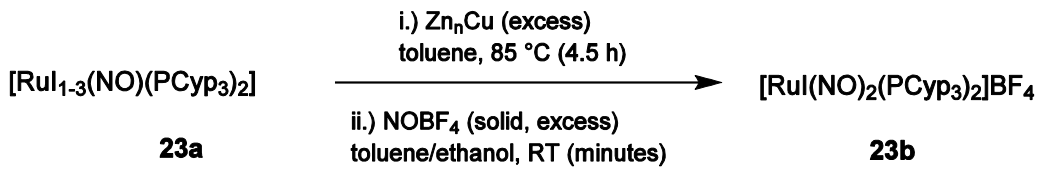

Starting substances: **23a** ($[RuI_{1-2}(NO)(PCyp_3)_2]$), zinc-copper couple, toluene, ethanol, dichloromethane, nitrosyl tetrafluoroborate.

Procedure: Compound **23a** (1.09 g) and zinc-copper couple (2.09 g) were suspended in toluene (38 mL) and heated at 85°C for 4.5 hours. The initially orange suspension turned dark green. After cooling to 50°C, the suspension was filtered in order to remove excess alloy. To the resulting solution first ethanol (3.3 mL) and then $NOBF_4$ (in small quantities) were added until the colour changed from dark green to red-orange. During the course of several days, few reddish brown crystals could be obtained.

Empirical formula: $C_{30}H_{54}BF_4IN_2O_2P_2Ru$ (851.49 g mol^{-1}, **23b**).

Yield: 0.22 g (0.26 mmol), reddish brown crystals, soluble in dichloromethane.

Elemental analysis (calcd. for $C_{36}H_{66}BF_4IN_2O_2P_2Ru$, 851.49 g mol^{-1}), found (calcd.): C 42.15% (42.32%), H 6.35% (6.39%), I 14.06% (14.90%), N 3.33% (3.29%).

$^{31}P\{^1H\}$ NMR spectroscopy (CH_2Cl_2, 270 MHz): δ = 34.2 (s) ppm.

MS: ($M^+ = C_{36}H_{66}IN_2O_2P_2Ru^+$, 764.68 g mol^{-1}): FAB$^+$: *m/z* = 765.1716 (Ru_1-pattern, $[M]^+$, calcd. 765.1757), 735.1802 (Ru_1-pattern, $[M - NO]^+$, calcd. 735.1778).

IR spectroscopy (RT, solid), (intensity): *v* = 2947 (w), 2867 (w), 1809 (m, NO), 1772 (m, NO), 1448 (w), 1300 (vw), 1245 (w), 1138 (w), 1087 (m), 1046 (s), 907 (w), 764 (w), 633 (w), 618 (w) cm^{-1}.

IR spectroscopy (RT, in CH_2Cl_2): *v*(NO) = 1794, 1759 cm^{-1}.

X-ray structure analysis: qq069 (see Fig. 2.25).

5.5.18 $[RuCl(NO)_2(P^iPr_3)_2]BF_4$

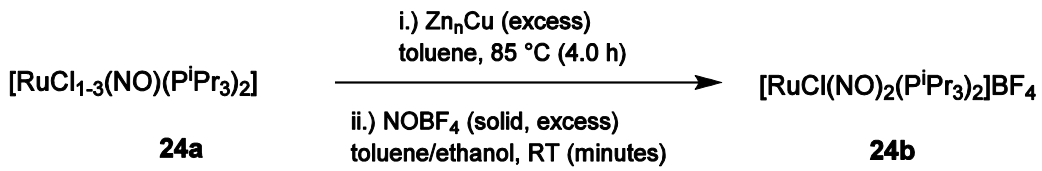

Starting substances: 24a ([$RuCl_{1–3}(NO)(P^iPr_3)_2$]), zinc-copper couple, toluene, ethanol, dichloromethane, nitrosyl tetrafluoroborate.

Procedure: Compound **24a** (0.285 g) and zinc-copper couple (2.30 g) were suspended in toluene (27.3 mL) and heated at 85°C for 4 hours. The initially orange suspension turned dark green. After cooling to 50°C, the suspension was filtered in order to remove excess alloy. To the resulting solution first ethanol (2.5 mL) and then $NOBF_4$ (in small quantities) were added until the colour changed from dark green to orange. After several hours, orange crystals could be obtained.

Empirical formula: $C_{18}H_{42}BClF_4N_2O_2P_2Ru$ (603.81 g mol^{-1}, **24b**).

Yield: 0.129 g, orange crystals, soluble in dichloromethane.

Elemental analysis (calcd. for $C_{18}H_{42}BClF_4N_2O_2P_2Ru$, 603.81 g mol^{-1}), found (calcd.): C 30.59% (38.93%), H 6.16% (7.78%), N 3.89% (4.32%).

$^{31}P\{^1H\}$ NMR spectroscopy (CH_2Cl_2, 270 MHz): δ = 61.7 (s) ppm.

MS: (M^+ = $C_{18}H_{42}ClN_2O_2P_2Ru^+$, 517.01 g mol^{-1}): FAB$^+$: *m/z* = 517.1461 (Ru_1-pattern, [*M*]$^+$, calcd. 517.1455), 487.1479 (Ru_1-pattern, [*M* − NO]$^+$, calcd. 487.1474).

IR spectroscopy (RT, solid), (intensity): *v* = 2974 (vw), 1808 (w, NO), 1682 (m, NO), 1459 (w), 1391 (vw), 1255 (w), 1091 (m), 1047 (vs), 1026 (vs), 883 (w), 795 (w), 652 (m) cm^{-1}.

IR spectroscopy (RT, in CH_2Cl_2): *v*(NO) = 1809, 1759, 1714 cm^{-1}.

X-ray structure analysis: rv114 (see Fig. 2.26).

5.5.19 $[RuBr(NO)_2(P^iPr_3)_2]BF_4$

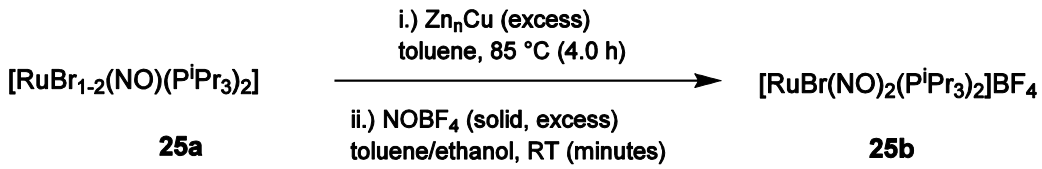

Starting substances: **25a** ($[RuBr_{1-3}(NO)(P^iPr_3)_2]$), zinc-copper couple, toluene, ethanol, dichloromethane, nitrosyl tetrafluoroborate, *n*-hexane.

Procedure: Compound **25a** (0.685 g) and zinc-copper couple (2.56 g) were suspended in toluene (55 mL) and heated at 85°C for 4 hours. The initially orange suspension turned dark green. After cooling to 50°C, the suspension was filtered in order to remove excess alloy. To the resulting solution first ethanol (2.5 mL) and then $NOBF_4$ (in small quantities) were added until the colour changed from dark green to red-orange. Overnight orange-brown crystals could be obtained.

Empirical formula: $C_{18}H_{42}BBrF_4N_2O_2P_2Ru$ (648.26 g mol^{-1}, **25b**).

Yield: 0.361 g, orange crystals, soluble in dichloromethane.

Elemental analysis (calcd. for $C_{18}H_{42}BBrF_4N_2O_2P_2Ru$, 648.26 g mol^{-1}), found (calcd.): C 34.28% (33.35%), H 6.81% (6.53%), N 3.99 % (4.32%).

$^{31}P\{^1H\}$ NMR spectroscopy (CH_2Cl_2, 270 MHz): δ = 59.8 (s), 41.9 (s) ppm.

MS: ($M^+ = C_{18}H_{42}BrN_2O_2P_2Ru^+$, 561.46 g mol^{-1}): FAB$^+$: *m/z* = 563.0953 (Ru_1-pattern, $[M]^+$, calcd. 563.0943), 531.0965 (Ru_1-pattern, $[M - NO]^+$, calcd. 531.0968).

IR spectroscopy (RT, solid), (intensity): *v* = 1797 (m, NO), 1744 (m, NO), 1689 (m, NO), 1461 (w), 1248 (w), 10921 (m), 1048 (vs), 1027 (vs), 880 (m), 673 (m), 648 (w) cm^{-1}.

IR spectroscopy (RT, in CH_2Cl_2): *v*(NO) = 1802, 1765 cm^{-1}.

X-ray structure analysis: qv016 (see Fig. 2.27 and Fig. 2.28).

5.5.20 $[RuI(NO)_2(P^iPr_3)_2]BF_4$

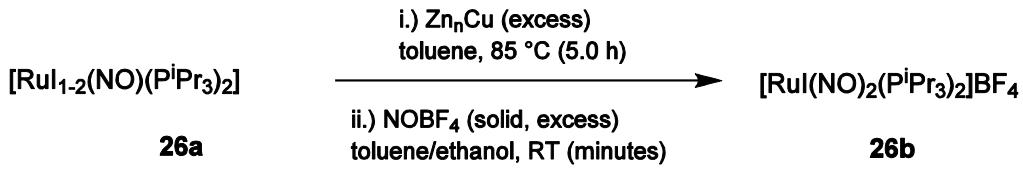

Starting substances: **26a** ($[RuI_{1-2}(NO)(P^iPr_3)_2]$), zinc-copper couple, toluene, ethanol, dichloromethane, nitrosyl tetrafluoroborate.

Procedure: Compound **26a** (0.336 g) and zinc-copper couple (2.39 g) were suspended in toluene (16 mL) and heated at 85°C for 5 hours. The initially orange suspension turned dark green. After cooling to 50°C, the suspension was filtered in order to remove excess alloy. To the resulting solution first ethanol (1.3 mL) and then $NOBF_4$ (in small quantities) were added until the colour changed from dark green to red-orange. During the course of several days, crystals formed.

Empirical formula: $C_{18}H_{42}BIF_4N_2O_2P_2Ru$ (695.26 g mol^{-1}, **26b**).

Yield: 0.019 g (0.027 mmol), fine, dark red crystals, soluble in dichloromethane and acetone.

Elemental analysis (calcd. for $C_{18}H_{42}BIF_4N_2O_2P_2Ru$, 695.26 g mol^{-1}), found (calcd.): C 31.66% (31.09%), H 6.31% (6.09%), N 4.14 % (4.03%).

$^{31}P\{^1H\}$ NMR spectroscopy (CH_2Cl_2, 270 MHz): δ = 53.2 (s) ppm.

MS: ($M^+ = C_{18}H_{42}IN_2O_2P_2Ru^+$, 608.46 g mol^{-1}): FAB$^+$: *m/z* = 609.0795 (Ru_1-pattern, $[M]^+$, calcd. 609.0815), 579.0803 (Ru_1-pattern, $[M - NO]^+$, calcd. 579.0835).

IR spectroscopy (RT, solid), (intensity): *v* = 2975 (w), 2938 (w), 2358 (w), 1790 (s, NO), 1748 (s, NO), 1713 (m, NO), 1659 (m), 1462 (m), 1389 (w), 1370 (w), 1297 (w), 1249 (m), 1162 (w), 1092 (s), 1047 (vs), 1026 (vs), 932 (m), 879 (m), 792 (w), 668 (s), 615 (m), 606 (m).

IR spectroscopy (RT, in CH_2Cl_2): *v*(NO) = 1801, 1768 cm^{-1}.

X-ray structure analysis: rv245.

5.5.21 $[\{Ru(NO)_2(P^iPr_3)\}_2(\mu\text{-}I)]BF_4$

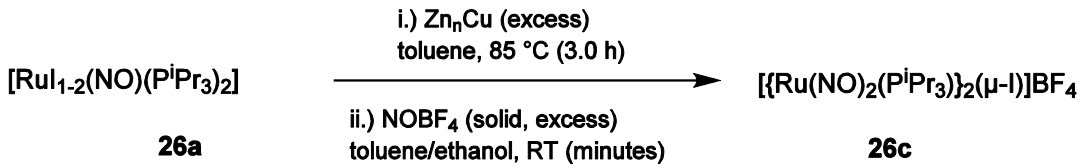

Starting substances: **26a** ($[RuI_{1-2}(NO)(P^iPr_3)_2]$), zinc-copper couple, toluene, ethanol, dichloromethane, nitrosyl tetrafluoroborate.

Procedure: Compound **26a** (0.887 g) and zinc-copper couple (2.00 g) were suspended in toluene (40 mL) and heated at 85°C for 3 hours. The initially orange suspension turned dark green. After cooling to 55°C, the suspension was filtered in order to remove excess alloy. To the resulting solution first ethanol (3.0 mL) and then $NOBF_4$ (in small quantities) were added until the colour changed from dark green to red-orange. Overnight orange-brown crystals could be obtained.

Empirical formula: $C_{18}H_{42}BIF_4N_4O_4P_2Ru_2$ (856.34 g mol^{-1}, **26b**).

Yield: 0.374 g (0.495 mmol), fine, dark red crystals, soluble in dichloromethane and acetone.

Elemental analysis (calcd. for $C_{18}H_{42}BIF_4N_4O_4P_2Ru_2$, 856.34 g mol^{-1}), found (calcd.): C 25.55% (25.25%), H 5.05% (4.94%), N 6.49 % (6.54%).

$^{31}P\{^1H\}$ NMR spectroscopy (CH_2Cl_2, 270 MHz): δ = 80.2 (s), 42.1 (s) ppm.

MS: ($M^+ = C_{18}H_{42}IN_2O_2P_2Ru^+$, 769.53 g mol^{-1}): FAB$^+$: *m/z* = 770.4 (Ru_2-pattern, $[M]^+$, calcd. 771.0), 740.4 (Ru_2-pattern, $[M - NO]^+$, calcd.), 709.4 (Ru_2-pattern, $[M - 2\ NO]^+$, calcd.).

IR spectroscopy (RT, solid), (intensity): *v* = 2975 (vw), 2361 (vw), 1781 (w), 1738 (m), 1704 (m), 1459 (w), 1388 (w), 1247 (vw), 1160 (vw), 1089 (m), 1046 (vs), 1024 (vs), 933 (w), 882 (w), 670 (m), 647 (w), 614 (w).

IR spectroscopy (RT, in CH_2Cl_2): *v*(NO) = 1797 (s), 1756 (s) and 1734 (m) cm^{-1}.

X-ray structure analysis: rv366 (see Fig. 2.38).

5.6 {RuNO}^{8} intermediate products and {RuNO}^{6} side products

5.6.1 [RuCl(NO)(PPh$_3$)$_2$]

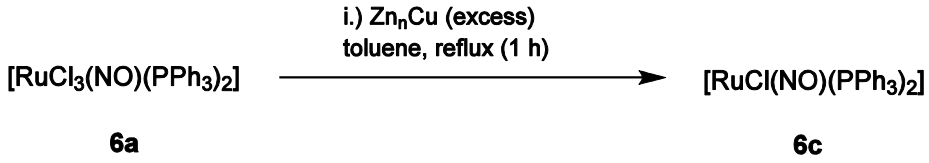

Literature: D. Morales-Morales, R. Redón, R.E. Cramer, *Inorg. Chimica Acta.* **2001**, *321*, 181–184.

Starting materials: 6a ([RuCl$_3$(NO)(PPh$_3$)$_2$], zinc-copper couple, toluene, n-pentane.

Procedure: Compound **6a** (0.902 g, 1.18 mmol) and an alloy of zinc-copper (1.21 g) were suspended in toluene (40 mL) and heated under refluxing conditions for 1 h. The initially chartreuse suspension turned green during the course of the reaction. The hot suspension was filtered in order to remove excess alloy. Upon cooling, dark green crystals formed. The yield could be increased by concentrating the solution to approximately 3 mL *in vacuo*. The mother liquor was pipetted off, the solid was washed with n-pentane and dried *in vacuo*.

Empirical formula: $C_{36}H_{30}ClNOP_2Ru$ (691.10 g mol^{-1}, **6c**).

Yield: 0.502 g (0.726 mmol, 61.5%).

Elemental analysis: (calcd. for $C_{36}H_{30}ClNOP_2Ru \cdot 0.25\ C_7H_8$, 714.13 g mol^{-1}), found (calcd.): C 63.49% (63.14%), H 4.54% (4.52%), N 1.60% (1.96%).

^{31}P{^{1}H} NMR spectroscopy (CH_2Cl_2, 109 MHz): δ = 33.6 (s) ppm.

MS: (*M* = $C_{36}H_{30}ClNOP_2Ru$, 691.10 g mol^{-1}): FAB$^+$: *m/z* = 691.5 (Ru_1-pattern, [*M*]$^{\cdot+}$, calcd. 691.0535).

IR spectroscopy (RT, solid), (intensity): *v* = 1767 (w, NO), 1729 (s, NO), 1478 (m), 1433 (m), 1261 (w), 1182 (w), 1092 (s), 1026 (w), 997 (w), 801 (w), 747 (s), 713 (m), 691 (vs), 618 (w), 604 (w) cm^{-1}.

X-ray structure analysis: qq081 (see Fig. 2.3).

5.6.2 [RuCl(NO)(P^tBuPh_2)$_2$]

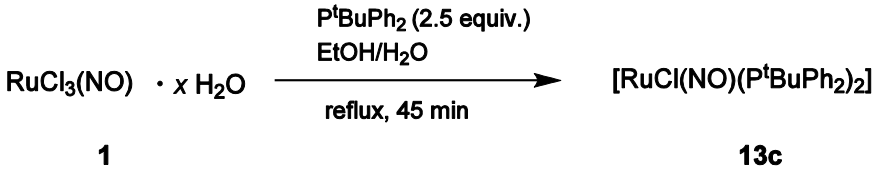

Starting materials: 1 ([$RuCl_3(NO) \cdot x\ H_2O$], P^tBuPh_2 (*tert*-butyldiphenylphosphane), ethanol.

Procedure: Compound **1** (0.421 g, 1.65 mmol), dissolved in ethanol (20 mL), was added to a solution of *tert*-butyldiphenylphosphane (1.00 g, 4.13 mmol) in hot ethanol (10 mL). The reaction mixture was kept under refluxing conditions for 45 minutes. After cooling the mixture to ambient temperature, the resulting suspension was filtered. The green filtrate was stored at 4 °C. After several days, dark green crystals formed.

Empirical formula: $C_{32}H_{38}ClNOP_2Ru$ (651.12 g mol^{-1}, **13c**).

IR spectroscopy (RT, solid), (intensity): *v* = 3405 (vw), 3077 (vw), 2964 (vw), 2926 (vw), 2898 (vw), 2865 (vw), 2359 (vw), 2339 (vw), 1770 (vw), 1714 (s, NO), 1586 (vw), 1571 (vw), 1478 (w), 1459 (vw), 1433 (m), 1392 (w), 1366 (w), 1357 (vw), 1310 (vw), 1260 (w), 1179 (w), 1157 (w), 1092 (s), 1016 (w), 999 (w), 937 (vw), 878 (vw), 808 (w), 745 (vs), 693 (vs) cm^{-1}.

X-ray structure analysis: qn226 (see Fig. 2.6).

5.6.3 $[\{RuBr_2(NO)(PPh_3)\}_2(\mu\text{-}Br)_2]$

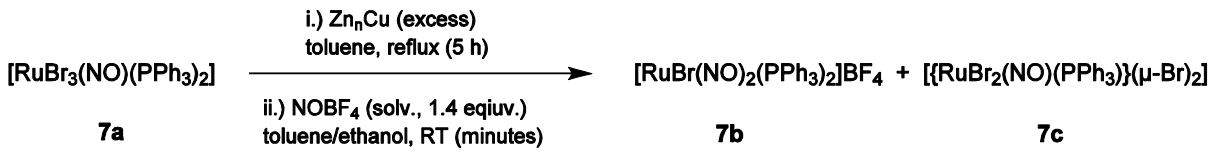

Starting materials: 7a ($[RuCl_3(NO)(PPh_3)_2]$), zinc-copper couple, toluene, nitrosyl tetrafluoroborate, *n*-hexane.

Procedure: Compound **7a** (0.27 g, 0.30 mmol) and an alloy of zinc-copper (0.35 g) were suspended in toluene (25 mL) and heated under refluxing conditions for 5 h. The initially light green suspension turned dark green during the course of the reaction. For removal of excess alloy the suspension was filtered. Afterwards a solution of $NOBF_4$ (0.049 g, 0.42 mmol) in toluene : ethanol (25 mL : 1.3 mL) was added, whereupon a rapid colour change from dark green to red orange occurred. Crystals, which could be analyzed as the dinitrosyl, formed upon storing at 4 °C and were filtered off. The solution was reduced *in vacuo* to three quarter of the original volume. Storing at 4 °C yielded red, platelet like crystals.

Empirical formula: $C_{36}H_{30}Br_6N_2O_2P_2Ru_2$ (1266.15 g mol^{-1}, **7c**).
X-ray structure analysis: qn038 (see Fig. 2.4).

5.6.4 $[\{RuI_2(NO)(PPh_3)\}_2(\mu\text{-}I)_2]$

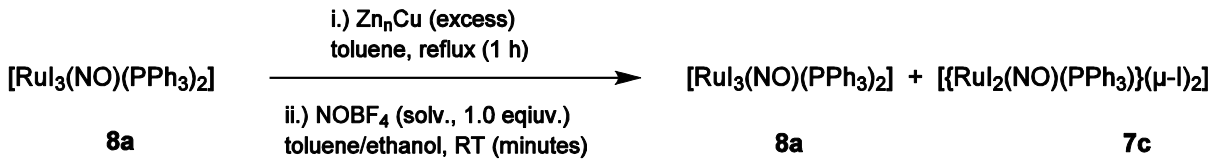

Starting materials: 8a ($[RuI_3(NO)(PPh_3)_2]$), zinc-copper couple, toluene, nitrosyl tetrafluoroborate, *n*-hexane.

Procedure: Compound **8a** (0.31 g, 0.30 mmol) and an alloy of zinc-copper (0.44 g) were suspended in toluene (24 mL) and heated under refluxing conditions for 1 h. Instead of turning green, the red suspension only deepened in colour. For removal of excess alloy the suspension was filtered. Afterwards a solution of $NOBF_4$ (0.035 g, 0.30 mmol) in toluene : ethanol (24 mL : 1.3 mL) was added, whereupon no visible colour change occurred. Hexagonal, platelet like, red crystals formed within one day and were filtered off. On concentrating the solution *in vacuo* to a volume of 33 mL, dark red rod like crystals formed.

Empirical formula: $C_{36}H_{30}I_6N_2O_2P_2Ru_2$ (1548.15 g mol^{-1}, **8c**), $C_{36}H_{30}I_3NOP_2Ru$ (1036.36 g mol^{-1}, **8a**).
X-ray structure analysis: pn394 (**8c**, rods, see Fig. 2.5), pn393 (**8a**, platelets, see Fig. 2.2).

5.7 Methods for the description of geometrical parameters

Coordination chemistry uses various geometric solids to obtain a systematic description of the numerous possible coordination figures. For the assignment of the coordination polyhedron formed by the first coordination sphere—which is comprised of the donor atoms attached to the metal centre and the metal centre itself—to ideal geometries, both τ_5-value analysis as well as continuous shape measurement (CShM) were applied in this work.

The analysis of the τ_5-value—deduced and first applied by Addison et *al.*[115]—enables the differentiation in trigonal bipyramidal and square planar pyramidal geometries. It further allows the qualitative estimate of the deviation from ideal geometries and indicates how far the structure is along the transformation path from one geometry to the other, in this case along the Berry pathway. For its application see Fig. 5.1. The value is calculated according to the formula shown below and was taken from the respective crystallographic .lis-files.

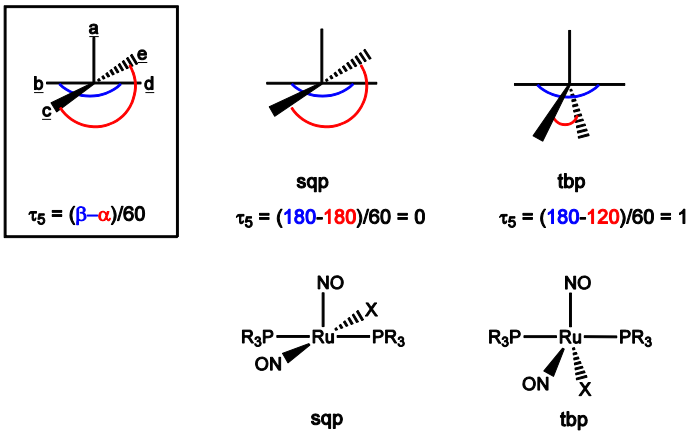

Fig. 5.1: Schematic representation for the determination of Addison's τ_5 value, α and β are the largest and second largest bond angles around the central atom.

A second tool for the geometrical description of coordination compounds is Alvarez's continuous shape measure.[116] The Platonic, the Archimedean and the Johnson solids as well as prisms and antiprisms serve as reference polyhedra. In this context, pentacoordination gives rise to five different geometries: The pentagon (*PP*-5), the vacant octahedron or Johnson square pyramid (*VOC*-5, J1), the trigonal bipyramid (*TBPY*-5), the square pyramid (*SPY*-5) and the Johnson trigonal bipyramid (*JTBPY-5*, J12). *PP*-5, *TBPY*-5 and *SPY*-5 are spherical reference shapes, meaning that the vertices have the same distance from the geometric centre. The non-spherical reference shapes are more adequate to describe edge-bonded polyhedral molecules such as boranes and metal clusters, whereas the spherical ones are more appropriate for the description of coordination polyhedra.
While the τ_5 value allows only the differentiation between two possible structures (tbp and sqp), the continuous shape measurement (CShM) enables the distinction between all five different geometries (the relevant denotations are shown in Fig. 5.2). Additionally, the shape maps allow a statement on the magnitude of deviation from a polyhedral interconversion path.

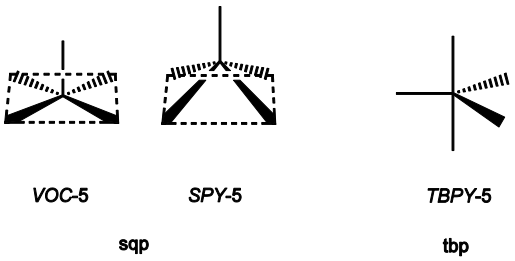

Fig. 5.2: Addison's τ_5 value differentiates only in sqp and tbp, wheras the CShM value takes into account the hight with which the central atom is situated above the basal plane.

The shape measure (S_P(R)) is derived from the distance of the equivalent atomic positions (q_k) in the reference shape and the respective structure and *N* as a normalisation factor to gain size independent values:

$$S_{\mathrm{P}}(\mathrm{R}) = \frac{\sum_{k=1}^{N} q_k^2}{N} \times 100 \tag{5.1}$$

From the definition of the equation given above, it is clear that the S_P(R) value lies between 0 and 100. The value reaches zero if the problem structure *P* and the reference structure *R* have the same shape and will increase with the degree of distortion.

For the stereochemical analysis of compounds which differ only slightly in geometrical parameters, it may be useful to differentiate between two alternative reference geometries (*P* and *T*), since this allows the generation of a shape map in which the adopted shapes can be plotted and easily compared to one another (see Fig. 5.3). Additionally, the lower left region of such a shape map corresponds to the minimum interconversion path between the two reference polyhedra. The shape measures of all structures *X* along such an interconversion path must obey the following equation:

$$\arcsin\frac{\sqrt{S_X(P)}}{10} + \arcsin\frac{\sqrt{S_X(T)}}{10} = \theta_{PT} \tag{5.2}$$

where θ_{PT} is the symmetry angle, a constant for each pair of polyhedra. Structures whose shape measures are not on the distortion path do not obey equation 5.2. Their deviation from this path can be calculated from the following equation:

$$\Delta_i(P,T) = \frac{1}{\theta_{PT}}\left[\arcsin\frac{\sqrt{S_i(P)}}{10} + \arcsin\frac{\sqrt{S_i(T)}}{10}\right] - 1 \tag{5.3}$$

This equation is referred to as path deviation function, where *i* refers to an arbitrary structure.

The disadvantage of the τ_5 value clearly shows in Fig. 5.3. It differentiates only between tbp and sqp. It does not allow for discrimination between *SPY*-5 and *VOC*-5, and accordingly, it does not discriminate between structures along the Berry path and those along the non-Berry path from *TBPY*-5 to *VOC*-5. Additionally it gives values > 1 for the umbrella opening or closing, which is favoured by tripod ligands. Thus, the continuous shape measurement has some advantages.

The CShM values were calculated with the program SHAPE, Version 2.0, by using the *x*, *y*, *z* values of the central atom and the donor atoms, derived from the respective crystal structures.

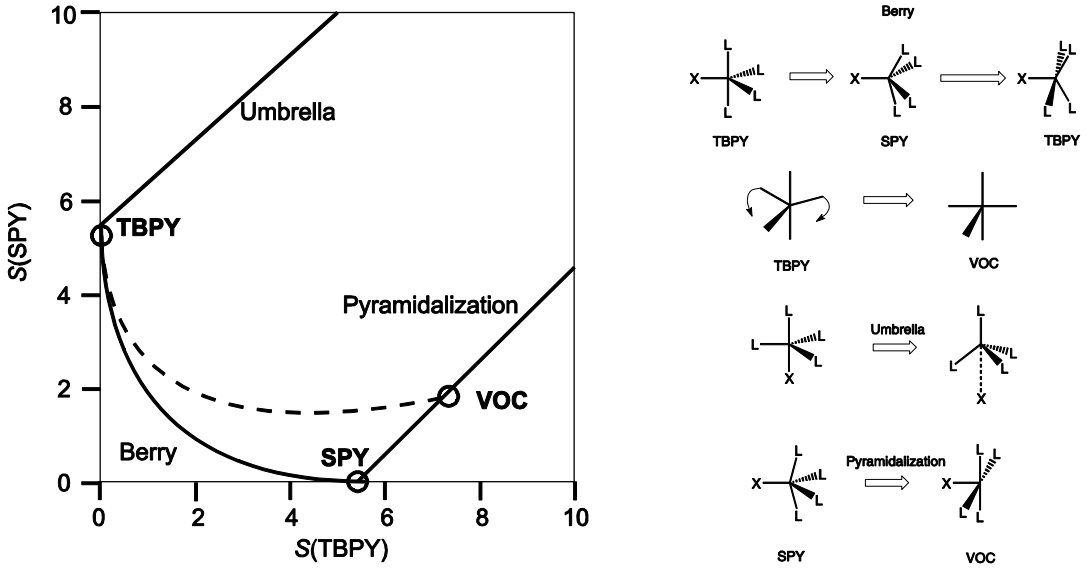

Fig. 5.3: Shape map for geometrical distortions of the trigonal bipyramid (*TBPY*-5) and the Berry square pyramid (*SPY*-5). The circles indicate the positions of the ideal shapes labelled in boldface. The dashed line indicates the path from the TBPY to the vacant octahedron (VOC), referred to as pseudo-Berry path. Copied from Reference [116].

5.8 Crystal structure determination and refinement

Crystals suitable for single-crystal X-ray diffraction were selected using a microscope (Leica MZ6 with polarisation filters), covered with paraffin oil and mounted either on a micro mount or a loop. The measurements were performed at 100, 103, 173 or 200 K on the following diffractometers: Enraf-Nonius Kappa-CCD, Oxford XCalibur 3 diffractometer, d8Venture diffractometer or d8Quest diffractometer with graphite-monochromated Mo-K_α radiation (λ = 0.71073 Å). The structures were solved by direct or Patterson methods (SIR-93[144], SHELXS-97[145]) and refined by full-matrix, least-squares calculations on F^2 (SHELXL-97[146]). Absorption correction was done with the program SADABS.[147] Anisotropic displacement parameters were refined for all non-hydrogen atoms. Distances and angles were calculated with the program PLATON.[148] Intermolecular contacts were analyzed with the programs PLATON and MERCURY.[148, 149]. Visualisation was performed with ORTEP-3[150], SCHAKAL[151] and MERCURY[149]. Further details on the structures are listed in Tables 6.1–6.11 within the Appendix. The values given there are defined as follows:

$$R(F) = \frac{\sum \left| |F_o| - |F_c| \right|}{\sum |F_o|} \qquad (5.4)$$

$$R_{\text{int}} = \frac{\sum \left| F_o^2 - \langle F_o \rangle^2 \right|}{\sum F_o^2} \tag{5.5}$$

$$R_w(F^2) = \sqrt{\frac{\sum w\left(F_o^2 - F_c^2\right)^2}{\sum w\left(F_o^2\right)^2}} \tag{5.6}$$

$$S = \sqrt{\frac{\sum w\left(F_o^2 - F_c^2\right)^2}{N_{\text{hkl}} - N_{\text{parameter}}}} \tag{5.7}$$

The weighting factors *w* and *P* are defined as follows:

$$w = \frac{1}{\sigma^2\left(F_o^2\right) + \left(xP\right)^2 + yP} \tag{5.8}$$

$$P = \frac{\max\left(F_o^2, 0\right) + 2F_c^2}{3} \tag{5.9}$$

In analogy to SHELXL-97, the values of the parameters *x* and *y* were adopted to minimise the variance of $w\left(F_c^2 / F_o^2\right)$ for several (intensity-ordered) groups of reflexes.

The coefficient U_{eq} is defined as:

$$U_{\text{eq}} = \frac{1}{3}\sum_{i=1}^{3}\sum_{j=1}^{3} U_{ij} a_i a_j a_i^* a_j^* \tag{5.10}$$

5.9 Analysis of the temperature dependence of atomic displacement parameters (ADPs)

"At any instant of time every atom *k* in a crystal is displaced from its equilibrium position x(*k*) by an instantaneous displacement u(*k*). As diffraction experiments measure the crystal structure averaged over space and time, the relevant quantities are ADPs."[152] This means displacement parameters (graphically represented by ellipsoids, in whose volume the electrons are found with 50% probability) describe the extent to which an atom vibrates from its equilibrium position. Since the oscillation period (10^{-14} s) is longer than the duration of an X-ray flash (10^{-18} s), the vibration will be temporarily resolved during the diffraction experiment but is averaged over the measurement period.[153]
The relation between displacement parameter, structure factor and scattering angle is given in the following equation:

$$f' = f e^{-8\pi^2 U \frac{\sin^2\theta}{\lambda^2}} \tag{5.11}$$

U is the isotropic displacement factor, the mean squared vibrational amplitude. For anisotropic displacement parameters (ADPs), the equation will be transformed as follows:

$$f' = fe^{-2\pi^2(U^{11}h^2a^{*2}+U^{22}k^2b^{*2}+U^{33}l^2c^{*2}+2U^{12}hka^*b^*+2U^{13}hla^*c^*+2U^{23}klb^*c^*)} \quad (5.12)$$

In an orthogonal coordinate system the terms U_{11}, U_{22} and U_{33} correspond to the main axes of the ellipsoid U_1, U_2 and U_3, i.e. to the mean-square displacement amplitudes. At room temperature they have values of about 0.005–0.02 Å^2 in inorganic compounds, 0.02–0.06 Å^2 in organic compounds and may be up to 0.1–0.2 Å^2 for easily vibrating terminal atom groups.[152]

In addition to information on motion, information on disorder is also encoded in the magnitudes of the ADPs, since large thermal ellipsoids can be due both to large motion or a disorder in alternative positions which are so close to each other that the resolution power of the diffractometer is insufficient to recognise two separate positions. If diffraction is performed as a function of temperature it is possible to differentiate between dynamic processes and disorder phenomena, since the former is temperature dependent, whereas the latter is not. In the high-temperature classical regime (harmonic thermal motion), the mean-square displacement amplitudes are linearly dependent on temperature and extrapolate to U = 0 Å^2 at 0 K if only dynamic processes distribute to the magnitude of the ADPs. If the y intercept deviates significantly (≥ 0.005 Å^2) from zero at zero Kelvin, disorder can be assumed.[132, 153–155]

Crystals of the compounds **9b** and **22b**, for which a displacement of the nitrosyl groups as reason for the similar bonding modes was discussed, were measured by means of single-crystal X-ray diffraction at five different temperatures (293 K, 248 K, 203 K, 153 K and 103 K for **9b** and 273 K, 233 K, 193 K, 153 K, 113 K for **22b**), starting from the highest one.
The structures measured at the different temperatures were determined and refined and the largest eigenvalue of the mean-square atomic displacements of the oxygen atoms of the nitrosyl groups was plotted against the temperature, thus allowing a statement on disorder and dynamic effects.

5.10 Photocrystallography and investigations on PLI

Photocrystallography combines spectroscopic and crystallographic techniques. The cooled sample is mounted on the diffractometer and irradiated *in situ*. If the light-induced state is sufficiently stable, irradiation can precede diffraction. This is an advantage when the energy input of the laser leads to a temperature increase above the specific temperature of decay of the metastable state. If the life-time of the metastable state is too short, a stroboscopic experiment can be performed, in which a pulsed laser source is combined with a pulsed X-ray probe source.
Due to the fact that only part of the molecules is converted into the metastable state, the diffraction is made on a disordered crystal. But, other than in the normal case, information of one of the components of the disorder is available, since the non-irradiation-affected component can be determined from the ground state crystal. In order to deconvolute the second component, the non-

affected component has to be subtracted from the superposition of the non-affected and affected part. This is done by the use of a photodifference electron-density map, which is related to the Fourier difference density maps routinely employed in crystal structure solution. The missing electron density is calculated by subtraction of the calculated electron-density derived from the model from the experimentally observed density.

$$\Delta\rho(r) = \frac{1}{V_{\text{cell}}} + \sum_H (F_{\text{obs}}(H) - F_{\text{calc}}(H))\, e^{-2\pi i H r}) \tag{5.13}$$

$$F_{photo-irradiated} = (1-P)F'_{\text{GS}} + PF_{\text{Pi}} + F_{\text{rest}} \tag{5.14}$$

F_{calc} is the calculated structure factor and corresponds to the ground state structure factor additionally taking into account any changes in cell dimensions. F_{obs} is the observed structure factor and corresponds to the structure factor from the experiment after irradiation. *H* defines the reciprocal lattice positions. Equation 5.14 which is valid when assuming random distribution of the photo-converted molecules and the presence of only two species, shows how the structure factor of the irradiated crystal is composed. The superscripts “GS” and “PI” correspond to the ground and photo-induced molecular states, respectively. *P* is the conversion percentage and “rest” means non-affected moieties such as co-crystallised solvents or counterions. F'_{gs} does not necessarily have to be identical to F_{gs}, (structure factor of the ground state), since slight rotations or movements of the ground-state molecules due to a changed molecular and electronic environment are possible. Thus, the parameters of refinement are the description of the structure of the light-induced species, its population, parameters describing the translations and rotations of the ground-state species treated as rigid bodies as well as slight differences in unit cell dimensions.[156]

Low-temperature infrared spectroscopy and photocrystallographic experiments were performed at the *Institut Jean Barriol* in the *Laboratoire de Cristallographie, Résonance Magnétique et Modélisations* in Nancy, France.

Diffraction data were first collected in the ground state at 10 K using a helium cryostream system. A separate sample was irradiated with light of the wavelength 405 nm for 40 minutes until the stationary point was reached. Complete diffraction data was collected in the photo-stationary state at temperatures (10K) far below the specific temperature of decay (110 K). With respect to the ground state, no space-group changes could be observed. To visualise the light-induced changes in electronic density, and thereby deriving structural changes from the GS to the MS, a photo-difference map was calculated, using four different models (see RESULTS, chapter 2.11). Common independent reflections of the GS and the photo-irradiated state, used to calculate the photo-difference map by Fourier transform of the $F_{\text{photo-irradiated}}$(hkl) – F_{GS}(hkl) difference, comprised 85% of possible reflections (θ_{max} = 29.6°); the Fourier maps are therefore reliable. Since the population of the metastable state under the diffraction experimental conditions could not be measured precisely, the degree of population is a necessary refinement parameter, with the constraint $P_{GS} + P_{MS} = 1$.

5.11 Quantum chemical computations

To support the statement that the bonding parameters of the nitrosyl groups, given from the particular crystal structures, derive neither from disorder or dynamic effects nor from packing effects or intermolecular interactions, the bonding parameters, the geometries and the *v*(NO) stretching frequencies were predicted by a Kohn-Sham-DFT-based procedure.[157, 158] The ORCA program package[118] was used for the calculations. Geometry optimisation was done with the Becke-Perdew BP86 functional[119, 120] and Ahlrich's tzvp basis sets[121] for all atoms except ruthenium and iodine, which were treated with scalar relativistic all electron calculations. Stationary points were confirmed with subsequent frequency analysis. Frequency analysis for the *v*(NO) stretching frequencies were calculated by the same level of theory used in the geometry optimisation. The experimental and calculated *v*(NO) stretching frequencies, τ_5-values and the bond lengths for Ru–NO an N–O were compared. For a better comparison of the calculated and experimental N–O bond lengths, the latter were subjected to a libration correction.[129]

6 Appendix

6.1 Additional information

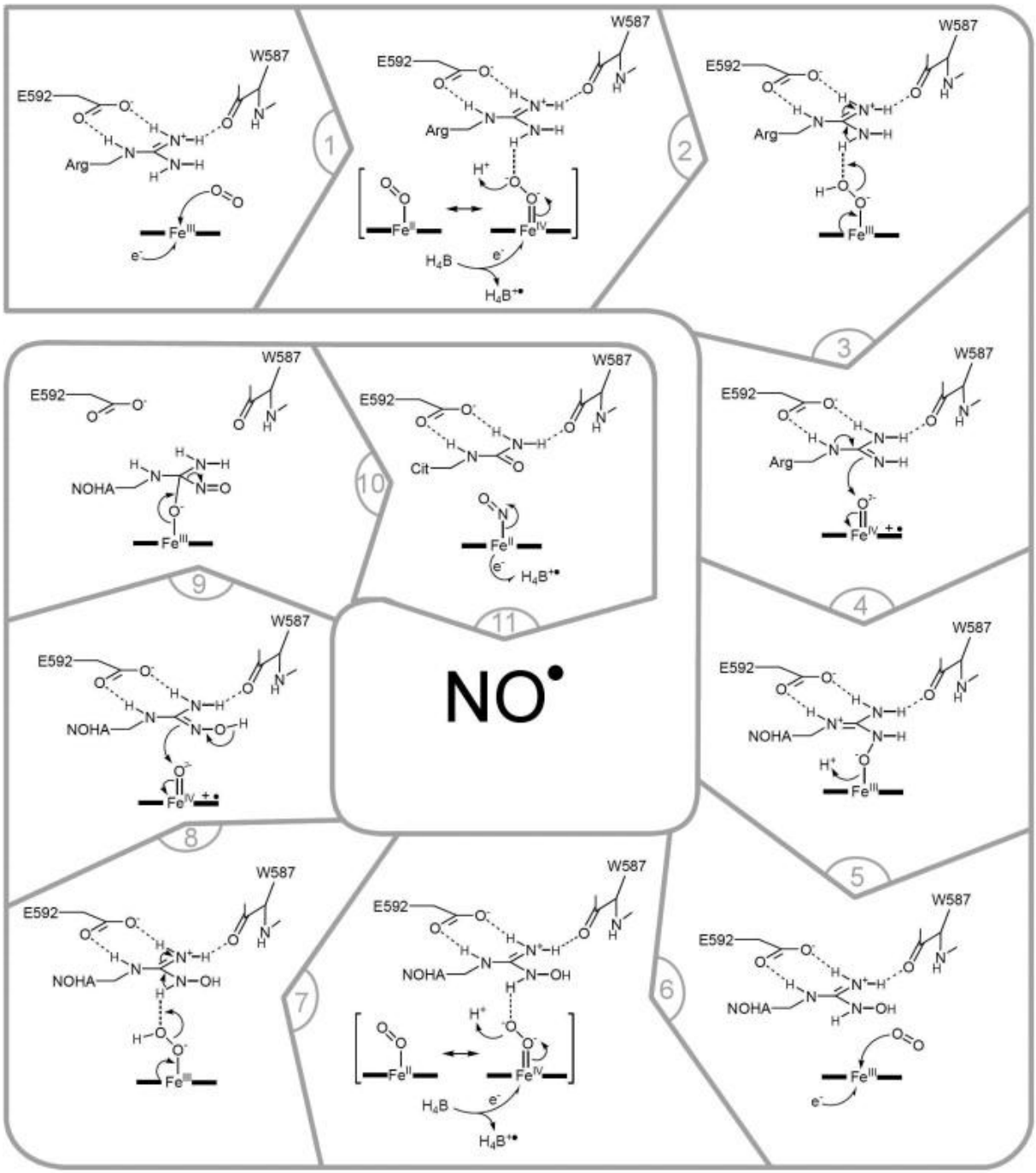

Fig. 6.1: Probable reaction mechanism for the synthesis of nitric oxide by the heme protein NOS assuming an oxidoferryl complex as the monooxygenating agent for L-Arg and NOHLA.[34]

6.2 Packing diagrams of the crystal structures

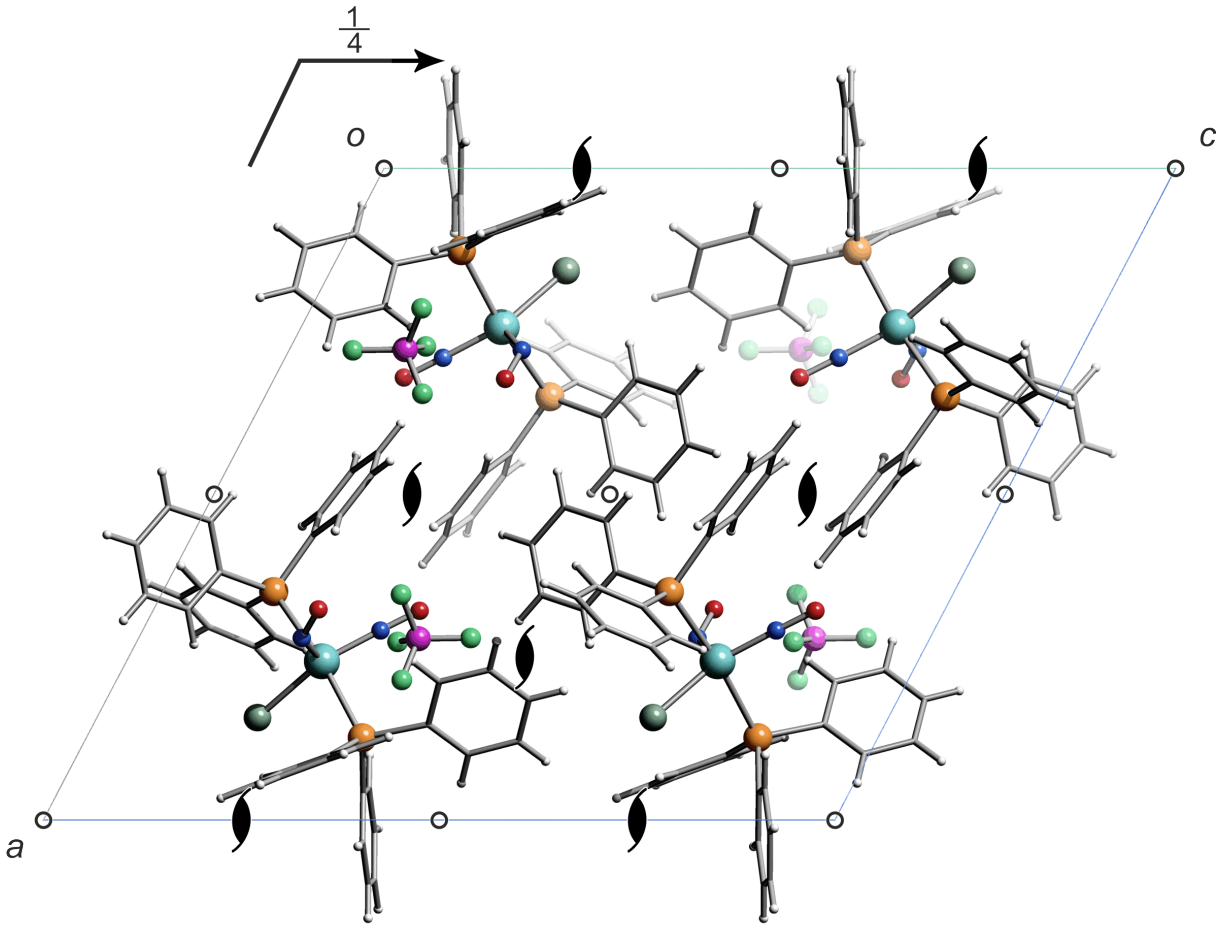

Fig. 6.2 (pn320): SCHAKAL packing diagram of **6b** in the monoclinic space group $P2_1/c$ with view along [010]. The symmetry elements of the space group $P2_1/c$ are overlaid. Atoms: carbon (grey, wireframe), hydrogen (white), boron (magenta), chlorine (dark green), fluorine (light green), nitrogen (blue), oxygen (red), phosphorus (orange), ruthenium (turquoise).

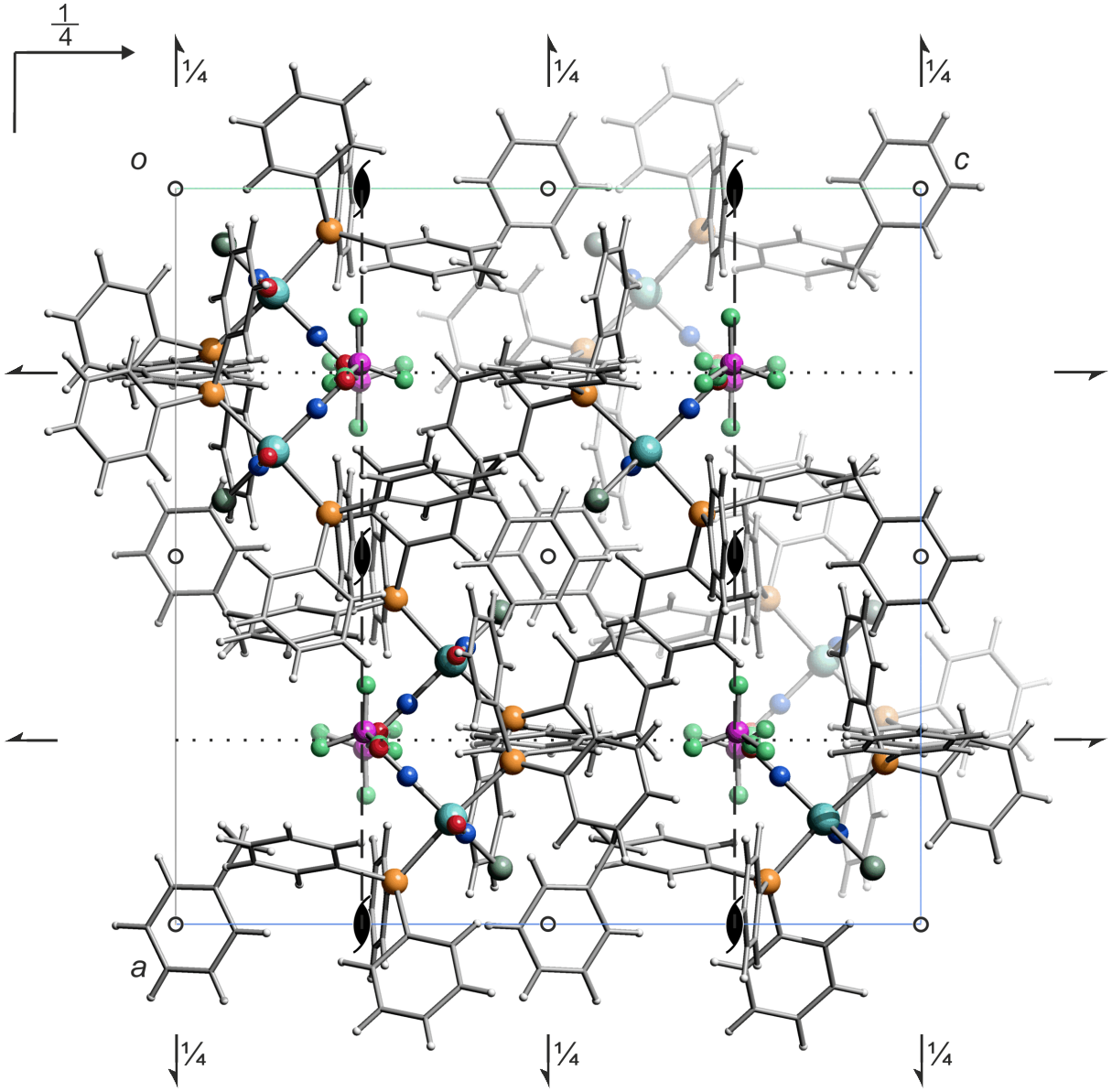

Fig. 6.3 (qn137): SCHAKAL packing diagram of **6b** · C_7H_8 in the monoclinic space group *Pbca* with view along [010]. The symmetry elements of the space group *Pbca* are overlaid. Atoms: carbon (grey, only depicted as coupling link), hydrogen (white), boron (magenta), chlorine (dark green), fluorine (light green), nitrogen (blue), oxygen (red), phosphorus (orange), ruthenium (turquoise).

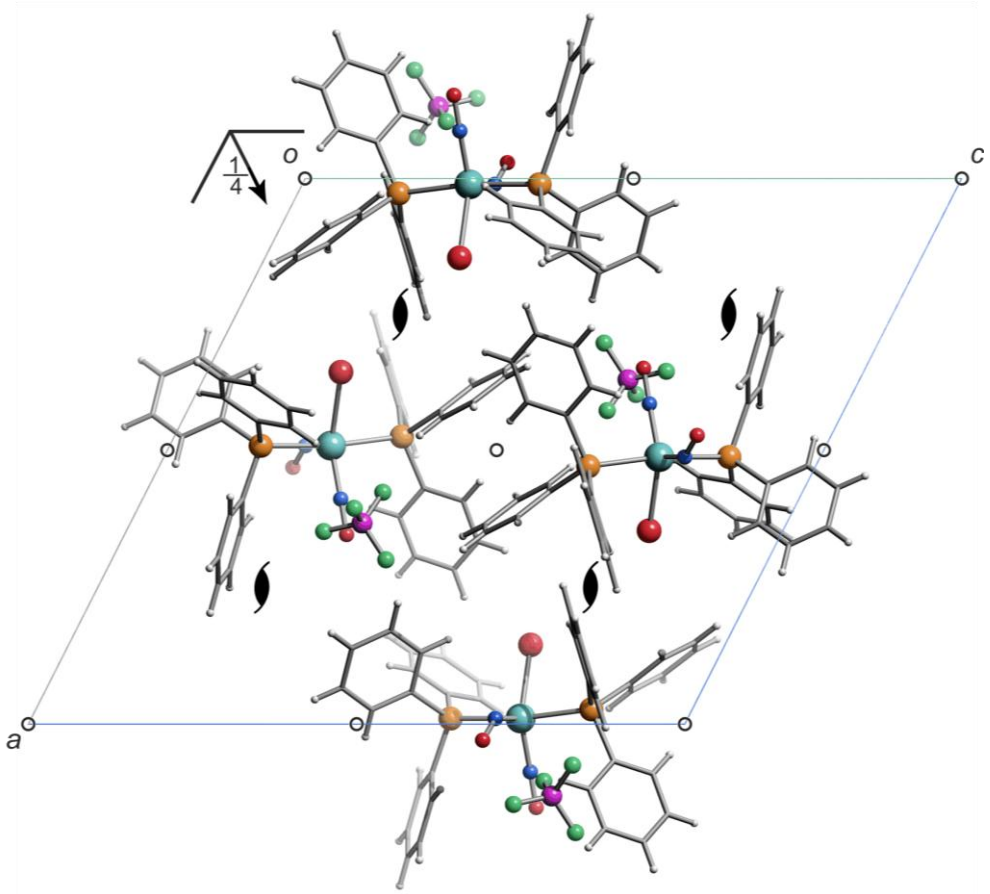

Fig. 6.4 (pn390): SCHAKAL packing diagram of **7b** in the monoclinic space group $P2_1/n$ with view along [010]. The symmetry elements of the space group $P2_1/n$ are overlaid. Atoms: carbon (grey, only depicted as coupling link), hydrogen (white), boron (magenta), bromine (reddish brown), fluorine (light green), nitrogen (blue), oxygen (red), phosphorus (orange), ruthenium (turquoise).

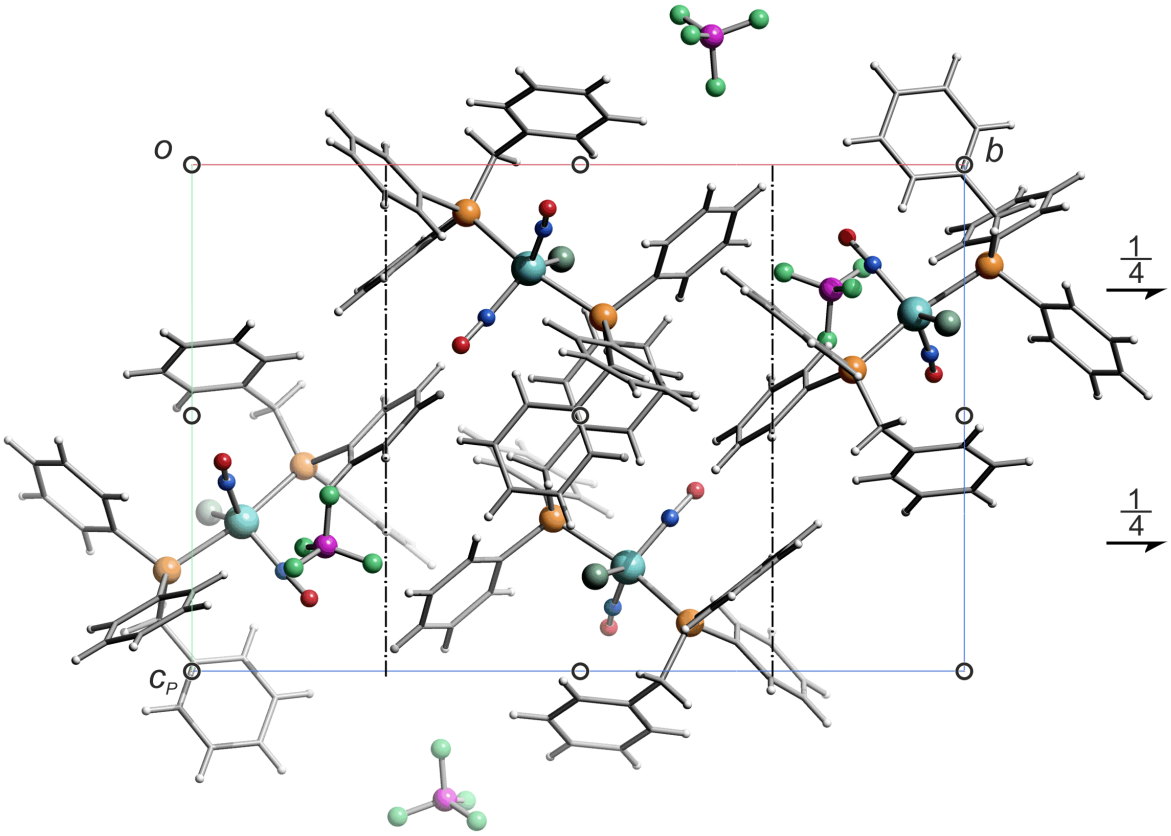

Fig. 6.5 (qo093): SCHAKAL packing diagram of **8b** in the monoclinic space group $P2_1/n$ with view along [100]. The symmetry elements of the space group $P2_1/n$ are overlaid. Atoms: carbon (grey, only depicted as coupling link), hydrogen (white), boron (magenta), chlorine (dark green), fluorine (light green), nitrogen (blue), oxygen (red), phosphorus (orange), ruthenium (turquoise).

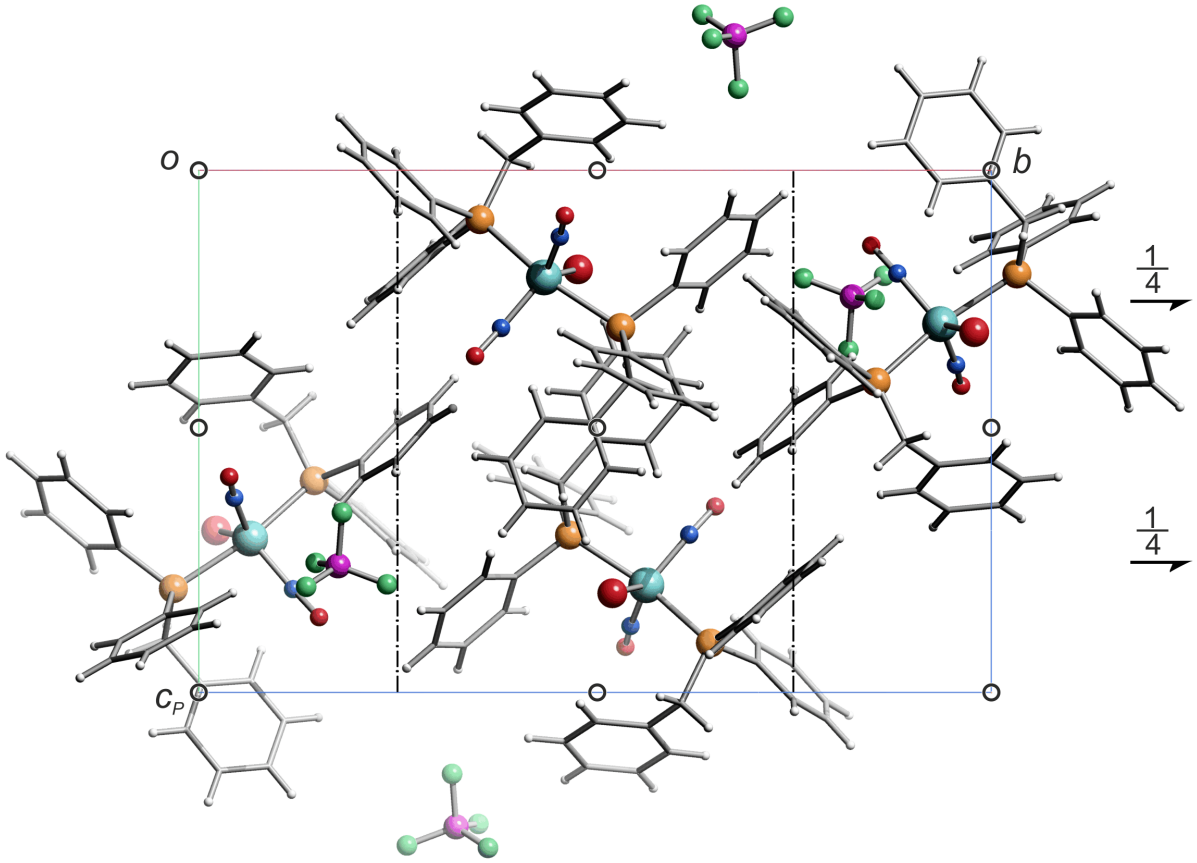

Fig. 6.6 (qn031): SCHAKAL packing diagram of **9b** in the monoclinic space group $P2_1/n$ with view along [100]. The symmetry elements of the space group $P2_1/n$ are overlaid. Atoms: carbon (grey, only depicted as coupling link), hydrogen (white), boron (magenta), bromine (reddish brown), fluorine (light green), nitrogen (blue), oxygen (red), phosphorus (orange), ruthenium (turquoise).

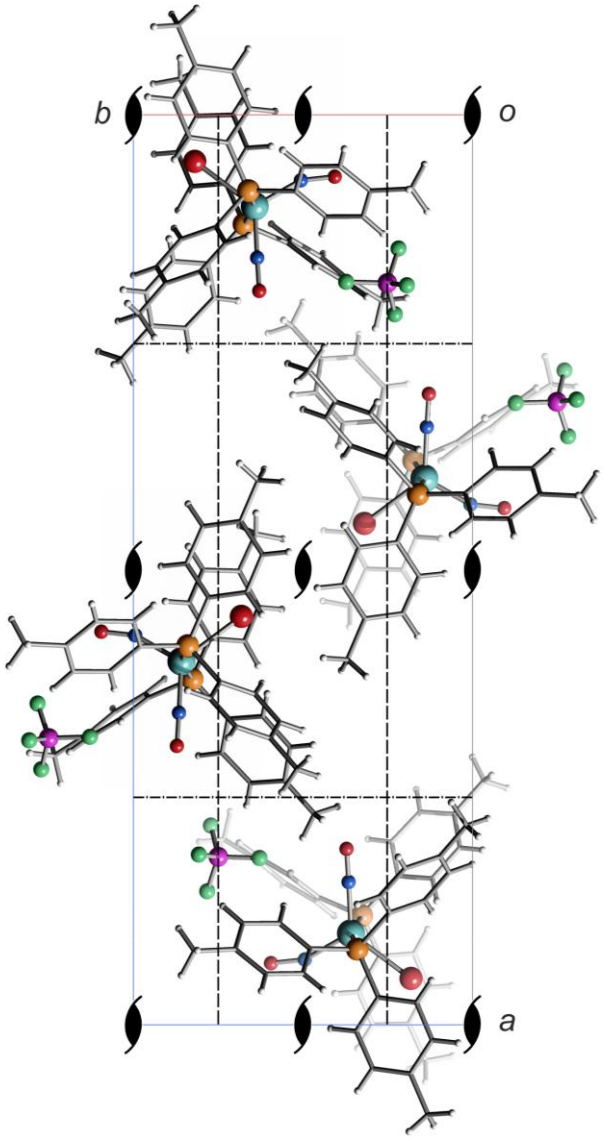

Fig. 6.7 (qo067): SCHAKAL packing diagram of **14b** in the orthorhombic space group $Pna2_1$ with view along [001]. The symmetry elements of the space group $P2_12_12_1$ are overlaid. Atoms: carbon (grey, only depicted as coupling link), Hydrogen (white), boron (magenta), bromine (reddish brown), fluorine (light green), nitrogen (blue), oxygen (red), phosphorus (orange), ruthenium (turquoise).

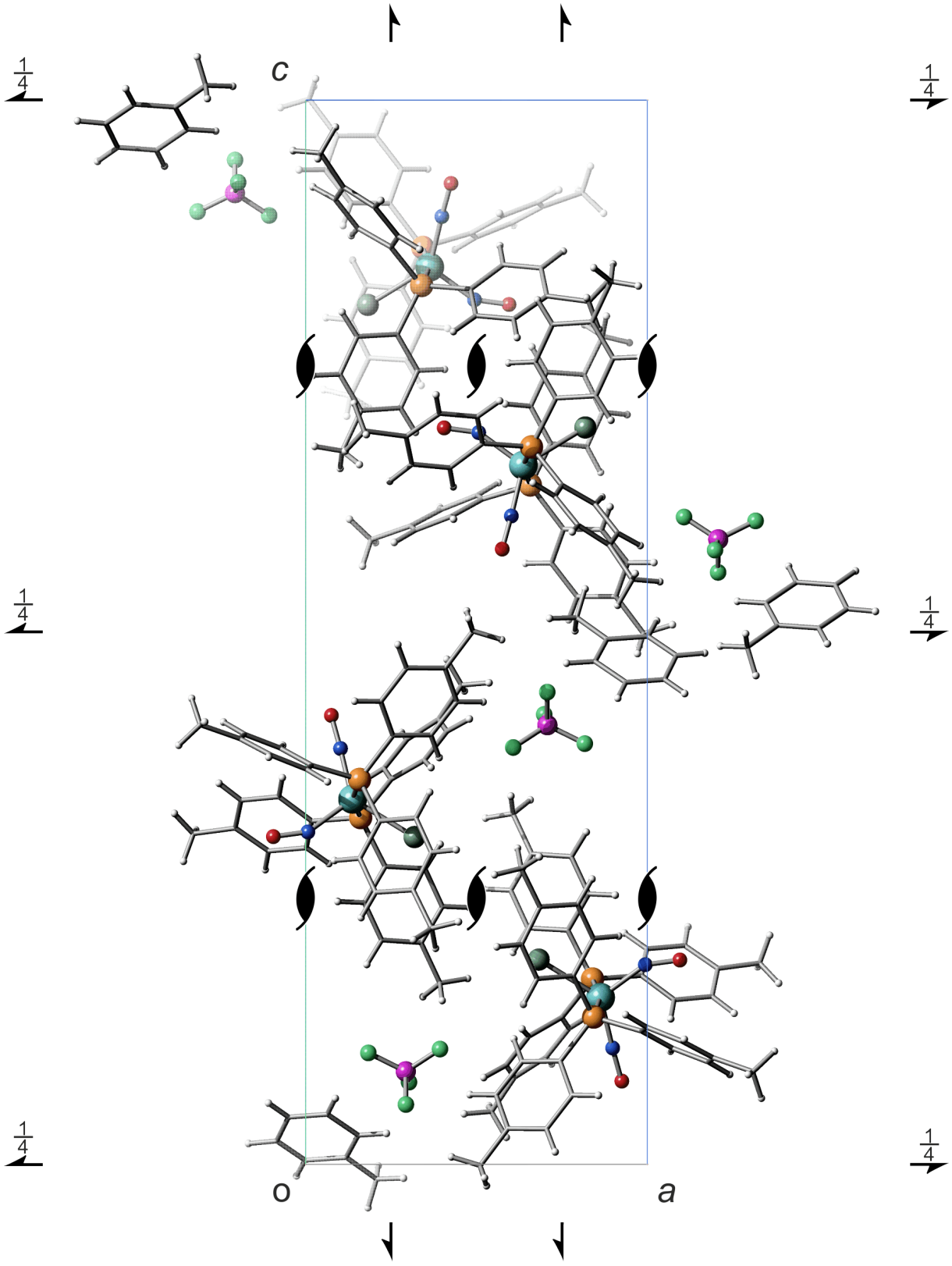

Fig. 6.8 (qn102): SCHAKAL packing diagram of **15b** in the orthorhombic space group $P2_12_12_1$ with view along [010]. The symmetry elements of the space group $P2_12_12_1$ are overlaid. Atoms: carbon (grey, only depicted as coupling link), hydrogen (white), boron (magenta), chlorine (dark green), fluorine (light green), nitrogen (blue), oxygen (red), phosphorus (orange), ruthenium (turquoise).

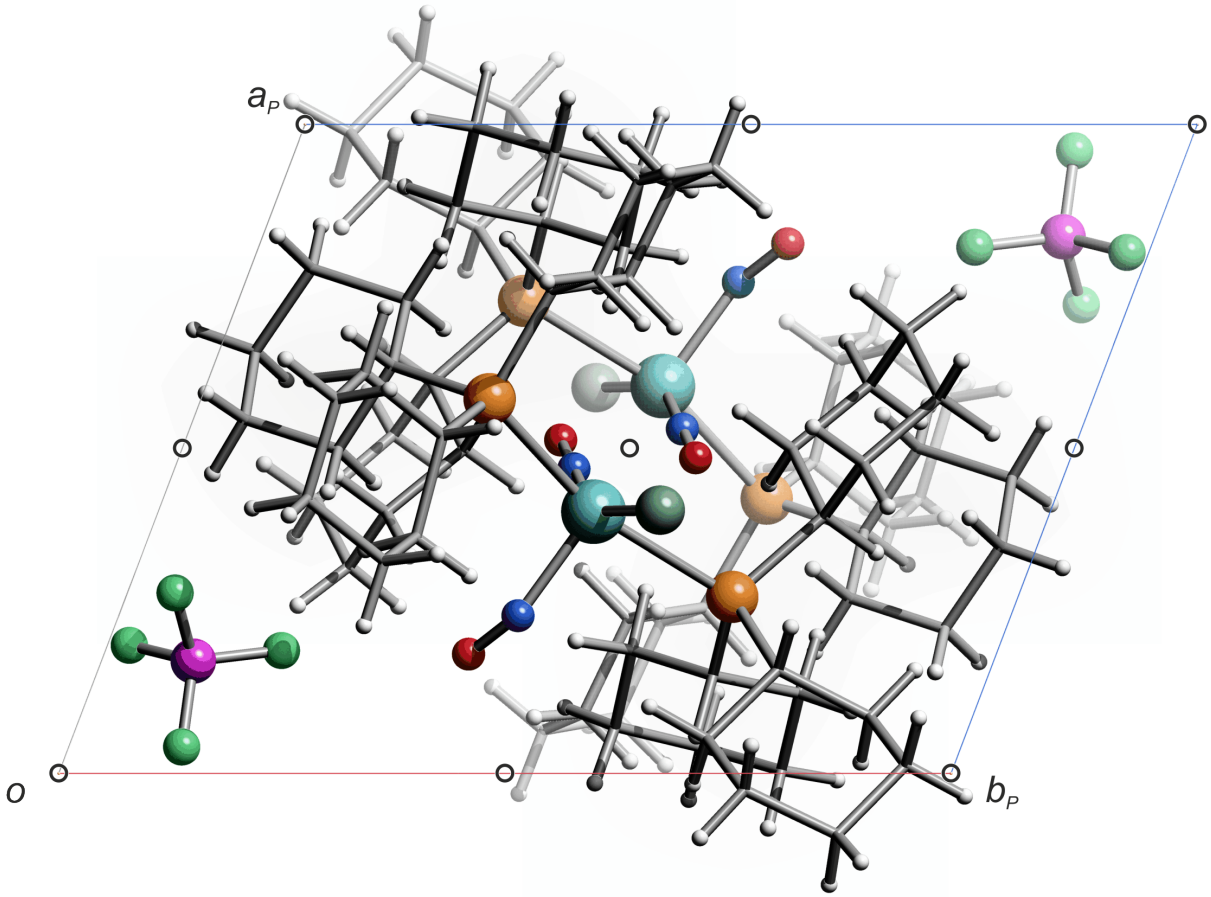

Fig. 6.9 (qv027): SCHAKAL packing diagram of **18b** in the triclinic space group $P\bar{1}$ with view along [001]. The symmetry elements of the space group $P\bar{1}$ are overlaid. Atoms: carbon (grey, only depicted as coupling link), hydrogen (white), boron (magenta), chlorine (green), fluorine (light green), nitrogen (blue), oxygen (red), phosphorus (orange), ruthenium (turquoise).

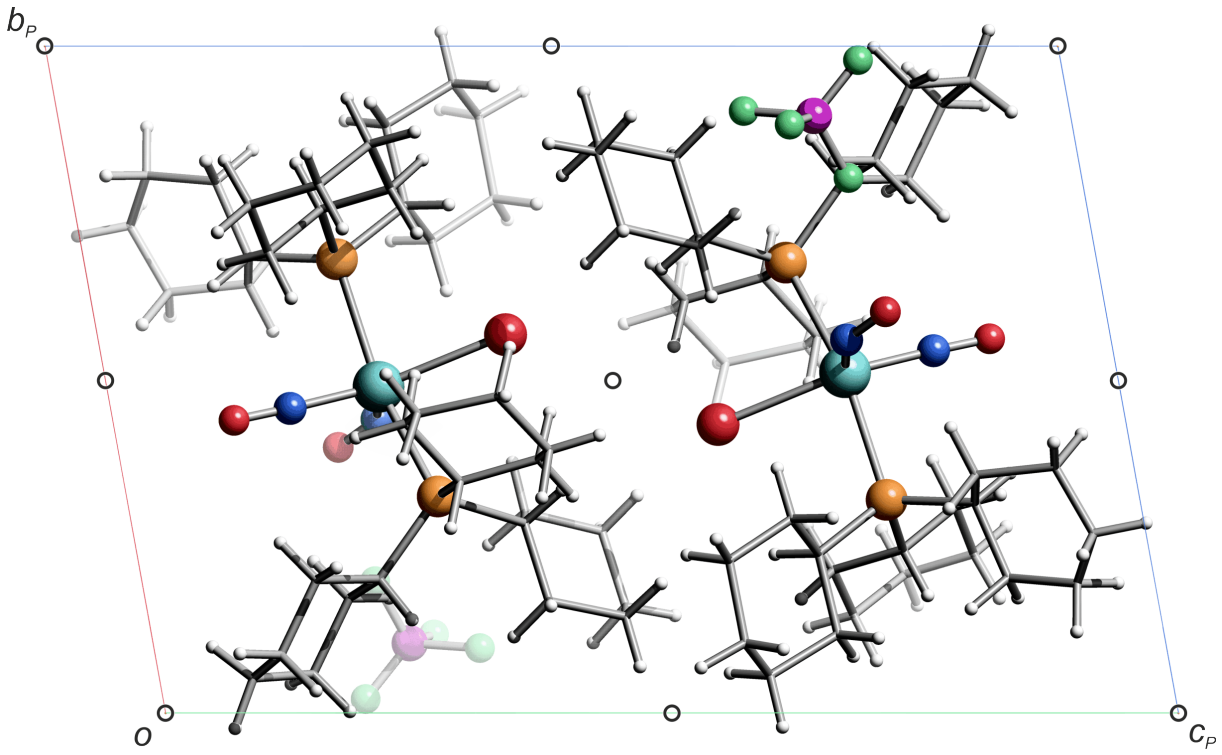

Fig. 6.10 (qq031): SCHAKAL packing diagram of **19b** in the triclinic space group $P\bar{1}$ with view along [100]. The symmetry elements of the space group $P\bar{1}$ are overlaid. Atoms: carbon (grey, only depicted as coupling link), hydrogen (white), boron (magenta), bromine (reddish brown), fluorine (light green), nitrogen (blue), oxygen (red), phosphorus (orange), ruthenium (turquoise).

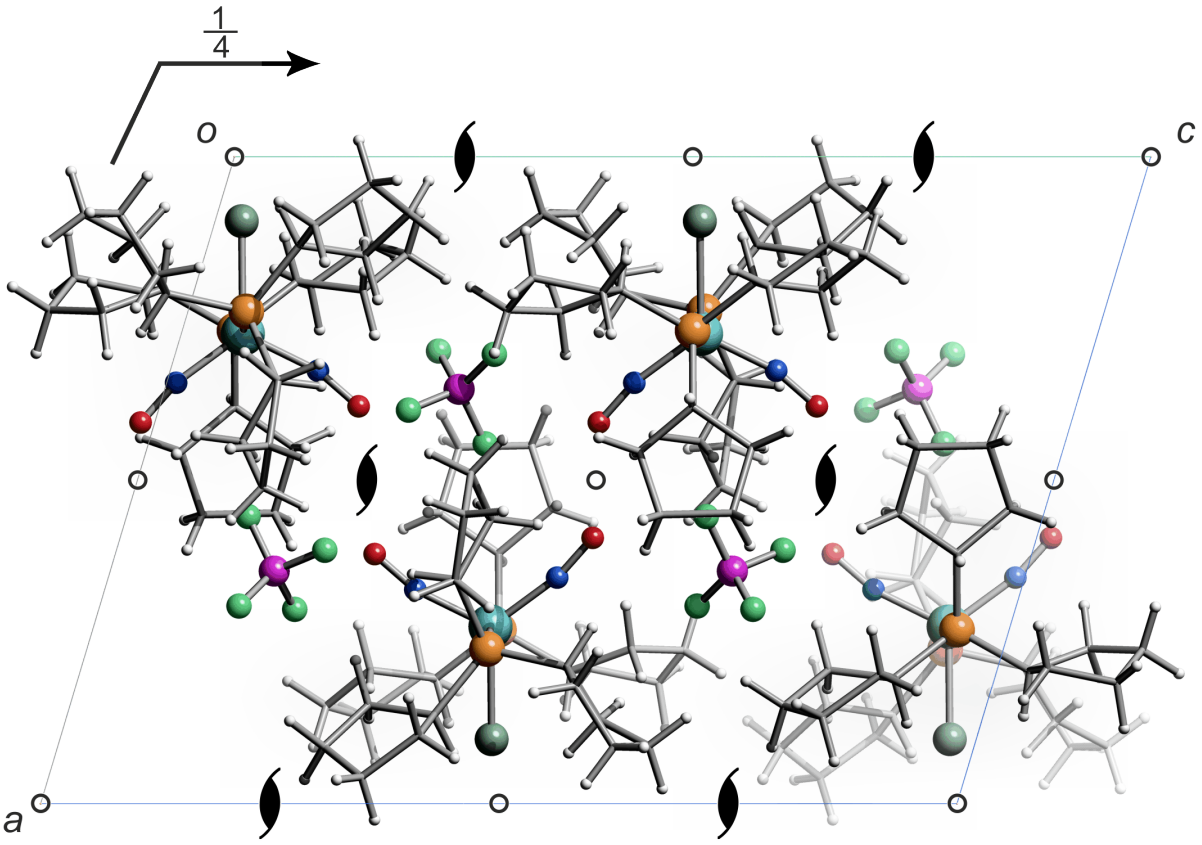

Fig. 6.11 (rv021): SCHAKAL packing diagram of **21b-2** in the monoclinic space group $P2_1/c$ with view along [010]. The symmetry elements of the space group $P2_1/c$ are overlaid. Atoms: carbon (grey, only depicted as coupling link), hydrogen (white), boron (magenta), chlorine (dark green), fluorine (light green), nitrogen (blue), oxygen (red), phosphorus (orange), ruthenium (turquoise).

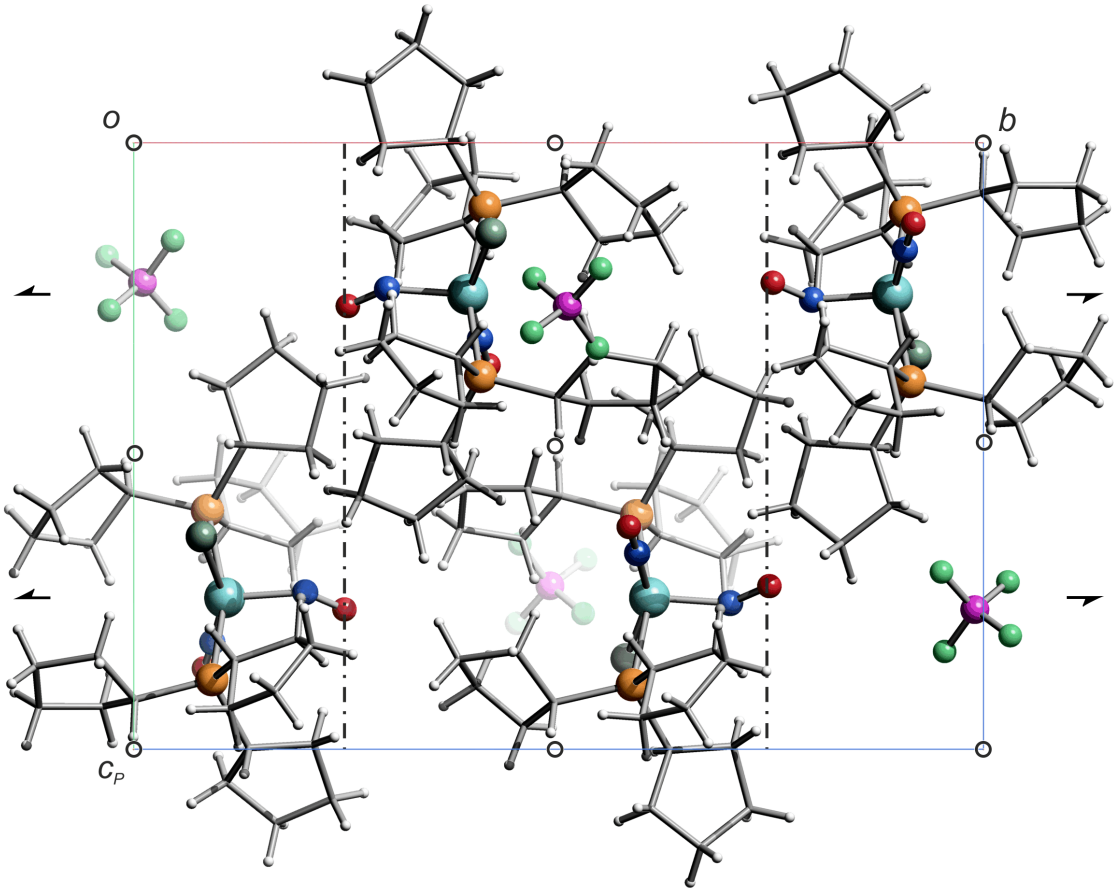

Fig. 6.12 (qq041): SCHAKAL packing diagram of **21b-1** in the monoclinic space group $P2_1/n$ with view along [100]. The symmetry elements of the space group $P2_1/n$ are overlaid. Atoms: carbon (grey, only depicted as coupling link), hydrogen (white), boron (magenta), chlorine (dark green), fluorine (light green), nitrogen (blue), oxygen (red), phosphorus (orange), ruthenium (turquoise).

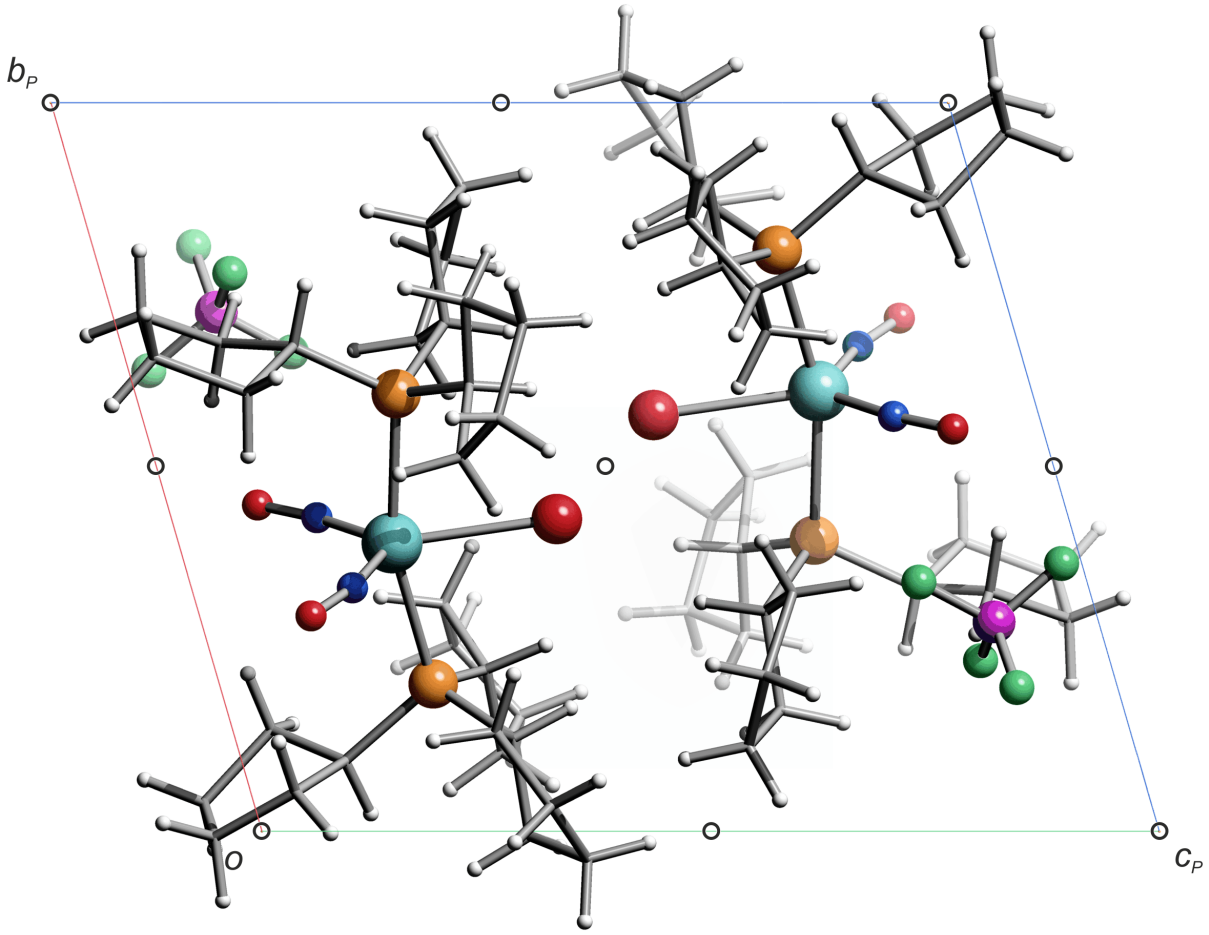

Fig. 6.13 (qo145): SCHAKAL packing diagram of **22b** in the triclinic space group $P\bar{1}$ with view along [100]. The symmetry elements of the space group $P\bar{1}$ are overlaid. Atoms: carbon (grey, only depicted as coupling link), hydrogen (white), boron (magenta), bromine (reddish brown), fluorine (light green), nitrogen (blue), oxygen (red), phosphorus (orange), ruthenium (turquoise).

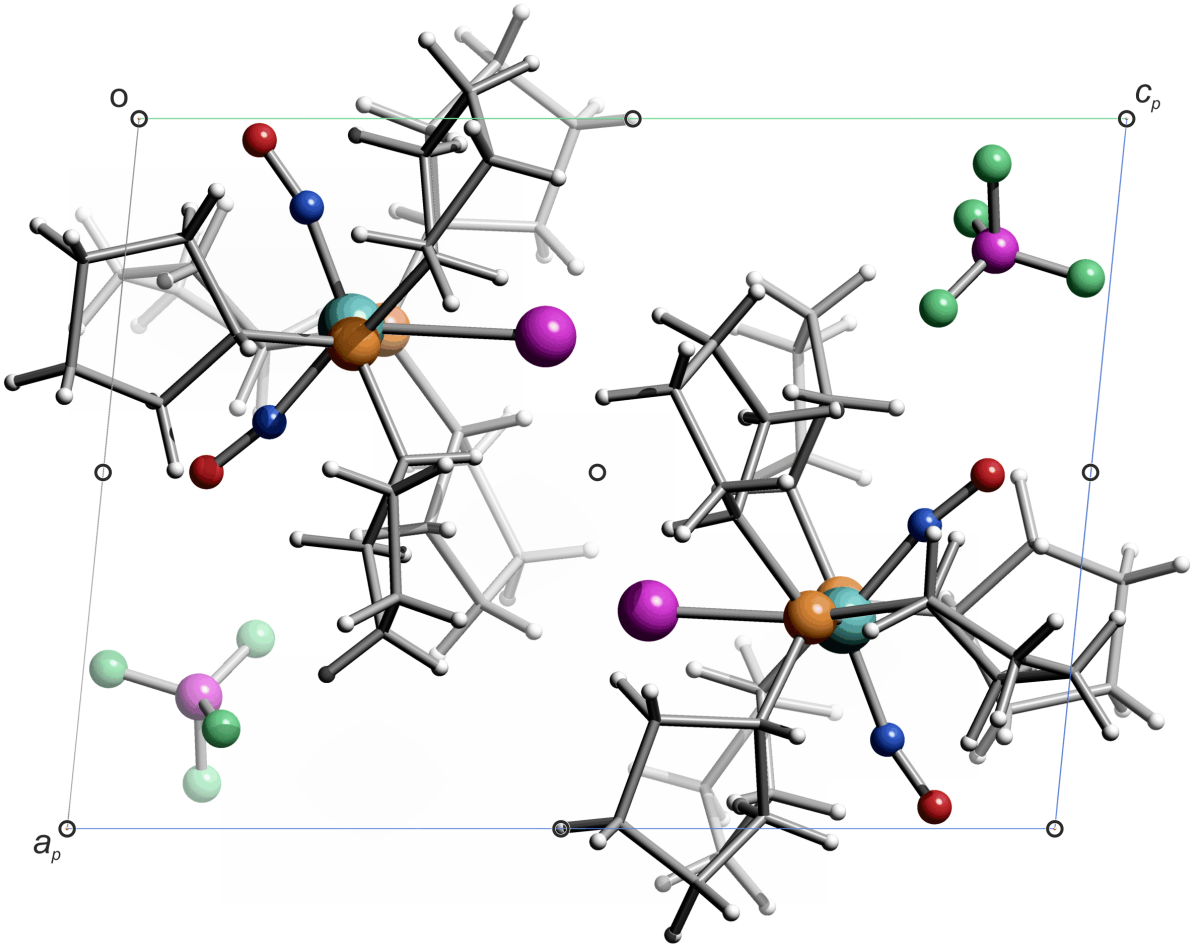

Fig. 6.14 (qq069): SCHAKAL packing diagram of **23b** in the triclinic space group $P\bar{1}$ with view along [010]. The symmetry elements of the space group $P\bar{1}$ are overlaid. Atoms: carbon (grey, only depicted as coupling link), hydrogen (white), boron (magenta), fluorine (light green), iodine (lilac), nitrogen (blue), oxygen (red), phosphorus (orange), ruthenium (turquoise).

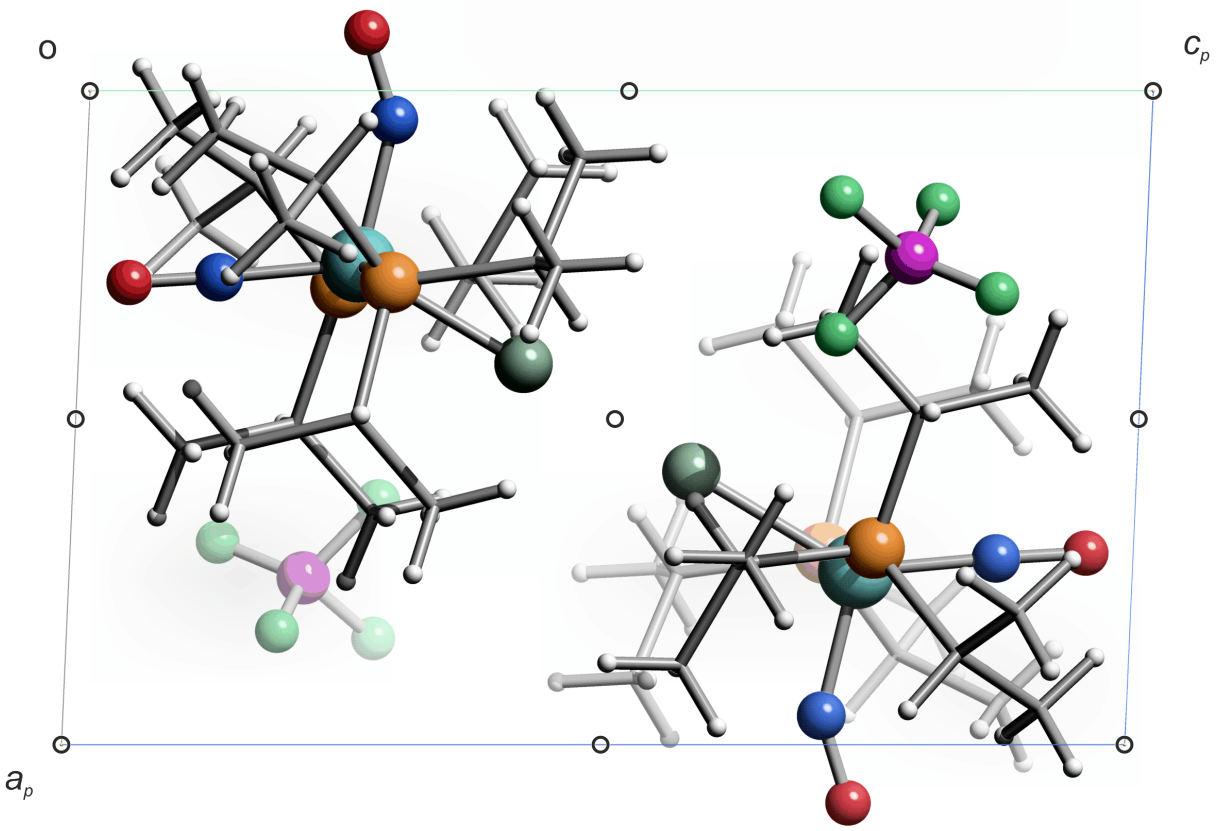

Fig. 6.15 (rv114): SCHAKAL packing diagram of **24b** in the triclinic space group $P\bar{1}$ with view along [010]. The symmetry elements of the space group $P\bar{1}$ are overlaid. Atoms: carbon (grey, only depicted as coupling link), hydrogen (white), boron (magenta), chlorine (dark green), fluorine (light green), nitrogen (blue), oxygen (red), phosphorus (orange), ruthenium (turquoise).

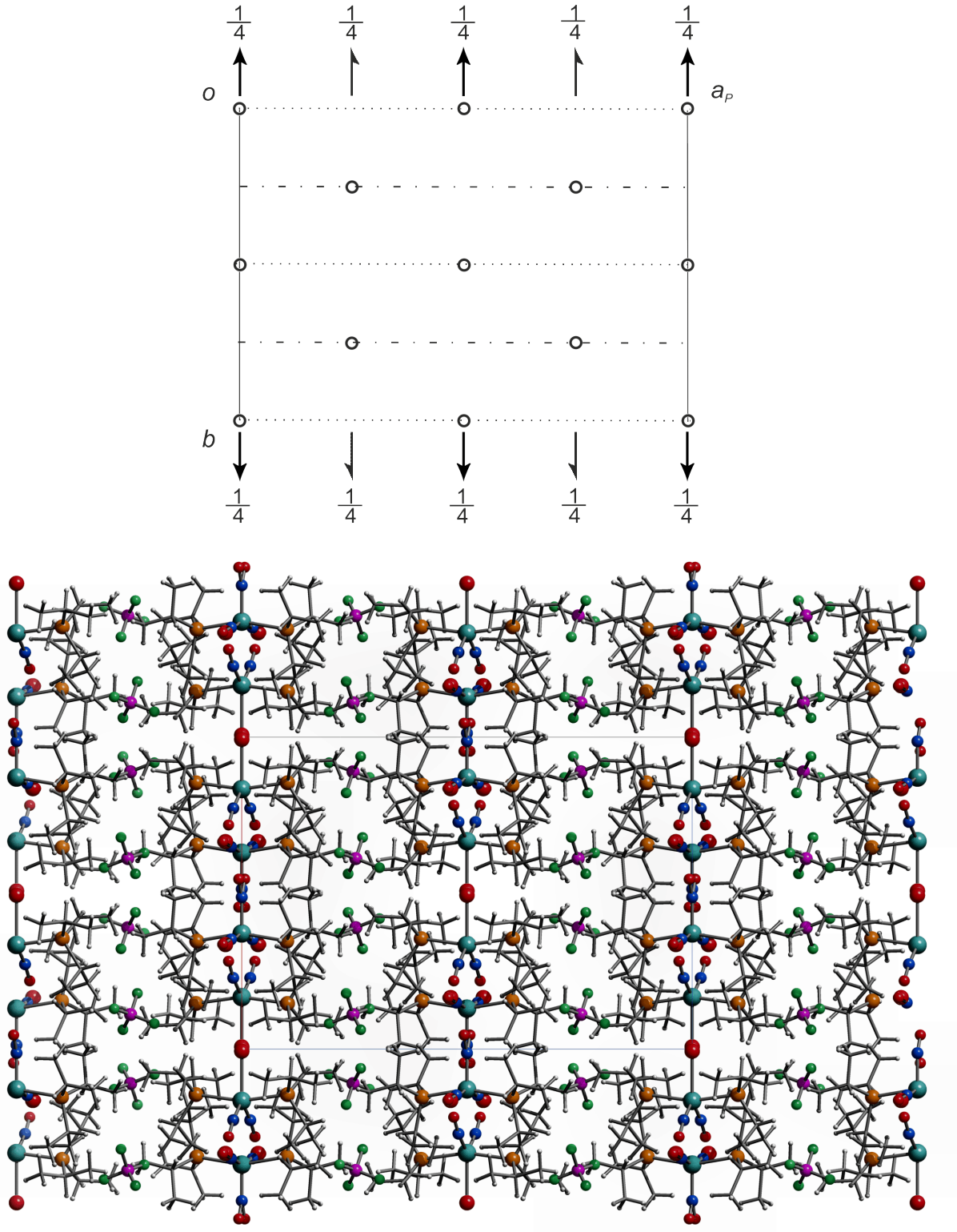

Fig. 6.16 (qv016): SCHAKAL packing diagram of **25b** in the monoclinic space group *C2/c* with view along [001]. The symmetry elements of the space group *C2/c* are overlaid. Atoms: carbon (grey, only depicted as coupling link), hydrogen (white), boron (magenta), chlorine (dark green), fluorine (light green), nitrogen (blue), oxygen (red), phosphorus (orange), ruthenium (turquoise).

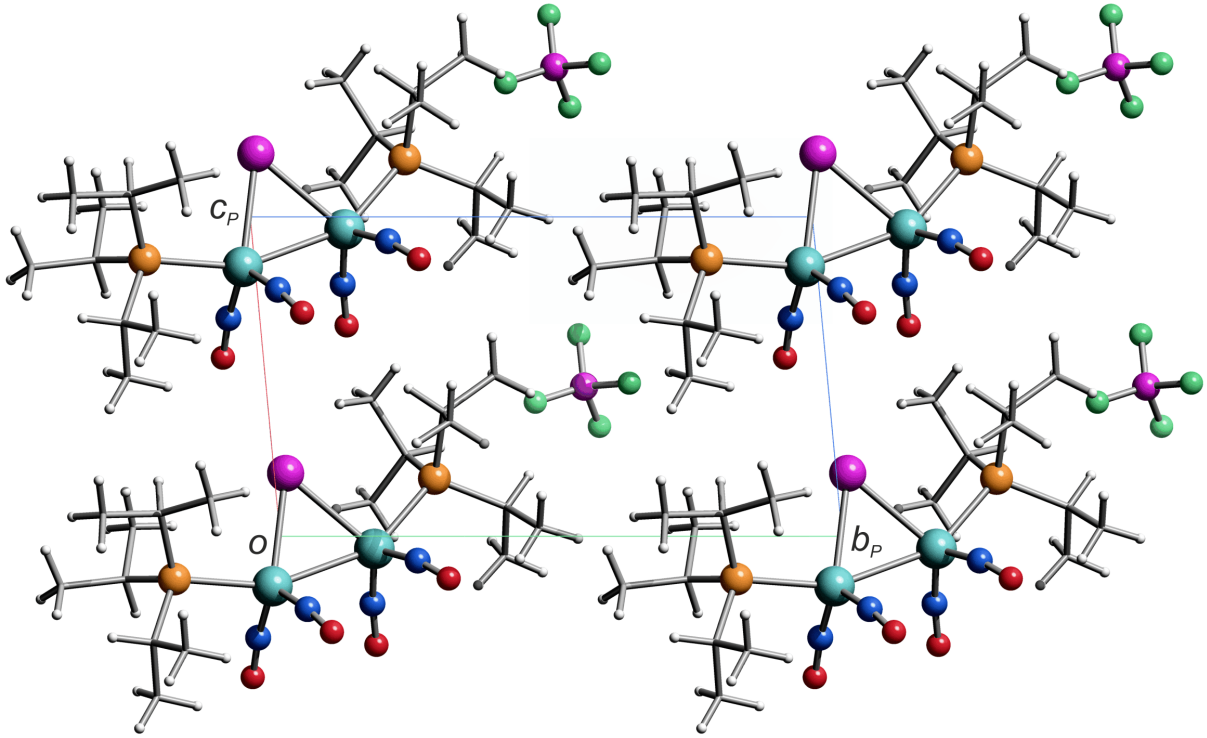

Fig. 6.17 (rv366): SCHAKAL packing diagram of **26c** in the triclinic space group *P*1 with view along [100]. Atoms: carbon (grey, only depicted as coupling link), hydrogen (white), boron (magenta), iodine (lilac), fluorine (light green), nitrogen (blue), oxygen (red), phosphorus (orange), ruthenium (turquoise).

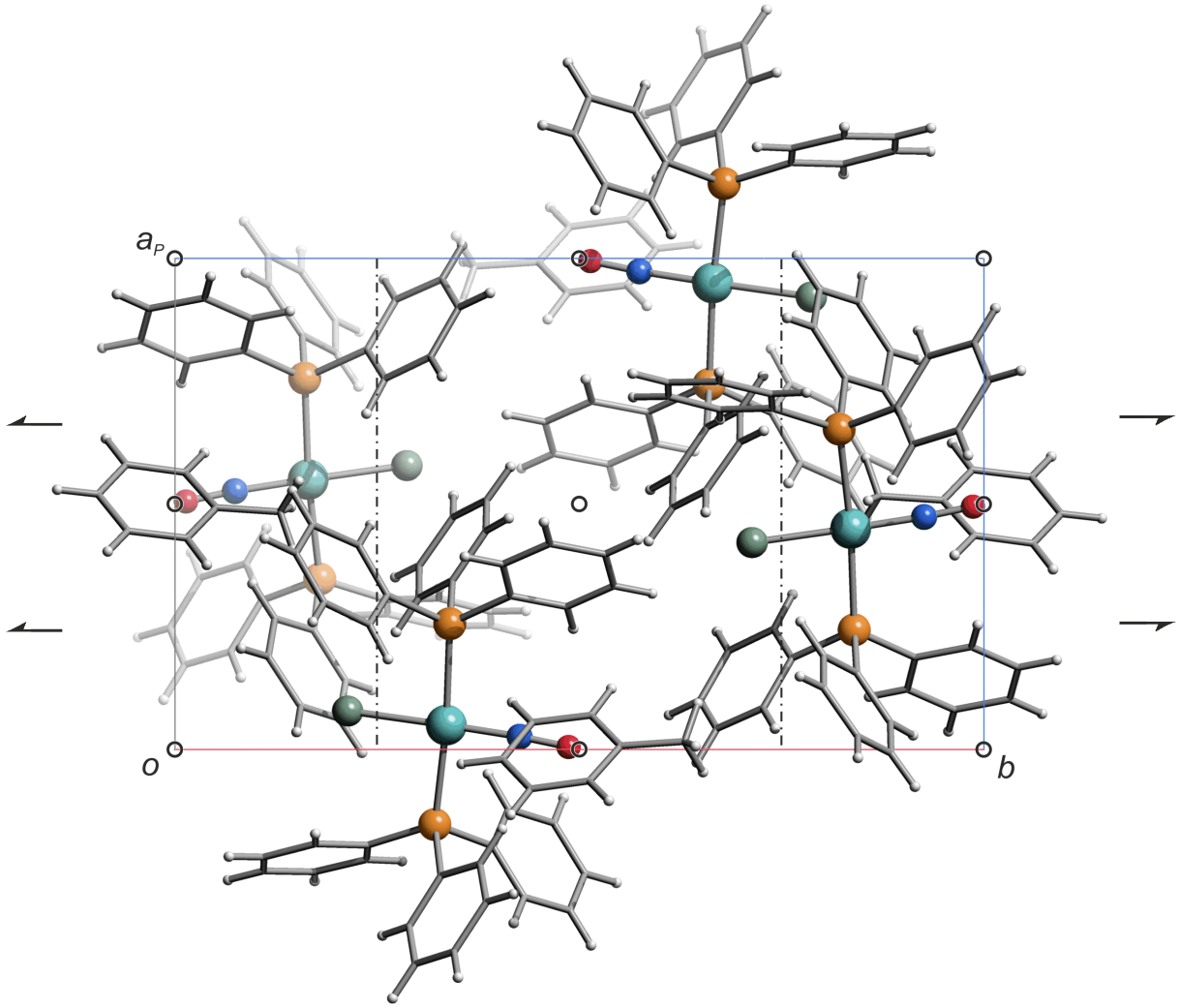

Fig. 6.18 (qq081): SCHAKAL packing diagram of **8c** in the monoclinic space group $P2_1/n$ with view along [001]. The symmetry elements of the space group $P2_1/n$ are overlaid. Atoms: carbon (grey, only depicted as coupling link), hydrogen (white), chlorine (dark green), nitrogen (blue), oxygen (red), phosphorus (orange), ruthenium (turquoise).

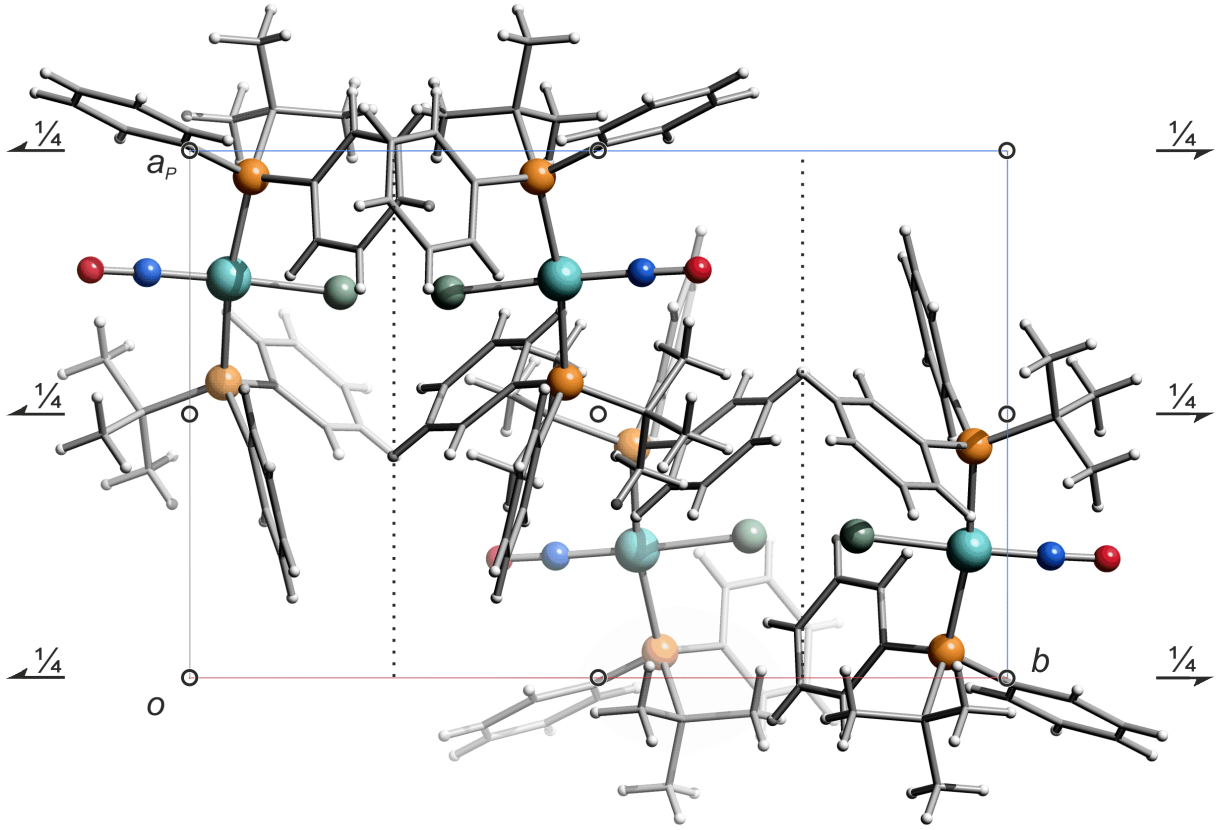

Fig. 6.19 (qn226): SCHAKAL packing diagram of **13c** in the monoclinic space group $P2_1/c$ with view along [001]. The symmetry elements of the space group $P2_1/c$ are overlaid. Atoms: carbon (grey, only depicted as coupling link), hydrogen (white), chlorine (dark green), nitrogen (blue), oxygen (red), phosphorus (orange), ruthenium (turquoise).

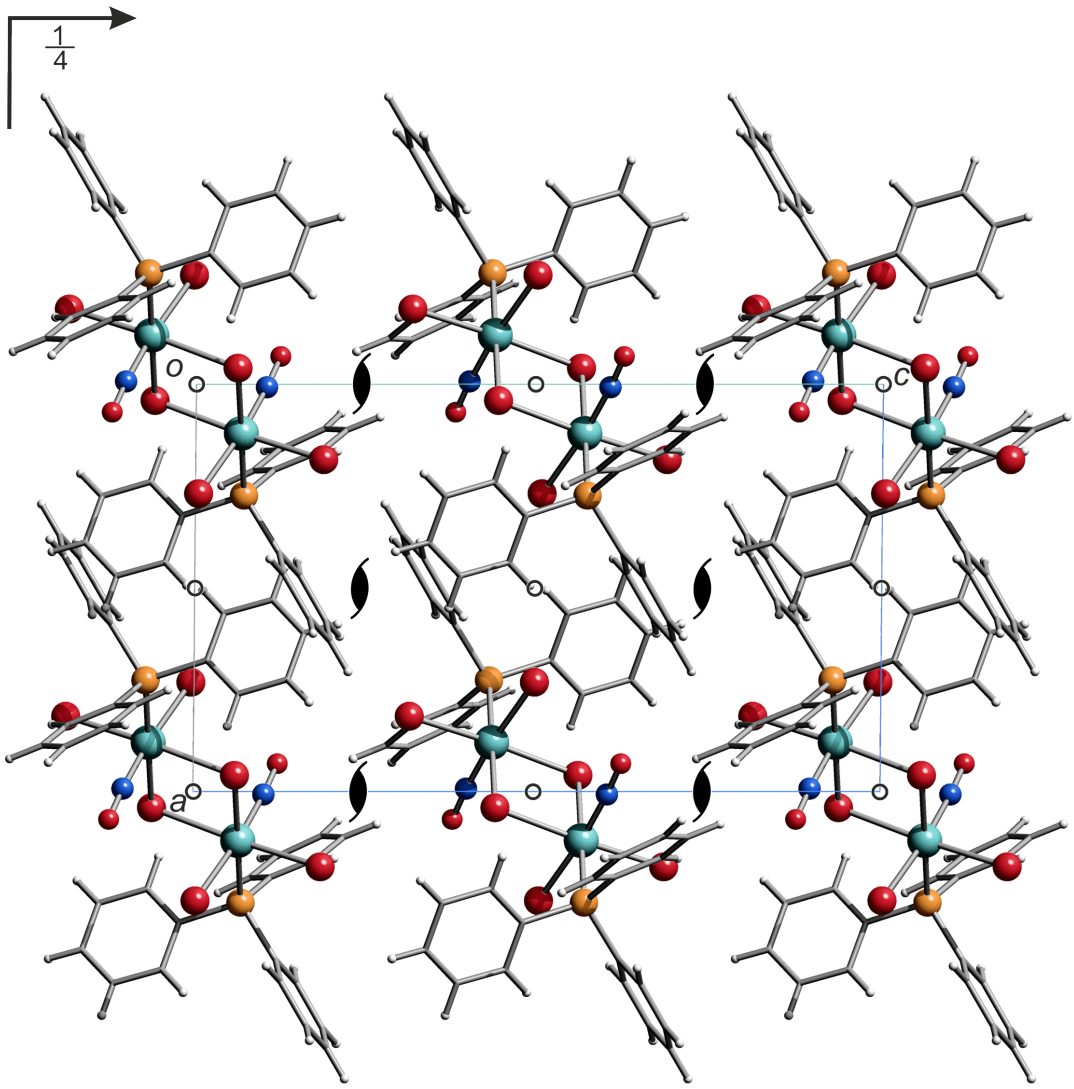

Fig. 6.20 (qn038): SCHAKAL packing diagram of **7c** in the monoclinic space group $P2_1/c$ with view along [010]. The symmetry elements of the space group $P2_1/c$ are overlaid. Atoms: carbon (grey, only depicted as coupling link), hydrogen (white), bromine (reddish brown), nitrogen (blue), oxygen (red), phosphorus (orange), ruthenium (turquoise).

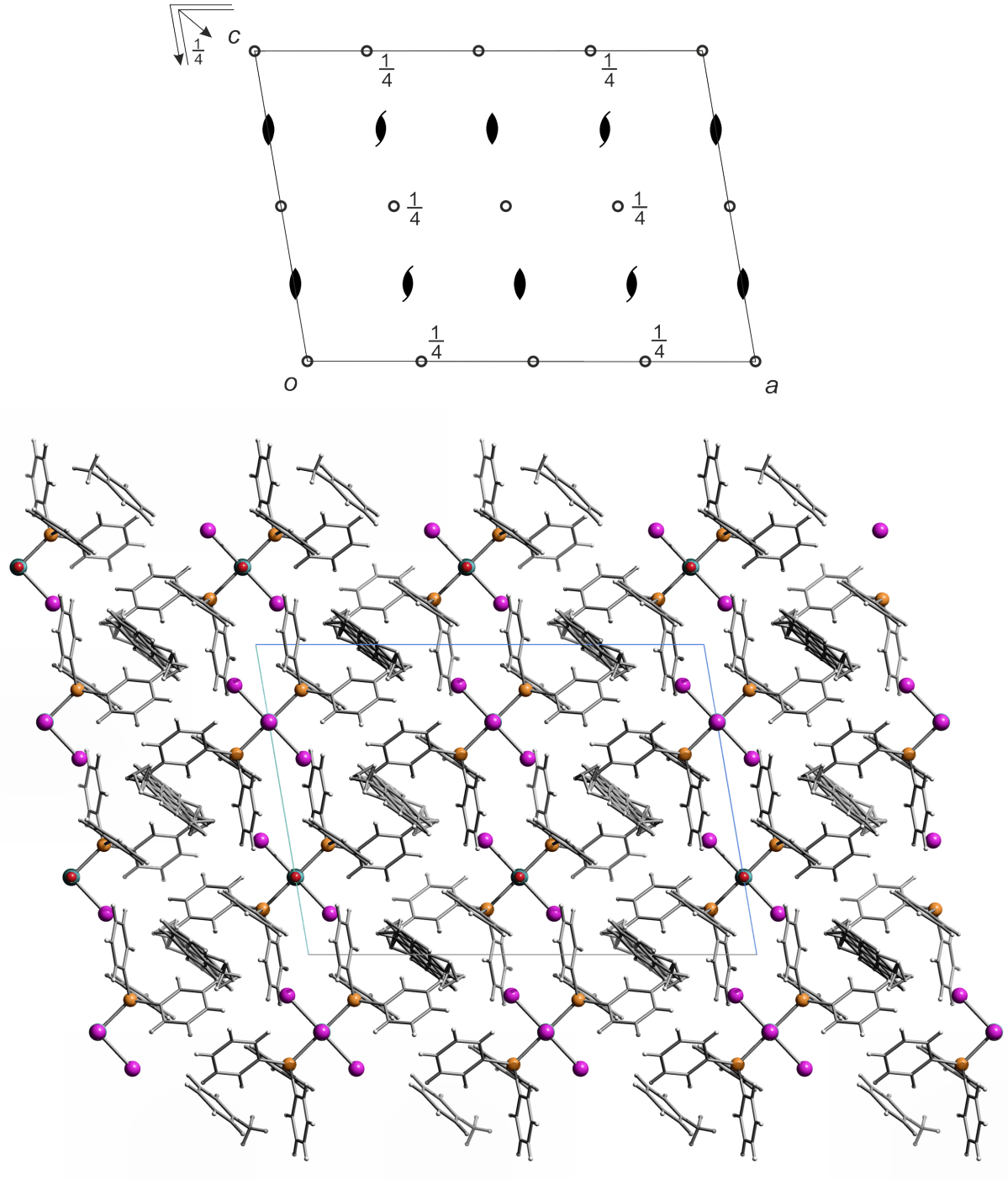

Fig. 6.21 (pn393): SCHAKAL packing diagram of **8a** · C_7H_8 in the monoclinic space group *C*2/*c* with view along [010]. The symmetry elements of the space group *C*2/*c* are overlaid. Atoms: carbon (grey, only depicted as coupling link), hydrogen (white), iodine (lilac), nitrogen (blue), oxygen (red), phosphorus (orange), ruthenium (turquoise). Co-crystallised toluene is disordered *via* an inversion centre.

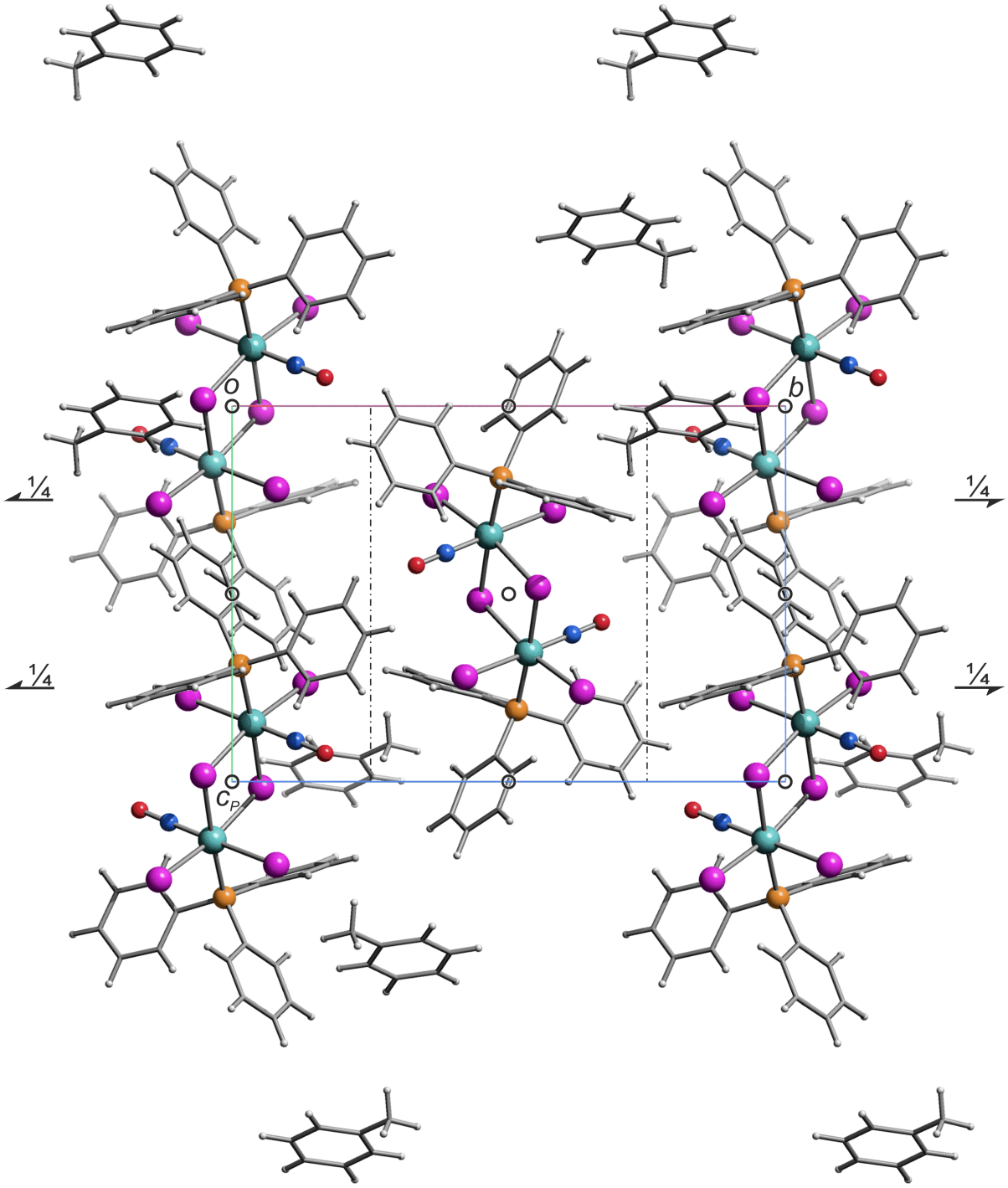

Fig. 6.22 (pn394): SCHAKAL packing diagram of **8c** · C_7H_8 in the monoclinic space group $P2_1/n$ with view along [100]. The symmetry elements of the space group $P2_1/n$ are overlaid. Atoms: carbon (grey, only depicted as coupling link), hydrogen (white), iodine (lilac), nitrogen (blue), oxygen (red), phosphorus (orange), ruthenium (turquoise).

6.3 Crystallographic tables

Table 6.1 Crystallographic data of $[RuCl(NO)_2(PPh_3)_2]BF_4$ (**6b**) and $[RuBr(NO)_2(PPh_3)_2]BF_4$ (**7b**).

	6b	**6b** · C_7H_8	**7b**
netto formula	$C_{36}H_{30}BClF_4N_2O_2P_2Ru$	$C_{43}H_{38}BClF_4N_2O_2P_2Ru$	$C_{36}H_{30}BBrF_4N_2O_2P_2Ru$
M_r/g mol^{-1}	807.89	900.02	852.35
crystal system	monoclinic	orthorhombic	monoclinic
space group	$P2_1/c$	$Pbca$	$P2_1/n$
a/Å	19.2204(3)	21.0163(3)	19.2932(3)
b/Å	9.9060(2)	18.4947(3)	9.96620(10)
c/Å	20.6933(4)	21.2811(3)	20.7107(3)
β/°	117.6270(10)	90.00	116.9370(10)
V/Å^3	3490.73(11)	8271.8(2)	3550.20(8)
Z	4	8	4
ρ/g cm^{-3}	1.537	1.445	1.595
μ/mm^{-1}	0.675	0.578	1.714
crystal size/mm	0.07 × 0.06 × 0.04	0.185 × 0.133 × 0.120	0.25 × 0.22 × 0.18
temperature/K	173(2)	200(2)	173(2)
diffractometer	KappaCCD	KapaCCD	KappaCCD
radiation	MoK_α	MoK_α	MoK_α
anode	rotating anode	rotating anode	rotating anode
rated input/kW	3.025	3.025	3.025
θ range /°	3.15–27.51	3.22–27.48	3.15–27.50
reflexes for metric	12357	34388	14511
absorption correction	none	none	none
reflexes measured	22356	60243	28118
independent reflexes	7924	9464	8113
R_{int}	0.0357	0.0722	0.0359
mean $\sigma(I)/I$	0.0422	0.0432	0.0311
reflexes with $I \geq 2\sigma(I)$	6007	6253	6515
x, y (weighting scheme)	0.0290, 2.4182	0.0395, 9.3766	0.0313, 2.6960
hydrogen refinement	[a]	[a]	[a]
parameters	442	505	442
restraints	0	0	0
$R(F_{obs})$	0.0347	0.0407	0.0303
$R_w(F^2)$	0.0809	0.1072	0.0745
S	1.045	1.029	1.013
shift/error$_{max}$	0.001	0.000	0.001
max. electron density/e Å^{-3}	0.828	0.849	0.845
min. electron density/e Å^{-3}	−0.527	−0.401	−0.808

[a] All H atoms were calculated in idealised positions, riding on their parent atoms.

Table 6.2 Crystallographic data of $[RuCl(NO)_2(PPh_2Bn)_2]BF_4$ (**8b**).

	8b (293 K)	**8b** (248 K)	**8b** (203 K)
netto formula	$C_{38}H_{34}BClF_4N_2O_2P_2Ru$	$C_{38}H_{34}BClF_4N_2O_2P_2Ru$	$C_{38}H_{34}BClF_4N_2O_2P_2Ru$
M_r/g mol^{-1}	835.94	835.94	835.94
crystal system	monoclinic	monoclinic	monoclinic
space group	$P2_1/n$	$P2_1/n$	$P2_1/n$
a/Å	13.1197 (13)	13.1114(9)	13.0423 (4)
b/Å	21.006 (2)	20.9350(16)	20.9379 (8)
c/Å	13.8668 (13)	13.8377(12)	13.7807 (5)
β/°	91.774 (9)	91.974(8)	91.718 (3)
V/Å^3	3819.8 (6)	3796.0(5)	3761.5 (2)
Z	4	4	4
ρ/g cm^{-3}	1.454	1.463	1.476
μ/mm^{-1}	0.619	0.623	0.629
crystal size/mm	0.30 × 0.27 × 0.17	0.30 × 0.27 × 0.17	0.30 × 0.27 × 0.17
temperature/K	293	248 (2)	203 (2)
diffractometer	Oxford XCalibur	Oxford XCalibur	Oxford XCalibur
radiation	MoK_α	MoK_α	MoK_α
anode	fine-focused sealed tube	fine-focused sealed tube	fine-focused sealed tube
rated input/kW	2.00	2.00	2.00
θ range /°	4.20–28.75	4.14–32.29	4.15–32.15
reflexes for metric	3776	4658	5258
absorption correction	multi-scan	multi-scan	multi-scan
transmission factors	0.791–1.000	0.989–1.000	0.988–1.000
reflexes measured	17610	23880	24559
independent reflexes	8667	12332	12185
R_{int}	0.0400	0.0411	0.0380
mean $\sigma(I)/I$	0.0673	0.0755	0.0651
reflexes with $I \geq 2\sigma(I)$	5506	7378	8102
x, y (weighting scheme)	0.0427, 0.0337	0.0443, 1.9709	0.0336, 1.0572
hydrogen refinement	[a]	[a]	[a]
parameters	479	459	488
restraints	0	0	0
$R(F_{obs})$	0.0484	0.0569	0.0468
$R_w(F^2)$	0.1237	0.1114	0.1084
S	1.048	1.043	1.037
shift/error$_{max}$	0.000	0.001	0.001
max. electron density/e Å^{-3}	0.485	0.950	0.849
min. electron density/e Å^{-3}	−0.476	−0.547	−0.542

[a] All H atoms were calculated in idealised positions, riding on their parent atoms.

Table 6.3 Crystallographic data of $[RuCl(NO)_2(PPh_2Bn)_2]BF_4$ (**8b**) and $[RuBr(NO)_2(PPh_2Bn)_2]BF_4$ (**9b**).

	8b (153 K)	**8b** (103 K)	**9b**
netto formula	$C_{38}H_{34}BClF_4N_2O_2P_2Ru$	$C_{38}H_{34}BClF_4N_2O_2P_2Ru$	$C_{38}H_{34}BBrF_4N_2O_2P_2Ru$
M_r/g mol^{-1}	835.94	835.94	880.40
crystal system	monoclinic	monoclinic	monoclinic
space group	$P2_1/n$	$P2_1/n$	$P2_1/n$
a/Å	12.9805 (4)	12.9469 (4)	13.1175(2)
b/Å	20.8824 (7)	20.7987 (6)	20.7878(3)
c/Å	13.7090 (5)	13.6465 (4)	13.6911(2)
β/°	91.563 (4)	91.274 (3)	92.1940(10)
V/Å^3	3714.6 (2)	3673.80 (19)	3730.61(10)
Z	4	4	4
ρ/g cm^{-3}	1.495	1.511	1.568
μ/mm^{-1}	0.637	0.644	1.634
crystal size/mm	0.30 × 0.27 × 0.17	0.30 × 0.27 × 0.17	0.114 × 0.100 × 0.044
temperature/K	153 (2)	103 (2)	173 (2)
diffractometer	Oxford XCalibur	Oxford XCalibur	KappaCCD
radiation	MoK_α	MoK_α	MoK\a
anode	fine-focused sealed tube	fine-focused sealed tube	rotating anode
rated input/kW	2.00	2.00	3.025
θ range /°	4.17–28.75	4.18–28.74	3.14–27.48
reflexes for metric	9874	7862	15906
absorption correction	multi-scan	multi-scan	multi-scan
transmission factors	0.844–1.000	0.958–1.000	0.830–0.931
reflexes measured	29144	21238	29667
independent reflexes	8618	8425	8530
R_{int}	0.0449	0.0435	0.0445
mean $\sigma(I)/I$	0.0425	0.0492	0.0409
reflexes with $I \geq 2\sigma(I)$	6977	6900	6420
x, y (weighting scheme)	0.0349, 2.2268	0.0409, 3.1573	0.0306, 2.4499
hydrogen refinement	[a]	[a]	[a]
parameters	479	470	478
restraints	0	0	0
$R(F_{obs})$	0.0357	0.0384	0.0338
$R_w(F^2)$	0.0915	0.1009	0.0789
S	1.068	1.060	1.030
shift/error$_{max}$	0.000	0.001	0.001
max. electron density/e Å^{-3}	0.739	1.612	0.479
min. electron density/e Å^{-3}	−0.593	−0.894	−0.629

[a] All H atoms were calculated in idealised positions, riding on their parent atoms.

Table 6.4 Crystallographic data of $[RuCl(NO)_2\{P(p\text{-tolyl})_3\}_2]BF_4 \cdot C_7H_8$ (**14b**) and $[RuBr(NO)_2\{P(p\text{-tolyl})_3\}_2]BF_4$ (**15b**).

	14b	**15b**
netto formula	$C_{49}H_{50}BClF_4N_2O_2P_2Ru$	$C_{42}H_{42}BBrF_4N_2O_2P_2Ru$
M_r/g mol^{-1}	984.18	936.51
crystal system	orthorhombic	orthorhombic
space group	$P2_12_12_1$	$Pna2_1$
a/Å	11.1280(2)	30.542(5)
b/Å	12.0220(2)	11.373(5)
c/Å	34.6881(6)	12.190(5)
V/Å^3	4640.60(14)	4234(3)
Z	4	4
ρ/g cm^{-3}	1.409	1.469
μ/mm^{-1}	0.521	1.444
crystal size/mm	0.230 × 0.136 × 0.058	0.20 × 0.13 × 0.03
temperature/K	173(2)	293(2)
diffractometer	KappaCCD	XCalibur
radiation	MoKα	MoKα
anode	rotating anode	fine-focused sealed tube
rated input/kW	3.025	2.00
θ range /°	3.13–27.48	3.13–27.48
reflexes for metric	14400	5355
absorption correction	none	none
reflexes measured	31536	15261
independent reflexes	10588	6133
R_{int}	0.0592	0.0513
mean $\sigma(I)/I$	0.0635	0.0641
reflexes with $I \geq 2\sigma(I)$	8363	5341
x, y (weighting scheme)	0.0303, 3.2272	0.0353, 0.0000
hydrogen refinement	[a]	[a]
parameters	577	503
restraints	0	1
$R(F_{obs})$	0.0438	0.0390
$R_w(F^2)$	0.0904	0.0887
S	1.043	1.023
shift/error$_{max}$	0.003	0.001
max. electron density/e Å^{-3}	0.638	0.736
min. electron density/e Å^{-3}	−0.308	−0.814

[a] All H atoms were calculated in idealised positions, riding on their parent atoms.

Table 6.5 Crystallographic data of $[RuCl(NO)_2(PCy_3)_2]BF_4$ (**18b**), $[RuBr(NO)_2(PCy_3)_2]BF_4$ (**19b**) and $[RuI(NO)_2(PCy_3)_2]BF_4$ (**20b**).

	18b	**19b**	**20b**
netto formula	$C_{36}H_{66}BClF_4N_2O_2P_2Ru$	$C_{36}H_{66}BBrF_4N_2O_2P_2Ru$	$C_{36}H_{66}BF_4IN_2O_2P_2Ru$
M_r/g mol^{-1}	844.18	888.64	935.63
crystal system	triclinic	triclinic	orthorhombic
space group	$P\bar{1}$	$P\bar{1}$	$Pca2_1$
a/Å	10.1237(3)	10.152(4)	29.645(3)
b/Å	13.1351(4)	13.095(5)	14.4732(9)
c/Å	16.2864(4)	18.857(7)	20.678(3)
α/°	80.7850(10)	95.262(14)	
β/°	85.1250(10)	102.251(18)	
γ/°	68.7460(10)	109.874(19)	
V/Å^3	1991.49	2267.0(15)	8872.1(7)
Z	2	2	8
ρ/g cm^{-3}	1.408	1.302	1.401
μ/mm^{-1}	0.594	1.344	1.169
crystal size/mm	0.112 × 0.081 × 0.060	0.109 × 0.105 × 0.088	0.30 × 0.11 × 0.04
temperature/K	100 (2)	273	173(2)
diffractometer	Bruker D8Venture	D8 Quest	Oxford XCalibur
radiation	MoK_α	MoK_α	MoK_α
anode	Bruker TXS	Bruker I\mS	fine-focus sealed tube
rated input/kW	2.5	0.05	2.0
θ range /°	2.83–27.49	2.2541–22.5473	4.20–26.31
reflexes for metric	117	134	7914
absorption correction	multi-scan	multi-scan	multi-scan
transmission factors	0.795–0.862	0.586–0.646	0.871–1.000
reflexes measured	35979	60261	29769
independent reflexes	9180	8643	11453
R_{int}	0.0533	0.0861	0.0402
mean $\sigma(I)/I$	0.0508	0.0551	0.0464
reflexes with $I \geq 2\sigma(I)$	7511	6361	9784
x, y (weighting scheme)	0.0510, 3.4857	0.1541, 9.9830	0.0987, 29.1049
hydrogen refinement	[a]	[a]	[a]
parameters	461	476	833
restraints	0	0	1
$R(F_{obs})$	0.0431	0.0742	0.0548
$R_w(F^2)$	0.1106	0.2583	0.1632
S	1.042	1.092	1.035
shift/error$_{max}$	0.001	0.000	0.001
max. electron density/e Å^{-3}	2.727 (1.60 Å from C18)	3.362 (4.00 Å from C35)	2.388
min. electron density/e Å^{-3}	−0.814	−0.743	−1.289

[a] All H atoms were calculated in idealised positions, riding on their parent atoms.

Table 6.6 Crystallographic data of $[RuCl(NO)_2(PCyp_3)_2]BF_4$ (**21b**) and $[RuBr(NO)_2(PCyp_3)_2]BF_4$ (**22b**).

	21b-2	**21b-1**	**22b** (113 K)
netto formula	$C_{30}H_{54}BClF_4N_2O_2P_2Ru$	$C_{30}H_{54}BClF_4N_2O_2P_2Ru$	$C_{30}H_{54}BBrF_4N_2O_2P_2Ru$
M_r/g mol^{-1}	760.02	760.02	804.47
crystal system	monoclinic	monoclinic	triclinic
space group	$P2_1/c$	$P2_1/n$	$P\bar{1}$
a/Å	14.3483(8)	12.664(6)	10.8145(7)
b/Å	12.5016(7)	19.479(9)	12.3066(9)
c/Å	19.4893(12)	14.921(7)	13.8538(9)
α/°			104.889(6)
β/°	106.688(2)	111.23(2)	91.394(5)
γ/°			108.105(6)
V/Å^3	3348.7(3)	3431(3)	1682.7(2)
Z	4	4	2
ρ/g cm^{-3}	1.508	1.471	1.588
μ/mm^{-1}	0.697	0.680	1.801
crystal size/mm	0.291 × 0.101 × 0.050	0.157 × 0.100 ×0.057	0.19 × 0.17 × 0.14
temperature/K	100	293(2)	113
diffractometer	D8 Venture	Bruker D8Quest	Oxford XCalibur
radiation	'Mo Kα	MoK_α	MoK_α
anode	Bruker TXS	Bruker I\mS	fine-focus sealed tube
rated input/kW	2.5	0.05	2.00
θ range /°	2.96–29.16	3.34–23.62	4.31–25.35
reflexes for metric	142	118	2586
absorption correction	multi-scan	multi-scan	multi-scan
transmission factors	0.069–0.722	0.679–0.746	0.989–1.000
reflexes measured	130884	78628	7909
independent reflexes	9061	7892	5780
R_{int}	0.0634	0.0914	0.0315
mean $\sigma(I)/I$	0.0305	0.0639	0.0724
reflexes with $I \geq 2\sigma(I)$	7470	4633	4679
x, y (weighting scheme)	0.0451, 8.2946	0.0390, 4.7712	0.0135, 0.2175
hydrogen refinement	[a]	[a]	[a]
parameters	398	427	388
restraints	0	0	0
$R(F_{obs})$	0.0415	0.0504	0.0388
$R_w(F^2)$	0.1059	0.1132	0.0816
S	1.052	1.038	1.060
shift/error$_{max}$	0.001	0.002	0.000
max. electron density/e Å^{-3}	2.368 (1.01 Å from C8)	0.571	0.760
min. electron density/e Å^{-3}	−0.937	−0.381	−0.564

[a] All H atoms were calculated in idealised positions, riding on their parent atoms.

Table 6.7 Crystallographic data of $[RuBr(NO)_2(PCyp_3)_2]BF_4$ (**22b**).

	22b (153 K)	**22b** (193 K)	**22b** (233 K)
netto formula	$C_{30}H_{54}BBrF_4N_2O_2P_2Ru$	$C_{30}H_{54}BBrF_4N_2O_2P_2Ru$	$C_{30}H_{54}BBrF_4N_2O_2P_2Ru$
M_r/g mol^{-1}	804.47	804.47	804.47
crystal system	triclinic	triclinic	triclinic
space group	$P\bar{1}$	$P\bar{1}$	$P\bar{1}$
a/Å	10.7881(7)	10.6634(6)	10.6061(5)
b/Å	12.3342(9)	12.3972(8)	12.4576(7)
c/Å	13.8933(9)	14.0285(8)	14.1425(9)
α/°	104.916(6)	104.851(5)	104.826(5)
β/°	91.354(6)	91.200(5)	91.111(4)
γ/°	107.901(6)	107.314(5)	106.940(4)
V/Å^3	1689.3(2)	1701.8(2)	1719.1(2)
Z	2	2	2
ρ/g cm^{-3}	1.582	1.570	1.554
μ/mm^{-1}	1.794	1.781	1.763
crystal size/mm	0.19 × 0.17 × 0.14	0.19 × 0.17 × 0.14	0.19 × 0.17 × 0.14
temperature/K	153(2)	193(2)	233(2)
diffractometer	Oxford XCalibur	Oxford XCalibur	Oxford XCalibur
radiation	MoK_α	MoK_α	MoK_α
anode	fine-focus sealed tube	fine-focus sealed tube	fine-focus sealed tube
rated input/kW	2.00	2.00	2.00
θ range /°	4.30–25.35	4.39–25.35	4.16–25.35
reflexes for metric	2580	3241	3712
absorption correction	multi-scan	multi-scan	multi-scan
transmission factors	0.976–1.000	0.985–1.000	0.981–1.000
reflexes measured	8660	8635	9397
independent reflexes	6102	6138	5330
R_{int}	0.0317	0.0241	0.0268
mean $\sigma(I)/I$	0.0731	0.0556	0.0443
reflexes with $I \geq 2\sigma(I)$	4798	5119	4510
x, y (weighting scheme)	0.0223, 1.0312	0.0431, 7.9282	0.0445, 6.9554
hydrogen refinement	[a]	[a]	[a]
parameters	388	388	388
restraints	0	0	0
$R(F_{obs})$	0.0407	0.0525	0.0496
$R_w(F^2)$	0.0919	0.1288	0.1224
S	1.039	1.029	1.035
shift/error$_{max}$	0.000	0.000	0.000
max. electron density/e Å^{-3}	0.830	2.112 (0.82 Å from Br1)	1.159
min. electron density/e Å^{-3}	−0.559	−1.475	−1.330

[a] All H atoms were calculated in idealised positions, riding on their parent atoms.

Table 6.8 Crystallographic data of $[RuI(NO)_2(PCyp_3)_2]BF_4$·(**23b**).

	22b (273 K)	**23b**
netto formula	$C_{30}H_{54}BBrF_4N_2O_2P_2Ru$	$C_{30}H_{54}BF_4IN_2O_2P_2Ru$
M_r/g mol^{-1}	804.47	851.47
crystal system	triclinic	triclinic
space group	$P\bar{1}$	$P\bar{1}$
a/Å	10.5646(5)	10.4351(3)
b/Å	12.4979(7)	12.4604(4)
c/Å	14.1969(8)	14.3846(4)
α/°	104.825(5)	105.9226(12)
β/°	90.938(4)	90.8080(13)
γ/°	106.823(4)	106.6948(13)
V/Å^3	1726.24(2)	1714.00(9)
Z	2	2
ρ/g cm^{-3}	1.548	1.650
μ/mm^{-1}	1.756	1.504
crystal size/mm	0.19 × 0.17 × 0.14	0.226× 0.146 × 0.104
temperature/K	273(2)	200 (2)
diffractometer	Oxford XCalibur	Bruker D8Quest
radiation	MoK_α	Mo K\a
anode	fine-focus sealed tube	Bruker I\mS
rated input/kW	2.00	0.05
θ range /°	4.34–25.35	2.40–27.65
reflexes for metric	4092	122
absorption correction	multi-scan	multi-scan
transmission factors	0.978–1.000	0.502–0.563
reflexes measured	9186	31068
independent reflexes	6255	7837
R_{int}	0.0220	0.0272
mean $\sigma(I)/I$	0.0419	0.0254
reflexes with $I \geq 2\sigma(I)$	5306	6560
x, y (weighting scheme)	0.0495, 4.4485	0.0416, 10.5087
hydrogen refinement	[a]	[a]
parameters	388	407
restraints	0	0
$R(F_{obs})$	0.0463	0.0473
$R_w(F^2)$	0.1207	0.1213
S	1.037	1.046
shift/error$_{max}$	0.000	0.001
max. electron density/e Å^{-3}	1.194	2.531 (0.82 Å from I1)
min. electron density/e Å^{-3}	−1.226	−3.257

[a] All H atoms were calculated in idealised positions, riding on their parent atoms.

Table 6.9 Crystallographic data of $[RuCl(NO)_2(P^iPr_3)_2]BF_4$ (**24b**), $[RuBr(NO)_2(P^iPr_3)_2]BF_4$ (**25b**) and $[\{Ru(NO)_2(P^iPr_3)\}_2(\mu\text{-}I)]BF_4$ (**26c**).

	24b	**25b**	**26c**
netto formula	$C_{18}H_{42}BClF_4N_2O_2P_2Ru$	$C_{18}H_{42}BBrF_4N_2O_2P_2Ru$	$C_{18}H_{42}BF_4IN_4O_4P_2Ru_2$
M_r/g mol^{-1}	603.81	648.27	856.35
crystal system	triclinic	monoclinic	triclinic
space group	$P\bar{1}$	$C2/c$	$P1$
a/Å	8.0664(6)	25.5181(9)	7.989(5)
b/Å	12.7931(9)	15.9734(6)	8.434(5)
c/Å	14.3849(11)	14.3915(5)	13.137(5)
α/°	114.416(4)		91.165(5)
β/°	91.746(5)	115.204(2)	97.389(5)
γ/°	91.295(5)		118.210(5)
V/Å^3	1350.04(17)	5307.7(3)	770.2(7)
Z	2	8	1
ρ/g cm^{-3}	1.485	1.623	1.846
μ/mm^{-1}	0.839	2.262	2.140
crystal size/mm	0.15 × 0.09 × 0.03	0.134 × 0.056 × 0.037	0.120 × 0.080 × 0.020
temperature/K	100(2)	100(2)	123(2)
diffractometer	D8 Venture	D8 Venture	D8 Venture
radiation	Mo Kα	Mo Kα	Mo Kα
anode	Bruker TXS	Bruker TXS	Bruker TXS
rated input/kW	2.5	2.5	2.5
θ range /°	2.52–24.86	2.74–27.64	3.04–26.83
reflexes for metric	9922	118	9456
absorption correction	multi-scan	multi-scan	multi-scan
transmission factors	0.630–0.745	0.684–0.746	0.664–0.745
reflexes measured	42773	44638	9822
independent reflexes	4587	6131	3277
R_{int}	0.0963	0.0697	0.0000
mean $\sigma(I)/I$	0.0591	0.0416	0.0188
reflexes with $I \geq 2\sigma(I)$	3525	4973	3227
x, y (weighting scheme)	0.0858, 7.6844	0.0281, 14.5172	0.0248, 0.5086
hydrogen refinement	[a]	[a]	[a]
Flack parameter[b]			0.100(14)
parameters	308	332	337
restraints	0	0	3
$R(F_{obs})$	0.0618	0.0335	0.0174
$R_w(F^2)$	0.1790	0.0761	0.0431
S	1.081	1.027	1.058
shift/error$_{max}$	0.001	0.001	0.001
max. electron density/e Å^{-3}	1.574	1.302	0.649
min. electron density/e Å^{-3}	−1.598	−0.902	−0.433

[a] All H atoms were calculated in idealised positions, riding on their parent atoms. [b] See Ref. [159]

Table 6.10 Crystallographic data of [RuCl(NO)(PPh_3)$_2$] (**6c**), [RuCl(NO)(P^tBuPh_2)$_2$] (**13c**) and [{RuBr(μ-Br)(NO)(PPh_3)}$_2$] (**7c**).

	6c	**13c**	**7c**
netto formula	$C_{36}H_{30}ClNOP_2Ru \cdot 0.5\ C_7H_8$	$C_{32}H_{38}ClNOP_2Ru$	$C_{36}H_{30}Br_6N_2O_2P_2Ru_2$
M_r/g mol^{-1}	737.14	651.09	1266.16
crystal system	monoclinic	monoclinic	monoclinic
space group	$P2_1/n$	$P2_1/c$	$P2_1/c$
a/Å	11.7064(4)	12.0777(2)	10.9679(2)
b/Å	18.6843(6)	16.8711(2)	10.1499(2)
c/Å	16.2716(5)	16.6346(3)	18.5053(3)
α/°	90	90	90
β/°	104.3450(10)	115.6850(10)	90.5071(12)
γ/°	90	90	90
V/Å^3	3448.05(19)	3054.61(8)	2059.99(6)
Z	4	4	2
ρ/g cm^{-3}	1.417	1.416	2.041
μ/mm^{-1}	0.657	0.731	6.664
crystal size/mm	0.291 × 0.096 × 0.055	0.367 × 0.316 × 0.132	0.223 × 0.202 × 0.079
temperature/K	200(2)	293(2)	173(2)
diffractometer	Bruker D8Quest	KappaCCD	KappaCCD
radiation	Mo Kα	Mo Kα	Mo Kα
anode	Bruker I\mS	rotating anode	rotating anode
rated input/kW	0.05	3.025	3.025
θ range /°	2.45–26.43	3.51–27.67	3.50–27.48
reflexes for metric	130	13788	8842
absorption correction	multi-scan	none	none
transmission factors	0.603–0.647	–	–
reflexes measured	57770	26304	14991
independent reflexes	7068	7074	4714
R_{int}	0.0601	0.0389	0.0365
mean $\sigma(I)/I$	0.0331	0.0289	0.0309
reflexes with $I \geq 2\sigma(I)$	5564	5957	4098
x, y (weighting scheme)	0.0250, 1.6290	0.0267, 1.6571	0.0420, 4.1690
hydrogen refinement	[a]	[a]	[a]
parameters	444	343	226
restraints	0	0	0
$R(F_{obs})$	0.0289	0.0277	0.0314
$R_w(F^2)$	0.0619	0.0683	0.0840
S	1.030	1.057	1.053
shift/error$_{max}$	0.006	0.001	0.001
max. electron density/e Å^{-3}	0.324	0.353	0.995
min. electron density/e Å^{-3}	−0.292	−0.494	−1.410

[a] All H atoms were calculated in idealised positions, riding on their parent atoms.

Table 6.11 Crystallographic data of $[RuI_3(NO)(PPh_3)_2] \cdot C_7H_8$ (**8a** · C_7H_8), $[\{RuI(\mu\text{-}I)(NO)(PPh_3)\}_2] \cdot C_7H_8$ (**8c** · C_7H_8).

	8a	**8c**
netto formula	$C_{43}H_{38}I_3NOP_2Ru$	$C_{50}H_{46}I_6N_2O_2P_2Ru_2$
M_r/g mol^{-1}	1127.45	1732.37
crystal system	monoclinic	monoclinic
space group	*C*2/*c*	$P2_1/n$
a/Å	24.2611(6)	12.3830(3)
b/Å	9.8421(2)	18.1580(3)
c/Å	17.0144(4)	13.2614(3)
α/°	90	90
β/°	99.6860(10)	111.5430(10)
γ/°	90	90
V/Å^3	4004.79(16)	2773.53(10)
Z	4	2
ρ/g cm^{-3}	1.870	2.074
μ/mm^{-1}	2.819	3.980
crystal size/mm	0.06 × 0.04 × 0.02	0.154 × 0.078 × 0.063
temperature/K	173(2)	173(2)
diffractometer	KappaCCD	KappaCCD
radiation	Mo Kα	Mo Kα
anode	rotating anode	rotating anode
rated input/kW	3.025	3.025
θ range /°	3.19–27.40	3.30–27.48
reflexes for metric	8754	11872
absorption correction	none	none
reflexes measured	16511	20956
independent reflexes	4540	6345
R_{int}	0.0606	0.0502
mean $\sigma(I)/I$	0.0460	0.0472
reflexes with $I \geq 2\sigma(I)$	3244	4613
x, *y* (weighting scheme)	0.0239, 17.4568	0.0522, 9.5945
hydrogen refinement	[a]	[a]
parameters	218	266
restraints	0	0
$R(F_{obs})$	0.0369	0.0420
$R_w(F^2)$	0.0772	0.1119
S	1.065	1.027
shift/error$_{max}$	0.001	0.001
max. electron density/e Å^{-3}	2.070	1.916
min. electron density/e Å^{-3}	−0.725	−0.764

[a] All H atoms were calculated in idealised positions, riding on their parent atoms.

7 Bibliography

[1] E. Coulotta, D.E. Koshland, *Science* **1992**, *258*, 1862–1865.

[2] J. F. Noxon, *Geophys. Res. Lett.* **1976**, *3*, 463–465.

[3] H. G. Schlegel, *Allgemeine Mikrobiologie*, 7. Edition, Thieme Stuttgart · New York **1992**.

[4] Holleman, Wiberg, *Lehrbuch der Anorganischen Chemie*, 102. Edition, Walter de Gruyter, Berlin · New York, **2007**, p. 711.

[5] W. Ostwald, patent GB190200698: *Improvements in the Manufacture of Nitric Acid and Nitrogen Oxides,* **1902.**

[6] J. Kesselmeier, *Forschungsbericht Max-Planck-Institut für Chemie*, **2012**.

[7] Holleman, Wiberg, *Lehrbuch der Anorganischen Chemie*, 102. Edition, Walter de Gruyter, Berlin · New York, **2007**, p. 522.

[8] H. Marquardt, S.G. Schäfer, R. McClellan, F. Welsch, *Toxicology* **1999**, Academic Press, 1. Edition, pp. 823–826.

[9] Holleman, Wiberg, *Lehrbuch der Anorganischen Chemie*, 102. Edition, Walter de Gruyter, Berlin · New York, **2007**, pp. 518–522.

[10] H-J. Galla, *Angew. Chem.* **1993**, *105*, 399–402.

[11] H. Zankl, *Die Launen des Zufalls - Wissenschaftliche Entdeckungen von Archimedes bis heute*, 1. Edition, Primus Verlag, Darmstadt, **2002**, p. 221.

[12] *Der Gynäkologe* **1998**, Springer, *11*, 989.

[13] R. F. Furchgott, *Physiology or Medicine* **1998**, 152–169.

[14] F. Murad, *Angew. Chem. Int. Ed.* **1999**, *38*, 1856–1868.

[15] L.J. Ignarro, *Angew. Chem. Int. Ed.* **1999**, *38*, 1882–1892.

[16] R.M.J. Palmer, A.G. Ferige and S. Moncada, *Nature*, **1987**, *327*, 524–526.

[17] M.J. Rand, C.G. Li, *Annu. Rev. Physiol*. **1995**, *57*, 659–682.

[18] H.D. Langtry, A. Marham, D*rugs* **1999**, 57, 967–989.

[19] D.A. Wink, *Science* **1991**, *254*, 1001–1003.

[20] D. Chaterjee, A. Mitra, *Platinum Metals Rev.* **2006**, *50*, 62–69.

[21] A. Wanat, T. Schneppensieper, A. Karocki, G. Stochel, R. van Eldik, *J. Chem. Soc., Dalton Trans.*, **2009**, 941–950.

[22] A. Saxon, H.E. Kattlove, *Blood* **1976**, *47*, 957–961.

[23] R.M.J. Palmer, A.G. Ferige and S. Moncada, *Nature* **1987**, *327*, 524–526.

[24] C. Miller, M. Miller, B. McMullin, G. Regev, L. Serghides, K. Kain, J. Road, Y. Av-Gay, *Journal of Cystic Fibrosis* **2012**, *11*, 324–331.

[25] C. Roegler, J. Lehmann, *Pharm. Unserer Zeit* **2010**, *39*, 351–358.

[26] J.J. Oliver, J.W. Dear, D.J. Webb, *Hypertension* **2010**, *39*, 62–67.

[27] E.M. Schuman, D.V. Madison, *Science* **2010**, *254*, 1503–1506.

[28] R. M. Palmer, S. Moncada, *Biochem. Biophys. Res. Commun*. **1989**, *158*, 348–352.

[29] D. Bredt, S. Snyder, *Proc. Natl. Acad. Sci USA* **1990**, *87*, 682–685.

[30] D. Stuehr, H. Cho, N. Kwon, M. Weise, C. Nathans, *Proc. Natl. Acad. Sci USA* **1991**, *88*, 7773–7777.

[31] S. Pfeiffer, B. Mayer, B. Hemmens, *Angew. Chem. Int. Ed.* **1999**, *38*, 714–731.

[32] S. Archer, *FASEB J.* **1993**, *7*, 349–360.

[33] T.S. Hakim, K. Sugimori, E.M. Camporesi, G. Anderson, *Physiol. Meas.* **1996**, *17*, 267–277.

[34] S. Daff, *Nitric Oxide* **2010**, *23*, 1–11.

[35] J.S. Beckmann, W.H. Koppenol, *Am. J. Physiol. C* **1996**, *271*, 1424–1437.

[36] I. Fridovich, *Annu. Rev. Biochem*. **1995**, *64*, 97–112.

[37] W.A. Pryor, G.L. Squadrito, *Am. J. Physiol. L* **1995**, *12*, 699–722.

[38] R.J.P. Williams, *Chem. Soc. Rev.* **1996**, 77–83.

[39] J.M.C. Ribeiro, O. Marinotti, R. Gonzales, *Br. J. Pharmacol.* **1990**, *101*, 932–936.

[40] B.A. Trimmer, R.J. Aprille, D.M. Dudzinski, C.J. Lagace, S.M. Lewis, T. Michel, S. Quazi, R.M. Zayas, *Science* **2001**, *292*, 2486–2488.

[41] L.E. Laverman, A. Wanat, J. Oszajca, G. Stochel, P.C. Ford, R. van Eldik, *J. Am. Chem. Soc*. **2001**, 123,285–293.

[42] E.A. Brucker, J.S. Olson, M. Ikeda-Saito, G.N. Phillips, *Proteins: Structure, Function, and Genetics* **1998**, *30*, 352–356.

[43] D.M. Minning, A.J. Gow, J. Bonaventura, R. Braun, M. Dewhirst, D.E. Goldberg, J.S. Stamler *Nature* **1999**, *401*, 497–502.

[44] J.H. Enemark, R.D. Feltham, *Coord. Chem. Rev.* **1974**, *13*, 339–406.

[45] Holleman, Wiberg, *Lehrbuch der Anorganischen Chemie*, 102. Edition, Walter de Gruyter, Berlin · New York, **2007**, p. 707.

[46] Y. Liu, Y. Guo, J. Lin, G. Huang, C. Duan, F. Li, *Mol. Phys.* **2001**, *99*, 1457–1461.

[47] I.G. Zacharia, W.M. Deen, *Ann. Biom. Eng*., **2005**, *33*, 214–222.

[48] J.A. McCleverty, *Chem. Rev.* **2004**, *104*, 403–418.

[49] L.K. Bell, D.M.P. Mingos, D.G. Tew, L.F. Larkworthy, B. Sandell, D.C. Povey, J. Mason, *J. Chem. Soc., Chem. Commun.* **1983**, 125–126

[50] E. Riedel, *Moderne Anorganische Chemie*, 3. Edition, Walter de Gruyter, Berlin · New York, **2007,** pp. 664–666.

[51] P. Coppens, I. Novozhilova, A. Kovalevsky, *Chem. Rev.* **2002**, *102*, 861–883.

[52] D.V. Fomitchev, I. Novozhilova, P. Coppens, *Tetrahedron* **2000**, *56*, 6813–6820.

[53] H. Zöllner, T. Woike, W. Krasser, S. Haussühl, *Z. Kristallogr*. **1989**, *188*, 139.

[54] U. Hauser, V. Oestreich, H.D. Rohrweck, *Z. Physik A* **1977**, *280*, 17–25.

[55] M.D. Carducci, M. R. Pressprich, P. Coppens, *J. Am. Chem. Soc.* **1997**, 2669–2678.

[56] A. Zangl, P. Klüfers, D. Schaniel, T. Woike, *Dalton Trans.* **2009**, 1043–1045.

[57] A. Zangl, P. Klüfers, D. Schaniel, T. Woike, *Inorg. Chem. Commun.* **2009**, 1064–1066.

[58] H. Giglmeier, T. Kerscher, P. Klüfers, D. Schaniel, T. Woike, *Dalton Trans.* **2009**, 9113–9116.

[59] P.S. Schaiquevich, J.A. Guidea, P.J. Aymonino, *Inorg. Chim. Acta* **2000**, *303*, 277–281.

[60] D.V. Fomitchev, T.R. Furlani, P. Copppens, *Inorg. Chem.* **1978**, *37*, 1519–1526.

[61] O. Crichton, A.J. Rest, *J. Chem. Soc., Dalton Trans.* **1977**, 986–993.

[62] O. Crichton, A.J. Rest, *J. Chem. Soc., Dalton Trans.* **1978**, 202–207.

[63] O. Crichton, A.J. Rest, *J. Chem. Soc., Dalton Trans.* **1978**, 208–215.

[64] D. Schaniel, T. Woike, N.-R. Behrnd, J. Hauser, K.W. Krämer, T. Todorova and B. Delley, *Inorg. Chem.,* **2009**, *48*, 11399–11406.

[65] S. Frelay, H.W. Schmalle, G. Francese, H. Stoeckli-Evans, M. Imlau, D. Schaniel, T. Woike, *Inorg. Chem.* **2004**, *43*, 3500–3506.

[66] M. Imlau, S. Haussühl, T. Woike, R. Schieder, V. Angelov, R.A. Rupp, K. Schwarz, *Appl. Phys. B* **1999**, *68*, 877–885.

[67] D. Schaniel, T. Woike, B. Delley, C. Boskovic, D. Biner, K.W. Krämer, H.-U. Güdel, *Phys. Chem. Chem. Phys.* **2005**, *7*, 1164–1170.

[68] D. Schaniel, B. Cormary, I. Malfant, L. Valade, T. Woike, B. Delley, K.W. Krämer, H.-U. Güdel, *Phys. Chem. Chem. Phys.* **2005**, *9*, 3717–3724.

[69] M. Herberhold, A. Razavi, *Angew. Chem. Int. Ed*. **1972**, *11*, 1092–1094.

[70] M.M. Doeff, R.G. Pearson, *Inorg. Chim. Acta* **1986**, *117*, 151–155.

[71] L. Schlecht, G. Hamprecht, F. Spoun, patent DE613400: *Verfahren zur Herstellung von Kobaltnitrosylcarbonyl und Kobaltnitrosyl bzw. von Kobaltnitrosyl allein*, **1932**.

[72] L. Playfair, *Proc. Roy. Soc. (London)* **1849**, *5*, 845; L. Playfair, *Justus Liebigs Ann. Chem*. **1850**, *74*, 317–340.

[73] P.R.H. Alderman, P.G. Owston, J.M. Rowe, *Acta Cryst.* **1962**, 13, 668–673.

[74] D.J. Hodgson, N.C. Payne, J.A. McGinnety, R.G. Pearson, J.A. Ibers, *J. Am. Chem. Soc.* **1968**, *90*, 4486–4488.

[75] J. Huheey, E. Keiter, R.Keiter, *Anorganische Chemie - Prinzipien von Struktur und Reaktivität*, 3. Edition, Walter de Gruyter, Berlin · New York, **2003**, pp. 766–768.

[76] F. Seel, *Z. Anorg. Allg. Chem.* **1942**, *249*, 308–324; F. Seel, *Z. Anorg. Allg. Chem.* **1957**, *293*, 91.

[77] N.V. Sidgwick, R.W. Bailey, *Proc. Roy. Soc. (London) A* **1934**, *144*, 521–537.

[78] A.D. Walsh, *J. Chem. Soc.* **1953**, 2266–2288.

[79] T.J. Greenhough, B.W.S. Kolthammer, P Legzdins, J. Trotter, *Acta Cryst. B* **1980**, *36*, 795–799.

[80] B.L. Haymore, J.C. Huffman, N.E. Butler, *Inorg. Chem.* **1983**, *22*, 168–170.

[81] D. Nietlispach, H.W. Bosch, H. Berke, *Chem. Ber.* **1994**, *127*, 2403–2415.

[82] A. Llamazares, H.W. Schmalle, H. Berke, *Organometallics* **2001***, 20,* 5277–5288.

[83] M-C. Hung, M-C. Tsai, G-H Lee, W-F. Liaw, *Inorg. Chem.* **2006**, *45*, 6041–6047.

[84] S.-W. Yeh, C.-W. Lin, Y.W. Li, I-J. Hsu, C.-H. Chen, L.-Y. Jang, J.-F. Lee, W.-F. Liaw, *Inorg. Chem.* **2012**, *51*, 4076–4087.

[85] H. Lewandowska, M. Kalinowska, K. Brzóska, K. Wójciuk, G. Wójciuk, M. Kruszewski, *Dalton Trans.* **2011**, *40*, 8273–8289.

[86] H. C. Lok, Y.S. Rahmanto, C.L. Hawkins, D.S. Kalinowski, C.S. Morrow, A.J. Townsend, P. Ponka, D.R. Richardson, *J. Biol. Chem.* **2012**, *287*, 607–618.

[87] D.R. Richardson, H.C. Lok, *Biochimica et Biophysica Acta* **2008***,* 638–651.

[88] C.A. Bosworth, J.C. Toledo, Jr., J.W. Zmijewski, Q. Li, J.R. Lancaster, Jr. Lok, *Proc. Natl. Acad. Sci. USA* **2009***, 106,* 4671–4676.

[89] M. L. Roussin, *Ann. Chim. Phys.* **1858***, 52,* 285–303.

[90] W. Kaim, B. Schwederski, *Bioanorganische Chemie*, 3. Edition, Teubner, Stuttgart · Leipzig · Wiesbaden, **2004.**

[91] D.C. Harris, *Canadian Mineralogist* **1974**, *12*, 280–284.

[92] H. Bielawa, O. Hinrichsen, A. Birkner, M. Muhler, *Angew. Chem. Int. Ed.* **2001**, *40,* 1061–1063.

[93] A. Fürstner, *Angew. Chem. Int. Ed.* **2000**, *39*, 3012–3043.

[94] D. Kuang, S. Ito, B. Wenger, C. Klein, J.-E. Moser, R. Humphry-Baker, S.M. Zakeeruddin, M. Grätzel, *J. Am. Chem. Soc.* **2006**, *128*, 4146–4154.

[95] M.C. Moreno-Bondi, O.S. Wolfbeis, M.J.P. Leiner, B.P.H. Schaffar, *Anal. Chem.* **1990**, *62*, 2377–2380.

[96] R. Dierichs, *Histochemistry* **1979**, *64*, 171–187.

[97] C.S. Allardyce, P.J. Dyson, *Platinum Metals Rev.* **2001**, *45*, 62–69.

[98] S.P. Fricker, *Platinum Metals Rev.* **1995**, *39*, 150–159

[99] C.A. Tolman, *Chem. Rev*. **1977**, *77*, 313–348.

[100] C.A. Streuli, *Anal. Chem*. **1960**, *32*, 985-987.
[101] C. Elschenbroich, A. Salzer, *Organometallics : A Concise Introduction,* 2nd Ed. Wiley-VCH: Weinheim, **1992**.
[102] D. Steinborn, *Grundlagen der metallorganischen Komplexkatalyse*, 2. Edition, Vieweg + Teubner, Wiesbaden, **2010**.
[103] A.P. Gaughan, B.J. Corden, R. Eisenberg, J.A. Ibers, *Inorg. Chem.* **1974**, *13*, 786–791.
[104] N. Arulsamy, D.S. Bohle, J.A. Imonigie, R.C. Moore, *Polyhedron.* **2007**, *26*, 4737–4745.
[105] L.A. Watson, M. Pink, K.G. Caulton, *J. Mol. Chem. Catal. A* **2004**, *224*, 51–59.
[106] D.M.P. Mingos, D.J. Sherman and I.D. Williams, *Transition Met. Chem.* **1987**, *12*, 493–496.
[107] A. Pierpont, A. Eisenberg, *Inorganic Chemistry*, **1972**, *11*, 1088–1094.
[108] M.R. Crimmin, R.G. Bergman and F.D. Toste, *Angew. Chem. Int. Ed.*, **2011**, *50*, 4484–4487.
[109] J.R. Durig, W.A: McAllister, J.N. Willis, E.E. Mercer, *Spectrochim. Acta.* **1966**, *22*, 1091–1100.
[110] M.J. Cleare, W.P. Griffith, *J. Chem. Soc. A* **1967**, *7*, 1144–1147.
[111] J.M. Fletcher, I.L. Jenkins, F.M. Lever, F.S. Martin, A.R. Powell, R. Todd, *J. Inorg. Nucl. Chem.* **1955**, *1*, 378–401.
[112] *Cambridge Structural Database* (version 5.34, november 2012).
[113] Morales-Morales, R. Redón, R.E. Cramer, *Inorg. Chimica Acta.* **2001**, *321*, 181–184.
[114] E. Riedel, *Moderne Anorganische Chemie*, 3. Edition, Walter de Gruyter, Berlin · New York, **2007**, pp. 399–401.
[115] A.W. Addison, T.N. Rao, J. Reedijk, J.van Rijn, G.C. Verschoor, *J. Chem. Soc. Dalton Trans.* **1984**, 1349–1356.
[116] S. Alvarez, P. Alemany, D. Casanova, J. Cirera, M. Llunell, D. Avnir, *Coord. Chem. Rev.*, **2005**, *249*, 1693–1708.
[117] A. Pierpont, A. Eisenberg, *J. Am. Chem. Soc.*, **1970**, *92*, 4760.
[118] F. Neese, ORCA – an ab initio, density functional and semiempirical program package, Version 2.9 University of Bonn, **2006**.
[119] A.D. Becke, *Phys. Rev. A* **199**9, *38*, 3098.
[120] J.P. Perdew, *Phys. Rev. B* **1986**, *33*, 8822.
[121] A. Schaefer, H. Horn and R. Ahlrichs, *J. Chem. Phys.* **1992**, *97*, 2571.
[122] F. Weigend, R. Ahlrichs, Phys. Chem. Chem. Phys. **2005**, *7*, 3297.
[123] C. Lee, W. Yang, R.G. Parr, *Phys. Rev. B: Condens. Matter Mater. Phys.* **1988**, 37, 785–789.
[124] S.H. Vosko, L. Wilk, M. Nusair, *Can. J. Phys.* **1980**, *58*, 1200–1211.
[125] P.J. Stepehns, F.J. Devlin, C.F. Chabalowski, M.J. Frisch, *J. Phys. Chem.* **1994**, 98, 11623–11627.
[126] A.D. Becke, *J. Chem. Phys.* **1993**, *98*, 5648–5652.
[127] B. Miehlich, A. Savin, H. Stoll, H. Preuss, *Chem. Phys. Lett.* **1989**, 157, 200–206.
[128] J. Tao, J.P. Perdew, V.N. Staroverov, G.E. Scuseria, *Phys. Rev. Lett.* **2003**, *91*.
[129] F.L. Hirshfeld, *Acta Cryst. A* **1976**, *32*, 239–244.
[130] D. Andrea, U. Häußermann, M. Dolg, H. Stoll, H. Preuß, *Theor. Chim. Acta* **1990**, *77*, 123–141.
[131] T.H. Dunning, P.J. Hay, *in Modern Theoretical Chemistry*, ed. H.F. Schaefer, Plenum, New York, 3rd edn **1976**, vol. 3, pp 1–28.
[132] S. Smeets, P. Parois, H.-B. Bürgi, M. Lutz, *Acta Cryst*. *B* **2011**, *67*, 53–62.
[133] Mathworks, MATLAB, version 7.12, **2011**.
[134] T. Mayer, H.-C. Böttcher, *Z. Naturforsch*. **2013**, *68b*, 743–746.
[135] J.T. Thomas, J.H. Robertson, E.G. Cox, *Acta Cryst.* **1958**, *11*, 599–604.

[136] J. Mason, D.M.P. Mingos, D. Sherman, R.W.M. Wardle*, J. Chem. Soc, Chem. Commun.* **1984**, 1223–1225.
[137] B.L. Haymore, J.A. Ibers, *Inorg. Chem.* **1975**, *14*, 360–370.
[138] A.R. Rossi, R. Hoffmann, *Inorg. Chem.* **1975**, *14*, 365–374.
[139] K.N. Raymond, P.W.R. Corfield, J.A. Ibers, *Inorg. Chem.* **1968**, *7*, 1362–1372.
[140] D. Schaniel, T. Woike, N.-R. Behrnd, J. Hauser, K.W. Krämer, T. Teodorova, B. Delley, *Inorg. Chem.* **2009**, *48*, 11399–11406.
[141] A. Klein, Y. von Mering, A. Uthe, K. Butsch, D. Schaniel, N. Mockus, T. Woike, *Polyhedron* **2010**, *29*, 2553–2559.
[142] M.H.B. Stiddard, R.E. Townsend, *J. Chem. Soc. D* **1969**, 1372.
[143] D.J. Hodgson, N.C. Payne, J.A. McGinnety, R.G. Pearson, J.A. Ibers, *J. Am. Chem. Soc.* **1968**, *90*, 4486–4488.
[144] A. Altomare, M.C. Burla, M. Camalli, E.L. Cascarano, C. Giacovazzo, A. Guagliardi, A.G.G. Moliterni, G. Polidori, R. Spagna, *J. Appl. Crystallogr.* **1999**, *32*, 115–119.
[145] G.M. Sheldrick, *Acta Crystallogr. A* **1990**, *46*, 467–473.
[146] G.M. Sheldrick, *Acta Crystallogr. A* **2008**, *64*, 112–122.
[147] G.M. Sheldrick, SADABS Version 2: Multi-scan Absorption Correction Program, **2001**.
[148] A.L. Spek, PLATON: A multipurpose Crystallographic Tool, **2008**.
[149] C.F. Macrae, P.R. Edgington, P. McCabe, E. Pidcock, G.P. Shields, R. Taylor, M. Towler, J. van de Streek, MERCURY: Visualisation and analysis of cystal structures, J. Appl. Cryst. **2006**, *39*, 453–457.
[150] C.K. Johnson, M.N. Burnett, L.J. Farrugia, ORTEP-III: Thermal Ellipsoid Plot Program for Crystal Structure Illustrations, **1999**.
[151] E. Keller, SCHAKAL99: A Fortran Program for the Graphical Representation of Molecular and Crystallographic Models, **1999**.
[152] W. Massa, *Kristallstrukturbestimmung*, 6. Edition, Vieweg+Teubner, Wiesbaden **2009**.
[153] H.-B. Bürgi, M. Förtsch, *J. Mol. Struct.* **1999**, *485–486*, 457–463.
[154] H.-B. Bürgi, *Annu. Rev. Phys. Chem*. **2000**, 51, 275–296.
[155] H.-B. Bürgi, S.C. Capelli, *Helv. Chim. Acta* **2003**, *86*, 1625–1640.
[156] P. Coppens, I. Novozhilova, A. Kovalevsky, *Chem. Rev.* **2002**, *102*, 861–883.
[157] W. Kohn, L.J. Sham, *Phys. Rev.* **1965**, *137*(6A), 1697–705.
[158] W. Kohn, L.J. Sham, *Phys. Rev.* **1966**, *145*(2), 561–567.
[159] H.D. Flack, *Acta Cryst. A* **1983**, 39, 876–881.

Danksagung

Mein Dank gilt allen, die durch ihre Unterstützung zu dieser Arbeit beigetragen haben:

Ich danke Herrn Prof. Dr. Peter Klüfers für die freundliche Aufnahme in seinen Arbeitskreis und eine Themenstellung, die mir die Auseinandersetzung mit einer interessanten, vielfältigen und schönen Chemie ermöglicht hat. Ebenso bedanken möchte ich mich für den gewährten wissenschaftlichen Freiraum bei der Bearbeitung dieses Themas, die hervorragenden Arbeitsbedingungen sowie wertvolle Anregungen.

Herrn Prof. Dr. Hans-Christian Böttcher danke ich für wichtige Anregungen in der Chemie der Metallnitrosyle und zur Erstellung des Zweitgutachtens für die vorliegende Arbeit.

Besonderer Dank gilt ebenso Herrn Prof. Dr. Dominik Schaniel und Dr. Theo Woike für die sorgfältigen und gewissenhaften PLI- und Tieftemperatur-IR-Messungen meiner Proben sowie hilfreiche Kommentare und Anregungen aus dem Blickwinkel der Physik.

Frau Lida Holowatyj-den Toom danke ich für die Hilfe bei allen organisatorischen Dingen, das Korrekturlesen von Publikationen und der vorliegenden Arbeit sowie ihre stets herzliche und hilfsbereite Art.

Frau Christine Neumann und Sandra Albrecht danke ich vielmals für geteiltes Leid und geteilte Freude beim "großen Kristallisationsexperiment für die Neutronenbeugung".

Xaver Kästele und Christine Neumann danke ich für wertvolle praktische Tipps, die wichtigen Hinweise zur Laborsicherheit und ihre stete Hilfsbereitschaft.

Sandra Albrecht, Helene Giglmeier und Dr. Peter Mayer danke ich für geduldige und gründliche Einführung in die Praxis des Kristallaufsetzens.

Den Administratoren – Thorsten Allscher, Martin Steinborn Markus Wolf und Xaver Wurzenberger – danke ich vielmals für die schnelle Behebung jeglicher computerbezogener Probleme.

Herzlichen Dank auch an jene, die mir bei der Durchsicht der Arbeit geholfen haben: Anja Belz, Thomas Hörner, Leonie Lindner, Christine Sturm, Markus Wolf und Xaver Wurzenberger.

Thorsten Allscher, Tobias Mayer und Richard Betz möchte ich für die Einführung ins Lösen von Kristallstrukturen danken.

Sämtlichen Mitgliedern des Arbeitskreises Klüfers, denen ich im Verlaufe meiner Doktorarbeit begegnen durfte, danke ich vielmals für die stets hilfsbereite, freundschaftliche Atmosphäre und die schönen gemeinsamen Stunden, vor allem meinen lieben Laborkollegen Sarah Illi, Xaver Kästele und Anja Belz.

Herzlichen Dank auch an alle meine F-Praktikanten – Thorben Schlücker, Min Zhang und Meike Simon – und "Bacheloranden" – René Rahimoff, Midori Shiratori, Anna Kaufmann, Nathalie Rott und Johannes Ketterle – für ihre sorgfältige, gewissenhafte und fleißige Mitarbeit an meinem Promotionsthema.

Großer Dank gilt den Mitarbeitern der Analytik – Herrn Peter Mayer, Frau Christine Neumann, Herrn Robert Eicher, Frau Gertraud Käser, Frau Brigitte Breitenstein, Dr. Werner Spahl, Dr. Peter Mayer und Prof. Dr. Konstantin Karaghiosoff – für das engagierte Messen meiner Proben.

Meiner Familie und meinem Mann danke ich für die jahrelange Unterstützung während des Studiums und der Promotion.

Posterpräsentationen

A. Gallien, M. Wolf, P. Klüfers: MNICs, DNICs und deren Ruthenium-Analoga, 8*. Koordinationschemie-Treffen* **2012**, Darmstadt.

A. Gallien, P. Klüfers: DNIC-analoge Rutheniumverbindungen, *16. Vortragstagung der Wöhlervereinigung für Anorganische Chemie* **2012**, Göttingen.

A. Gallien, P. Klüfers: $\{Ru(NO)_2\}^8$ Komplexe des Typs $[RuX(NO)_2(PR_3)_2]BF_4$, *9. Koordinationschemie-Treffen* **2013**, Bayreuth.

A. Gallien, P. Klüfers: Structural and spectroscopic properties of $\{Ru(NO)_2\}^8$ compounds of the general formula $[RuX(NO)_2(PR_3)_2]BF_4$, *Bioinorganic Symposium* **2013**, München.